



**HAL**  
open science

# Flow-Induced Vibrations and Noise of Periodic Structural Systems

Fabrizio Errico

► **To cite this version:**

Fabrizio Errico. Flow-Induced Vibrations and Noise of Periodic Structural Systems. Other. Université de Lyon; Università degli studi di Napoli Federico II, 2020. English. NNT: 2020LYSEC002 . tel-02877526

**HAL Id: tel-02877526**

**<https://theses.hal.science/tel-02877526>**

Submitted on 22 Jun 2020

**HAL** is a multi-disciplinary open access archive for the deposit and dissemination of scientific research documents, whether they are published or not. The documents may come from teaching and research institutions in France or abroad, or from public or private research centers.

L'archive ouverte pluridisciplinaire **HAL**, est destinée au dépôt et à la diffusion de documents scientifiques de niveau recherche, publiés ou non, émanant des établissements d'enseignement et de recherche français ou étrangers, des laboratoires publics ou privés.

N° d'ordre NNT : 2020LYSEC02



# THÈSE DE DOCTORAT DE L'UNIVERSITÉ DE LYON

opérée au sein de l'École Centrale de Lyon

en co-tutelle avec l'Università di Napoli Federico II

**École Doctorale ED162**

Mécanique - Énergétique - Génie Civil - Acoustique

Spécialité : Génie Mécanique

par :

**Fabrizio ERRICO**

---

## Flow-Induced Vibrations and Noise in Periodic Structural Systems

---

Jury composé de :

Alain BERRY, Université de Sherbrooke  
Randolph LEUNG, The Hong Kong Polytechnic University

Rapporteur

Rapporteur

Jean-François DEÛ, CNAM Paris  
Annalisa FREGOLENT, Università di Roma la Sapienza  
Romain RUMPLER, KTH Royal Institute of Technology  
Andrea CAMMARANO, University of Glasgow

President

Examinatrice

Examinateur

Examinateur

Olivier BAREILLE, École Centrale de Lyon  
Francesco FRANCO, Università di Napoli Federico II  
Sergio DE ROSA, Università di Napoli Federico II  
Mohamed ICHCHOU, École Centrale de Lyon

Co-Directeur Invité

Co-Directeur Invité

Co-Directeur de thèse

Directeur de thèse



# Acknowledgements

These last three years have been a tortuous, difficult, formative and beautiful journey. At the beginning I wanted to explore and rock everything. I was a boy who left home for the first time to go live in a foreign country, of which he knew only "Bonjour", "Merci", "Baguette" and "Zidane".

Today, after three intense years, I appreciate this country so much; it has welcomed me and helped me grow so much that it wants to live there. The little boy has turned into a more mature man, who has seen, at least, how the world goes for good and bad things.

Now is the time for new challenges and new stimuli. I will have a baggage of experience that I could acquire only thanks to some people that I will list here.

Thanks to Prof S. De Rosa and Prof. F. Franco from UniNa and Prof. M. Ichchou and Prof. O. Bareille from ECL for giving me this opportunity among dozens and dozens of candidates. Thank you for supporting and guiding me on an ambitious research path and also going further when difficulties have arisen.

Thanks to all the VIPER members for the good times shared in the various conferences and meetings.

Thanks to H. Beriot, S. Le Bras and O. Atak for the welcome, support and experience in Siemens.

Thanks to F. Castelli, M. Bergamini and M. Maggioni for having hosted me and the legendary Dino for the good times spent in Lamiflex.

Thanks to Prof. N. Atalla and O. Robin for welcoming us and teaching us their secrets on testing at the Université de Sherbrooke.

Thanks to Jean-Marc, Nassardin, Benoit, Lyes, Giulia, Christophe and Pascal for having enlivened the days and having shared some good moments in the E6, where we were surrounded by an environment not so gentle for foreigners.

Thanks to Alessandro, Mirko, the Russos, Rekkia, Fabrizio, Nicola, Manuel, Luca, Lorenzo, Erasmo, Gigi and Renato for not letting the distance modify our relationship.

Thanks to the people without whom I could not have had such fun in these three years. Thanks to Dario for making us "go crazy" and "feed badly". Thanks to Giuseppe and Alessandro for having always found the way to have fun even in bizarre offices and in conditions that only those who work in Naples can imagine. Thanks to Giovanni "Juen", the "Trusted Brother" with whom I shared professional and private life for more than six years, with the hope of continuing, even though we are getting old. Thanks to the brilliant minds that allowed us to play and have fun on the various "cavall! Rall' a ber...", "cucc n'daer", "Karekeyo", "Joseff" etc etc...

A special thanks to the people who tried to hinder this path, with moves more or less mean. Thanks to you I have matured and improved.

An equally special thanks to the people who instead have always supported me, regardless of the different paths we have taken.

Thanks to Jeremy, Roberto, Stefano, Marco, Dario, Giorgio, Pietro, Luca, for the wonderful moments spent together and the friendship. As the magic Stefano said in one of his moments: "We found ourselves alone and in foreign land and we helped ourselves. our bond will never end."

Thanks to Jacques for always helping me in times of difficulty and being a great person.

Thanks to Miriam, for being a special woman and for what she means to me today.

And finally, Thank you to my Family. I have never felt their support wavering even in small things. To my Mother Valeria and my Father Antonio, who, after so many sacrifices, have seen their children leave to explore the world, I say: your children are proud of you and they understand only now your efforts and your love. Even if we might be on the other side of the world, we will always be with you and we can make the "difference" through your teachings... Whether it was given with a "cucchiarella", a flower or a "zoccolo", it doesn't matter. To my sister Claudia, the most important person to me. A woman with attributes who helped me from the moment she threw me newborn, careless of danger, through the hospital halls, until she supported me at the beginning of this adventure, when they didn't even want to rent me the  $15m^2$  studio because I didn't have French parents.

Grazie a Tutti e...Forza Napoli.

# Ringraziamenti

Questi ultimi tre anni sono stati un percorso tortuoso, difficile, formativo e bellissimo. Ai blocchi di partenza avevo voglia di esplorare e spaccare tutto. Ero un ragazzino che per la prima volta abbandonava casa per andare a vivere in un paese straniero, di cui conosceva solo i vari "Bonjour", "Merci", "Baguette" e "Zidane".

Oggi, dopo tre anni intensi, apprezzo talmente tanto questo paese, che mi ha accolto e che mi ha aiutato a crescere, da volerci vivere. Il ragazzino si è trasformato in un uomo più maturo, che ha visto, pur in minima misura, come funziona il mondo, nel bene e nel male.

Ora è tempo di nuove sfide e nuovi stimoli. Li affronterò con un bagaglio di esperienza che ho potuto acquisire solo grazie ad alcune persone che elencherò qui.

Grazie al Prof S. De Rosa e Prof. F. Franco di UniNa e il Prof. M. Ichchou e Prof. O. Bareille di ECL per avermi dato questa opportunità tra decine e decine di candidati. Grazie per avermi supportato e guidato in un percorso di ricerca ambizioso ed essere andati anche oltre quando si sono presentate delle difficoltà.

Grazie ai membri di VIPER per i bei momenti condivisi nelle varie conferenze e riunioni.

Grazie a H. Beriot, S. Le Bras e O. Atak per l'accoglienza, il supporto e l'esperienza in Siemens.

Grazie a F. Castelli, M. Bergamini e M. Maggioni per avermi ospitato e il mitico Dino per i bei momenti trascorsi in Lamiflex.

Grazie al Prof. N. Atalla e O. Robin per averci accolto ed insegnato i loro segreti sulla parte sperimentale all'Université de Sherbrooke.

Grazie a Jean-Marc, Nassardin, Benoit, Lyes, Giulia, Christophe e Pascal per aver allietato le giornate ed aver condiviso dei bei momenti nell'E6, dove siamo stati circondati da un ambiente ostico agli stranieri.

Grazie ad Alessandro, Mirko, the Russos, Rekkia, Fabrizio, Nicola, Manuel, Luca, Lorenzo, Erasmo, Gigi e Renato per non aver lasciato che la distanza estinguesse il nostro rapporto.

Grazie alle persone senza le quali non avrei potuto passare dei momenti di grande divertimento in questi tre anni. Grazie a Dario per averci fatto "uscire pazzi" ed "allattare male". Grazie a Giuseppe ed Alessandro per aver trovato sempre il modo di divertirci anche in uffici indecenti e in condizioni che solo chi lavora a Napoli può immaginare. Grazie a Giovanni "Juen", il "frato fidato" con cui condivido vita professionale e privata da più di sei anni, con la speranza di continuare ancora, pur essendo diventati grandi. Grazie ai geni che ci hanno permesso di giocare sui vari "Cavall! rall' a ber...", "Cucc n'daer", "Karekeyo", "Joseff" ecc ecc...

Un Grazie particolare alle persone che hanno provato ad ostacolare questo percorso, con mosse più o meno meschine. Grazie a voi sono maturato e migliorato.

Un Grazie altrettanto particolare alle persone che invece mi hanno sempre supportato, indipendentemente dalle strade prese.

Grazie a Jeremy, Roberto, Stefano, Marco, Dario, Giorgio, Pietro, Luca, per i bellissimi momenti passati insieme e l'amicizia che ci lega. Come disse il buon Stefano in uno dei suoi magici momenti: "Ci siamo trovati soli e in terra straniera e ci siamo aiutati. Il nostro legame non si interromperà mai."

Grazie a Jacques per avermi sempre aiutato nei momenti di difficoltà ed essere una persona fantastica.

Grazie a Miriam, per essere una donna speciale e per quello che significa oggi per me.

Ed infine, Grazie alla mia Famiglia. Non ho mai sentito vacillare il loro supporto anche nelle piccole cose. A mia Madre Valeria e mio Padre Antonio, che, dopo tanti sacrifici, hanno visto i propri figli partire per esplorare il mondo, dico: i vostri figli sono orgogliosi di voi e che capiscono solo ora i vostri sforzi e il vostro amore. Anche se dovessimo essere dall'altra parte del mondo, saremo sempre con voi e potremo fare la "differenza" grazie ai vostri insegnamenti...Che siano stati impartiti con una cucchiarella, un fiore o con uno zoccolo, poco importa. A mia Sorella Claudia, la persona per me più importante. Una donna con gli attributi che mi ha aiutato da quando mi lanciava appena nato, incurante del pericolo, tra i corridoi dell'ospedale, fino a quando mi ha supportato, all'inizio di questa avventura, quando non volevano fittarmi neanche lo scantinato di 15  $m^2$  perchè non avevo i genitori francesi.

Grazie a Tutti e...Forza Napoli.

# Abstract

Most of the literature considers different works on the flow-induced noise and vibrations for basic structural parts, such as Kirchhoff plates. The main objective of this research is to extend the work done to periodic structures targeting a number of novelties with regards to different scales: the aerodynamic scale, the periodicity scale and the frequency scale.

Even though analytical and Finite Element (FE)-based numerical approaches have been developed to deal with specific problems, some limits still persist. For example, the computational effort can easily become cumbersome even for simple structural shapes or for increasing excitation frequency; the convective wavelengths, for most industrially-relevant cases, are largely smaller than flexural ones and, thus, the meshing requirements become more demanding. When the structural complexity increases, even small scale models might require a high number of elements increasing computational cost.

In the frameworks of FE and WFE based methods, this work proposes two numerical approaches to deal with the vibrations and noise induced by a Turbulent Boundary Layer (TBL) excitation on periodic structural systems.

Firstly, a 1D WFE (Wave Finite Element) scheme is developed to deal with random excitations of flat, curved and tapered finite structures: multi-layered and homogenised models are used. In this case a single substructure is modelled using finite elements. At each frequency step, one-dimensional periodic links among nodes are applied to get the set of waves propagating along the periodicity direction; the method can be applied even for cyclic periodic systems. The set of waves is successively used to calculate the Green transfer functions between a set of target degrees of freedom and a subset representing the wetted (loaded) ones. Subsequently, using a transfer matrix approach, the flow-induced vibrations are calculated in a FE framework.

Secondly, a 2D WFE approach is developed in combination with a wavenumber-space load synthesis to simulate the sound transmission of infinite flat, curved and axisymmetric structures: both homogenised and complex periodic models are analysed. In this case, finite-size effects are accounted using a baffled window equivalence for flat structures and a cylindrical analogy for curved panels.

The presented numerical approaches have been validated with analytical, numerical and experimental results for different test cases and under different load conditions. In particular, analytical response and classic FEM have been used as references to validate the flow-induced vibrations of plates and cylinders under turbulent boundary layer load; FE method has been used also to validate a tapered conical-cylindrical model under diffuse acoustic field excitation and the flow-induced noise computations under TBL.

From experimental point of view, the approach has been validated comparing results in terms of transmission loss evaluated on aircraft fuselage panels (composite honeycomb and doubly-ribbed curved panels) under diffuse acoustic field excitation.

Finally, the use of the presented methodologies for the vibroacoustic optimization of sand-

wich plates, is analysed and proposed through some case-studies. Standard periodic core designs are modified tailoring the bending and shear waves' propagation versus frequency against the acoustic and convective wavenumbers. The resulting sound transmission losses are computed using the numerical approaches developed in this work and validated with measurements under diffuse acoustic field, taken from 3D-printed models. Strong increases of sound transmission loss are observed for fixed mass of the plates and between 1.5 kHz and 10 kHz.

# Résumé

La plupart de la littérature considère différents travaux sur le bruit et les vibrations induit par l'écoulement du fluide pour les pièces structurales de base, comme les plaques de Kirchhoff. L'objectif principal de cette recherche est d'étendre le travail effectué à des structures périodiques ciblant un certain nombre de nouveautés en ce qui concerne différentes échelles: l'échelle aérodynamique, l'échelle de périodicité et l'échelle de fréquence.

Même si des approches analytiques et numériques fondées sur des éléments finis (FE) ont été élaborées pour traiter des problèmes particuliers, certaines limites persistent. Par exemple, l'effort de calcul peut facilement devenir lourd même pour les formes structurales simples ou pour augmenter la fréquence d'excitation; les longueurs d'onde convectives, pour la plupart des cas d'intérêt industriel, sont largement plus petites que les longueurs d'onde flexionnelles et, par conséquent, les maillages deviennent plus exigeantes. Lorsque la complexité structurelle augmente, même les modèles à petite échelle peuvent nécessiter un grand nombre d'éléments augmentant le coût de calcul.

Dans les cadres des méthodes basées sur la FE, ce travail propose deux approches numériques pour traiter les vibrations et le bruit induits par une excitation de la couche limite turbulente (TBL) sur les systèmes structurels périodiques. Tout d'abord, une méthode 1D WFE (Wave Finite Element) est développée pour traiter les excitations aléatoires de structures finies plates, courbes et coniques: modèles multicouches et homogénéisés sont utilisés. Dans ce cas, une seule sous-structure est modélisée à l'aide d'éléments finis. À chaque pas de fréquence, des liens périodiques unidimensionnels entre les noeuds sont appliqués pour obtenir l'ensemble des ondes se propageant le long de la direction de la périodicité; la méthode peut être appliquée même pour les systèmes périodiques cycliques.

L'ensemble des vagues est successivement utilisé pour calculer les fonctions de transfert de Green entre un ensemble de degrés de liberté cibles et un sous-ensemble représentant les zones chargées. En utilisant une matrice de transfert, les vibrations induites par l'écoulement sont calculées dans un cadre FE.

Ensuite, une approche 2D WFE est développée en combinaison avec une synthèse de charge basé sur le nombre d'ondes pour simuler la transmission sonore de structures infinies plates, courbes et axisymétriques: des modèles périodiques homogénéisés et complexes sont analysés. Dans ce cas, les effets de taille finie sont comptabilisés en utilisant une équivalence pour les structures plates et une analogie cylindrique pour les panneaux courbes. Les approches numériques présentées ont été validées avec des résultats analytiques, numériques et expérimentaux pour différents cas d'essai et dans des conditions de charge différentes. En particulier, la réponse analytique et la FEM classique ont été utilisées comme références pour valider les vibrations des plaques et des cylindres sous charge de la couche limite turbulente; la méthode FE a également été utilisée pour valider une structure complexe et effilée sous excitation acoustique diffuse et le calcul du bruit induit par couche limite turbulente. Du point de vue expérimental, l'approche a été validée en comparant les résultats en termes

de perte de transmission acoustique évaluée sur les panneaux de fuselage des avions (panneaux composites en nid d'abeille et panneaux courbes à double nervure) sous excitation diffuse du champ acoustique.

Enfin, l'utilisation des méthodologies présentées pour l'optimisation vibroacoustique des plaques sandwich, est analysée et proposée à travers certaines études de cas. Les conceptions périodiques standard du cœur sont modifiées en adaptant la propagation des ondes de flexion et de cisaillement par rapport à la fréquence, aux nombres d'ondes acoustiques et convectives. Les transmissions du son sont calculées à l'aide des approches numériques développées dans ce travail et validées avec des mesures sous champ acoustique diffus avec des modèles imprimés en 3D. De fortes augmentations de la perte de transmission sonore sont observées entre 1,5 kHz et 10 kHz, pour une masse fixe des plaques.

# List of Publications

The following manuscript is based on these manuscripts and/or part of them.

## International Journals (Peer-Reviewed)

- **F. Errico**, M. Ichchou, F. Franco, S. De Rosa, O. Bareille, C. Droz, *Schemes for the sound transmission of flat, curved and axisymmetric structures excited by aerodynamic and acoustic sources*, Journal of Sound and Vibrations, 476, 221-238, 2019.  
doi: /10.1016/j.jsv.2019.05.041.
- **F. Errico**, G. Tufano, O. Robin, N. Guenfoud, M. Ichchou, N. Atalla, *Simulating the sound transmission loss of complex curved panels with attached noise control materials using periodic cell wavemodes*, Applied Acoustics 156, 21-28, 2019.  
doi: /10.1016/j.apacoust.2019.06.027
- **F. Errico**, M. Ichchou, S. De Rosa, O. Bareille, F. Franco, *The modelling of the flow-induced vibrations of periodic flat and axial-symmetric structures with a wave-based method*, Journal of Sound and Vibrations 424, 32-47, 2018.  
doi: /10.1016/j.jsv.2018.03.012
- **F. Errico**, S. De Rosa, M. Ichchou, F. Franco, O. Bareille, *Dispersion curves of infinite laminate panels through a modal analysis of finite cylinders*, Wave Motion 83, 80-93, 2018.  
doi: /10.1016/j.wavemoti.2018.08.007.
- G. Tufano, **F. Errico**, O. Robin, C. Droz, M. Ichchou, B. Pluymers, W. Desmet, N. Atalla, *K-space analysis of complex large-scale meta-structures using the inhomogeneous wave correlation method*, Mechanical Systems and Signal Processing 135, 2020.  
doi: /10.1016/j.ymsp.2019.106407
- **F. Errico**, M. Ichchou, S. De Rosa, F. Franco, O. Bareille, *Investigations about periodic design for broadband increased sound transmission loss of sandwich panels using 3D-printed models*, Mechanical Systems and Signal Processing, 106432.  
doi: /10.1016/j.ymsp.2019.106432
- **F. Errico**, S. De Rosa, F. Franco, G. Petrone, M. Ichchou, *Aeroelastic effects on the wave propagation and sound transmission of plates and shells*, AIAA Journal, In Press.
- **F. Errico**, M. Ichchou, S. De Rosa, O. Bareille, F. Franco, *A WFE and Hybrid FE/WFE technique for the Forced Response of Stiffened Cylinders*, Advances in Aircraft and Spacecraft Science, Vol. 5 (1), 1–19, 2018.  
doi: /10.12989/aas.2018.5.1.001

- **F. Errico**, S. De Rosa, F. Franco, M. Ichchou, G. Petrone, *An investigation on the vibrations of laminated shells under aeroacoustic loads using a WFE approach*, Advances in Aircraft and Spacecraft Science, Vol. 6 (6), 463–479, 2018.  
doi:/10.12989/aas.2019.6.6.463

## International Conferences

- **F. Errico**, G. Petrone, F. Franco, S. De Rosa, M. Ichchou, *Passive Vibration Control of Tyres using Embedded Mechanical Resonators*, MEDYNA2020 – 3rd Euro-Mediterranean Conference on Structural Dynamics and Vibroacoustics, Naples - Italy, February 2020.
- **F. Errico**, M. Ichchou, F. Franco, S. De Rosa, G. Petrone, O. Bareille, *Experimental Investigation of reduced sound transmission of sandwich panels using 3D-printed models*, MEDYNA2020 – 3rd Euro-Mediterranean Conference on Structural Dynamics and Vibroacoustics, Naples - Italy, February 2020.
- **F. Errico**, M. Ichchou, S. De Rosa, F. Franco, O. Bareille, *On the effect of distributed embedded resonators in curved sandwich panels loaded by turbulent boundary layer*, SMART 2019 – 9th ECCOMAS Thematic Conference on Smart Structures and Materials, Paris - France, July 2019.
- **F. Errico**, S. De Rosa, F. Franco, M. Ichchou, G. Petrone, *The investigation of aeroelastic effects on the elastic wave propagation and radiated noise of periodic structures*, INTERNOISE 2019 – 48th International Congress and Exhibition on Noise Control Engineering, Madrid - Spain, June 2019.
- **F. Errico**, M. Ichchou, S. De Rosa, O. Bareille, F. Franco, *A load approximation for the vibroacoustic analysis of periodic structures to fluid excitation*, ISMA-USD Conference 2018, Leuven - Belgium, September 2018.
- **F. Errico**, M. Ichchou, S. De Rosa, O. Bareille, F. Franco, *A wave finite element technique for the the flow-induced vibrations of periodic and axial-symmetric structures*, Noise and Vibration Emerging methods - NOVEM2018, Balearic Islands - Spain, May 2018.

## Submitted/In Review

### Journal

- G. Tufano, **F. Errico**, M. Ichchou, W. Desmet, O. Bareille, B. Pluymers, *On the effect of axial and ring stiffeners on the vibro-acoustic response of curved structures*, Submitted to the Journal of Sound and Vibration.

# Contents

<b>1</b>	<b>Introduction</b>	<b>17</b>
1.1	Framework of the Research . . . . .	17
1.2	Motivations . . . . .	17
1.3	Thesis Outline . . . . .	19
<b>2</b>	<b>Literature Review</b>	<b>23</b>
2.1	Characterisation of Random Vibrations . . . . .	23
2.2	Aeroacoustic Excitations . . . . .	24
2.2.1	Models for TBL Autospectrum . . . . .	24
2.2.2	Models of TBL Correlation Functions . . . . .	27
2.2.3	Acoustic Excitation: Diffuse Acoustic Field . . . . .	29
2.3	Flow-Induced Vibrations and Noise . . . . .	30
2.3.1	Modal Approaches . . . . .	30
2.3.2	Energy Approaches . . . . .	34
2.3.3	Non-lifting Aeroelastic coupling . . . . .	36
2.4	Elastic Waves in Periodic Structures . . . . .	38
2.4.1	The Wave Finite Element Method . . . . .	39
2.5	Periodic Design Investigation . . . . .	44
2.5.1	Periodically Ribbed Structures . . . . .	45
2.6	Thesis Novelties versus Literature . . . . .	46
<b>3</b>	<b>Modelling the Flow-Induced Vibrations with a 1D WFE Approach</b>	<b>47</b>
3.1	The Proposed Method . . . . .	47
3.1.1	The Transfer Matrix Method . . . . .	47
3.1.2	The Wave Finite Element Method (WFEM) . . . . .	48
3.1.3	Curvature Simulation . . . . .	50
3.2	Forced Vibrations for a Punctual Load . . . . .	51
3.2.1	The Direct Field . . . . .	51
3.2.2	Waves at Boundaries . . . . .	52
3.2.3	The Scattering Matrix . . . . .	52
3.2.4	Waves Propagation . . . . .	53
3.2.5	Incident Field and Waves Superposition . . . . .	54
3.2.6	An axisymmetric 1D-WFE formulation for wavefields along circular paths . . . . .	55
3.2.7	Variable mesh for Homogenised Layers . . . . .	56
3.3	Results for Deterministic Load . . . . .	57
3.3.1	Results for periodicity along a rectilinear direction . . . . .	57

3.3.2	Results for periodicity along a circular direction . . . . .	60
3.4	Results for Stochastic Load . . . . .	64
3.4.1	Flat Panel under TBL excitation . . . . .	64
3.4.2	Un-stiffened Cylindrical Structure under TBL load . . . . .	65
3.4.3	Stacking Sequence Effects on the TBL-induced response of a Shell . . . . .	67
3.4.4	Stiffened Cylindrical Structure under TBL load . . . . .	68
3.4.5	Complex Axisymmetric Structure under Diffuse Acoustic Field . . . . .	70
3.5	Conclusions . . . . .	72
<b>4</b>	<b>The Prediction of the Flow-Induced Noise using a 2D Periodic Cell</b>	<b>75</b>
4.1	Introduction . . . . .	75
4.2	The Wave Finite element Method . . . . .	76
4.2.1	Modal Order Reduction: A Craig-Bampton Scheme . . . . .	77
4.2.2	Curvature Simulation . . . . .	78
4.2.3	Fluid-Structure Coupling . . . . .	79
4.2.4	A TMM-based extension for attached porous layers . . . . .	81
4.3	Stochastic Load Translation into Surface Waves . . . . .	82
4.3.1	Sound Transmission Loss . . . . .	84
4.4	Validations for Flat Structures . . . . .	85
4.4.1	Diffuse Acoustic Field load . . . . .	86
4.4.2	Turbulent Boundary Layer Excitation . . . . .	87
4.4.3	TBL Models: A flow-induced noise comparison . . . . .	89
4.5	Validations for Cylindrical Shells . . . . .	91
4.5.1	Diffuse Acoustic Field Transmission . . . . .	91
4.5.2	The Effective Transmission Loss of Cylinders . . . . .	92
4.6	Experimental Tests and Validations for Curved Panels . . . . .	94
4.6.1	Comparison with Literature Results . . . . .	94
4.6.2	Experimental Set-Up - Transmission Loss Measurements . . . . .	94
4.6.3	Thick Sandwich Panel . . . . .	98
4.6.4	Ribbed Aircraft Fuselage Panel . . . . .	99
4.7	Discussion on approximations and limits of the approach . . . . .	101
4.8	Convergence Aspects . . . . .	102
4.8.1	TBL Model: Corcos . . . . .	102
4.8.2	TBL Model: Chase . . . . .	104
4.8.3	The Influence of the Cross-Flow Components . . . . .	104
4.9	Conclusions . . . . .	107
<b>5</b>	<b>Non-Lifting Aeroelastic Coupling using WFE</b>	<b>109</b>
5.1	Introduction . . . . .	109
5.2	Aerodynamic Loading in Periodic Framework . . . . .	110
5.2.1	The Piston Theory . . . . .	110
5.2.2	Subsonic Aerodynamic Flows . . . . .	112
5.3	Numerical Results . . . . .	113
5.3.1	Wave Propagation in Plates and Shells . . . . .	113
5.3.2	Sound Transmission under Turbulent Boundary Layer . . . . .	115
5.4	Conclusion . . . . .	118

<b>6</b>	<b>Periodic Design for Reduced Sound Radiation</b>	<b>119</b>
6.1	Corrugated-Walls Design for Sandwich Panels . . . . .	120
6.1.1	Double-Wall Panel with Mechanical Links . . . . .	120
6.1.2	Rectangular-Cored Sandwich Panel . . . . .	121
6.1.3	Experimental Set-Up . . . . .	121
6.1.4	Waves Tailoring versus Acoustic Wavenumbers . . . . .	122
6.1.5	Sound Transmission Loss under DAF excitation . . . . .	127
6.2	Axial and Ring Stiffening of Curved Panels . . . . .	129
6.2.1	Effects on the Sound Transmission Loss . . . . .	129
6.2.2	The effect of pitch distance on sound radiation . . . . .	131
6.3	Embedded Resonators in Curved Panels . . . . .	134
6.3.1	Resonators' Efficiency for Different Excitation Models . . . . .	134
6.3.2	Resonators' Efficiency around the Ring Frequency of Shells . . . . .	137
6.3.3	Metamaterial Designs Analysed . . . . .	139
6.3.4	Dispersion Curves . . . . .	141
6.3.5	Sound Transmission Loss under TBL excitation . . . . .	141
6.4	Concluding Remarks . . . . .	144
<b>7</b>	<b>Conclusions and Prospectives</b>	<b>147</b>
7.1	Achievements . . . . .	147
7.2	Future Developments . . . . .	148
	<b>Appendices</b>	<b>149</b>
<b>A</b>	<b>Geometrical Details of Proposed Designs</b>	<b>151</b>
<b>B</b>	<b>Reducing Tyre Vibrations using Embedded Mechanical Resonators</b>	<b>153</b>
B.1	Introduction . . . . .	153
B.2	Proposed design . . . . .	153
B.2.1	Force vibrations of resonant configurations . . . . .	154
B.3	Concluding remarks . . . . .	157
<b>C</b>	<b>Dispersion of Periodic Media through Modal Analysis of Rings</b>	<b>159</b>
C.1	Introduction . . . . .	159
C.2	Reference Solutions . . . . .	160
C.2.1	Isotropic beam and plate . . . . .	161
C.2.2	The Classical Lamination Theory (CLPT) . . . . .	161
C.3	The Proposed Analogy . . . . .	162
C.4	Validations . . . . .	164
C.4.1	Analytic Validation: Infinite Beam and Ring . . . . .	164
C.4.2	Analytic Validation: Infinite Cylinder Ovaling Modes . . . . .	165
C.4.3	Numerical Validation: Isotropic Panel . . . . .	167
C.4.4	Laminated Panel . . . . .	167
C.4.5	Complex Structural Shapes . . . . .	172
C.5	Conclusions . . . . .	174



# Chapter 1

## Introduction

### 1.1 Framework of the Research

This project has received funding from the European Union's Horizon 2020 research and innovation programme under the Marie Skłodowska-Curie grant agreement No. 675441. The research of the candidate is conducted following the Early Stage Researcher No. 2 objectives and topics within the VIPER Project. The research topic in question is *Aerodynamic Loading of Periodic Structures*.

VIPER is a European Joint Doctorate network focused on research in Vibroacoustic of Periodic media. Structural periodic design is a powerful strategy for lightweight structures achievements while remaining a convenient solution for manufacturing aspects. One of the research targets is the inclusion of vibroacoustic design rules at early stage of products development through the use of periodic media which exhibit proper dynamic filtering effects. In order to understand how periodic concepts can improve the broadband vibroacoustic signatures and performances, the VIPER project aims at developing and validating tools for the design of global vibroacoustic treatments based on periodic patterns, allowing passive control of structural and acoustical paths in layered concepts.

Dealing with large scale periodic structural-acoustic concepts involves a multi-scale aspect that needs specific numerical tools. A two scale strategy will be pursued to handle periodicity effects: the meso-scale, related to the cell or the span size, and the macro-scale related to the final structure size. Bridging the cell scale behaviour and the vibroacoustic indicators is a challenging issue which will dramatically improve the macro structural design. As the cell topology and constitutive materials are important data, VIPER considers the combination of different materials and structural arrangements, in which viscoelastic, poroelastic, auxetic materials will play a major role.

VIPER has a multi-disciplinary character, coupling expertise from material science, vibration and acoustics as well as applied mathematics. It can offer different applications in transports (aeronautics and space, automotive), energy and civil engineering sectors, where vibroacoustic integrity and comfort can be crucial points.

### 1.2 Motivations

Flow-induced vibrations are among the major causes of high noise levels and, thus, reduced internal comfort, for almost all modern transport means. It is a main issue in the aeronautical, automotive, naval and rail industry.

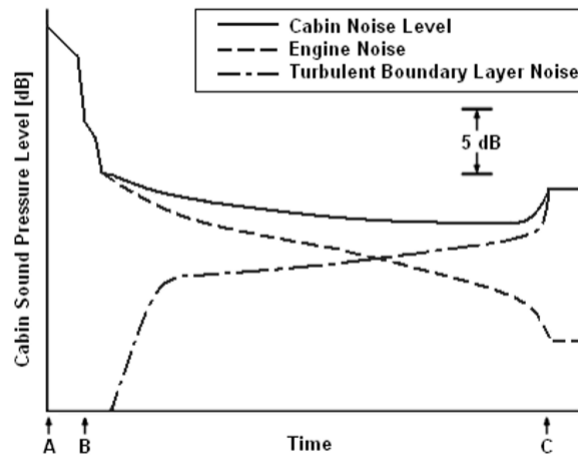


Figure 1.1: Typical noise levels in a jet aircraft cabin during take-off and climb to cruising altitude, as described in [1]; A) start of take-off roll; B) lift-off from the runway; C) stabilized level flight at cruising altitude and air speed.

Aircraft interior noise is, in reality, a result of several sources:

- Blade passage frequency tones of the engines and their harmonics (for propellers) and/or jet noise (for turbofans/jets).
- Structure-borne noise caused by un-balanced forces within the engines (inducing vibrations into the aircraft structure).
- On-board systems, such as the auxiliary power unit, pressurization and air-conditioning systems.
- Aerodynamic noise, in which turbulent boundary layer induced noise is included, which is characterized by a fluctuating pressure field, random by nature, which excites the fuselage skins.

The turbulent boundary layer is the highest contributor to internal flow-induced noise in an aircraft cabin, in cruise flight conditions, which are, for commercial passenger aircraft, the operations conducted for the majority of the flight time [1]. The situation gets even worse with increasing flight speed [2]. Reduced levels of cabin noise, which can only be achieved by using dedicated predictive tools, are desirable both for comfort and health-related issues of the passengers. High low-frequency noise levels, especially for long-time exposures, can produce hearing loss, fatigue, loss of concentration, and reduced comfort [3, 4]. Particularly, the low-frequency sound can lead to annoyance, deficit of attention, reduced wakefulness and sleep disturbances; in the worst cases the respiratory, heart, stomach and intestine functions can be altered by the environment.

In addition to the comfort and health problems typical of transport means, another main engineering issues caused by the flow-induced vibrations is connected to space launch vehicles. Missile and launchers' fairings are subject to a strong aeroacoustic environment, random in nature and of frequency broadband extent. This arousal of noise and vibrations may deteriorate fragile structures and equipment, including electronic components of on-board

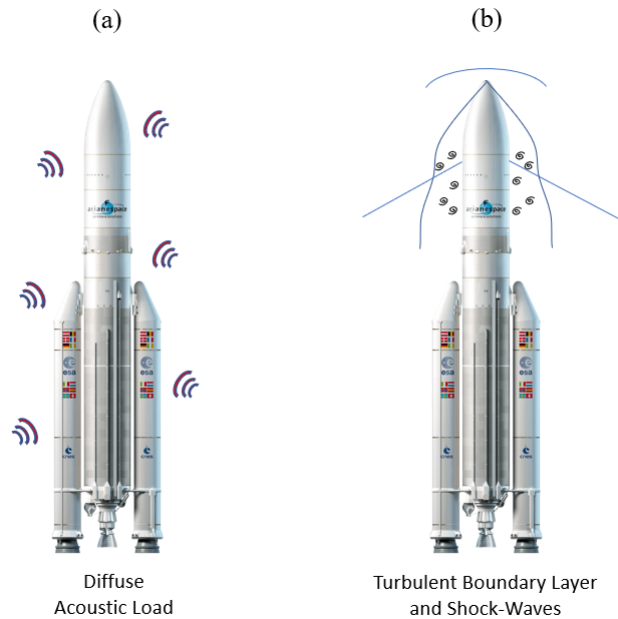


Figure 1.2: Typical aeroacoustic loadings on a space launcher structure during the lift-off (a) and the ascent phase (b).

equipments. Aeroacoustic fatigue can even occur for reusable components. These strong pressure fluctuation levels influence the weight and the cost of the launch vehicle. Then, it is necessary to carry out a predictive model of the structure and model the fluid-structure interaction properly, in order to determine the vibration levels of the structures and internal equipment, in the entire frequency spectrum, before the system gets operational. Nowadays most of the methodological issues are associated with the complexity of the analytical modelling and the computational cost of the numerical simulations.

### 1.3 Thesis Outline

This manuscript is organised as follows:

- Chapter 2 gives a literature review to frame the state-of-the-art methods and researches connected the similar topics.
- Chapter 3 proposes a combination of a WFE and transfer matrix (TM) method to compute the flow-induced vibrations of structures with linear and cyclic periodicity. Enhanced WFE formulations are developed for the forced response of flat, curved and axisymmetric finite periodic structures with and without impedance variations along the waveguides. Validations are proposed using full finite element (FEM) computations and analytical methods.
- Chapter 4 develops a 2D WFE approach for the prediction of the flow-induced noise of periodic flat and curved structures. A load approximation in the wavenumber domain is developed to link any type of excitation with the structural periodicity scale. The

results are validated for homogeneous and heterogeneous flat and curved structures using analytical, numerical and experimental results.

Experimental tests are performed in coupled reverberant-semi-anechoic rooms; a large scale thick composite sandwich panel and a thin aluminium fuselage panel with stiffening elements (stringers and frames) are analysed for validation purposes.

- Chapter 5 analyses the possibility of including aeroelastic coupling within a periodic cell scale to include the effects of a stronger fluid-structure coupling in the prediction of the sound transmission loss under aerodynamic excitation. The effects of the one-sided flow are also studied on the elastic wave propagation identifying dynamic instabilities for supersonic flows.
- Chapter 6 shows a coupled numerical-experimental work on the periodic cell design. The numerical methods developed in the previous chapters are used to investigate some periodic designs and the chosen solutions are the 3D printed and tested in a small Transmission Loss facility. Experimental evidence of increased vibroacoustic performance for fixed structural mass are given.

A conceptual scheme is proposed in Fig. 1.3.

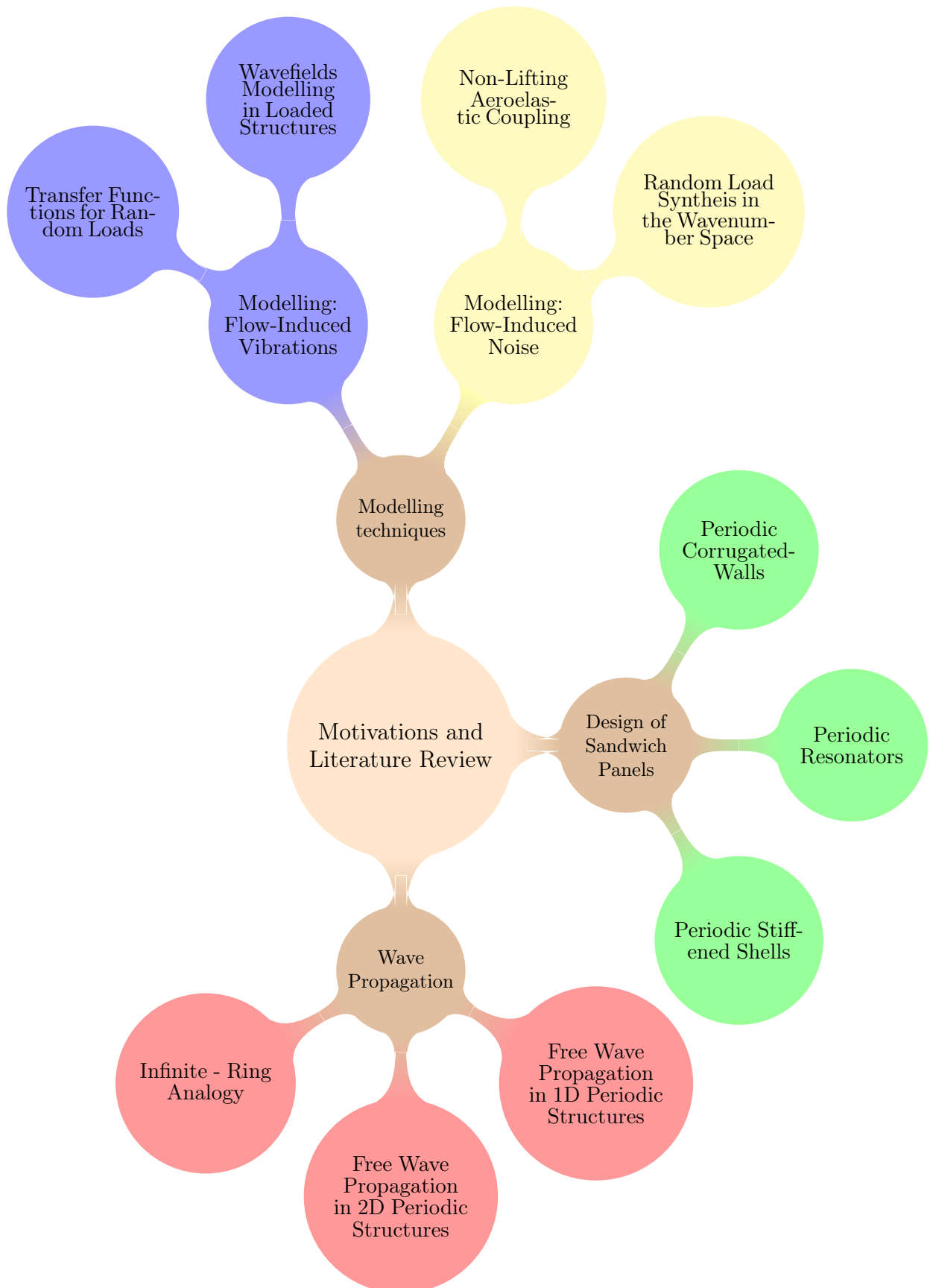


Figure 1.3: Conceptual map of the present work.



## Chapter 2

# Literature Review

The main focus of this work is placed on modelling the flow-induced vibrations and noise of periodic and homogeneous structures, in the most general combination of structural complexities and excitation models. Many authors, even though not specifically for periodic media, contributed to the vibroacoustic modelling of simple structural models under aeroacoustic sources. Higher order theories have also been developed to include the auto-excited forces induced by the coupling between the structural vibrations and the flow field.

Most of the approaches available in the literature, differ depending on the frequency region of interest. Generally, in fact, the structural dynamic behaviour might strongly change depending on the frequency of analysis. For example, in the Low Frequencies (LF), the response exhibits isolated modal resonances and has local characteristics. This region is usually investigated through deterministic methods, such as the Finite Element Method (FEM) and/or the Boundary Element Method (BEM). In the High Frequencies (HF), the diffuseness of the field prevents any isolated resonance condition and the response is independent on local parameters. In this cases the structure can be investigated through probabilistic techniques, such as the Statistical Energy Analysis (SEA) and/or the Energy Distribution Approach (EDA). Differently, the Mid Frequencies (MF), represent a region of intermediate behaviour for which well-established prediction techniques are not yet available; while actual FE-based method require an unacceptable computational effort due to the huge size of models, even for small structural scales, the assumptions of probabilistic methods are not valid yet.

In this chapter, most of the relevant literature is reviewed, for each of the macro areas investigated within the present manuscript.

### 2.1 Characterisation of Random Vibrations

The response to a random spatially-correlated load is expressed in terms of power spectral density, deduced from the correlation function, defined as [5]:

$$R_{pp}(\xi, \tau) = \langle p(\mathbf{r}, t) \cdot p(\mathbf{r} + \boldsymbol{\xi}, t + \tau) \rangle \quad (2.1)$$

where the symbol  $\langle \rangle$  denotes the statistical average, the vector  $\mathbf{r}$  measures the distance of a given point from the origin of the reference system, while the vector  $\boldsymbol{\xi}$  is the vector of the relative distance among two given points. The space-frequency spectrum can then be written as follows:

$$S_{pp}(\xi, \omega) = \int_{-\infty}^{+\infty} R_{pp} e^{-i\omega\tau} d\tau \quad (2.2)$$

The  $S_{pp}$  function can also be expressed, in a general form, as:

$$S_{pp}(\boldsymbol{\xi}, \omega) = S_p(\omega) \Gamma_{pp}(\xi_x, \xi_y, \omega) \quad (2.3)$$

where  $S_p$  is the single-point auto-spectral density of the pressure fluctuations;  $\Gamma_{pp}$  represents the correlation between two points whose relative distances in the stream-wise and cross-wise directions are  $\xi_x$  and  $\xi_y$ , respectively.

The pressure field is assumed to be blocked (or frozen); the wall-pressure fluctuations are not affected by the structural vibration and, thus, a one way coupling is hypothesised [6, 7]. The pressure field is thus the same as observed on a rigid wall. The power spectral density of the structural velocity can be expressed as follows from the generalized Green functions [5, 6]:

$$S_{vv}(x, y, \omega) = \omega^2 \sum_r \sum_s \operatorname{Re}(\alpha_r(\omega) \alpha_s^*(\omega)) \Psi_r(x, y) \Psi_s(x, y) \cdot \int_{A_p} \int_{A_p} \Psi_r(x, y) \Psi_s(x', y') S_p(\omega) \Gamma(\xi_x, \xi_y, \omega) dA_p dA_p \quad (2.4)$$

where  $\Psi_r$  is the structural mode shape,  $A_p$  the area of the structure wetted by the flow and  $\alpha_r$  the modal receptance of the structure:

$$\alpha_r(\omega) = \frac{1}{\omega_r^2(1 + i\eta_r) - \omega^2} \quad (2.5)$$

where  $\omega_r$  and  $\eta_r$  represent the natural pulsation and the structural damping factor of the mode  $\Psi_r$ . The stream-wise and cross-wise distances,  $\xi_x$  and  $\xi_y$ , are  $|x - x'|$  and  $|y - y'|$  respectively.

The most important factor in Eq. 2.4 is the joint acceptance function  $j_{rs}$  (Eq. 2.6). It is a double surface integral of the product of the correlation function of the load and the mode shapes of the structure. The main issue connected to Eq. 2.6 is given by the complexity and feasibility in expressing the structural mode shapes in analytical form and performing the integration of its product with a random, and generally exotic, correlation function  $\Gamma$ .

$$j_{rs}(\omega) = \frac{1}{A_p^2} \int_{A_p} \int_{A_p} \Psi_r(x, y) \Psi_s(x', y') \Gamma(\xi_x, \xi_y, \omega) dA_p dA_p \quad (2.6)$$

## 2.2 Aeroacoustic Excitations

The second-order statistics of the wall pressure fluctuations beneath a fully developed TBL are generally modelled as a random process, homogeneous in space and stationary in time, that can be characterised by the cross-spectral density function [5, 7].

### 2.2.1 Models for TBL Autospectrum

Most of the existent turbulent boundary layer models differ both for their autospectrum ( $S_p$  in Eq. 2.3) and correlation model ( $\Gamma$  in Eq. 2.3). These models are usually defined from empirical relations which depend on characteristic scales that might be different case-by-case.

A representation of a typical TBL autospectrum  $S_p$  is plotted in Fig. 2.1, as a function of the dimensionless frequency. The spectrum shows different characteristic slopes depending on

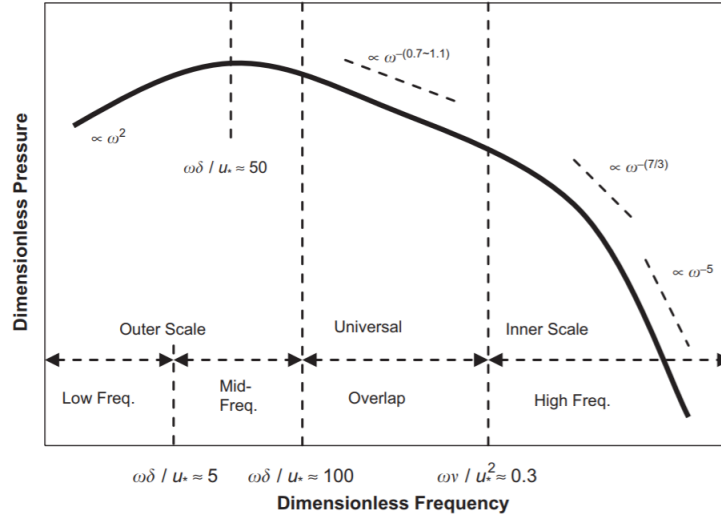


Figure 2.1: Representation of a TBL wall pressure spectrum for different frequency ranges [8].

the considered frequency range. There is no single-scaling that is able to represent correctly the spectrum over all the frequency ranges and thus several scales are used depending on the considered frequency region. They are presented in [8].

In particular, the displacement thickness  $\delta^*$  and the momentum thickness  $\theta^*$  are integral length scales defined by:

$$\begin{aligned} \delta^* &= \int_0^\delta \left(1 - \frac{U}{U_0}\right) dy \\ \theta^* &= \int_0^\delta \frac{U}{U_0} \left(1 - \frac{U}{U_0}\right) dy \end{aligned} \tag{2.7}$$

where  $U$  is the speed of the flow in the boundary layer,  $U_0$  the flow speed outside the boundary layer and  $\delta$  the thickness of the layer.

Some of the most common models are here reported:

### Corcos - Robert

This single-sided spectrum is defined as a function of the outer scaling variables  $U_0$ ,  $\delta^*$  and  $q$  (free-stream dynamic pressure) by the following relation [9]:

$$S_p(\omega) \left( \frac{U_0}{q^2 \delta^*} \right) = \begin{cases} 2 \cdot 2.14 \cdot 10^{-5} & \omega \delta^* / U_0 < 0.25 \\ 2 \cdot 7.56 \cdot 10^{-6} (\omega \delta^* / U_0)^{-0.75} & 0.25 < \omega \delta^* / U_0 < 3.5 \\ 2 \cdot 1.27 \cdot 10^{-4} (\omega \delta^* / U_0)^{-3} & \omega \delta^* / U_0 > 3.5 \end{cases} \tag{2.8}$$

For a flat plate with zero-pressure gradient, Finnveden et al. [10] showed that Robert model agrees with their experimental data with a maximum difference of 1 dB.

### Cockburn - Robertson

Cockburn and Robertson [11] calibrated the model when investigating the vibration response of spacecraft shrouds to in-flight fluctuating pressures. They established the following spectrum model  $S_p$  for flows at transonic and supersonic speeds, using empirical data:

$$S_p(\omega) \left( \frac{U_0}{q^2 \delta} \right) = \frac{E_{p^2}}{q^2 \left( \frac{\omega_0 \delta}{U_0} \right) \left[ 1 + \frac{\omega}{\omega_0} \right]^{0.9}} \quad (2.9)$$

where:

$$E_{p^2} = \left( \frac{0.006 \cdot q}{1 + 0.14 M_0^2} \right)^2; \quad \omega_0 = 2\pi \cdot 0.346 U_0 / \delta, \quad (2.10)$$

where  $M_0$  is the Mach number that becomes negligible at transonic and subsonic speeds [11].

### Smolyakov - Tkachenko

Smolyakov and Tkachenko [12] measured spatial pressure correlations as a function of spatial separation and boundary layer thickness, and fitted exponential curves to their results. The model of Smolyakov and Tkachenko writes as follows [12]:

$$S_p(\omega) \left( \frac{U_0}{\tau_\omega^2 \delta^*} \right) = \frac{5.1}{1 + 0.44 \left( \frac{\omega \delta^*}{U_0} \right)^{7/3}} \quad (2.11)$$

where  $\tau_\omega$  represents the wall-shear stress. The resulting low wavenumber levels are an improvement on the Corcos prediction, but are still higher than experimental values, so a correction was added to the model to bring it into agreement without significantly affecting the convective peak levels [13].

### Chase - Howe

Howe proposed the following model using the variable scaling  $\delta^*$  and  $\tau_\omega$  [8, 14]:

$$S_p(\omega) \left( \frac{U_0}{\tau_\omega^2 \delta^*} \right) = \frac{2\bar{\omega}^2}{(\bar{\omega}^2 + 0.0144)^{3/2}} \quad (2.12)$$

where  $\bar{\omega}^2 = \omega \delta^* / U_0$ . According to Hwang et al. [8], since this spectrum does not decay faster than  $\omega^{-1}$  at high frequencies, the model applicability appears to be limited near or below the universal range  $\omega \nu / u_\tau^2 < 0.3$ , being  $\nu$  the fluid viscosity and  $u_\tau$  the wall friction velocity.

### Efimtsov

The model proposed by Efimtsov [8, 15] accounts for the effects of the Reynolds number  $R_e$ . In particular, the autospectrum is expressed as:

$$\frac{S_p(\omega)}{\rho_0^2 u_\tau^3 \delta} = \frac{2\pi \alpha_r \beta_r}{(1 + 8\alpha_r^3 Sh^2)^{1/3} + \alpha_r \beta_r R_e (Sh/R_e)^{10/3}} \quad (2.13)$$

Table 2.1: TBL autospectrum models and input parameters

Model:	$U_0$	$\rho_0$	$u_\tau$	$\nu$	$\delta$	$\delta^*$	$\tau_\omega$	$R_e$
Corcos - Robert	●	○	○	○	○	●	○	○
Cockburn - Robertson	●	○	○	○	●	○	○	○
Smolyakov - Tkachenko	●	○	○	○	○	●	●	○
Chase - Howe	●	○	○	○	○	●	●	○
Efimtsov	○	●	●	●	●	○	○	●
Goody	●	○	●	●	●	○	●	●

where  $\alpha_r = 0.01$ ,  $\beta_r = (1 + (R_{e0}/R_e)^3)^{1/3}$ ,  $Sh = \omega\delta/u_\tau$  and  $R_{e0} = 3000$ . This model applies to zero-pressure gradient boundary layers. It has been calibrated from measurements of TBL wall pressure fluctuations on aircraft. It is valid for a wide range of Mach Number ( $0.01 < M_0 < 4$ ), Reynolds numbers ( $6 \cdot 10^2 < R_e < 1.5 \cdot 10^5$ ) and Strouhal numbers ( $0.2 < Sh < 10^4$ ).

### Goody

The Goody model is limited to zero pressure gradient flows but takes into account the effect of the Reynolds number variations through the time scale ratio  $R_T (= (\delta/U_0)/(\nu/u_\tau^2))$ . This model shows a good agreement with experimental data over the Reynolds number range [1400, 23400]. The spectrum can be expressed as:

$$S_p(\omega) \left( \frac{U_0}{\tau_\omega \delta} \right) = \frac{C_2(\omega\delta/U_0)^2}{[(\omega\delta/U_0)^{0.75} + C_1]^{3.7} + [C_3(\omega\delta/U_0)]^7} \quad (2.14)$$

where  $C_1 = 0.5$ ,  $C_2 = 3.0$ ,  $C_3 = 1.1R_T^{-0.57}$ .

A comparison between the different models is exploited in [8]. A comparison in terms of needed parameters and characteristics is summarised in Table 2.1.

### 2.2.2 Models of TBL Correlation Functions

The function  $\Gamma_{pp}(\xi_x, \xi_y, \omega)$  in Eq. 2.3 characterizes the spatial correlations of the wall pressure fluctuations. A generic correlation spectrum in the wavenumber domain ( $\Gamma_{pp}(k_x, k_y, \omega)$ ) is provided in [16] and reported in Fig. 2.2. Considering the wavenumber domain, an amplitude increase is evident for wavenumbers close to the convective wavenumber  $k_c = \omega/U_c$ , where  $U_c$  is the convective speed (generally  $0.8 U_0$ ) of the turbulent structures in the boundary layer. The energy part associated with the acoustic is centered around the origin  $k = 0$  and is bounded by the acoustic wavenumber  $k_0$ . Between the acoustic and hydrodynamic region, for  $k_0 < k < k_c$ , a sub-convective zone is identified.

Some of the most common models are here reported:

#### Corcos

The first characterisation of the wall pressure fluctuations of a turbulent boundary layer has been carried out by Corcos [9, 13], on experimental measurements. This model, which does not take into account the position of each point on the structure, considering just the relative distances, is one of the simplest and most used in literature. Specifically, the cross spectral

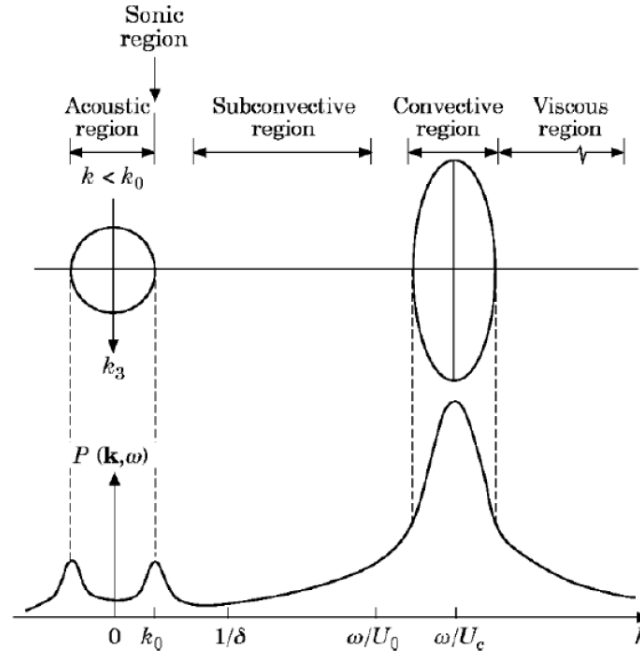


Figure 2.2: Correlation spectra  $\Gamma_{pp}$  in the wavenumber domain [16].

density of the pressure fluctuations, through the assumption of separation of variables, is function of the relative distance among points, the convection velocity and the frequency. The coherence model for the wall pressure fluctuations proposed by Corcos can be expressed through the product of two separate functions in the stream-wise and cross-wise directions, respectively:

$$\Gamma_{pp}(\xi_x, \xi_y, \omega) = e^{-\alpha_x |\omega \xi_x / U_c|} e^{-\alpha_y |\omega \xi_y / U_c|} e^{i |\omega \xi_x / U_c|} \quad (2.15)$$

$U_c$  is the convective flow speed and  $\alpha_x$  and  $\alpha_y$  are the correlation coefficients. Some assumptions are present in this model as the separation of variables, the exponential form of the functions, the dependency on the distances instead of the point locations and the stream-wise harmonic variation accounted. It has to be underlined, also, that the correlation coefficients,  $\alpha_x$  and  $\alpha_y$ , are to be determined from wind tunnel gallery measurements of the spatial coherence of the wall pressure fluctuations, which is, of course, a limit to its applicability. However, this model is extensively used in literature as a predictive model, due to the possibility to use a range of universal values for the correlation coefficients if the assumptions of no-gradients effects and fully developed turbulent boundary layer (TBL) are assumed [17]. In any case, more than other models, the Corcos one is the best choice for simplicity versus predictive capabilities.

Many other models have been proposed to improve the accuracy of the Corcos model in the estimation of the WPFs (Wall Pressure Fluctuations) in the sub-convective domain, which is the wavenumber domain comprised between the acoustic and the convective wavenumber. Some of these models are directly linked to the Corcos one [15, 18], on the contrary, others do not take into account the separation of the stream-wise and cross-wise coherence [12, 14].

When moving to the wavenumber domain, the spectra  $\Gamma_{pp}(k_x, k_x, \omega)$  becomes:

$$\Gamma_{pp}(k_x, k_x, \omega) = \frac{4\alpha_x\alpha_y}{\left[\alpha_y^2 + \frac{U_c^2 k_y^2}{\omega^2}\right] \left[\alpha_x^2 + \left(1 + \frac{U_c k_x}{\omega}\right)^2\right]} \quad (2.16)$$

### Efimtsov

The Efimtsov model [15], for example, is based on the Corcos formulation; the idea is to introduce a dependency of the correlation lengths  $U_c(\omega\alpha_x)^{-1}$  and  $U_c(\omega\alpha_y)^{-1}$  with respect to the boundary layer thickness  $\delta$ , the wall friction velocity  $u_T$  and the Mach number  $M_0 = U/a_0$ , where  $a_0$  is the speed of sound. The expression of  $\Gamma$  is identical to Corcos's formulation (Eq. 2.15) with:

$$\frac{U_c}{\omega\alpha_x} = \delta \left( \left( \frac{a_1 S_h u_T}{U_c} \right)^2 + \frac{a_2^2}{S_h^2 + (a_2/a_3)^2} \right)^{-1/2} \quad (2.17)$$

$$\frac{U_c}{\omega\alpha_y} = \begin{cases} \delta \left( \left( \frac{a_4 S_h u_T}{U_c} \right)^2 + \frac{a_5^2}{S_h^2 + (a_5/a_6)^2} \right)^{-1/2} & M_0 < 0.75; \\ \delta \left( \left( \frac{a_4 S_h u_T}{U_c} \right)^2 + a_7^2 \right)^{-1/2} & M_0 > 0.90; \end{cases} \quad (2.18)$$

where  $S_h = \omega\delta/u_T$ ,  $a_1 = 0.1$ ,  $a_2 = 72.8$ ,  $a_3 = 1.54$ ,  $a_4 = 0.77$ ,  $a_5 = 548$ ,  $a_6 = 13.5$ ,  $a_7 = 5.66$  [13, 15]. At high frequencies, this correlation function corresponds to a Corcos model with  $\alpha_x = 0.1$  and  $\alpha_y = 0.77$ . At low frequencies, the boundary layer parameters considerably modify the spectrum shape.

An extensive description of many turbulent boundary layer models is given in [8, 13]; a comparison is reported in Fig. 2.3.

### 2.2.3 Acoustic Excitation: Diffuse Acoustic Field

This load model, which represents the excitation of an infinite sum of uncorrelated plane waves, has the following correlation function, depending on the convective constant only:

$$\Gamma(\xi_x, \xi_y, \omega) = \frac{\sin(\omega\xi_x/U_c)}{\omega\xi_x/U_c} \frac{\sin(\omega\xi_y/U_c)}{\omega\xi_y/U_c} \quad (2.19)$$

The DAF is often used to describe the TBL load in the low frequencies since both models take into account the stream-wise and cross-wise correlations. Moving up with the frequency the DAF model strongly overestimates the exciting contribution of a TBL.

In this thesis, it is used to deal with cases in which the applicability of the Corcos model is impeded by the presence of pressure gradient effects [19].

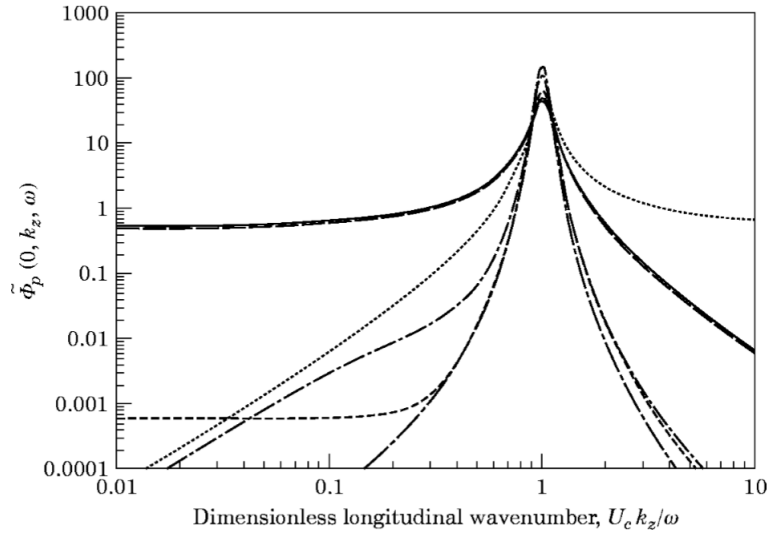


Figure 2.3: Wavenumber–frequency spectra for  $S_h = 248$ : —) Corcos [9]; - - -) Emtsov [15]; - - -) Smol'yakov and Tkachenko [12]; · · ·) Ffowcs Williams [18]; — · —) Chase I [14]; — · —, Chase II [13, 14]. The spectra are plotted against longitudinal wavenumber non-dimensionalized on the convective wavenumber [13].

## 2.3 Flow-Induced Vibrations and Noise

The vibrations, induced by a convective or an acoustic field exciting an elastic structure, arise strong interest in many engineering areas. These induced vibrations can even damage internal devices and payloads in the case of a space-launcher in the lift-off phase. As a result, the random vibrational and noise levels on the structures must be predicted in the design phase, in order to fix eventual issues before operating the system.

### 2.3.1 Modal Approaches

The predictive methodologies actually available in literature are mainly modal-based [5–7, 20, 21]. De Rosa et al. [7] presented both the exact and numerical procedures for the response of a simply-supported plate under a turbulent boundary layer excitation. Hambric et al. [20], studied the effects of the boundary conditions of a flat plate on the flow-induced response, identifying how the modal acceptance function changes with respect to the convective wavenumber peaks. Da Rocha [22] analysed the influence on the boundary layer induced vibrations of different TBL models.

Among the modal approaches, the full finite element approach, which requires a discretisation of the structural operator in finite elements, is the most developed and diffuse. However, the main drawback is connected to the required number of the finite elements, which is, generally, strongly affected by the fluid loading wavelength at the design frequency of analysis [21]. This is, for most of applications, lower than the structural one, increasing, thus, the size of the problem in terms of degrees of freedom (DoF) (see Fig. 2.4).

Some authors propose different methods to reduce the computational cost associated with this approach. For example, a method of load approximation through equivalent deterministic forces, analysing the eigenvalues distributions of the load matrix for a general convective

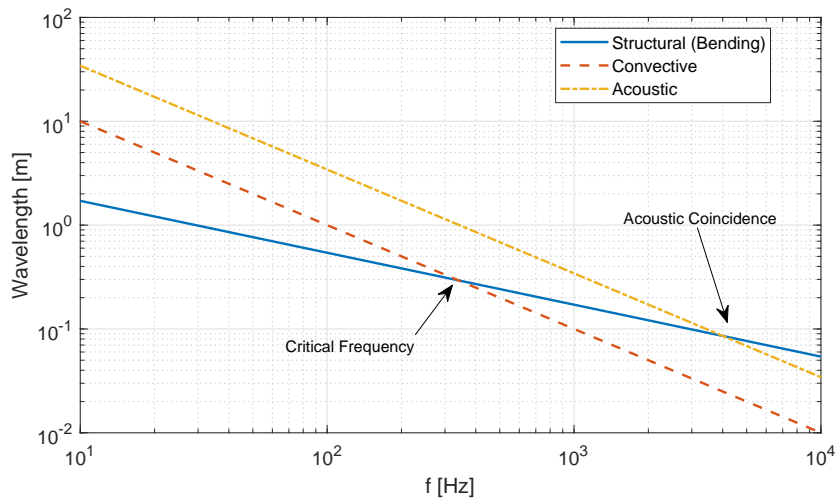


Figure 2.4: The structural, convective and acoustic wavelengths versus frequency for a 3mm-thick panel - Flow speed  $U_0 = 100m/s$

load distribution, called *PEDEM*, is proposed in [23]. Two frequency ranges are identified in which the convective load can be approximated through a purely coherent or purely incoherent equivalent load, proposing thus, a pseudo equivalent deterministic excitation method as an upgrade of the classic pseudo excitation method [23]. This approach proves to work very well in the LF (Low-Frequency) or HF (High-Frequency) range since the behaviour of the eigenvalues of the load matrix is easily predictable. In the MF (Mid-Frequency) range, some approximations have to be made and the accuracy lowers [24]. De Rosa et al. also studied the effects on the TBL-induced response of plates of concentrated masses, in [25], and non-lifting aeroelasticity, in [26, 27].

Another possibility is to use scaled models or similitude to reproduce the response of smaller systems, which have a reduced computational cost for given wavelength to describe, assuming fixed mesh sizes. In these cases, the main issues, are associated with the application of scaling laws to rebuild the response of the original system [19, 24]. Bonness et al. [28], on the other hand, propose a modelling approach for combining FE structural models of large and complex structures with TBL pressure fluctuations using asymptotic approximations of the modal force matrix; these are equivalent to full numerical integration when the TBL correlation lengths are one order of magnitude smaller than the structural wavelengths. Additionally, the asymptotic solution also removes any dependence of the structural mesh resolution [28]. Maxit [29] proposes the use of the wavenumber space to simulate random loads using uncorrelated wall plane waves. The non-correlation of the waves is imposed a-priori and the integration limits are case-dependent and justified by the filtering effects of the structure, which should also be known a-priori; these are not always applicable, especially if a complex media is analysed or high frequencies are approached, due to coupled bending wavemodes which might arise in the frequency band. The randomization of load cases is also required to avoid excessive computational cost [29].

Birgersson et al. [30], on the contrary, propose a spectral finite element method for the simulation of structural vibrations under distributed pressure fluctuations. The response of a plate to a distributed excitation with a plane pressure wave, is calculated with the spectral FEM and used as a reference when the cross-spectral density of the TBL wall pressure cross-

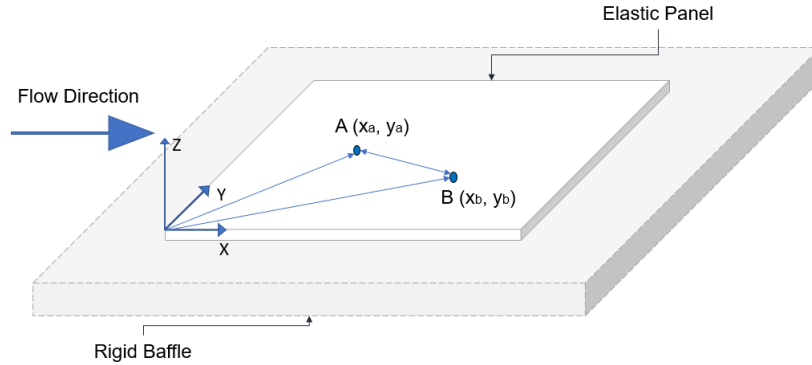


Figure 2.5: Sketch of the elastic plate in the rigid aerodynamic baffle.

correlation is expressed as a finite exponential Fourier series [30]. Finnveden et al. [10] then validated the approach with an experimental-numerical comparison.

### The response of a rectangular panel: Analytical Approach

A thin, flat and rectangular panel is made up with an isotropic material and simply supported on all four edges. It is mounted in an infinite rigid plane baffle flush with the TBL and the flow in the X direction, as in Fig. 2.5. The lengths of the panel in X and Y are respectively  $L_x$  and  $L_y$ .

The displacement cross-spectral density function between any arbitrary couple of points belonging to a thin, isotropic and homogeneous plate,  $A(x_a, y_a)$  and  $B(x_b, y_b)$ , due to an assigned stochastic distributed excitation, can be found with the following modal expansion as given by Elishakoff in [5]:

$$\mathbf{S}_{ww}(x_a, y_a, x_b, y_b, \omega) = \sum_j \sum_n \left[ \frac{\Psi_j(x_a, y_a) \Psi_n(x_b, y_b)}{Z_j^H(\omega) Z_n(\omega) \gamma_j \gamma_n} \right] S_p(\omega) A_{Q_j Q_n}(\omega) \quad (2.20)$$

where  $\Psi_j$  is the j-th mass-normalised analytic mode shape calculated in each of the points and  $\gamma_j$  is the generalized mass coefficient for the same mode order and  $Z_j$  is the dynamic structural impedance (Eq. 2.22);  $A_{Q_j Q_n}$  is the normalised joint acceptance integral (Eq. 2.21). In particular:

$$A_{Q_j Q_n}(\omega) = \int_0^{L_x} \int_0^{L_x} \int_0^{L_y} \int_0^{L_y} \left[ \frac{\Gamma_{pp}(x, y, x', y', \omega)}{S_p(\omega)} \Psi_j(x, y) \Psi_n(x', y') \right] dx dy dx' dy' \quad (2.21)$$

$$\gamma_j = \int_0^{L_x} \int_0^{L_y} \Psi_j^2(x, y) dx dy \quad Z_j(\omega) = m_s [\omega_j^2 - \omega^2 + i\eta\omega_j^2] \quad (2.22)$$

where  $m_s$  is surface density of the plate.

In details, the auto-spectral density of the displacement at a selected point is given as

follows:

$$\begin{aligned} \mathbf{S}_{ww}(x, y, \omega) &= \sum_j \left[ \frac{\Psi_j^2(x, y)}{|Z_j^2| \gamma_j^2} \right] S_p(\omega) A_{Q_j Q_j}(\omega) + \\ &+ \text{Re} \left[ \sum_j \sum_{n \neq j} \left[ \frac{\Psi_j(x, y) \Psi_n(x, y)}{Z_j^H(\omega) Z_n(\omega) \gamma_j \gamma_n} \right] S_p(\omega) A_{Q_j Q_n}(\omega) \right] \end{aligned} \quad (2.23)$$

where the last quantity is strictly real.

### The response in a Finite Element Framework

For a discretized approach, as standard FEM, the evaluation of the structural displacement cross-spectrum matrix to a statistically stationary and ergodic random excitation, such as TBL flow, can be performed as follows [5, 21, 24]:

$$\mathbf{S}_{ww}(\omega) = \mathbf{\Psi} \mathbf{H}(\omega) \mathbf{\Psi}^T \mathbf{S}_{FF}(\omega) \mathbf{\Psi} \mathbf{H}^*(\omega) \mathbf{\Psi}^T \quad (2.24)$$

where  $\mathbf{H}$  being a complex diagonal matrix with:

$$H_j(\omega) = \frac{1}{\omega_j^2 - \omega^2 + i\eta\omega_j^2} \quad (2.25)$$

and  $\mathbf{\Psi}$  is the real mass-normalised matrix of the modal shapes,  $\mathbf{S}_{FF}$  is the load matrix in discrete coordinates. The superscripts  $T$  and  $*$  denote, respectively, the matrix transposition and the conjugation. The output matrix  $\mathbf{S}_{ww}$  is the matrix of the auto and cross spectral densities of the structural field.

Each element of the load matrix has to be calculated solving a double integral on the nodal surface of the product of the structural shape functions ( $N_F$ ) and the wall pressure cross spectra as in Eq. (2.26):

$$S_{FF}^{i,j} = \int_{x_i - \Delta_x/2}^{x_i + \Delta_x/2} \int_{y_i - \Delta_y/2}^{y_i + \Delta_y/2} \int_{x_j - \Delta_x/2}^{x_j + \Delta_x/2} \int_{y_j - \Delta_y/2}^{y_j + \Delta_y/2} N_F^T \Gamma_{pp}(\xi_x^{ij}, \xi_y^{ij}, \omega) N_F dx_i dx_j dy_i dy_j \quad (2.26)$$

The size of the finite elements is, generally, strongly ruled by the fluid wavelength at the design frequency of analysis. For most of applications, this is lower than the structural one and the need of a finer mesh increases the size of the problem and, thus, the computational cost. For example, with reference to Fig.2.6, a structural mesh sized on 10 KHz is able to describe the fluid wavelength only up to  $\approx 2$  KHz. It is clear how, moving up with the frequency, the computational cost increases more and more. In Fig.2.6 it is also identifiable the *critical frequency* which is the point where the fluid wavelength equals the structural one. This double space integration on the wetted (excited) surface (Eq. (2.26)), can be approximated trying to reduce the time associated to this analysis step. Considering that the pressure fluctuations, due to TBL, do not fluctuate very quickly in the nodal area, given by  $\Delta_x \Delta_y$ , a direct lump-on-the-nodes of the wall pressure cross spectra is a good approximation of the integral, as in Eq.(2.27) [7, 21, 24]:

$$S_{FFL}^{i,j} = \Gamma_{pp}(\xi_x^{ij}, \xi_y^{ij}, \omega) \Delta_x^2 \Delta_y^2 \quad (2.27)$$

This approximation is always true if the frequency range is low or the nodal area is small enough to guarantee that the pressure is effectively not fluctuating much in the considered

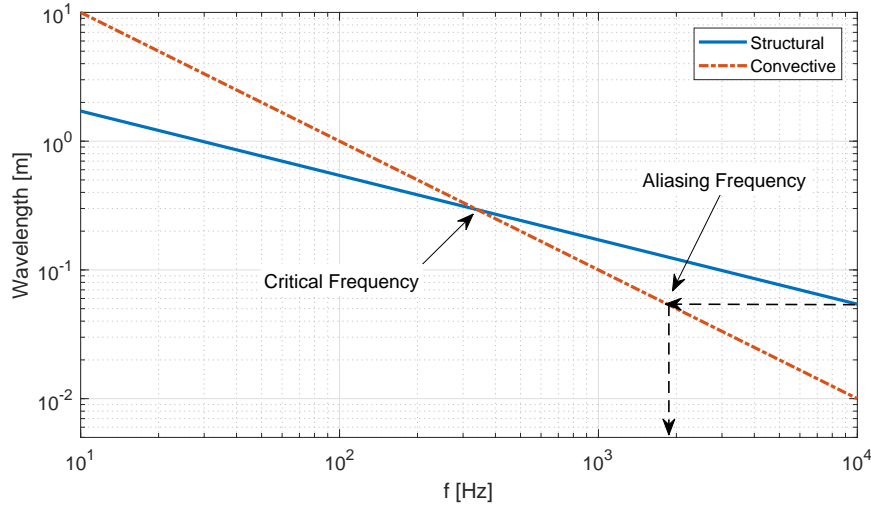


Figure 2.6: The structural and aerodynamic wavelengths versus frequency - Convective speed  $U_c = 100m/s$

spatial domain. Thus, once a mesh is defined, it is straightforward to evaluate the maximum frequency where the fluid pressure fluctuations are well described, which is called *aliasing frequency*. Overcoming this value, the load matrix is no more an accurate discretization of the pressure fluctuations and the model exponentially loses accuracy. A deep investigation on this numerical aspects is extensively made in literature, [21].

This numerical finite element-based approach is used as a reference for the results of this chapter, when an analytic approach is not available. These are, in fact, available only for flat simply-supported panels subjected to Corcos load [7].

### 2.3.2 Energy Approaches

On the other hand, moving to high-frequencies, energy-based approaches can be used, such as the Statistical Energy Analysis (SEA). The total mean energy of an SEA subsystem excited by a spatially correlated excitation is expressed as follows:

$$\langle \mathbf{S}_{E_r}(\omega) \rangle = \langle j_{mm}^r(\omega) \rangle \sum_m \int_{\Delta\omega} \frac{\omega^2 |\alpha_m(\omega)|^2 (L_x \cdot L_y)^2}{\Delta\omega} S_{pp}(\omega) d\omega \quad (2.28)$$

where the  $\langle \rangle$  symbol represents the ensemble average and  $\langle j_{mm}^r \rangle$  is the average of the joint acceptance functions over the resonant modes in the considered frequency band, for the generic subsystem  $r$ . Then, in an SEA framework, the energy influence coefficients  $A_{j,s}$  can be derived by:

$$A_{r,s} = \frac{\langle \mathbf{S}_{E_r} \rangle}{\langle \mathbf{P}_{in_s} \rangle} \quad (2.29)$$

where  $\mathbf{P}_{in_s}$  represents the injected power in the subsystem  $s$  (see Fig. 2.7) and can be expressed as:

$$\langle \mathbf{P}_{in_s} \rangle = \frac{1}{2} \sum_j \frac{\eta \omega_j^2}{\Delta\omega} \int_{\Delta\omega} \omega^2 |\alpha_j(\omega)|^2 S_{pp}(\omega) \langle j_{jj}^s(\omega) \rangle d\omega \quad (2.30)$$

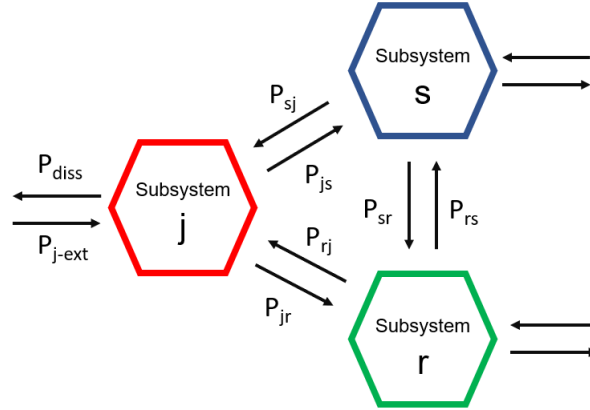


Figure 2.7: Graphical sketch of the energy exchange between SEA subsystems.

Among the methods proposed in literature, the most effective is surely the equivalent rain-on-the-roof method, [6, 31]. This approach considers the fact that even spatially-correlated fluctuations, when moving to high-frequencies, head towards uncorrelated models. Then, it is possible to evaluate an equivalent uncorrelated load which approximates the real load correlation function. This gives huge advantages to the calculation of the joint acceptance integral, which will become a function of this kind [6]:

$$j_{rs}(\omega) = \frac{1}{A_p^2} \int_{A_p} \int_{A_p} \Psi_r(x, y) \Psi_s(x', y') \delta(\xi_x) \delta(\xi_y) dA_p dA_p = \frac{\delta_{r,s}}{A_p^2} \quad (2.31)$$

where  $\delta$  represents the Delta Dirac function.

Finnveden [32] used a spectral finite element approach to get the modal densities and coupling loss factors of SEA subsystems loaded with stochastic excitations, as turbulent boundary layer, and validated the approach with measurements [10]. Similarly, Orrenius et al. [33, 34] proposed an SEA-based approach using a single 2D periodic cell for the calculation of SEA parameters. The numerical approach has been validated with measurements under a diffuse acoustic field, proving a general good correlation in the medium and high frequencies [33].

An efficient alternative in terms of computational cost is, for example, the transfer matrix method (TMM). It is a general method used for the prediction of the propagation of monochromatic plane waves in planar and multi-layered structures of infinite extent [35]. This approach is particularly easy for homogenised and infinite multilayers made up from a combination of elastic, porous and fluid layers, using a representation based on the plane wave propagation in different media in terms of transfer matrices. For example, considering Fig. 2.8, in the TMM context, a two by two transfer matrix is first computed at each wave heading  $\theta$  and for each couple of consecutive layers  $j$  and  $j + 1$ :

$$\begin{bmatrix} p_j \\ v_j \end{bmatrix} = \begin{bmatrix} 1 & Z_t(k_t, \theta) \\ 0 & 1 \end{bmatrix} \begin{bmatrix} p_{j+1} \\ v_{j+1} \end{bmatrix} \quad (2.32)$$

where the vectors  $\langle p, v \rangle$  represents the pressure-velocity state variables at the inlet and outlet of each layer,  $k_t$  the trace wavenumber, generally connected to the acoustic one ( $k_0 = \omega/c_0$ ) and  $Z_t$  the heading-dependent impedance [35, 36]. The matrices in Eq. 2.32 are then coupled to the matrices defining the source, the attached fluid, elastic or porous

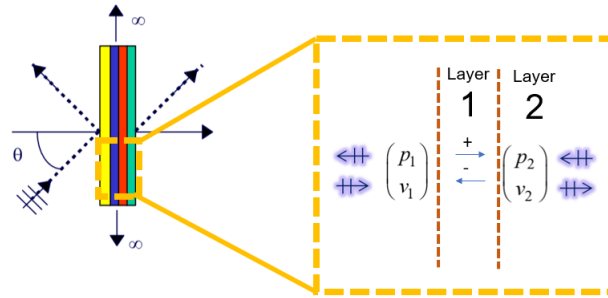


Figure 2.8: Sketch of a multi-layered laterally infinite system with pressure and velocities particles inward and outward of each layer.

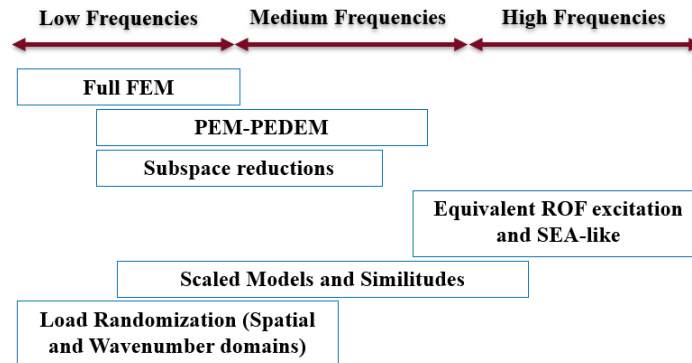


Figure 2.9: A simple scheme summarizing the main methods for the flow-induced vibrations and noise in finite structures and the frequency ranges where they are applicable, given hypotheses and computational cost.

layers and the semi-infinite receiver medium (transmission problem) [36]. The assembled Transfer Matrix of the system is then solved for the transmission coefficient of the system. Many applications of the TMM to the modelling of sound transmission of composite structures have already been validated [36, 37] for simple and complex excitation models. Finite size effects, important at low frequencies, can be included through appropriate corrections [38–40]. Within the frameworks of curved structures, alternative methods have also been presented. A mathematical model, for the transmission of airborne noise through the walls of an orthotropic cylindrical shell, has been firstly proposed by Koval, [41–43]. For curved composite laminates, the vibroacoustic problem has been further developed through a spectral approach based on a discrete lamina description, [44, 45]. Other semi-analytic approaches, based on a receptance method, have also been proposed in order to analyse the sound transmission of aircraft panels with stringers and ring frames, [46, 47].

A simple scheme summarising the placements versus frequency of most of the methods cited here, is given in Fig. 2.9.

### 2.3.3 Non-lifting Aeroelastic coupling

When developing the general formulation of the problem, in Eq. 2.4, the hypothesis of blocked pressure is used: the structural deformation/vibrations do not affect the fluid field

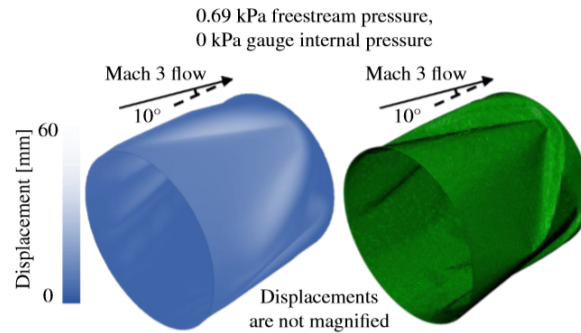


Figure 2.10: Example of buckled cylinder due to inclined supersonic/hypersonic flow [55].

outside and thus the pressure fluctuations are the same ones for a rigid body. However, a variation of the pressure field given by the elasticity (motion) of the structure, is always present.

The aeroelasticity of plates and shells faces the difficulty of distinguishing between the self-induced vibration components and the external one. Phenomenological non-linearities induce fatigue failures instead of catastrophic instantaneous failures, typical of the aeroelasticity of lifting surfaces [48, 49]. In this context, the modal approach is often preferred to a wave-based one, because it allows a clearer evaluation of the flutter conditions, analysing the effect of the aerodynamic induced forces on each structural mode or on one of their combination [48–50]. Amabili et al. [51] investigate the aeroelastic stability of simply supported, circular cylindrical shells in supersonic flow exploiting the non-linearities (large amplitudes) by using the Donnell non-linear shallow-shell theory; the effect of viscous structural damping is also taken into account. Similarly the flow-induced non-linear dynamics in circular vessels conveying flow is studied with a similar theoretical model by Amabili et al. in [52, 53]. An application to the non-linear flutter analysis of cylinders under supersonic flow is also given by Amabili et al. in [54]; both linear aerodynamics (first-order piston theory) and non-linear aerodynamics (third-order piston theory) are used.

More recently, Klock et al. [55], presented a FEM approach, with a third order piston theory, against experimental results for the local aeroelastic stability boundaries of an internally pressurized circular cylindrical shell applied to supersonic/hypersonic vehicles; the local instabilities are analysed even for inclined flow conditions (see Fig. 2.10)

With specific focus on the flow-induced vibrations for turbulent boundary layer excitation, the works from Ciappi et al. [26] and Vitiello et al. [27], show the plate TBL-induced responses with and in absence of subsonic aeroelastic coupling; The effect at higher frequencies is investigated using a free-field formulation in [26], while the shift of natural frequencies in the LF region has been studied in [27].

The effects of aerodynamics on the elastic structural waves' propagation, are also present in the literature [56–64]. J.W. Miles presents a work discussing the flutter of an isotropic infinite panel in a two-dimensional incompressible flow [56], driving the wave speed relative to the panel, identifying the flutter conditions versus the circular frequency. J.W. Miles also studies the supersonic flutter of a cylindrical shell using the same approach [57]. Similar investigations have been conducted by Olson [65, 66] on the supersonic flutter of shells. Olson [65], discusses also the use of the Piston Theory to model the auto-excited aerodynamic influence on a shell. Some experimental works trying to reproduce flutter conditions for

shells in a supersonic flow have been grouped and described by [67].

Benjamin analysed in [59] the three types of instabilities of laminar boundary layers over surfaces, that might arise due to the flexibility. Similarly, to study the same infinite-plate problem, Crighton & Oswell [60] develop an analytical model that described, in a neutral stability zone, some highly unusual wave propagation effects. The effect of mean flow on cylindrical structures has been then studied by [58] and [64], while sandwich structures have been investigated by Sorokin et al. [68].

## 2.4 Elastic Waves in Periodic Structures

A plane free wave that propagates along a periodic structure is assumed to take the form of a Bloch wave [69], as the one in Eq. 2.33:

$$\psi_r = e^{-i\beta r} u_r \quad (2.33)$$

where  $r$  is the distance vector,  $\beta$  is the propagation constant,  $u_r$  is a spatially periodic function.

The Bloch wave theory is largely employed in quantum mechanics and photonics crystal, and has been progressively applied in phononic physics and engineering periodic structures [69]. Bloch showed how electron wave functions (in crystals) have a basis consisting entirely of Bloch wave energy eigenstates.

This reflect in periodic structures to exhibit pass-bands and stop-bands, in that each disturbance can propagate freely only in specific frequency ranges, otherwise they decay with distance [69–71]. Some of the first applications in mechanics concern infinite lattices of spring-mass systems, and then the research is enlarged to bi-dimensional structures; a first review and application of the Floquet-Bloch theory to mechanics is given by Brillouin [72]. Lately, a description of the Floquet-Bloch theory to the mechanics of more complicated systems in a finite element framework, is given by Mead [73].

In the description of wave propagation characteristics, wave vectors can be expressed in terms of the reciprocal lattice basis, also periodic; one can analyse the wave vectors just in certain regions of the reciprocal lattice called First Brillouin zone [72]. A bi-dimensional periodic structure with a unit cell of size  $L_x$  and  $L_y$  is illustrated in Fig. 2.11 with the so-called *First Brillouin Zone* corresponding to the wavenumber space within  $[-\pi/L_x, \pi/L_x] \times [-\pi/L_y, \pi/L_y]$ . Given the symmetric properties in the reciprocal lattice, the wave analysis can be restricted to the *Irreducible Brillouin Zone* (zone OABC in Fig. 2.11).

The wavenumbers versus frequency along the *Irreducible Brillouin Zone* form the band structure, known as band diagram. The pass- and stop- bands of the free wave propagation in the periodic media can be identified from the band structure/dispersion relation. For bi-dimensional periodic structures, the stop band can be complete, if the specific wavemode type is unable to propagate in any direction, or partial, is the wave type can still propagate in one or more directions; the phenomenon is known also as wave beaming effect [75].

The stop bands mechanisms can be of different nature. The Bragg band-gap (scattering; see [71]) is physically connected to the wavelengths of the disturbance being of the same order of the periodicity scale. This creates a periodic impedance mismatch that induces a destructive interference among impinging and reflected elastic waves in the periodic media. On the contrary, resonance-induced stop-bands are connected to the resonance conditions of locally attached (or embedded) resonant elements that are triggered around their nature modal frequencies; The periodicity scale does not play a role in this case. Furthermore, it has

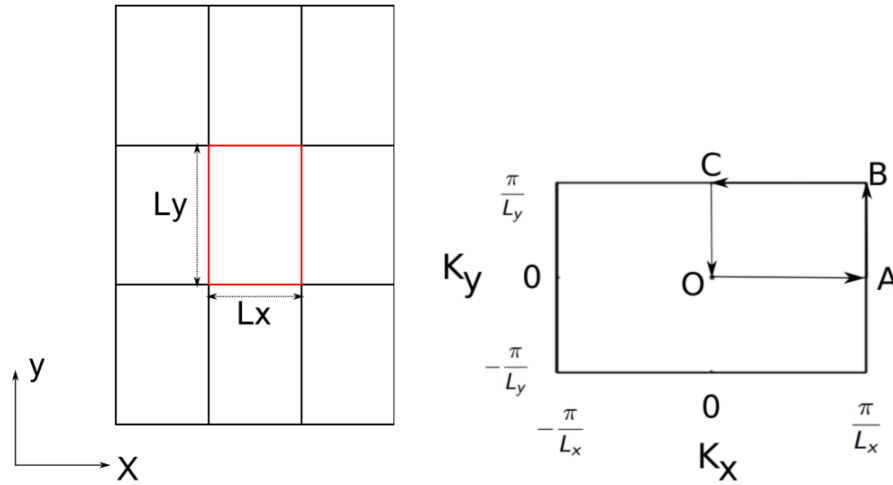


Figure 2.11: A bi-dimensional periodic structure with rectangular unit cell and its Brillouin zone [74].

been observed that unlike Bragg scattering which produces symmetric frequency-dependent transmission functions, local resonances exhibit Fano-like transmission characteristics [74, 76]. The distinction between the two mechanisms has also been addressed from the point of view of differences in wave shapes at stop band edges [77] and the nature of the spatial attenuation profile downstream to the periodic media [78].

### 2.4.1 The Wave Finite Element Method

The Wave Finite Element method is a technique to investigate wave motion in one-dimensional and two-dimensional periodic structures. In this method an elementary period of the structure, that, reproduced in one or two dimensions, recreates the target periodic (or homogeneous) structure, is modelled using conventional finite elements. Assuming time-harmonic motion, the dynamic stiffness equation of the elementary segment can be obtained; the extraction of the stiffness and mass matrices in a classic FE form, is required [79]. Periodicity conditions are then applied and an eigenvalue problem is formulated whose solutions give the dispersion curves and wavemodes. Unlike the Spectral Finite Element approach [80], does not require any analytical knowledge, case-by-case, of the shape functions of the elements. Conventional or commercial FE packages can be used for the scope, especially for complex cases.

One of the very first applications of the method is the one of Orris and Petyt [81], where a FE approach with a receptance method is proposed to simulate the dispersion curves of periodic structures. Later, the free wave propagation in rail track is analysed by Thompson [82] using a similar approach and by Gry then [83]. More recently, the one-dimensional wave-based methodologies for the wave propagation and the forced response of waveguides using a single periodic element, have been exploited [84, 85]. In the same context, the free wave propagation in simple waveguides is analysed by Mace et al. [86] for the estimation of energy and power inputs and group velocity. Waki et al. [87] apply the method for predicting flexural wave propagation in a plate and exploited the numerical issues of the method in [87].

One of the first applications of a two-dimensional wave finite element method for evaluating the propagation of elastic waves within cellular structures, such as a honeycomb plates is given in [75]. Duhamel [88] also apply the WFE approach to evaluate the Green's functions of a bi-dimensional structure. Manconi et al. [79, 89, 90], develop and investigate the two-dimensional WFE approach for the free wave propagation in isotropic and composite panels. The method has also been applied for the estimation of loss factors in viscoelastic laminated plates [91].

A Floquet-Bloch decomposition in a WFE framework has been proposed by Collet et al. [92], where an enhancement of the classic formulations allows the analysis of periodic structures with complex damping configurations and materials, resulting for example from active control schemes or the use of shunted piezoelectric patches. In addition, a stochastic wave finite element formulation to analyse uncertain elastic media has been presented in [93]. The analysis of the free and forced wave propagation of systems with a piezoelectric patches has also been investigated in [94]. Droz et al. [95, 96] and Zhou et al. [97, 98] develop a modal order reduction technique to analyse complex heterogeneous periodic structures characterised by many degrees of freedom in a FE framework. The methods make use of the free bounded modes at cell scale, which are assumed to be periodically repeated following the periodicity scale. Serra et al. [99] then presented a WFE formulation to analyse poroelastic homogeneous media.

Some applications to curved structures have been recently developed in [90, 100–102], showing how the method can be used also for the free and forced propagation along shells, by rotating the translational degrees of freedom of the elementary cells.

## 2D Periodic Conditions

The wave finite element method is an FE-based method applicable to periodic structures. The first step is to perform a FE discretisation of the unit cell and extract the mass and stiffness matrices,  $\mathbf{M}$  and  $\mathbf{K}$  respectively. Classic meshing considerations for an appropriate wavelength description are valid as in any FE framework. With reference to Fig. 4.1, the dynamic stiffness equation of the segment can be written as:

$$[\mathbf{K} - \omega^2 \mathbf{M}] \mathbf{q} = \mathbf{D} \mathbf{q} = \mathbf{f} + \mathbf{e}, \quad (2.34)$$

where  $\mathbf{q}$ ,  $\mathbf{f}$  and  $\mathbf{e}$  are the vectors of nodal degrees of freedom (DoFs), internal and external forces, respectively;  $\mathbf{D}$  is the dynamic stiffness matrix. For periodic structures, assuming time and space harmonic excitation, the periodicity conditions are translated in a magnitude and phase link among each point belonging to the periodic pattern, based on complex propagating constants for each elastic wave. Displacements and forces at any point of the cell can thus be connected to the ones of a limited subset, exploiting periodic links, as follows:

$$\mathbf{q}_A = \mathbf{I} \lambda_Y \mathbf{q}_F; \quad \mathbf{q}_R = \mathbf{I} \lambda_X \mathbf{q}_L; \quad \mathbf{q}_2 = \mathbf{I} \lambda_X \mathbf{q}_1; \quad \mathbf{q}_3 = \mathbf{I} \lambda_Y \mathbf{q}_1; \quad \mathbf{q}_4 = \mathbf{I} \lambda_X \lambda_Y \mathbf{q}_1; \quad (2.35)$$

with

$$\lambda_X = e^{-ik_X L_X}, \quad \lambda_Y = e^{-ik_Y L_Y}, \quad (2.36)$$

where  $k_X$  and  $k_Y$  are wavenumbers of the propagating wave in the periodicity directions  $X$  and  $Y$ , while  $L_X$  and  $L_Y$  represent the cell lengths along the same directions, respectively;  $\mathbf{I}$  is the identity matrix. Assembling in a block-diagonal form the periodicity condition matrices, as in Eq. 2.35, a periodicity matrix  $\mathbf{\Lambda}$  can be used to link the total displacements

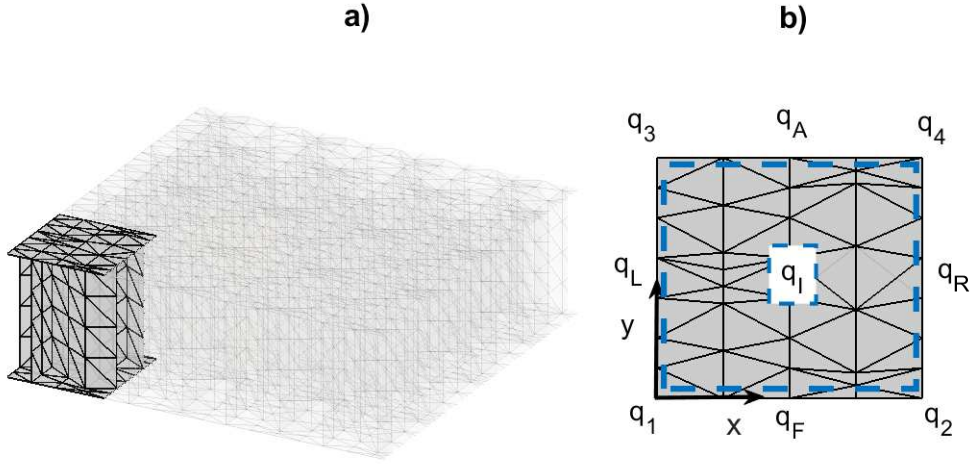


Figure 2.12: Example of a FE cell model with periodicity along the X-Y directions.

and forces vectors to a reduced subset of degrees of freedom. Pre-multiplying Eq.4.1 by  $\Lambda^H$ , where  $H$  stands for the hermitian operator, the dynamic stiffness matrix of the reduced model ( $\mathbf{D}_S$ ) is given by Eq. 4.2.

$$\mathbf{D}_S = \Lambda^H [\mathbf{K} - \omega^2 \mathbf{M}] \Lambda. \quad (2.37)$$

Given the equilibrium of the internal forces between consecutive cells, only potential external forces are considered [89], thus  $\Lambda^H \Lambda \mathbf{f}_r = 0$ .

The problem in Eq. 4.2, in absence of external forces, represents a three-parametric eigenproblem in  $\omega$ ,  $\lambda_X$  and  $\lambda_Y$ , that can be solved by imposing two of the variables at each step [89]. In this way, the propagating wavemodes and the corresponding constants of propagation can be derived.

The eigenvalue problem of Eq. 4.2 is here derived in the simpler case of an in-plane homogenised periodic cell (see Fig. 2.13), where the whole set of degrees of freedom ( $\mathbf{q}$ ) is equal to:

$$\mathbf{q} = \begin{bmatrix} \mathbf{q}_1 \\ \mathbf{q}_2 \\ \mathbf{q}_3 \\ \mathbf{q}_4 \end{bmatrix} = \begin{bmatrix} \mathbf{I} \\ \mathbf{I} \lambda_X \\ \mathbf{I} \lambda_Y \\ \mathbf{I} \lambda_X \lambda_Y \end{bmatrix} \mathbf{q}_1 = \Lambda \mathbf{q}_1. \quad (2.38)$$

In this case, decomposing the dynamic stiffness matrix considering the four corners, Eq. 4.1 becomes:

$$\begin{bmatrix} \mathbf{D}_{11} & \mathbf{D}_{12} & \mathbf{D}_{13} & \mathbf{D}_{14} \\ \mathbf{D}_{21} & \mathbf{D}_{22} & \mathbf{D}_{23} & \mathbf{D}_{24} \\ \mathbf{D}_{31} & \mathbf{D}_{32} & \mathbf{D}_{33} & \mathbf{D}_{34} \\ \mathbf{D}_{41} & \mathbf{D}_{42} & \mathbf{D}_{43} & \mathbf{D}_{44} \end{bmatrix} \cdot \begin{bmatrix} \mathbf{q}_1 \\ \lambda_X \mathbf{q}_1 \\ \lambda_Y \mathbf{q}_1 \\ \lambda_X \lambda_Y \mathbf{q}_1 \end{bmatrix} = \mathbf{0}. \quad (2.39)$$

At this stage, when the propagation constants are imposed and the frequency derived, the problem becomes a standard linear eigenvalue problem. If one wavenumber and the

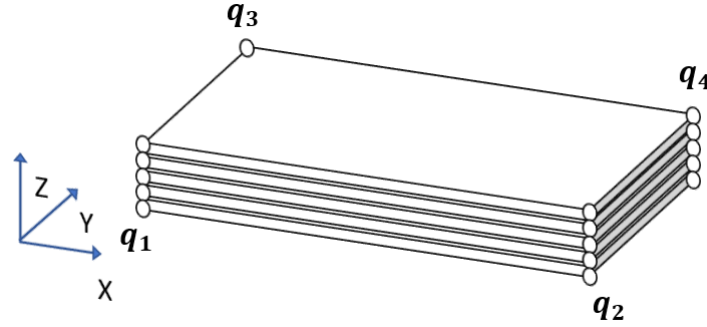


Figure 2.13: Example of an in-plane (X-Y) homogenised FE cell model.

frequency are fixed, deriving the other one from Eq. 4.2, the problem becomes quadratic. For example, exploiting Eq. 4.2 using Eq. 2.39, the following form is derived:

$$\begin{aligned}
 & [(\mathbf{D}_{11} + \mathbf{D}_{22} + \mathbf{D}_{33} + \mathbf{D}_{44})\lambda_x\lambda_y + (\mathbf{D}_{12} + \mathbf{D}_{34})\lambda_x^2\lambda_y + \\
 & \quad (\mathbf{D}_{13} + \mathbf{D}_{24})\lambda_x\lambda_y^2 + \mathbf{D}_{32}\lambda_x^2 + \mathbf{D}_{23}\lambda_y^2 + \\
 & (\mathbf{D}_{21} + \mathbf{D}_{43})\lambda_x + (\mathbf{D}_{31} + \mathbf{D}_{42})\lambda_y + \mathbf{D}_{14}\lambda_x^2\lambda_y^2 + \mathbf{D}_{41}]\mathbf{q}_1 = 0
 \end{aligned} \tag{2.40}$$

Solving the quadratic eigenvalue problem in  $\lambda_x$  or  $\lambda_y$ , the dispersion curves of the media can be derived. Similarly, for a non-homogenised structure, as the one in Fig. 4.1, an eigenproblem equivalent to the one in Eq. 2.40, can be derived starting from the following equation:

$$\begin{bmatrix}
 \mathbf{D}_{II} & \mathbf{D}_{FI} & \mathbf{D}_{LI} & \mathbf{D}_{1I} & \mathbf{D}_{AI} & \mathbf{D}_{RI} & \mathbf{D}_{2I} & \mathbf{D}_{3I} & \mathbf{D}_{4I} \\
 \mathbf{D}_{IF} & \mathbf{D}_{FF} & \mathbf{D}_{LF} & \mathbf{D}_{1F} & \mathbf{D}_{AF} & \mathbf{D}_{RF} & \mathbf{D}_{2F} & \mathbf{D}_{3F} & \mathbf{D}_{4F} \\
 \mathbf{D}_{IL} & \mathbf{D}_{FL} & \mathbf{D}_{LL} & \mathbf{D}_{1L} & \mathbf{D}_{AL} & \mathbf{D}_{RL} & \mathbf{D}_{2L} & \mathbf{D}_{3L} & \mathbf{D}_{4L} \\
 \mathbf{D}_{I1} & \mathbf{D}_{F1} & \mathbf{D}_{L1} & \mathbf{D}_{11} & \mathbf{D}_{A1} & \mathbf{D}_{R1} & \mathbf{D}_{21} & \mathbf{D}_{31} & \mathbf{D}_{41} \\
 \mathbf{D}_{IA} & \mathbf{D}_{FA} & \mathbf{D}_{LA} & \mathbf{D}_{1A} & \mathbf{D}_{AA} & \mathbf{D}_{RA} & \mathbf{D}_{2A} & \mathbf{D}_{3A} & \mathbf{D}_{4A} \\
 \mathbf{D}_{IR} & \mathbf{D}_{FR} & \mathbf{D}_{LR} & \mathbf{D}_{1R} & \mathbf{D}_{AR} & \mathbf{D}_{RR} & \mathbf{D}_{2R} & \mathbf{D}_{3R} & \mathbf{D}_{4R} \\
 \mathbf{D}_{I2} & \mathbf{D}_{F2} & \mathbf{D}_{L2} & \mathbf{D}_{12} & \mathbf{D}_{A2} & \mathbf{D}_{R2} & \mathbf{D}_{22} & \mathbf{D}_{32} & \mathbf{D}_{42} \\
 \mathbf{D}_{I3} & \mathbf{D}_{F3} & \mathbf{D}_{L3} & \mathbf{D}_{13} & \mathbf{D}_{A3} & \mathbf{D}_{R3} & \mathbf{D}_{23} & \mathbf{D}_{33} & \mathbf{D}_{43} \\
 \mathbf{D}_{I4} & \mathbf{D}_{F4} & \mathbf{D}_{L4} & \mathbf{D}_{14} & \mathbf{D}_{A4} & \mathbf{D}_{R4} & \mathbf{D}_{24} & \mathbf{D}_{34} & \mathbf{D}_{44}
 \end{bmatrix}
 \begin{bmatrix}
 \mathbf{I} & \mathbf{0} & \mathbf{0} & \mathbf{0} \\
 \mathbf{0} & \mathbf{I} & \mathbf{0} & \mathbf{0} \\
 \mathbf{0} & \mathbf{0} & \mathbf{I} & \mathbf{0} \\
 \mathbf{0} & \mathbf{0} & \mathbf{0} & \mathbf{I} \\
 \mathbf{0} & \mathbf{I}\lambda_Y & \mathbf{0} & \mathbf{0} \\
 \mathbf{0} & \mathbf{0} & \mathbf{I}\lambda_X & \mathbf{0} \\
 \mathbf{0} & \mathbf{0} & \mathbf{0} & \mathbf{I}\lambda_X \\
 \mathbf{0} & \mathbf{0} & \mathbf{0} & \mathbf{I}\lambda_Y \\
 \mathbf{0} & \mathbf{0} & \mathbf{0} & \mathbf{I}\lambda_X\lambda_Y
 \end{bmatrix}
 \begin{bmatrix}
 \mathbf{q}_I \\
 \mathbf{q}_F \\
 \mathbf{q}_L \\
 \mathbf{q}_1
 \end{bmatrix}
 = \mathbf{0}. \tag{2.41}$$

### 1D Periodic Conditions

Considering a single repetitive substructure of a 1D periodic media (see Fig. 2.14), the waves and their cross-sectional waveshapes (wavemodes) travelling in the structure can be calculated by solving the eigenproblem which derives from imposing the 1D Floquet's conditions (periodicity). These are defined by imposing the equilibrium of the displacement and forces among the common hypernodes of two subsequent periodic cells (see Fig. 2.14). Damping can be modelled by viscous damping matrix and/or  $\mathbf{K}$  being complex, as in this case. In the following dynamic stiffness equations, the left and right side hypernodes are

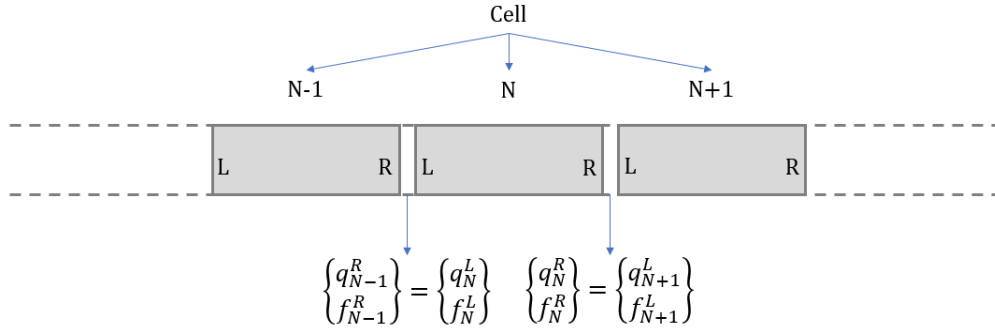


Figure 2.14: Two adjacent elementary cells of a waveguide.

defined with the letters  $L$  and  $R$  respectively.

$$\begin{bmatrix} \mathbf{D}_{LL} & \mathbf{D}_{LR} \\ \mathbf{D}_{RL} & \mathbf{D}_{RR} \end{bmatrix} \begin{Bmatrix} \mathbf{q}_L \\ \mathbf{q}_R \end{Bmatrix} = \begin{Bmatrix} \mathbf{F}_L \\ \mathbf{F}_R \end{Bmatrix} \quad (2.42)$$

where  $\mathbf{D} = [\mathbf{K} - \omega^2 \mathbf{M}]$ . For unit-cells involving complex cross-sections, a state vector reduction can be used to reduce the computational effort [96]. It can be combined with Craig-Bampton (CB) dynamic condensation method of the inner degrees of freedom in case of structural periodicity [95].

Imposing continuity of displacements and equilibrium of forces at the interface between adjacent points, and putting all in a matrix form, one can get the so-called Transfer Matrix,  $\mathbf{T}$ , [84, 85, 87, 89]. It relates the nodal displacements and forces (evaluated on the left side) between two adjacent substructures, as in Fig. 2.14.

$$[\mathbf{T}] = \begin{bmatrix} -\mathbf{D}_{LR}^{-1} \mathbf{D}_{LL} & \mathbf{D}_{LR}^{-1} \\ -\mathbf{D}_{RL} + \mathbf{D}_{RR} \mathbf{D}_{LR}^{-1} \mathbf{D}_{LL} & -\mathbf{D}_{RR} \mathbf{D}_{LR}^{-1} \end{bmatrix} \quad (2.43)$$

It has been demonstrated that the eigenvalues of the transfer matrix occur in reciprocal pairs as  $\lambda_j^+ = 1/\lambda_j^-$  corresponding to pairs of positive (+) and negative (-) going waves, respectively. The positive and negative going eigenvectors  $\phi_j^-$  and  $\phi_j^+$  are associated with the above eigenvalues and are called wavemodes, which are the displacement and force distributions in the substructure section [85, 95, 103]. Every wavemode can be partitioned into a sub-vector of DoFs,  $\Phi_q^{+,-}$ , and internal forces/moments,  $\Phi_f^{+,-}$ .

Positive waves are characterized by the magnitude of the propagating constant being inferior to unity ( $|\lambda_j^+| < 1$ ), which means that if the wave propagates, its amplitude must decrease in travelling along the positive-defined directions.

A transformation between the physical domain, where the system behaviour is described in terms of  $\mathbf{q}$  and  $\mathbf{f}$ , and the wave domain, where the behaviour is described in terms of waves of amplitudes  $\mathbf{a}^+$  and  $\mathbf{a}^-$  travelling in the positive and negative directions, is derived through these matrices [104, 105]. In particular

$$\begin{Bmatrix} \mathbf{q}_L \\ \mathbf{f}_L \end{Bmatrix} = \begin{bmatrix} \Phi_q^+ & \Phi_q^- \\ \Phi_f^+ & \Phi_f^- \end{bmatrix} \begin{Bmatrix} \mathbf{a}^+ \\ \mathbf{a}^- \end{Bmatrix} \quad (2.44)$$

Where  $\mathbf{a}^{+,-}$  are the wave amplitudes of the positive and negative going waves. The filtering issues associated with the wave basis are deeply investigated in literature [84, 89, 106] and

are not repeated here. At each frequency step, when and if new wavemodes cut-on, these are included in the wavemode-basis.

The forced vibrations can be evaluated through the superposition of the direct and reverberant field. The first is the result of the excitation and the second is the incident wavefield. The problem has been analysed in literature by different authors [105–107].

### Waves' Filtering

The proper selection of propagating waves can be done considering the imaginary part of the propagating constant of each wavemode. The criteria are to be chosen case by case and a well established method is still not available in literature. In the present work, the criteria used can be summarized in the following way, considering  $\alpha$  as a tolerance parameter:

$$\text{imag}|k_i \cdot L_X| < \alpha \quad (2.45)$$

Where  $k_i$  and  $L_X$  are the wavenumber associated to the wavemode  $i$  and the spatial step among the cells of the periodic structure. Physically this means considering the only contribution, to structural response, of the propagating (or close-to) waves; at each frequency step, when and if new wavemodes cut-on, these are included in the wave base.

However, a remark has to be made about this. The evanescent field might still have a significant effect on the response around the excitation point (near field). On the other hand, the effect is negligible as soon as we analyse the field far from the singularity. The ideal criteria would select correctly the number of waves to retain in the wave base considering also the distance from the excitation point.

## 2.5 Periodic Design Investigation

In transport industry, the requirements for light and stiff structures often lead to sandwich structural solutions. The design of the core of sandwich panels can induce different anisotropies keeping a high stiffness-to-mass ratio. On the other hand, while a reduced mass is an advantage for fixed structural resistance, it generally induces lower vibroacoustic performance. Therefore, the design of sandwich panels for reduced acoustic radiation, limiting the mass of the system, has received more and more attention in the last decades [108–111]. One of the main reasons for a larger acoustic radiation of sandwich panels is the shear core effect in the mid-frequencies [108–113]; the transition from global bending to core shear is fundamental [114]. The effects of this wavemode transition has been investigated by describing panel using an equivalent shear core [115–117].

Some authors tried to design the core geometry in order to optimize the sound transmission. Palumbo et al. [118] and Grosveld et al. [119] proved experimentally the increase of vibroacoustic performance of honeycomb-cored sandwich plates when periodical voids and recesses are included in the core original geometry. While this approach creates regions of reduced bending stiffness, a strong benefit is observed in the sound transmission loss for large frequency bands. A brilliant work was also proposed by Hambric et al. [120]; a complex structural honeycomb panel is optimised by altering the original design, targeting a different the bending wave speed in the media versus the acoustic one. In [113] the suitability of orthotropic cores is investigated to exploit directivity properties of an incident pressure field as compared to the performance obtained with isotropic cores; in particular those having a trusslike geometry are investigated to control the core stiffness along two orthogonal directions in a decoupled manner.

With the arise of new numerical approaches that imply the periodic structure theory (as the Wave Finite Element Method), some topological design researches have been conducted. Baho et al [121], for instance, used a wavemode energy method, coupled with a wave assurance criterion (WAC), to predict the transition frequency of honeycomb panels modelled using a single periodic cells. In addition, the core geometry effects on the shear-core transition and sound transmission loss of honeycomb sandwich plates, are investigated in [122]. Zergoune et al. [122] show the transmission loss sensitivity to most of the classic topological parameters of honeycomb cored sandwich panels, such as angles between walls, thickness and deformation of hexagonal core cells. Similarly, sandwich panels with arbitrary shaped core are studied in [123]. Again, a comparative study of periodic cells that share the same mass-to-stiffness ratio, is performed to achieve a significant variation of the transition frequency and modal density, compared to classic honeycomb.

Alternative approaches, are connected to the use of periodically distributed resonant elements on a host plate [124–127]. Even though, in this case, the addition of mass cannot be avoided, some difficulties persist in targeting broadband enhancements of the acoustic performance of the panels. Particularly interesting is the work from Liu et al. [126] which focuses on tuning spring-mass elements (the resonators) around the first coincidence region of the original panel to avoid the transmission loss drop typical in those regions. However, the work is mainly conducted, as for other works in the literature, for simplified excitation models or single acoustic plane-waves. Differently, the resonators are also used to target the ring frequency of shells, which is typically a tonal problem [127].

### 2.5.1 Periodically Ribbed Structures

The presence of axial and ring stiffeners on aircraft fuselages, space launchers fairings and submarines structures is a very common design choice. These solutions are widely used in many engineering applications, ensuring a compromise between weight and high apparent rigidity. Many works investigating the vibro-acoustic behavior of stiffened cylindrical shells can be found in literature [128–134]. The response of ribbed panels under mechanical force or fluid-load excitation is studied by different authors. In the context of fluid-loaded plates, Mace et al. [135, 136] developed a plane-wave based approach to investigate periodically stiffened plates.

Maxit et al. [137] investigated the flow-induced response of periodically stiffened plate in the wavenumber domain, proposing also a discrete Fourier Transform to obtain the same information in the physical space. A vibroacoustic analysis of stiffened composite panels is shown in [138], in which the influence of the shape and the position of the stiffening elements is analyzed.

Using the generalized nearfield acoustical holography, the calculation of the vibration and of the sound radiation of a submerged cylinder excited by a point force is shown in [139]; the analysis was then extended in wavenumber domain in [140]. Photiadis et al. [141] investigated the acoustic response of a ribbed shell in the wavenumber domain, identifying the flexural behavior in the mid-frequency range. Meyer et al. [142] experimentally investigated the influence of internal frames on the response of stiffened aluminum cylindrical shells, focusing on the analysis of the effect of the non-axisymmetric frames on the radiation efficiency.

Some works analysed the sound radiation of ring-stiffened shells as a function of the number of stiffeners and their pitch [132, 143]. For example, Laulagnet et al. [143] treated the sound radiation problem using stiffeners of hollow cross-section, to simulate real industrial case-studies; tangential and radial forces are applied on the skins and the stiffeners and

the fluid-structure interaction modelled using a modal decomposition. Lee et al. [144] investigated the problem varying the angle of incidence of an acoustic plane wave excitation. The circumferential stiffeners induce an increased sound transmission loss before the ring frequency, that is simultaneously slightly reduced with respect to the one of the bare case. On the contrary, shells with axial stiffeners are investigated in terms of acoustic radiation in [145]. The presence of axial stiffeners is studied only in terms of additional impedance and difference configurations are analysed by varying the number of axial stiffeners.

## 2.6 Thesis Novelties versus Literature

The main objective of this thesis work is to develop methods able to simulate the vibrations and the radiated noise of periodic structural systems in a fast and accurate manner, independently on the structural complexity, curvature, excitation model and mean-flow effects. The minimum targets are to overcome the state-of-the-art in:

- The reduced flexibility and applicability of analytical approaches, valid only for simple structural elements under specific load models.
- The computational cost issues associated with classic finite element based numerical approaches .
- The reduced frequency bands of validity of energy-based approaches and find hybrid approaches to account for complex periodic cell dynamics in an energy analysis context
- The complexity of accounting for mean-flow effects on complex-shaped structures

The basic idea is to use, as often done for the analysis of structural dispersion, periodic cell approaches to reduce the modelling complexity and computational effort. However, this requires a description, in a periodic framework, of a loading environment which follows non-periodic schemes and/or different scales. In fact, as described previously in this chapter, especially for complex-shaped structures, the main issue is to have an accurate description of the structural mechanics at cell scale and link the periodic structural frameworks with a totally random and non-periodic excitation environment.

Then, the final target of this thesis work is to apply the methodologies to investigate periodic designs for enhanced vibroacoustic performance. In this context, the targets are:

- Provide design guidelines for existent core designs in sandwich panels, by using periodic structure theory
- Investigate the effects of periodic design or stiffening of flat and curved structures under complex loading conditions (i.e. aerodynamic)
- Investigate the effects of periodic add-ons (i.e mechanical resonators) on the flow-induced response.

## Chapter 3

# Modelling the Flow-Induced Vibrations with a 1D WFE Approach

In this chapter, the stochastic response of periodic flat and axial-symmetric structures under random and spatially-correlated loads, is analysed. Wave-based formulations, in a FEM framework, are developed to deal with a large variety of test-cases and coupled with a transfer matrix method. Although giving a lower computational cost, the present approach keeps the same accuracy of classic finite element methods. When dealing with homogeneous structures, the accuracy is also extended to higher frequencies, without increasing the time of calculation. Depending on the complexity of the structure and the frequency range, the computational cost can be reduced more than two orders of magnitude. The presented methodology is here validated both for simple and complex structural shapes, under deterministic and random loads.

### 3.1 The Proposed Method

The following approach is based on a combination of the transfer matrix method with a wave finite element method for periodic structures. A new formulation is proposed in order to deal with cyclic periodic structures.

#### 3.1.1 The Transfer Matrix Method

The method uses a transfer matrix between the fluid excitation and specific target degrees of freedom. This is built through the evaluation of the Green functions of each target DoF. Assuming a field of interest  $v$  (displacement, velocity, acceleration, pressure etc.) the response to the random load can be calculated as such:

$$S_{vv}(x_i, x_j, \omega) = \Theta_v^T(x_i, \omega) \mathbf{S}_{FF}(\omega) \Theta_v(x_j, \omega) \quad (3.1)$$

where  $\Theta_v$  is the transfer matrix, which is a  $m \times t$  matrix, and  $S_{vv}$  is the matrix of the auto/cross spectral densities of the field  $v$ . The value of  $t$  is associated to the target DoFs while the value of  $m$  is dependent on the fluid mesh (wetted surface); Fig. 3.1 shows an illustrative example. If, on the contrary, the excitation is distributed but deterministic, Eq. 3.2 can be used instead.

$$V(x_i, \omega) = \mathbf{L}_v^T(x_i, \omega) \mathbf{P}_F(\omega) \quad (3.2)$$

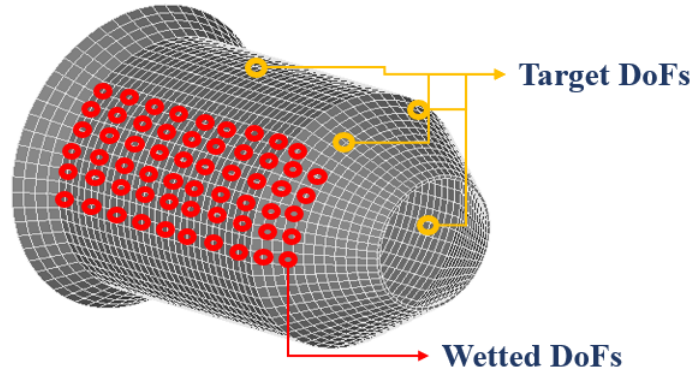


Figure 3.1: Illustration of degrees of freedom distribution in a transfer matrix framework: target ( $t$ ) degrees of freedom and wetted/loaded ones ( $m$ ).

where  $V$  is the target quantity of interest, while  $\mathbf{P}_F$  is the matrix describing the pressure load distribution.

This method gives an immediate advantage in the possibility to easily choose the value of  $t$  depending on the analysis needs; it can be even one or the total number of DoFs of the model.

It is important to point out that the values of  $t$  and  $m$ , apart from being flexible and objectives oriented, are always inferior to the total number of degrees of freedom of the whole FE model. Moreover, the non-wetted degrees of freedom do not increase the problem size, even if included in the system dynamics when computing the transfer matrix, being able to choose the values of  $t$  and  $m$  almost arbitrary.

The elements  $\Theta_v^{i,j}$  of the transfer matrix are values of the transfer Green function between the two points  $i$  and  $j$ . This work proposes to numerically calculate these elements through the a wave-based technique, based on section 2.4, and the Maxwell-Betti reciprocal work theorem; This theorem states that for a linear elastic structure subjected to two sets of forces  $P$  and  $Q$ , the work done by the set  $P$  through the displacements produced by the set  $Q$  is equal to the work done by the set  $Q$  through the displacements produced by the set  $P$ .

### 3.1.2 The Wave Finite Element Method (WFEM)

The adopted wave-based technique is a wave finite element (WFE) method applicable for homogeneous and periodic structures, based on section 2.4. The method makes use of the periodic conditions to derive, through an eigenvalue problem, the wavemodes of the periodic media. The solution is based on a wavemode approach, in which the problem is analysed through the superposition of different wavefields, [72, 73, 87, 89]. The method perfectly fits our need to calculate the Green functions due to its flexibility.

Considering a single repetitive substructure of our periodic media, the waves and their cross-sectional waveshapes (wavemodes), travelling in the structure, can be calculated by solving the eigenproblem which derives from imposing the Floquet's conditions (periodicity). In the 1D case the periodicity conditions are defined by imposing the equilibrium of the displacement and forces among the common hypernodes of two subsequent periodic cells (Fig. 2.14).

Starting from the dynamic stiffness matrix problem of a partial assemble of cells, reordering the DoFs so that internal, left and right nodes's degrees of freedom are properly separated,

one can move to the eigenvalue problem imposing the periodic conditions, assuming time and space harmonic excitation. Damping can be modelled by viscous damping matrix  $\mathbf{C}$  or by  $\mathbf{K}$  being complex. In the following equations, the left and right side hypernodes are defined with the letters  $L$  and  $R$  respectively:

$$\begin{bmatrix} \mathbf{D}_{ll} & \mathbf{D}_{lr} & \mathbf{D}_{li} \\ \mathbf{D}_{rl} & \mathbf{D}_{rr} & \mathbf{D}_{ri} \\ \mathbf{D}_{il} & \mathbf{D}_{ir} & \mathbf{D}_{ii} \end{bmatrix} \begin{Bmatrix} \mathbf{q}_L \\ \mathbf{q}_R \\ \mathbf{q}_I \end{Bmatrix} = \begin{Bmatrix} \mathbf{F}_L \\ \mathbf{F}_R \\ \mathbf{F}_I \end{Bmatrix}, \quad (3.3)$$

where  $\mathbf{D} = [\mathbf{K} - \omega^2 \mathbf{M}]$ . Condensing the internal degrees of freedom (I), substituting the third equation of Eq. (3.3), in the first two, one obtains his base-work equation:

$$\begin{bmatrix} \mathbf{D}_{LL} & \mathbf{D}_{LR} \\ \mathbf{D}_{RL} & \mathbf{D}_{RR} \end{bmatrix} \begin{Bmatrix} \mathbf{q}_L \\ \mathbf{q}_R \end{Bmatrix} = \begin{Bmatrix} \mathbf{F}_L \\ \mathbf{F}_R \end{Bmatrix}, \quad (3.4)$$

with:

$$\begin{aligned} \mathbf{D}_{RR} &= \mathbf{D}_{rr} - \mathbf{D}_{ri} \mathbf{D}_{ii}^{-1} \mathbf{D}_{ir} \\ \mathbf{F}_R &= \mathbf{F}_r - \mathbf{D}_{ri} \mathbf{D}_{ii}^{-1} \mathbf{F}_I \\ \mathbf{D}_{LL} &= \mathbf{D}_{ll} - \mathbf{D}_{li} \mathbf{D}_{ii}^{-1} \mathbf{D}_{il} \\ \mathbf{F}_L &= \mathbf{F}_l - \mathbf{D}_{li} \mathbf{D}_{ii}^{-1} \mathbf{F}_I \end{aligned} \quad (3.5)$$

where  $B$  stands for cell boundary, left or right. Eq.(3.5) is general, but in the cases here analysed, the forces on the inner nodes are considered null. This is valid within the framework of homogenized structures and it is used in this work for validation purposes. Other techniques can be used to condense the inner nodes, as a Craig-Bampton (CB) dynamic condensation method. This is strongly suggested for complex cross-sectional shapes [95, 96, 146].

Imposing continuity of displacements and equilibrium of forces at the interface between adjacent points and putting all in a matrix, the Transfer matrix,  $\mathbf{T}$ , can be derived, [84, 85, 87, 89]. It relates the nodal displacements and forces (evaluated on the left side) between two adjacent substructures:

$$\mathbf{T} = \begin{bmatrix} -\mathbf{D}_{LR}^{-1} \mathbf{D}_{LL} & \mathbf{D}_{LR}^{-1} \\ -\mathbf{D}_{RL} + \mathbf{D}_{RR} \mathbf{D}_{LR}^{-1} \mathbf{D}_{LL} & -\mathbf{D}_{RR} \mathbf{D}_{LR}^{-1} \end{bmatrix}. \quad (3.6)$$

It has been demonstrated that the eigenvalues of the transfer matrix occur in reciprocal pairs as  $\lambda_j^+ = 1/\lambda_j^-$  corresponding to pairs of positive (+) and negative (-) going waves, respectively, [72, 73, 89]. The positive and negative going eigenvectors  $\phi_j^-$  and  $\phi_j^+$  are associated with the above eigenvalues. These eigenvectors are referred to as wavemodes, which are the displacement and force distributions in the substructure section [85, 96, 103]. Every wavemode can be partitioned into a sub-vector of DoFs,  $\Phi_q^{+,-}$ , and internal forces/moments,  $\Phi_f^{+,-}$ .

Positive waves are characterized by the magnitude of the propagating constant being inferior to unity ( $|\lambda_j^+| < 1$ ), which means that if the wave propagates its amplitude must decrease in travelling. If  $|\lambda_j^+| = 1$  then the time average power transmission in the positive direction is evaluated to select the positive and negative going waves.

A transformation between the physical domain, where the system behaviour is described in terms of  $\mathbf{q}$  and  $\mathbf{f}$ , and the wave domain, where the behaviour is described in terms of

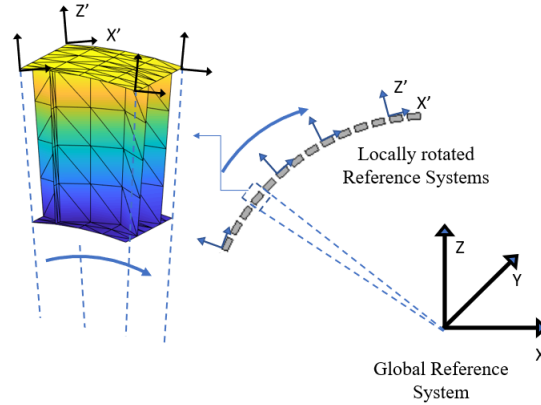


Figure 3.2: The rotation of the global reference into the local one in each location and layer of the cell.

waves of amplitudes  $\mathbf{a}^+$  and  $\mathbf{a}^-$  travelling in the positive and negative directions, is derived through these matrices [95, 105, 146]. In particular

$$\begin{Bmatrix} \mathbf{q}_L \\ \mathbf{f}_L \end{Bmatrix} = \begin{bmatrix} \Phi_q^+ & \Phi_q^- \\ \Phi_f^+ & \Phi_f^- \end{bmatrix} \begin{Bmatrix} \mathbf{a}^+ \\ \mathbf{a}^- \end{Bmatrix} \quad (3.7)$$

where  $\mathbf{a}^{+,-}$  are the wave amplitudes of the positive and negative going waves. It is important to emphasize that the wavemode-basis needs a filtering process to avoid numerical issues in the analysis. This is mainly addressable to the presence of waves which do not propagate in a certain frequency range but which are still present in the base as complex or purely imaginary wavenumbers. Maintaining these components in the wavebase is not a conceptual mistake but it generally gives numerical conditioning. Physically, this means considering the only contribution, to structural response, of the propagating or close-to propagating waves. At each frequency step, when and if new wavemodes cut-on, these are included in the wavemode-basis.

### 3.1.3 Curvature Simulation

In the present thesis, a WFE formulation is presented in order to deal with complex axial-symmetric structures. The main issue of the standard WFE approach relies in the complexity in dealing with axisymmetric non-cylindrical structures since each subsection is different from the previous one. Moving along the rotation axis, each point behaves on a circumference of different radius, or complex shapes.

The first idea is to simulate the curvature of our substructure through the rotation of the degrees of freedom at the borders, as shown in Fig. 3.2, [101].

A rotational matrix  $\mathbf{r}$  is defined and assembled in a block diagonal matrix,  $\mathbf{Rot}$ . It is intended to be done for each curvature; in this case a single curvature is considered.

$$\mathbf{Rot}_j = \begin{bmatrix} \mathbf{r}_j & 0 & \dots & 0 \\ 0 & \mathbf{r}_j & \dots & 0 \\ \vdots & & & \vdots \\ 0 & \dots & & \mathbf{r}_j \end{bmatrix} \quad (3.8)$$

As in Fig. 3.2, the curvature simulation must be made for every layer composing the elementary cell. Each layer can have a different nature and even fluid-structure coupling at cell scale can be included if fluid layers are present [89].

Hence the mass and stiffness matrices of the curved waveguide are obtained from the flat ones:

$$\begin{aligned}\mathbf{M} &= \mathbf{Rot}_j^T \mathbf{M}_{flat} \mathbf{Rot}_j \\ \mathbf{K} &= \mathbf{Rot}_j^T \mathbf{K}_{flat} \mathbf{Rot}_j.\end{aligned}\tag{3.9}$$

Imposing the periodicity conditions, the wave propagation is automatically considered along the curved path and the results are circumferential wavemodes; the waves analysed along the locally curved reference ( $X'$  in Figs. 3.2) are circumferential and/or helical waves.

Moreover, considering the relationships among arcs and angles, one can analyse the wave propagation using the circumferential wavenumber and the angular distance between points (Eq. 3.10). This is useful since, for tapered structures, different points run different lengths along the curved path, causing some technical issues.

$$\lambda_\theta = e^{-i\mathbf{k}_\theta \Delta\theta}\tag{3.10}$$

where  $k_\theta = k_x R = k_x \Delta_x / \Delta\theta$  is the circumferential wavenumber and  $\Delta\theta$  is the angular distance. It is worth to emphasize that the curvature simulation, showed here, aims at connecting the edge sections of the unit cell through a curved (discrete) system of coordinates. If point of inflections are present at cell scale, depending on the structure to be described, two approaches are possible, once the cell is modelled with the inflected parts. In one case, the wave propagation can be analysed along the global X-Y axes, simulating a flat waveguide with inflected sections. Otherwise, the cell curvature can be simulated using the nodal coordinates, even the ones belonging to the inflected part of the cell, to evaluate the local rotation of the coordinate system to be simulated; this is translated in a rotation matrix in Eq. 3.9.

## 3.2 Forced Vibrations for a Punctual Load

With reference to Fig. 3.3, the forced vibrations in a response point can be evaluated through the superimposition of the direct and reverberant field. The first is the result of the excitation and the second is the incident wavefield.

### 3.2.1 The Direct Field

Recalling Section 2.4, lets write the continuity of displacements and the equilibrium of the force at the excitation point using the wave-basis expansion, from which we can rewrite the equilibrium equations in matrix form:

$$\begin{bmatrix} \Phi_{s_q}^+ & -\Phi_{s_q}^- \\ \Phi_{s_f}^+ & -\Phi_{s_f}^- \end{bmatrix} \begin{Bmatrix} e^+ \\ e^- \end{Bmatrix} = \begin{Bmatrix} \mathbf{0} \\ \mathbf{f}_{ext} \end{Bmatrix}\tag{3.11}$$

where  $e^{+,-}$  is the vector of the amplitudes of the wavemodes. They define, in other words, the direct wavefield in a wave-basis framework. The inversion of the above left-hand side matrix can lead to numerical errors, especially for complex structures and cell shapes [87,

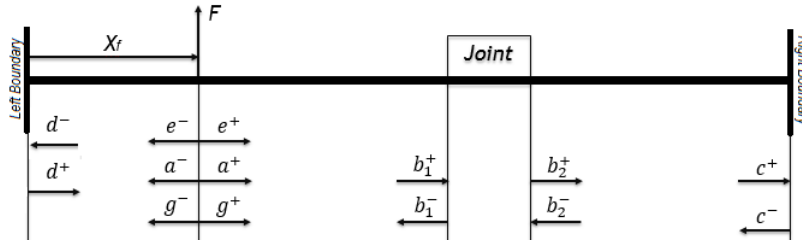


Figure 3.3: Waves in a finite waveguide excited by point load.

106]. Exploiting the orthogonality of the left and right eigenvectors, avoids this numerical issue; pre-multiplying both sides of the previous equation by the matrix of left eigenvectors properly rearranged [87, 106, 147]:

$$\begin{Bmatrix} e^+ \\ e^- \end{Bmatrix} = \begin{Bmatrix} \Psi s_f^+ \mathbf{f}_{ext} \\ -\Psi s_f^- \mathbf{f}_{ext} \end{Bmatrix} \quad (3.12)$$

This, of course, requires a left-eigenvalue problem, whose eigenvectors are  $\Psi s_f^{+,-}$ , to be solved too. Fig. 3.3 can be used as illustrative reference.

### 3.2.2 Waves at Boundaries

Waves incident upon boundaries are partially reflected, transmitted and absorbed. Instead, in the case of elastic boundary conditions, an incident wave is only reflected, without any transmission. In Fig. 3.3 this is illustrated with  $\mathbf{d}^{-,+}$  and  $\mathbf{c}^{-,+}$ , at the edges of the structure. Considering a generic wave of amplitude  $\mathbf{h}^+$  travelling in the medium, we can model the reflection and the subsequent opposite-going wave amplitude,  $\mathbf{h}^-$ , with the use of reflection matrices at boundaries. Given  $\mathbf{R}$  as the matrix of reflection coefficients, which depends on the type of constraint, the wave problem at the boundaries can be expressed as  $\mathbf{h}^{+,-} = \mathbf{R}\mathbf{h}^{-,+}$ . Each boundary condition can always be expressed in the form:  $\mathbf{A}\mathbf{f} + \mathbf{B}\mathbf{q} = \mathbf{0}$ . Substituting the wave base expansion for forces and displacements [105, 106]:

$$\begin{aligned} \mathbf{R}_{right} &= -(\mathbf{A}\Phi s_f^- + \mathbf{B}\Phi s_q^-)^{-1}(\mathbf{A}\Phi s_f^+ + \mathbf{B}\Phi s_q^+) \\ \mathbf{R}_{left} &= -(\mathbf{A}\Phi s_f^+ + \mathbf{B}\Phi s_q^+)^{-1}(\mathbf{A}\Phi s_f^- + \mathbf{B}\Phi s_q^-) \end{aligned} \quad (3.13)$$

where the matrices  $\mathbf{A}$  and  $\mathbf{B}$  are dependent on the type of constrain, as said. In the case of force-free boundaries, for example,  $\mathbf{A} = \mathbf{I}$  and  $\mathbf{B} = \mathbf{0}$ .

### 3.2.3 The Scattering Matrix

If some discontinuities, such as linear or complex joints, are reached by the waves, the scattering properties become largely impactful on the structural behaviour. Considering a junction as in Fig. 3.3 one can analyse the scattering properties taking into account the waves in the first and second waveguide, in terms of incident and outgoing (reflected and transmitted) wave amplitudes along the junction itself [148, 149]. In Fig. 3.3 this is

illustrated with  $\mathbf{b}_1^{-,+}$  and  $\mathbf{b}_2^{-,+}$ , at the edges of the structure. The scattering matrix  $\mathbf{s}$  can be defined taking into account what just said and thus has the following expression

$$\begin{Bmatrix} \mathbf{b}_1^- \\ \mathbf{b}_2^+ \end{Bmatrix} = \begin{bmatrix} \mathbf{s}_1 & \mathbf{s}_2 \\ \mathbf{s}_3 & \mathbf{s}_4 \end{bmatrix} \begin{Bmatrix} \mathbf{b}_1^+ \\ \mathbf{b}_2^- \end{Bmatrix} \quad (3.14)$$

where the scattering matrix has been splinted in four matrices:  $\mathbf{s}_1$  and  $\mathbf{s}_4$  represent transmission matrices, while  $\mathbf{s}_2$  and  $\mathbf{s}_3$  represent reflection ones. The joint is assumed to be infinite in the direction normal to the propagation one and is modelled using finite elements. This assumption does not affect the results even for finite-size structures. It is to be underlined that there is no restriction on the type of FE model to be used for the joint.

Condensing the FE of the junction to the borders and express the dynamic equation of the junction as condensed to its edges, one gets Eq. 3.15. Typical methods are static condensations or a component mode synthesis [95, 97]. If internal forces are present, these can be substituted by structurally equivalent forces at the joint interface.

$$\mathbf{D}_J \mathbf{Q}_J = \mathbf{F}_J \quad (3.15)$$

where  $\mathbf{Q}_J$  and  $\mathbf{F}_J$  are the vectors of dofs and nodal forces of the joint to its borders. Since the force and displacement vectors at the borders of the joint are in common with the two waveguides, they can be expressed in wave base using the wavemodes of each periodic substructure. Imposing the continuity and equilibrium conditions for the joint and using the eigenvectors of the two waveguides incident on the joint, the displacements  $\mathbf{Q}_J$  and the force field  $\mathbf{F}_J$  can be expressed in a wave-basis:

$$\mathbf{Q}_J = \begin{bmatrix} \Phi_q^{1,+} \mathbf{b}_1^+ + \Phi_q^{1,-} \mathbf{b}_1^- \\ \Phi_q^{2,+} \mathbf{b}_2^+ + \Phi_q^{2,-} \mathbf{b}_2^- \end{bmatrix} \quad (3.16)$$

$$\mathbf{F}_J = \begin{bmatrix} \Phi_f^{1,+} \mathbf{b}_1^+ + \Phi_f^{1,-} \mathbf{b}_1^- \\ -\Phi_f^{2,+} \mathbf{b}_2^+ - \Phi_f^{2,-} \mathbf{b}_2^- \end{bmatrix}. \quad (3.17)$$

Substituting the previous equations in the equilibrium equation of the joint (Eq. 3.15), condensed to boundaries, the scattering matrix can be obtained straightforwardly.

$$\mathbf{s} = \left[ -\mathbf{D}_J \begin{bmatrix} \Phi_q^{1,-} & \mathbf{0} \\ \mathbf{0} & \Phi_q^{2,+} \end{bmatrix} + \begin{bmatrix} \Phi_f^{1,-} & \mathbf{0} \\ \mathbf{0} & -\Phi_f^{2,+} \end{bmatrix} \right]^{-1} \left[ \mathbf{D}_J \begin{bmatrix} \Phi_q^{1,+} & \mathbf{0} \\ \mathbf{0} & \Phi_q^{2,-} \end{bmatrix} - \begin{bmatrix} \Phi_f^{1,+} & \mathbf{0} \\ \mathbf{0} & -\Phi_f^{2,-} \end{bmatrix} \right] \quad (3.18)$$

The inversion in the previous equation can cause numerical instabilities and the use of the left eigenvalues is required [148], as in the case of section 3.12. It should be underlined that the actual description is applicable also for lap joints, L-shaped, T-shaped or more complex junctions, as deeply investigated in [105] and [148].

### 3.2.4 Waves Propagation

Moving in the medium, the amplitude of all the waves changes, depending on the distance and the wave characteristics itself.

Their variations can be derived by applying the definition of propagation constant. For instance, if the waveguide has  $n$  wave components, the waves amplitudes at two points,

distant " $x$ " apart, are given by:  $\mathbf{h}^+ = \mathbf{Tr} \mathbf{s}^+$ , where  $\mathbf{Tr}$  is the wave propagation matrix. It can be expressed as:

$$\mathbf{Tr}(x) = \text{diag}\left(e^{-ik_1x}, e^{-ik_2x}, \dots, e^{-ik_nx}\right) \quad (3.19)$$

All the elements of the wave propagation matrix have a magnitude less or equal to the unity, by definition.

**Waves' Amplitudes link in the Waveguide** Using again Fig. 3.3 as reference we can evaluate the amplitude of waves in the reference point. The following is the set of equilibrium equations, made of algebraic equations in matrix form. At the excitation location, one can sum the incident and direct field:

$$a^+ = e^+ + g^+; \quad g^- = e^- + a^- \quad (3.20)$$

At boundaries, instead, the following reflection relations are valid (see Fig 3.3):

$$c^- = \mathbf{R}_{right}c^+; \quad d^+ = \mathbf{R}_{left}d^- \quad (3.21)$$

At the same time, along the waveguide, the following propagation relations hold:

$$g^+ = \mathbf{Tr}(x_f)d^+; \quad d^- = \mathbf{Tr}(x_f)g^-; \quad a^- = \mathbf{Tr}(L - x_f)c^-; \quad c^+ = \mathbf{Tr}(x_f)a^+. \quad (3.22)$$

### 3.2.5 Incident Field and Waves Superposition

Once the amplitudes of direct wavefield are known, the amplitudes of the waves can be calculated at a given response point by considering the excitation, reflection and propagation relations. Using again Fig. 3.3 as reference, the amplitude of waves in the reference point can be calculated.

In general, the structures might not be fully periodic. It might happen, however, that the entire structure can be identified as the sum of periodic parts connected through joints. In these cases, the technique presented above can still be considered valid if the scattering around the joint is taken into account.

Now, using all the previous equations the wave amplitudes can be evaluated in the driving point, in this case, the excitation location. Before doing that the scattering equation can be solved obtaining the values of the incoming and out-coming waves at the joint:

$$b_2^+ = [\mathbf{I} - \mathbf{s}_4 \mathbf{Tr}(L_2) \mathbf{R}_{left} \mathbf{Tr}(L_2)]^{-1} [\mathbf{s}_3 \mathbf{Tr}(L_1 - x_f)] a^+ \quad (3.23)$$

$$b_1^- = \mathbf{s}_1 \mathbf{Tr}(L_1 - x_f) a^+ + \mathbf{s}_2 \mathbf{Tr}(L_2) \mathbf{R}_{left} \mathbf{Tr}(L_2) b_2^+ \quad (3.24)$$

with  $L_1$  and  $L_2$  the lengths of the first (left) and second (right) waveguide,  $x_f$  the position of the force. The following form of the wave amplitudes is derived, assuming, in this case, that the force is applied, for example, on the first waveguide:

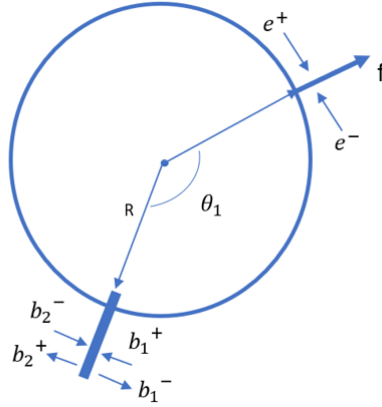


Figure 3.4: Waves in an axial-symmetric jointed structure excited by a point load

$$a^+ = [\mathbf{I} - \mathbf{Tr}(x_f)\mathbf{R}_{left}\mathbf{Tr}(x_f)\mathbf{Tr}(L_1 - x_f)\mathbf{s}_2\mathbf{Tr}(L_2)\mathbf{R}_{left}\mathbf{Tr}(L_2)]^{-1} \\ \mathbf{s}_3\mathbf{Tr}(L_1 - x_f) - \mathbf{Tr}(x_f)\mathbf{R}_{left}\mathbf{Tr}(x_f)\mathbf{Tr}(L_1 - x_f)\mathbf{s}_1\mathbf{Tr}(L_1 - x_f)]^{-1} \\ [e^+ + \mathbf{Tr}(x_f)\mathbf{R}_{left}\mathbf{Tr}(x_f)e^-] \quad (3.25)$$

$$a^- = \mathbf{Tr}(L_1 - x_f) [\mathbf{s}_2\mathbf{Tr}(L_2)\mathbf{R}_{left}\mathbf{Tr}(L_2) [\mathbf{I} - \mathbf{s}_4\mathbf{Tr}(L_2)\mathbf{R}_{left}\mathbf{Tr}(L_2)]^{-1} \\ \mathbf{s}_3\mathbf{Tr}(L_1 - x_f) - \mathbf{s}_1\mathbf{Tr}(L_1 - x_f)] a^+ \quad (3.26)$$

Finally, the response in the reception point can be then calculated applying the propagation relations to the target distance, [105–107, 147].

### 3.2.6 An axisymmetric 1D-WFE formulation for wavefields along circular paths

As previously done for flat waveguides, the response in a target point can be calculated considering the superposition of an equivalent direct field and the reverberant one, taking into account that, in the case of closed axial-symmetric structures, no real boundaries are present, if impedance variations do not appear. For example, with reference to the scheme in Fig.3.4, the same equations adopted in the case of a flat structure are valid and the response in a target point can be expressed as:

$$a^+ = [\mathbf{I} - \mathbf{Tr}(2\pi - \theta_1)\mathbf{s}_3\mathbf{Tr}(\theta_1) - \mathbf{Tr}(2\pi - \theta_1)\mathbf{s}_4\mathbf{Tr}(2\pi - \theta_1) [\mathbf{I} - \mathbf{Tr}(\theta_1)\mathbf{s}_2\mathbf{Tr}(\theta_1)]^{-1} \\ \mathbf{Tr}(\theta_1)\mathbf{s}_2\mathbf{Tr}(\theta_1)]^{-1} [e^+ + \mathbf{Tr}(2\pi - \theta_1)\mathbf{s}_4\mathbf{Tr}(2\pi - \theta_1) [\mathbf{I} - \mathbf{Tr}(\theta_1)\mathbf{s}_2\mathbf{Tr}(\theta_1)]^{-1} e^-] \quad (3.27)$$

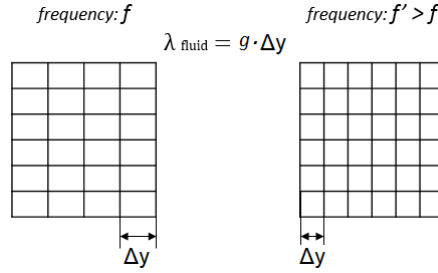


Figure 3.5: Mesh adaptation scheme

$$a^- = [\mathbf{I} - \mathbf{Tr}(\theta_1)\mathbf{s}_2\mathbf{Tr}(\theta_1)]^{-1} [e^- + \mathbf{Tr}(\theta_1)\mathbf{s}_1\mathbf{Tr}(\theta_1)a^+] - e^- \quad (3.28)$$

Eqs. (3.27) and (3.28) represent the general solution when an impedance variation is also present on the circumferential wave-path. In the case the axisymmetric structure is homogeneous, or simply there is no variation of impedance, Eq. (3.27) and (3.28) remain the same, while the values of the  $\mathbf{s}_J$  ( $J=1, \dots, 4$ ) matrices change in zeros and identity matrices since a full transmission must be simulated. For example, in the case of closed axisymmetric structures with no impedance variations, no scattering is present and assuming a  $\Delta\theta > 0$ , the reverberant field is simply given by:

$$\mathbf{g}^+ = \mathbf{Tr}(2\pi)\mathbf{b}^+ \quad \mathbf{g}^- = \mathbf{Tr}(2\pi - \Delta\theta)\mathbf{b}^- \quad (3.29)$$

### 3.2.7 Variable mesh for Homogenised Layers

The use of the WFE approach gives many advantages in building the transfer matrix  $\Theta_v$ . In particular, in Eq.(3.19), it is clear how the wave propagation can be taken into account using an analytic (non-discretised) system of coordinates; the coordinate system is not forced to respect the mesh spacings. This opens to the possibility of using variable meshes in the periodicity direction, evaluating the response in more intermediate point which do not strictly belong to the starting FE mesh. The value of  $m$ , connected to the mesh size on the wetted (external) surface, can be changed frequency-by-frequency imposing a different spatial step ( $\Delta y$ ), allowing a strong save in computational cost, with respect to the cases in which the mesh is initially set on the finest value. The size of the transfer matrix is, then, tuned on the fluid wavelength variation (i.e. versus the frequency of interest). In Fig. 3.5, a simple scheme illustrating this operation, with  $g$  as an integer generally comprised between 6 and 10 to correctly describe the desired wavelength.

A single coarse substructure can be used to analyse the dynamic problem to higher frequencies, instead of creating a finer representation of it through FE codes. The immediate results of this approach are evident when dealing with the stochastic response to random load. First of all the aliasing frequency moves forward enlarging the frequency range of accuracy for the approximation in Eq.(2.27). Then, given a frequency range of analysis, the computational advantage is higher and higher approaching the lower frequency limit of the band, since an equivalent coarser grid can be considered. In a next section, the effects of this numerical property is shown with a specific test-case.

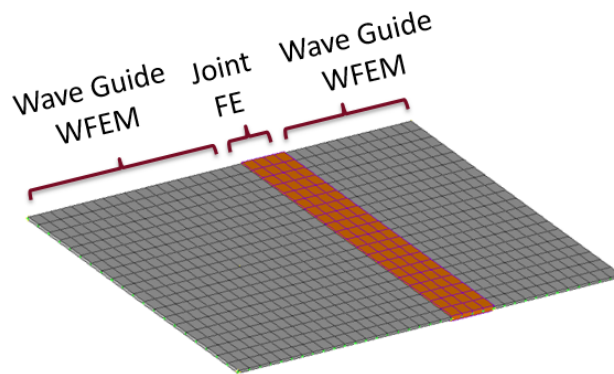


Figure 3.6: Simple representation of two in-plane jointed waveguides

### 3.3 Results for Deterministic Load

The above-described wave based methodologies are the instrument to calculate the Green functions of each target degree of freedom with respect to the wetted points, which are the nodes where the stochastic load is translated. The validation of the forced response to point load for flat structures, i.e. panels, using the standard WFE technique has been already done by many authors in literature [84, 85, 87, 89, 105] and is reproduced here only for the enhanced formulations that have been developed for jointed and periodic structures with cyclic periodicity.

#### 3.3.1 Results for periodicity along a rectilinear direction

In this section, a series of results are presented to assess the accuracy of the presented methodology.

The validation of the forced response to point load for flat structures, i.e. panels, using the standard WFE technique has been already done by many authors in literature [84, 85, 87, 89, 105].

##### In-plane Jointed Panel

With reference to Fig. 3.6, two isotropic panels are considered; they are waveguides, connected through a 2D in-plane junction, discretised using FE. Free-Free boundary conditions are implemented.

The proposed hybrid method is used to analyse the vibrations on the first (left) waveguide for a point force applied on the other panel domain. The FE model of the junction has been condensed to the borders using a static or dynamic condensation [95, 97].

As noticeable in Fig. 3.7 the accuracy of the present method is excellent in the whole frequency range of analysis.

##### Stiffened Cylinder with non-Periodic Holes

With reference to Fig. 3.8, a doubly-stiffened cylindrical model is considered as a waveguide but connected through a complex junction. The idea is to simulate, even if in a simplified model, the presence of windows in aircraft fuselages. This specific part, so, is modelled

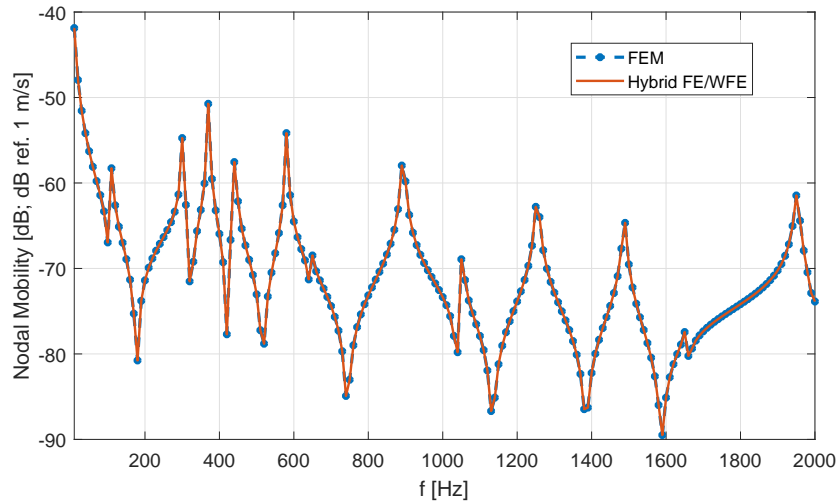


Figure 3.7: Nodal mobility on the first waveguide for a point load in the second one (see Fig. 3.6). The reference solution is calculated using FEM. Boundary conditions: Free-Free.

Table 3.2: Cylinder Geometry

Length	4.2 m
Diameter	2.8 m
Skins Thickness	$4.0 \cdot 10^{-3}$ m
Frames Thickness	$7.0 \cdot 10^{-3}$ m

using FE and condensed to the borders using a CB (Craig-Bampton) method, retaining 200 modes.

In particular, the skins are modelled using a composite material whose data are available in Table 3.1, while the frames and the stiffeners are in aluminium. The model is periodic and composed of 37 identical substructures. Solid elements are used to model as the skins and frames, while the stringers are modelled using beam elements.

Table 3.1: Material constants for cylinder skins

$E_x$	$E_y$	$G_{xy}$	$\nu_{xy}$	Layup
125 GPa	12.5 GPa	6.89 GPa	0.38	$[0, 90, +45, -45, 0]_{sym}$

Table 3.3: Hat-Stiffener Geometry

Height	$3.0 \cdot 10^{-2}$ m
Thickness	$5.0 \cdot 10^{-3}$ m
Upper Width	$2.0 \cdot 10^{-2}$ m
Lower Width	$3.0 \cdot 10^{-2}$ m

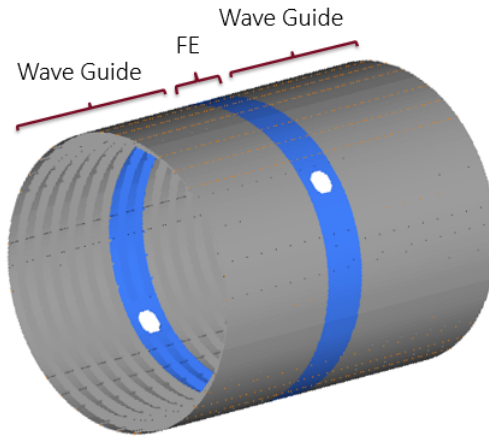


Figure 3.8: Two waveguides (stiffened cylinders) connected with a complex junction in between.

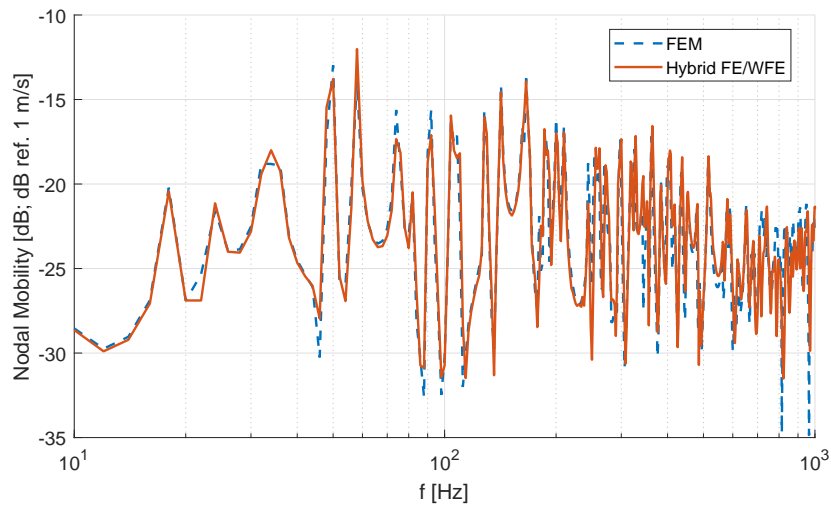


Figure 3.9: Nodal mobility on the first waveguide for a point load (see Fig. 3.8). The reference solution is calculated using FEM. Boundary conditions: Simply-Supported at the edges.

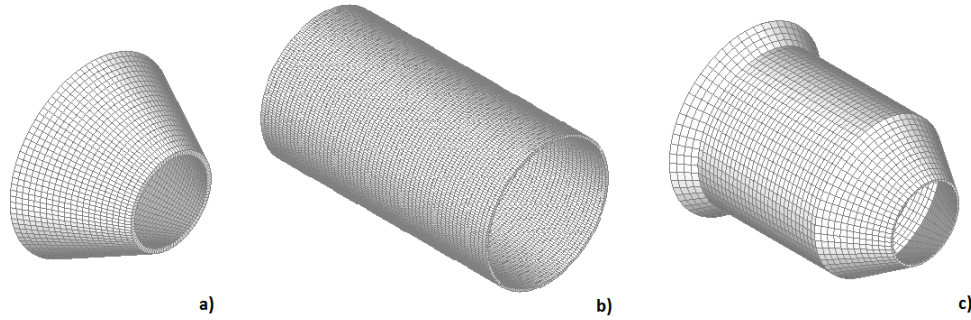


Figure 3.10: Axial-symmetric Models analysed - (a) Conical; (b) Cylindrical; (c) Complex - SYLDA

Table 3.4: Axial-symmetric models geometrical parameters

Data	Conical	Cylindrical	Complex - SYLDA
Length [m]	0.20	0.6	0.40
Diameter at $x = 0$ [m]	0.20	0.40	0.15
Diameter at $x = L$ [m]	0.40	0.40	0.34
Diameter at $x = L/2$ [m]	0.30	0.40	0.29
Skin thickness [mm]	4.0	4.0	7.0

The results in Fig. 3.9 show a good accuracy in the whole frequency range even if the numerical issues that arise in complex cases like this are exponentially higher due to the inversion of the scattering matrix and the wavemodes filtering of such an heterogeneous model

### 3.3.2 Results for periodicity along a circular direction

Three basic axisymmetric geometries are analysed: cylinder, cone and a complex assembly of them (Fig. 3.10). The latter is a scaled model of the SYLDA (SYstème de Lancement Double Ariane) structure, generally used in the Ariane V launcher for multiple simultaneous launch [103]. In any case, the structures are homogenized and made in aluminium. For sake of completeness, the geometrical properties of the models are reported in Table 3.4.

A full FE model is used in each case, as a reference, to compare and validate the numerical results. All the structures in Figs. 3.10 and 3.11 are modelled and the mass and stiffness matrices are extracted using a commercial code (ANSYS). In Fig. 3.12, 3.13 and 3.14, the frequency response functions, in different specific points ( $\Delta_x$  and  $\Delta_\theta$  the axial and circumferential coordinates, with respect to the point of application of the force), are compared for the present method and the full FEM. Both circumferential and coupled modes, typical for axial-symmetric structures, are identified and precisely described (Fig. 3.15) and it is evident how the proposed methodology provides very accurate results with the highest relative error, inside the whole frequency band, inferior to  $10^{-2}$  dB.

A case with impedance variations along the circumferential path of the axisymmetric structure is also analysed. The structure is a simple aluminium cylinder/ring with a section of different thickness, as shown in Fig. 3.16. The results, shown in Fig. 3.17, for a single point

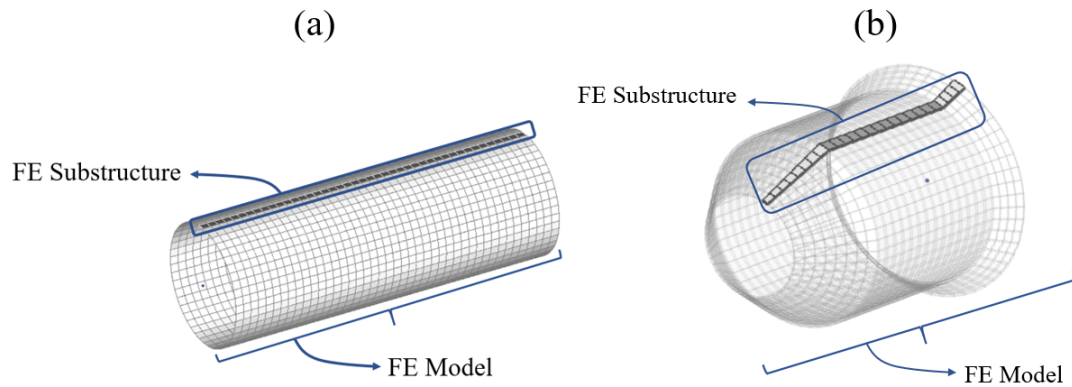


Figure 3.11: The relative substructures of the axial-symmetric models - (a) Cylindrical; (b) Complex - SYLDA

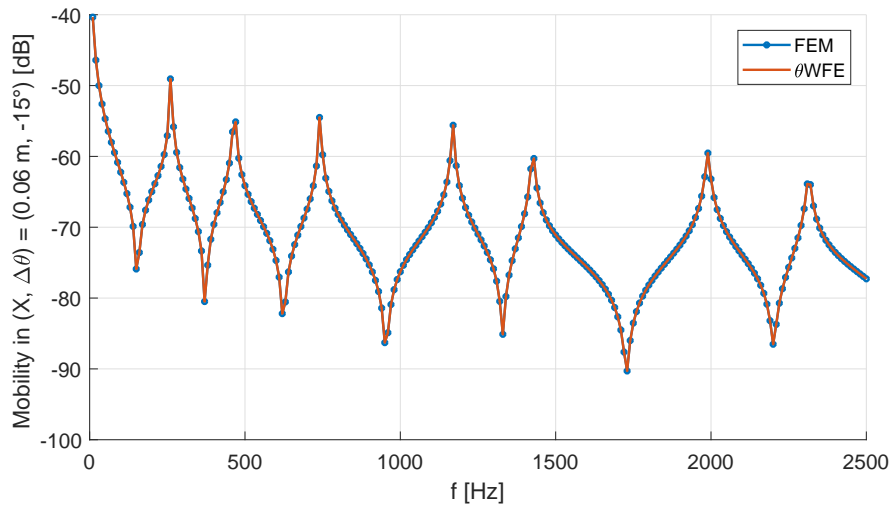


Figure 3.12: Mobility on the cylindrical model [dB ref. 1 m/s] - Numerical comparison between the present technique (formulation for curved wave paths -  $\theta$ WFE) and the full FEM for a point load excitation.

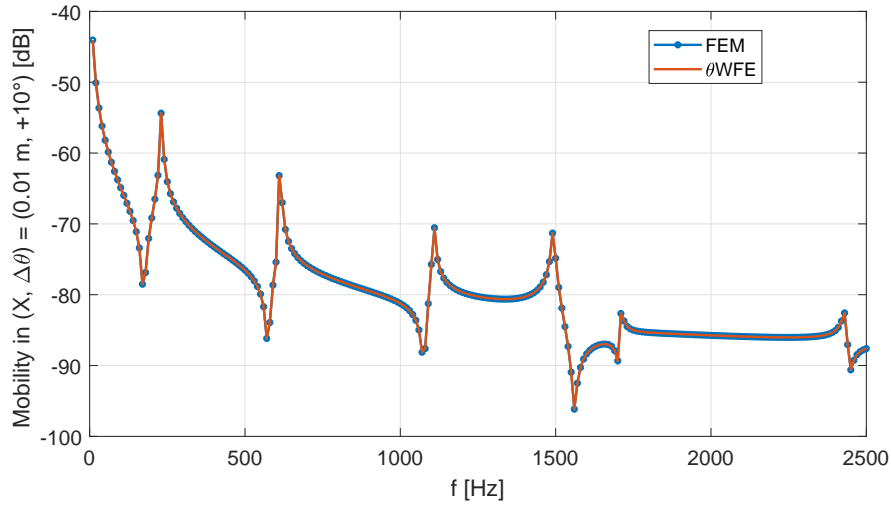


Figure 3.13: Mobility on the conical model [dB ref. 1 m/s] - Numerical comparison between the present technique (formulation for curved wave paths -  $\theta$ WFE) and the full FEM for a point load excitation.

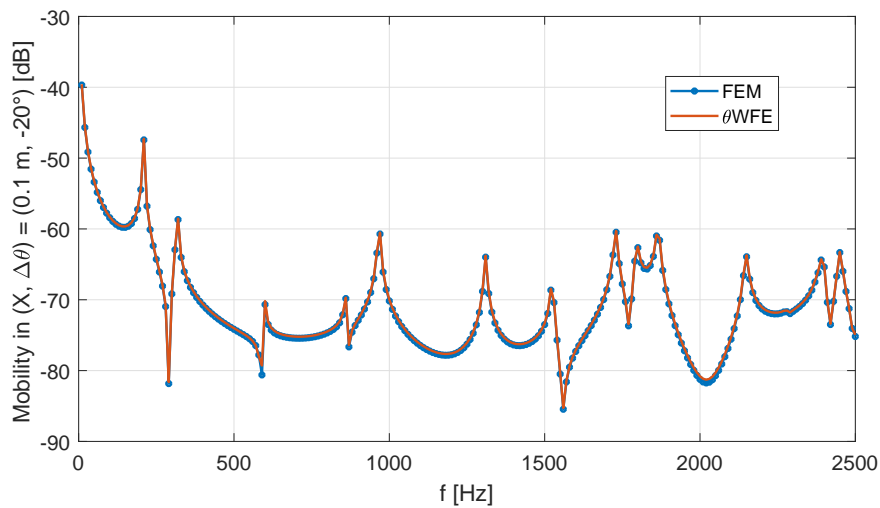


Figure 3.14: Mobility on the SYLDA model [dB ref. 1 m/s] - Numerical comparison between the present technique (formulation for curved wave paths -  $\theta$ WFE) and the full FEM for a point load excitation.

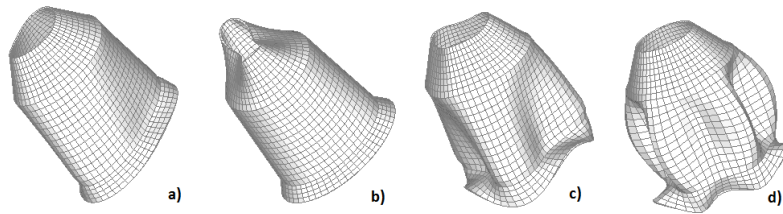


Figure 3.15: The circumferential and coupled modes for the SYLDA test-case; (a) 229.6 Hz, (b) 357.2 Hz, (c) 640.2 Hz, (d) 984.5 Hz

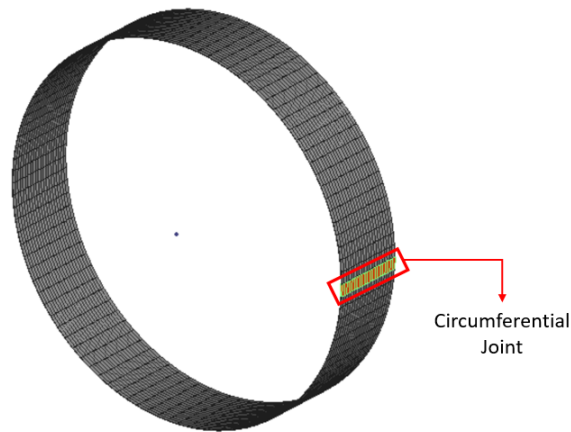


Figure 3.16: A cylindrical structure with impedance variations along the circumference.

load, are computed using Eqs. 3.27 and 3.28. The reference solution, again, is a full FEM computation. The results are in good agreement.

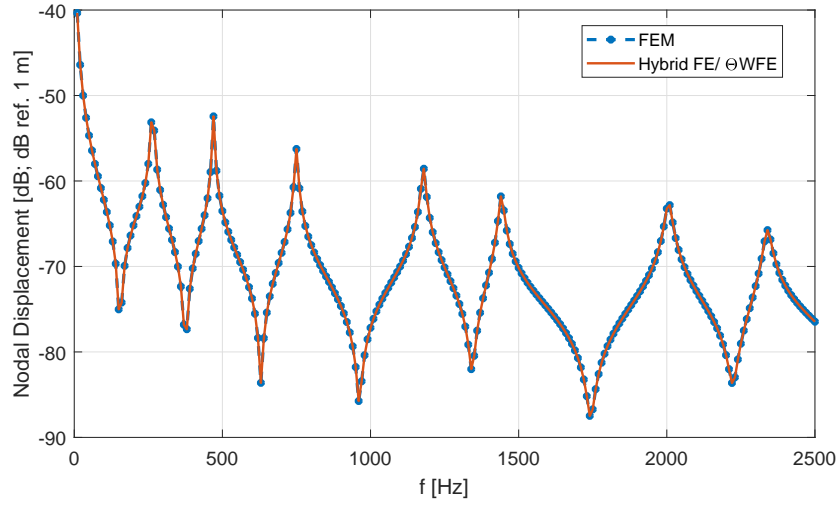


Figure 3.17: Nodal displacement on the model shown in Fig. 3.16 [dB ref. 1 m] - Numerical comparison between the present technique ( $\theta WFE$ ) and the full FEM for a point load excitation.

### 3.4 Results for Stochastic Load

In this section, a series of results for flat ad axial-symmetric structures under aeroacoustic load are presented to assess the accuracy of the presented methodology. It is worth to remind that, using the transfer matrix method, the accuracy validation of the deterministic response leads also to the validation of the stochastic one. In each of the following cases a 10-elements per minimum wavelength mesh is used for convergence purposes.

#### 3.4.1 Flat Panel under TBL excitation

A flat panel is considered, whose geometrical parameters are in Table 3.5, under a turbulent boundary layer load (Corcos model;  $\alpha_x = 0.15$ ;  $\alpha_y = 0.77$ ;  $U_c = 120$  m/s). The panel is made in aluminium:  $E = 7.0 \cdot 10^{10}$  Pa,  $\rho = 2750$  kg/m<sup>3</sup>,  $\nu = 0.33$  and 1% of structural damping. The analytic solution is used as a reference and a comparison between a full FEM and the proposed method is shown. The analytic approach can be developed only for a flat rectangular panel simply-supported to the edges under a Corcos TBL model, as it is in this case. The final equation is here shown for more clearness [7]:

$$S_{ww}(x_a, y_a, \omega) = \sum_j \sum_n \left[ \frac{\Psi_j(x_a, y_a) \Psi_n(x_a, y_a)}{Z_j^H(\omega) Z_n(\omega) \gamma_j \gamma_n} \right] A_{Q_j Q_n}(\omega) \quad (3.30)$$

where  $\Psi_j$  is the  $j$ th analytic mode shape,  $\gamma_j$  is the generalized mass coefficient for the same mode order,  $Z_j$  is the dynamic structural impedance and  $A_{Q_j Q_n}$  is the well-known joint acceptance integral.

The numerical load approximation in Eq. (2.27) is used for both the full FE model and the WFE-based. The mesh sizes are so that the aliasing frequency is 2000 Hz and the critical frequency is 580 Hz. The response is computed in any point of the mesh grid. Fig.3.18 reports the comparison of the results for a specific grid point. The present methodology,

Table 3.5: Panel geometrical parameters

Panel Geometrical Data	
Length stream-wise ( $x$ ) [m]	0.36
Length cross-wise ( $y$ ) [m]	0.20
Skin thickness [mm]	3.0

Table 3.6: Computational cost comparison for a flat panel to TBL load

Method	Design frequency	Elapsed time/frequency [sec]
FEM - Eq.(2.24) and Eq.(2.27)	6 kHz	82.65
WFE - Eq.(3.1) and Eq.(2.27)	6 kHz	3.25
WFE - TM and variable mesh	6 kHz in $y$ ; variable in $x$	1

through the use of a variable mesh, feasible due to the wave-based method coupled with the transfer matrix in Eq. (3.1), calculated step-by-step in the frequency domain, extends the accuracy even over the aliasing frequency. On the contrary, as expected, the FEM results become more and more inaccurate above the aliasing frequency. A difference in the modal content of the structural response between the analytic and numerical model is present. This is addressable to the analytic model being developed to take into account the only bending of the plate, while the FE-based methods, are modelled to take into account a more complete behaviour. Obviously, the possibility to easily refine the solution mesh moves the aliasing frequency to higher one. This explains the results enhancements versus the full FEM ones. Moreover the present method is much faster than the standard one, thus giving a double advantage for the analysis of these specific problems (Table 3.6). It is important to underline that, if a variable mesh is used, the elapsed time per frequency is given by an average on the whole frequency band, because the real time is very low when the computed frequency step is far from the upper limit of the frequency band and increases as the frequency increases up to the maximum frequency band. The flexibility of the method allows huge advantages in the easier link among the structural and fluid mesh. It must be emphasized also that all the degrees of freedom, which are not “wetted”, do not increase the problem size, but, at the same time, the response can be calculated even in “non-wetted” points.

Damping does not affect the mesh sizes, thus the computational cost, but, on the other hand, it can be modelled, in the framework of the dynamic stiffness matrix approach, through frequency-depending matrices [84, 95, 150]. The method, however, has a drawback in the eigenvalue problem, which must be solved at each frequency in order to obtain the wave-modes of the periodic structure. This might be a problem with very complex industrial structures, if an order reduction is not used.

### 3.4.2 Un-stiffened Cylindrical Structure under TBL load

The cylinder, described in Table 3.4, is used as a test-case here under TBL excitation, using a Corcos model. A simple application of this model to a cylindrical model is still acceptable, if the stream-wise direction is parallel to the axis of rotation and the cross-wise is assumed to be the circumferential one [151]. The  $\theta WFE$  method is used and compared with the full FE model.

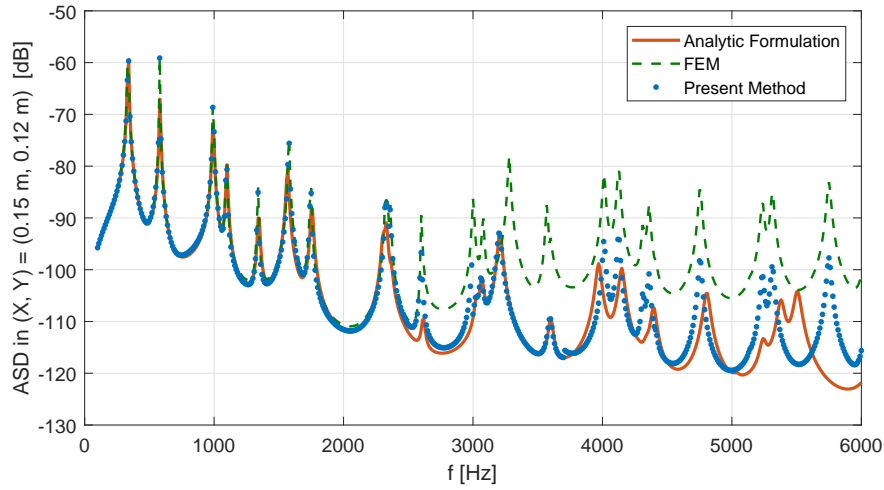


Figure 3.18: Analytic-Numerical results comparison for a flat panel subjected to TBL - Auto Spectral Density in one point, [dB ref. 1 m/s].

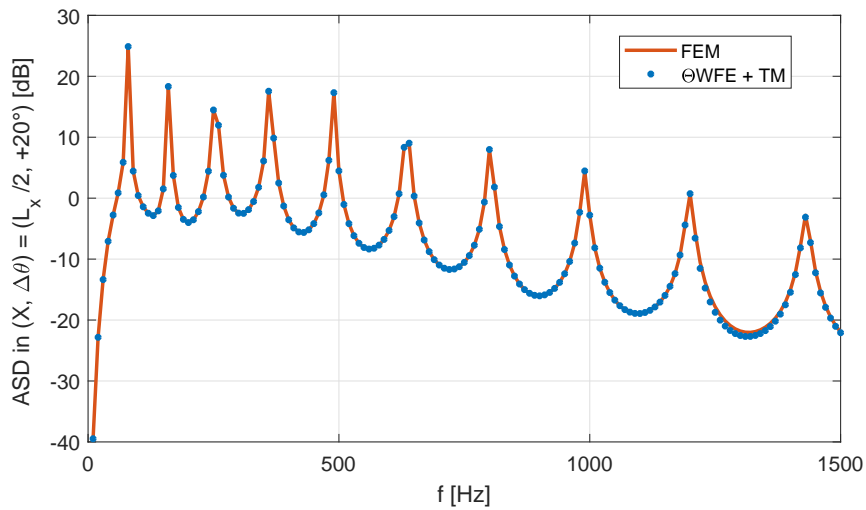


Figure 3.19: Numerical results comparison for a cylinder subjected to TBL - Auto Spectral Density in one point, [dB ref. 1 m/s].

Table 3.7: Computational cost for a cylindrical structure to TBL load

Method	Design frequency	Elapsed time/frequency [sec]
FEM - Eq.(2.24) and Eq.(2.27)	1.25 kHz	287.2
$\theta WFE$ - Eq.(3.1) and Eq.(2.27)	Variable	1

Table 3.8: Material Data of the Lamina

$E_X$ [GPa]	$E_Y$ [GPa]	$\rho$ [Kg/m <sup>3</sup> ]	$G_{XY}$ [GPa]	$G_{XZ}$ [GPa]	$\nu_{XY}$
129	8.25	1600	4.23	4.23	0.0192

In this case, the aliasing frequency is 1250 Hz and, as shown in Fig.3.19, the discrepancy among the FE scheme and the present method increases above this frequency. This can be addressed to the loss of validity of Eq.(2.27), which is circumvented with the present method through the use of variable meshes. The results show a good agreement in the whole frequency range, as expected, because, as previously stated, the validation of the method of calculation of the Green functions guarantees the results for the stochastic cases, assuming that the load description in discrete coordinates is correct.

It is worth underlining also the ease of use of this technique when dealing with pressure loads since the local system of coordinates, which becomes the only reference (lagrangian) when the curvature of the system is simulated, gives the chance of having always one axis normal to the surface so the load translation into nodes is easier than the one needed for classic FE methods and requires a lower size of the load matrix itself.

### 3.4.3 Stacking Sequence Effects on the TBL-induced response of a Shell

It is interesting now to compare different laminations for a composite laminate shell. In fact, a different stacking sequence can lead to a different wave propagation along the shell and thus a different vibration field for given excitation model. The set of configurations and stacking sequences analysed are listed in Table 3.8 and 3.9. Each lamina is 0.425mm thick and the laminate is composed by 8 layers, in each configurations. The 0° and 90° represent fibres orientations corresponding to the axial and circumferential directions of the cylinder. The choice of the sequences *A* and *B*, reported in Tab. 3.9, is justified by the need of having higher axial or circumferential bending stiffness, while the configurations *C* and *D*, apart from notching issues, that usually require ±45° orientations on the outside, is aiming at inducing helical bending waves, which attenuate the excitation of the purely circumferential and axial modes of the shell. Of course, the model must be purely cylindrical (not tapered) to avoid pressure gradient effects which would un-validate the application of the Corcos model. The convective speed is 180 m/s. The cylindrical model analysed is 0.2m long and is 3.4mm thick. The auto spectral densities of the radial velocity are averaged in four random points and compared. Different cylinder radius are analysed: 0.36m in Fig.3.20, 0.2m in

Table 3.9: Stacking Sequences

<b>A</b>	<b>B</b>	<b>C</b>	<b>D</b>
[90 <sub>2</sub> /0 <sub>4</sub> /90 <sub>2</sub> ]	[0 <sub>2</sub> /90 <sub>4</sub> /0 <sub>2</sub> ]	[±45/0 <sub>4</sub> / ± 45]	[±45/90 <sub>4</sub> / ± 45]

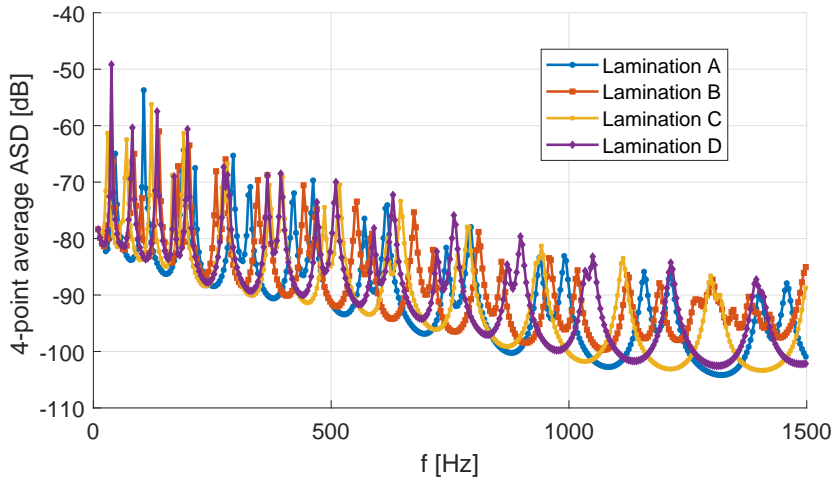


Figure 3.20: Numerical results comparison. Cylinder under TBL (Radius 0.36m) - Auto Spectral Density averaged on four response points, [dB ref. 1 m/s].

Table 3.10: Stiffeners geometrical parameters

Data	Circumferential	Longitudinal
Height [mm]	10.0	4.0
Bottom Width [mm]	5.0	3.0
Top Width [mm]	2.0	2.5
Thickness [mm]	2.0	1.0

Fig.3.21, 0.12m in Fig.3.22. The results show that altering the lamination sequence the structural modes shift in frequency. However, having kept the mass of the structure constant (each lamina has the same density), the dynamic content in frequency is similar among the cases, which would result in a similar radiated power. In fact Fig. 3.20 shows how, for the configurations analysed, not much difference is observed. On the other hand, when the radius of the cylinder is reduced, as in Fig. 3.22, it is clearer how the best result is achieved with the configuration A, which is the stiffest in the stream-wise direction. This is in accordance with the main energy content of the excitation being transported along the stream-wise direction.

### 3.4.4 Stiffened Cylindrical Structure under TBL load

Singly and doubly stiffened cylinders are often used in many engineering areas, so a stiffened structure is here considered for completeness. The structure is a build up of the cylinder analysed in the previous case and a pattern of frames and stringers. The considered sub-structure is shown in Fig. 3.23 and a condensation of the inner dynamics is performed before applying the  $\theta WFE$  method. A Corcos TBL load model is used to simulate the excitation of the outer surface and the response is calculated for all the nodes of the full FE model with the present technique and the reference method (FEM). The stringers and frames geometrical properties are described in Table 3.10.

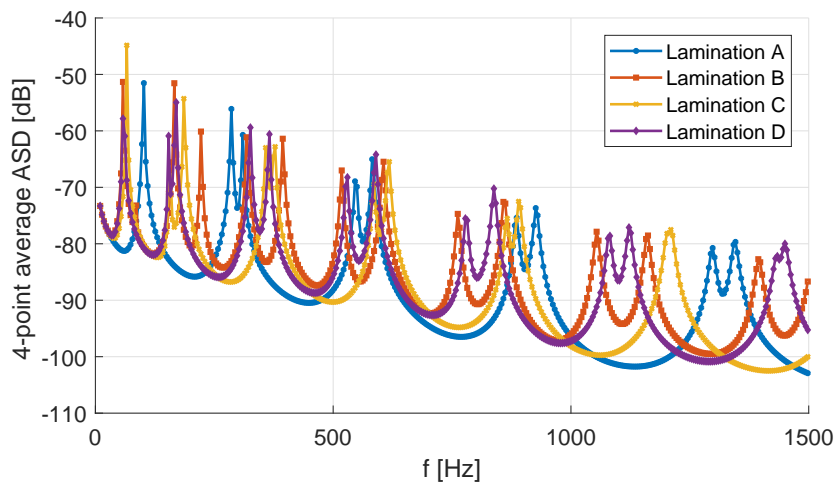


Figure 3.21: Numerical results comparison. Cylinder under TBL (Radius 0.20m) - Auto Spectral Density averaged on four response points, [dB ref. 1 m/s].

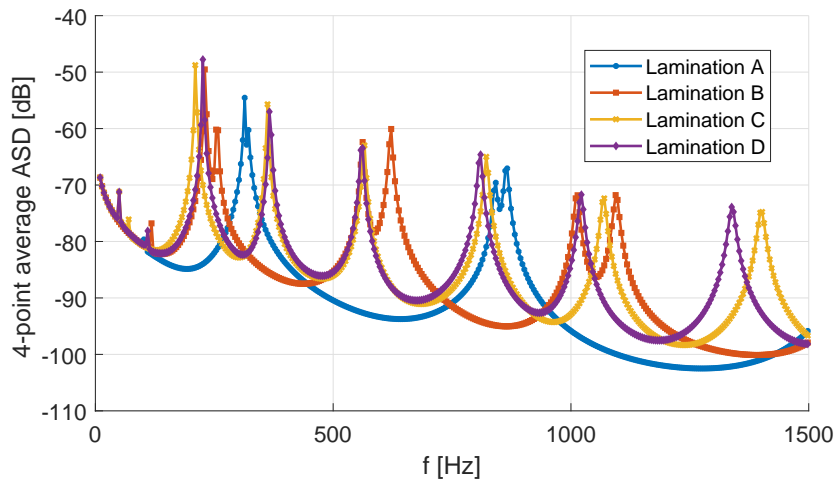


Figure 3.22: Numerical results comparison. Cylinder under TBL (Radius 0.12m) - Auto Spectral Density averaged on four response points, [dB ref. 1 m/s].

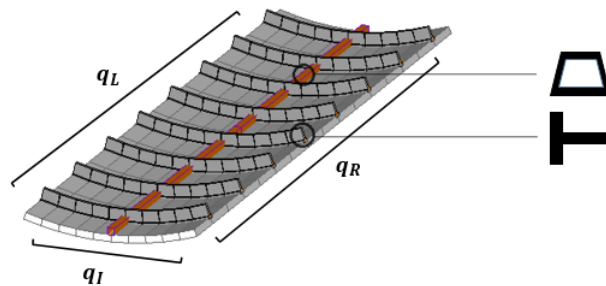


Figure 3.23: The elementary substructure used to analyse the structural response using the  $\theta$ WFE method

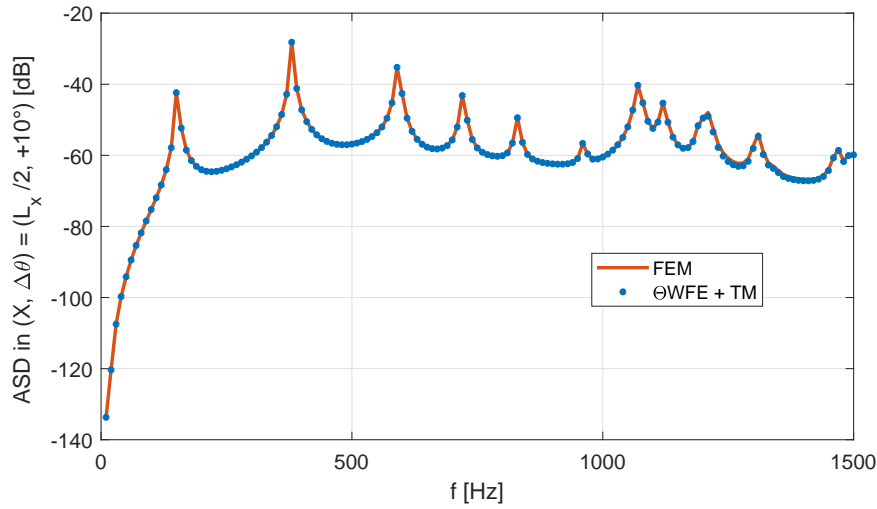


Figure 3.24: Numerical results comparison for a stiffened cylinder subjected to TBL - Auto Spectral Density in one response point, [dB ref. 1 m/s].

Table 3.11: Computational cost for a stiffened cylindrical structure to TBL load

Method	Design frequency	Elapsed time/frequency [sec]
FEM - Eq.(2.24) and Eq.(2.27)	1.5 kHz	197.8
$\theta WFE$ - Eq.(3.1) and Eq.(2.27)	1.5 kHz	1

In Fig. 3.24 the agreement among the curves proves again the accuracy of the method, as Table 3.11 proves the computational efficiency.

### 3.4.5 Complex Axisymmetric Structure under Diffuse Acoustic Field

A first analysis is conducted on the scaled model of the SYLDA presented in Figs. 3.10 and 3.11. The structures are homogenized and made in aluminium. For sake of completeness, the geometrical properties of the models are reported in Table 3.4. However, due to gradient effects, it is not completely correct to apply a Corcos model: an incident diffuse field (DAF) is thus simulated. In Fig. 3.11, the relative substructure used within the present approach is also shown. The DAF is often used to describe the TBL load in the low frequencies (i.e. load description on a space launcher fairing during take-off and climb phases), overestimating the effects for increasing excitation frequency.

Fig. 3.25 shows the comparison between a full stochastic FE method and the proposed  $\theta WFE$  with the TM approach. No variable meshes are used in this case: as expected, the two models are equivalent in terms of accuracy. Nevertheless the huge difference of the computational cost is in Table 3.12. The use of the transfer matrix, in fact, strongly increases the flexibility in terms of selection of the degrees of freedom, both for the target and the wetted, while the wave-based method to evaluate the Green functions allows the use of a reduced model for all the calculation steps.

In addition, a complex and tapered axisymmetric structure, similar to a space launcher fairing (Fig. 3.26), is used as a second complex test-case. An incident diffuse field (DAF)

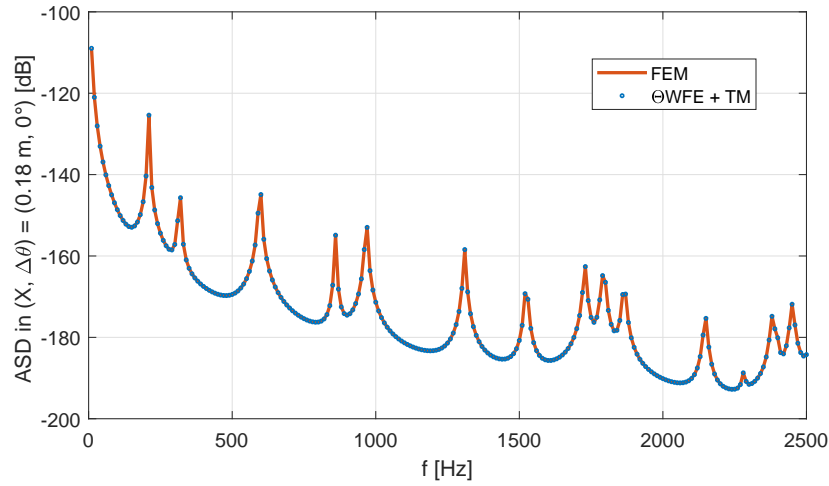


Figure 3.25: Numerical results for the SYLDA models subjected to DAF load - Auto Spectral Density in one point, [dB ref. 1 m/s].

Table 3.12: Computational cost for a complex axial-symmetric structure to DAF load

Method	Design frequency	Elapsed time/frequency [sec]
FEM - Eq.(2.24) and Eq.(2.27)	2.5 kHz	244.8
$\theta WFE$ - Eq.(3.1) and Eq.(2.27)	2.5 kHz	1

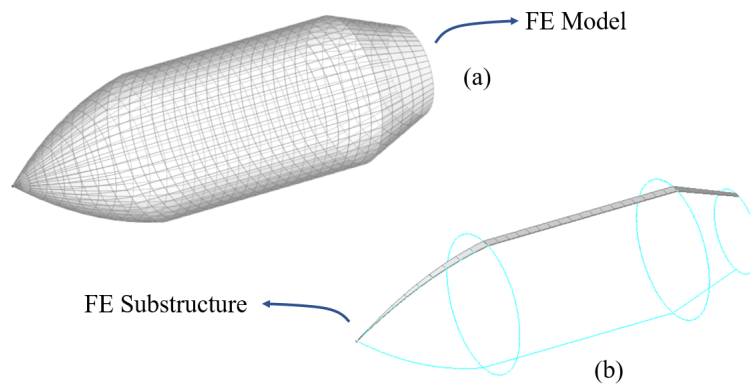


Figure 3.26: A tapered axisymmetric structure, used as a test-case: full finite element model (a); substructure in the framework of the proposed method (b).

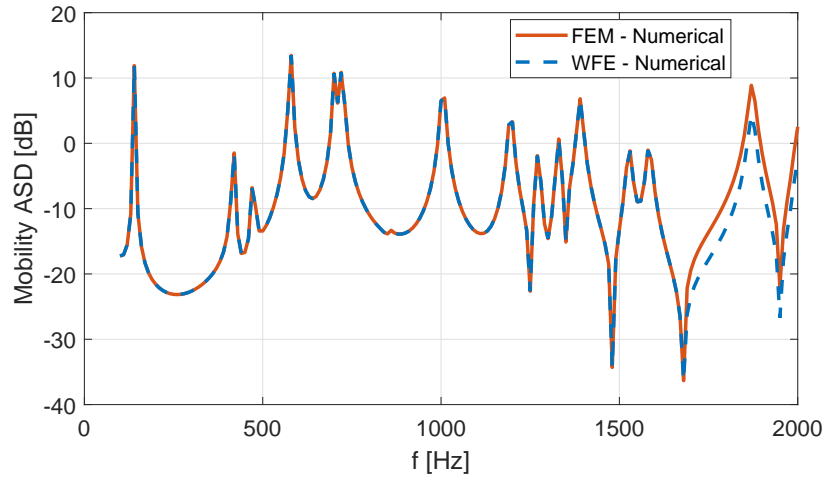


Figure 3.27: Numerical results comparison for a fairing-like structure under diffuse acoustic excitation - Auto Spectral Density in one point, [dB ref. 1 m/s].

is simulated, instead, since it is often used to describe the TBL load in the low frequencies (i.e. load description on a space launcher fairing during take-off and climbing phases), overestimating the effects for increasing excitation frequency. In Fig. 3.26, the relative substructure used within the present approach is also shown. The structure is made again of aluminium.

Fig. 3.27 shows the comparison between a full stochastic FE method and the proposed WFE with the TM approach. As expected, the two models are equivalent in terms of accuracy, up to the aliasing frequency, where the full stochastic finite element model starts to lose precision.

### 3.5 Conclusions

This chapter proposes a numerical methodology for the analysis of the flow-induced vibrations of periodic and axial-symmetric structures. The approach involves a transfer matrix to couple the translated load to the required (target) degrees of freedom. The method through which the Green functions are calculated is a wave finite element method, reformulated in the case of axial-symmetric structures to cope with complex and tapered shapes. Impedance variations are also accounted in the model for rectilinear and circumferential wave propagation. A dynamic or static condensation is also possible for complex cross-sectional geometries.

While the analytic methods are limited to very simple cases and the standard FEM approaches can only cope with the low frequency range, the present method allows an extension of the FE-based numerical analysis of the flow-induced structural vibrations to higher frequencies within the medium frequency range, for a given computational cost, or a reduced calculation time, given a frequency band of interest. The method uses FE matrices extracted from any commercial code, thus has also the advantage of being able to use all the available FE formulation.

Various test-cases are analysed in order to validate the methodology proposed. The transfer matrix building (Green functions calculation) is validated for the axial-symmetric wave-

based formulation, then, the stochastic response of cylinders and complex structures is calculated. The method proves being accurate and much faster than classic FEM, by two orders of magnitude. Depending on the complexity of the structure, the frequency range of analysis and the number of degrees of freedom of the single substructure, the computational cost save can be even higher. The robustness of the technique is proved both with uncorrelated and spatially-correlated loads. Moreover, the possibility to consider the wave propagation through an analytic system of coordinates and, consequently, through the use of variable meshes, gives huge advantages in extending the accuracy to higher frequency bands (over the aliasing frequency) having, at the same time, a great save in CPU time.

The flexibility of the proposed method to link the structural and fluid meshes gives the possibility of using a single substructure to analyse different test-cases. For a given substructure, many parameters can be arbitrary set to specific values: the curvature, the mesh spacing and extension of the structure along the periodicity direction. Within this framework, for example, an entire class of cylinders can be tested by using a single FE model.

The presence of complex structural parts which are not excited does not increase the size of the WFE problem even if the stochastic response can be easily evaluated in such points. Differently, the standard FEM approaches would experience a strong increase in the number of degrees of freedom of the problem.



## Chapter 4

# The Prediction of the Flow-Induced Noise using a 2D Periodic Cell

This chapter describes a methodology for computing the sound transmission loss of any flat, curved and cylindrical, homogeneous and periodic structure, under any type of acoustic and/or aerodynamic load. An approximate excitation model is introduced to reproduce uncorrelated and spatially-correlated loads using a wavenumber integration of surface waves. Then, a wave finite element formulation is developed and interfaced with the excitation models in order to cover industrially-relevant case studies. Analytical, numerical and experimental transmission losses are presented for validation purposes. Finite size effects are also taken into account using a spatial windowing and a cylindrical analogy, for curved structures. An investigation is carried out, under turbulent boundary layer excitation, versus the wavenumber-based integration parameters and domains.

### 4.1 Introduction

Sandwich composite structures are extensively used in modern aerospace industry as well as in the automotive, naval and civil ones because they are lighter and stronger than most advanced panels in aluminium alloys. The anisotropy of such structures can be easily modified by changing the material and the shape of the core, obtaining different wave propagation properties. However, these types of structures are also known for having poor vibroacoustic performances which, often, can result in higher interior noise levels. This problem has a strong impact in many engineering areas, from space launchers to aircraft fuselages. Strong efforts have been recently placed on advanced methodologies for the the modelling of acoustic radiation of laminates and sandwich panels, since, classical models, using for example the finite element method (FEM), lead to cumbersome computational cost. Some FEM applications for the vibroacoustic analysis of simple structures, under random aeroacoustic loads, are present in literature [6, 7, 20, 21, 24].

An efficient alternative in terms of computational cost is, for example, the transfer matrix method (TMM). It is a general method used for the prediction of the propagation of monochromatic plane waves in planar and multi-layered structures of infinite extent [35]. Many applications of the TMM to the modelling of sound transmission of composite structures have already been validated [36, 37].

Finite size effects, important at low frequencies, can be included through appropriate corrections, leading to a broadband accuracy of the method [38–40].

Alternatively, the wave finite element method (WFE), specifically for homogeneous and periodic structures, allows the modelling of just a single repetitive cell, applying on it the periodicity conditions for a correct description of the entire (infinite) waveguide [72, 73, 89, 104, 107, 152]. The use of finite elements, for the cell description, enhances this method allowing the description of any type of complex structural shape, even in case of curvature [90, 91, 100, 101]. While mainly used for the analysis of the elastic waves' propagation in periodic media, the application of the WFEM for the sound transmission of sandwich panels has been recently proposed, under a plane wave load [153, 154] or diffuse acoustic load [33, 34], even though, to authors' knowledge, no application is available for curved and complex configurations, under general loads.

Within the frameworks of curved structures, alternative methods have also been presented. A mathematical model, for the transmission of airborne noise through the walls of an orthotropic cylindrical shell, has been firstly proposed by Koval, [41–43]. For curved composite laminates, the vibroacoustic problem has been further developed through a spectral approach based on a discrete lamina description, [44, 45]. Other semi-analytic approaches, based on a receptance method, have also been proposed in order to analyse the sound transmission of aircraft panels with stringers and ring frames, [46, 47].

Periodic structures and innovative material configurations (often indicated as meta-materials), on the other hand, can be used as frequency-selecting structures. The related waveguides, because of their complex shapes, require a higher computational cost for an accurate numerical simulation. In addition, the knowledge and the modelling of the correct operating conditions are fundamental in automotive and aerospace applications. For example, whenever a convective flow is present, boundary layer models should be included for completeness. None of the models in literature, at this stage, allows the analysis of complex structural periodic shapes, in presence of curvature and under aeroacoustic excitations, at the same time. For example, in the work of Yang et al. [154] only infinite flat homogenised structures can be analysed under plane waves' excitation. On the other hand, in the case of curved structures, the work of Kingan et al. [155] is limited to a single plane wave excitation, once a circumferential number is fixed; thus the sound transmission of complex curved structures under stochastic excitation can not be obtained, in this case.

The novelty of the present work stands in overcoming some of these limits proposing a methodology for dealing with a wider range of case-studies, under operational conditions: space launcher fairings, fuselage panels, pipes, ducts and acoustic barriers. Periodic flat, curved and cylindrical structural designs can be compared in terms of their vibroacoustic performance, under any desired convective and acoustic load.

## 4.2 The Wave Finite element Method

A 2D periodic structure is composed by an assembly, along two arbitrary directions, of identical elementary cells. Using any FE commercial code, the mass and stiffness matrices of the cell, whenever complex, can be extracted and post-processed. Of course, since being FEs, all classic meshing considerations for an appropriate wavelength description are valid. With reference to Fig. 4.1, the dynamic stiffness equation of the segment can be written as

$$[\mathbf{K} - \omega^2 \mathbf{M}] \mathbf{q} = \mathbf{D} \mathbf{q} = \mathbf{f} + \mathbf{e} \quad (4.1)$$

where  $\mathbf{q}$ ,  $\mathbf{f}$  and  $\mathbf{e}$  are respectively the nodal vectors of degrees of freedom (DoFs), internal and external forces;  $\mathbf{K}$ ,  $\mathbf{M}$  and  $\mathbf{D}$  are the stiffness, mass and dynamic stiffness matrices.

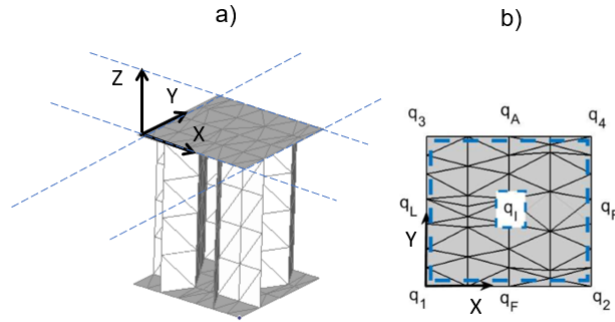


Figure 4.1: Example of a FE cell model with periodicity along the X-Y directions. a) Isometric view; b) Top view with nodes' subsets.

As in chapter 2, a periodicity matrix  $\Lambda$  (see Eq. 2.41), can be used to link displacements and forces in the periodic structure with a reduced subset of them (superscript *red*). A reduced dynamic stiffness equation can be derived as:

$$\mathbf{D}_S = \Lambda^H [\mathbf{K} - \omega^2 \mathbf{M}] \Lambda. \quad (4.2)$$

The linearity of the stress tensor with respect to the displacement field, in addition to the periodicity relations, leads to an equilibrium of the internal forces between neighbouring cells; thus only external forces are considered.

At this stage, different eigenvalue problems can be solved, if the target is the estimation of the dispersion curves of the periodic structure, [89, 95].

#### 4.2.1 Modal Order Reduction: A Craig-Bampton Scheme

The use of modal reduction is highly suggested for very fine meshes. In these cases, the internal degrees of freedom, defined before as  $\mathbf{q}_I$ , are substituted by the modal participation factors [96, 97]. Here an example of component mode synthesis (CMS) procedure, performed at the cell's scale, is shown. The aim of the CMS procedure is to achieve a significant reduction of the number of inner DOFs, by replacing displacements with the local modes of the cell. Here, the displacement vector  $\mathbf{q}$  defined in Eq. 4.1, is partitioned into the inner displacements,  $\mathbf{q}_{In}$ , and boundary displacements,  $\mathbf{q}_B$ . In this specific case, since the nodes belonging to the top and bottom of the cell are used for load translation, as shown in subsection 4.2.3,  $\mathbf{q}_{In}$  is a subset of the  $\mathbf{q}_I$  in Eq. 2.35. By using this division, Eq. 4.1 takes the form of Eq. 4.3:

$$\left( \begin{bmatrix} \mathbf{K}_{BB} & \mathbf{K}_{BIn} \\ \mathbf{K}_{InB} & \mathbf{K}_{InIn} \end{bmatrix} - \omega^2 \begin{bmatrix} \mathbf{M}_{BB} & \mathbf{M}_{BIn} \\ \mathbf{M}_{InB} & \mathbf{M}_{InIn} \end{bmatrix} \right) \begin{bmatrix} \mathbf{q}_B \\ \mathbf{q}_{In} \end{bmatrix} = \begin{bmatrix} \mathbf{f}_B \\ \mathbf{0} \end{bmatrix}, \quad (4.3)$$

where  $\mathbf{f}_{In}$  is zero, since no load is applied on this subset of nodes. The reduced basis involves the static boundary modes  $\Psi_B$  and component modes  $\Psi_C$ .

In this way the final displacements vector can be re-written as:

$$\begin{bmatrix} \mathbf{q}_B \\ \mathbf{q}_{In} \end{bmatrix} = \mathbf{G} \begin{bmatrix} \mathbf{q}_B \\ \mathbf{P}_{In} \end{bmatrix}; \quad \mathbf{G} = \begin{bmatrix} \mathbf{I} & \mathbf{0} \\ \Psi_B & \Psi_C \end{bmatrix} \quad (4.4)$$

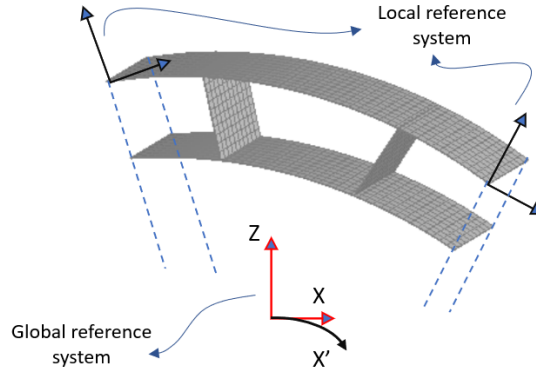


Figure 4.2: Rotation of the local system of reference for each node of the periodic cell FE model

where  $\mathbf{I}$  and  $\mathbf{0}$  are the identity and zero matrix respectively, and  $\mathbf{P}_{In}$  is the set of retained modal participation factors. The static boundary modes  $\Psi_B$  and component modes  $\Psi_C$  can be derived from Eq. 4.5,

$$\Psi_B = \mathbf{K}_{InIn}^{-1} \mathbf{K}_{InB}; \quad (\mathbf{K}_{InIn} - \omega^2 \mathbf{M}_{InIn}) \Psi_C = \mathbf{0}. \quad (4.5)$$

In the Craig—Bampton (CB) approach, the modal selection is based on the lower resonance frequencies. This method has been extended in a wave approach context, when the aim is to capture the local deformed shape of the periodic unit cell. This means that the displacements inside a unit-cell can be expanded on a subset of stationary modes [96, 97].

Finally the stiffness and mass matrices, that can be post-processed a-priori if curvature has to be simulated (see subsection 4.2.2), can be written in the reduced set of coordinates using the projection matrix  $\mathbf{G}$  defined by Eq. 4.4:

$$\begin{aligned} \mathbf{M}_{\text{Cond}} &= \mathbf{G}^T \mathbf{M} \mathbf{G} \\ \mathbf{K}_{\text{Cond}} &= \mathbf{G}^T \mathbf{K} \mathbf{G}. \end{aligned} \quad (4.6)$$

The set of retained modal participation factors,  $\mathbf{P}_{In}$ , can be, then, statically condensed at each frequency step.

#### 4.2.2 Curvature Simulation

Curved structures deserve also some interest. Here a method, to take into account the curvature effects, is presented. With reference to Fig. 4.2, the idea is to rotate the local reference for each node belonging to the cell FE.

The procedure followed is the same as in Chapter 3 in Eq. 3.9. The waves analysed along the locally curved reference ( $X'$  in Figs. 4.2 and 4.3) are circumferential waves. Forcing wavenumbers, imposed after Eq. 3.9, represent, in general, helical waves exciting the semi-infinite cylindrical panel/shell (Fig. 4.3). It is worth to emphasize that the curvature simulation, showed here, aims at connecting the edge sections of the unit cell through a curved (discrete) system of coordinates. If point of inflections are present, at cell scale, depending on the structure to be described, two approaches are possible, once the cell is modelled with the inflected parts. In one case, the wave propagation can be analysed along

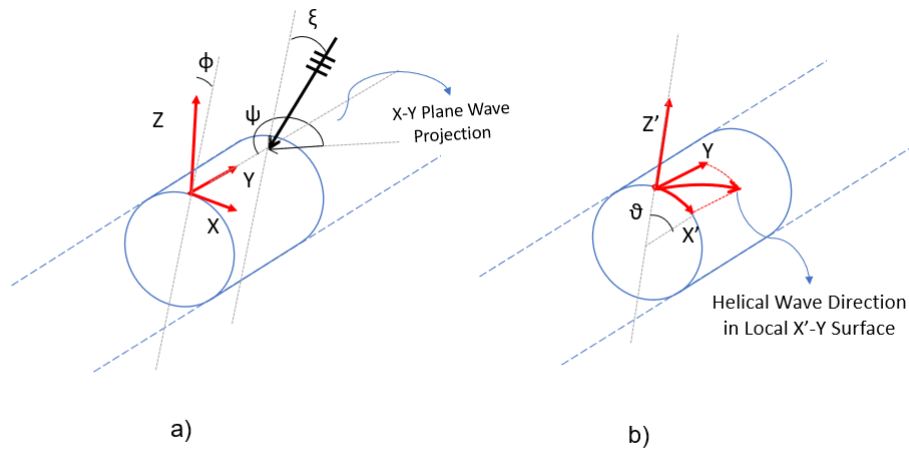


Figure 4.3: Global and Local reference systems used for waves along curved structures and shells. a) Global Cartesian reference; b) Local Curved Reference.

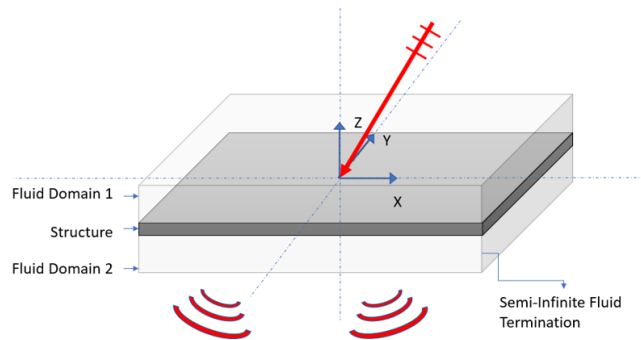


Figure 4.4: Illustration of an infinite the structure excited by a plane wave and radiating sound.

the global X-Y axes, simulating a flat waveguide with inflected sections. Otherwise, the cell curvature can be simulated using the nodal coordinates, even the ones belonging to the inflected part of the cell, to evaluate the local rotation of the coordinate system to be simulated; this is translated in a rotation matrix in Eq. 3.9.

### 4.2.3 Fluid-Structure Coupling

Let us assume a forcing wave impinging on one face of the structure, with an amplitude  $p_I$ . The structure, as a result, transmits and reflects waves in the fluid adjacent to the top and bottom surfaces. On the excited side (subscript 1), the sound field is the superposition of the incident and reflected acoustic sound waves, while, in the receiver side (subscript 2), it is given by the transmitted waves. Assuming the X-Y as the plane of reference (Fig. 4.4 as example), a forcing acoustic pressure wave can be defined, on the surface of the cell,

omitting the time harmonic dependence for simplicity, as (see Fig. 4.3a):

$$\begin{aligned} \text{Flat Surface : } PW &= p_I e^{-i(k_X X + k_Y Y - k_{Z,1} Z)}, \\ \text{Curved Surface : } HW &= p_I e^{-i(k_X R \sin \Phi + k_Y Y - k_{Z,1} R \cos \Phi)}, \end{aligned} \quad (4.7)$$

where,  $k_X$ ,  $k_Y$  and  $k_Z$  are the projections in the global X-Y-Z reference of the plane wave (see Fig. 4.3a). Here, in the case of curved surfaces, as described also in subsection 4.2.2, the assumed plane wave is approximated through its projection components on the locally curved surface (Fig. 4.3b):

$$HW = p_I e^{-i(k_{X'} X' + k_Y Y - k_{Z',1} Z')} \approx p_I e^{-i(k_\theta \theta + k_Y Y - k_R Z')}; \quad (4.8)$$

where  $k_{X'}$ ,  $k_Y$  and  $k_{Z'}$  are the wavenumber components in the new locally rotated reference (see Fig. 4.3b) and are directly proportional to the circumferential, axial and radial wavenumber components, respectively. It is worth to emphasize that a typical decomposition in cylindrical waves, implying the use of Bessel functions, is not necessary when using a locally rotated reference system as the one in Fig. 4.3b: Eq. 4.8 depicts helical waves in cylindrical coordinates and the equivalent plane waves in cartesian coordinates, respectively [89–91, 100].

From now on, the approximated representation of Eq. 4.8 is used independently on the curvature of the structural model; for infinite radius of curvature (flat structure), the local and global reference system coincide.

If in-plane homogeneous layers are assumed, the local wavenumber components  $k_X$  and  $k_Y$  are conserved along the structure, and the only parameter which can vary with the nature of the fluid (or the excitation) is the  $k'_Z$  component, derivable using the Helmholtz equation. When non-homogenised periodic cells are considered, multiple harmonics are added to the  $k_X$  and  $k_Y$  terms [156]. In this framework, the multiple harmonics that arise for periodic non-homogenised structures, are numerically accounted in the structural response of the radiating side (subscript 2). In fact, when applying the WFE, discrete periodic conditions are applied for the forcing (see Eq. 4.7) wavenumber couples  $k_X$  and  $k_Y$  (see Eqs. 2.35, 2.36 and 2.41) and for each node subset; the resulting free or forced structural vibration includes any periodicity effects in the frequency band of analysis.

To express the nodal forces on the periodic cell as a function of the pressure amplitudes in the forcing and radiating side of the structure, the dynamic stiffness of the fluids must be derived. From continuity of the normal particle velocity on the excited and radiating surfaces:

$$\begin{aligned} \rho_1 \omega^2 q_{in} &= \frac{\partial(p_I - p_R)}{\partial z}; & D_{f,1} &= \frac{-i\rho_1 \omega^2}{k_{Z,1}} \\ \rho_2 \omega^2 q_{rad} &= \frac{\partial(p_T)}{\partial z}; & D_{f,2} &= \frac{-i\rho_2 \omega^2}{k_{Z,2}} \end{aligned} \quad (4.9)$$

where  $\rho_1$  and  $\rho_2$  are the fluid densities,  $q_{in}$  and  $q_{rad}$  are the out-of-plane displacements, respectively of the incident and radiating surfaces, and  $D_{f,1}$  and  $D_{f,2}$  the dynamic stiffness of the fluid in the incident and radiating domains;  $p_I$ ,  $p_R$  and  $p_T$  are the incident, reflected and transmitted amplitudes of the sound pressure waves. It is important to notice that, regardless of the homogeneity of the structural model, the derivations over Z, in Eq. 4.9, makes the modelling of the radiating acoustic field somewhat non-sensitive to the presence or absence of multiple harmonics which might arise due to heterogeneity of the structure.

These effects are included in the dynamic stiffness of the cell in Eq. 4.2 and are accounted in the structural response.

The load imposed on the plate, by the forcing surface waves of trace wavenumbers  $k_X$  and  $k_Y$ , can be derived from the two pressure fields, on both sides of the structure; it is lumped on the wetted nodes of the finite element model. As the forces act normal to the surfaces, the only excited degrees of freedom are the ones connected to the out-of-plane displacements. These ones are identified with the subscript  $T$  (top) and  $B$  (bottom), while all other degrees of freedom (not excited) are identified by  $I$  (internal). The vector of the external forces can be written as:

$$\begin{bmatrix} \mathbf{e}_T^{red} \\ \mathbf{e}_I^{red} \\ \mathbf{e}_B^{red} \end{bmatrix} = \begin{bmatrix} \mathbf{S} \cdot (\mathbf{p}_I + \mathbf{p}_R) \\ \mathbf{0} \\ \mathbf{S} \cdot \mathbf{p}_T \end{bmatrix} \quad (4.10)$$

where  $\mathbf{S}$  is vector of the free nodal surface of each excited node and  $\mathbf{p}_I$ ,  $\mathbf{p}_R$  and  $\mathbf{p}_T$  are the nodal pressure vectors. A finer way to calculate consistent nodal forces, requires, however, the knowledge of the shape functions associated with the out-of-plane displacements [154]. The dynamic stiffness matrix and the reduced displacement vector can be rearranged in the same way as in Eq. 4.10, then an energetic equivalence through-thickness applied, condensing all the non-excited nodes [37]. Including the relation of Eq. 4.9, the dynamic problem results in:

$$\begin{bmatrix} \mathbf{D}_{S_{TT}}^c & \mathbf{D}_{S_{TB}}^c \\ \mathbf{D}_{S_{BT}}^c & \mathbf{D}_{S_{BB}}^c \end{bmatrix} \begin{bmatrix} \mathbf{p}_I - \mathbf{p}_R \\ \mathbf{p}_T \end{bmatrix} = \begin{bmatrix} \mathbf{S} \cdot \mathbf{D}_{f,1} \cdot (\mathbf{p}_I + \mathbf{p}_R) \\ \mathbf{S} \cdot \mathbf{D}_{f,2} \cdot (\mathbf{p}_T) \end{bmatrix} \quad (4.11)$$

where the superscript  $c$  indicates that the original  $\mathbf{D}_S$  matrix (Eq. 4.2) is condensed for the non excited ( $I$ ) degrees of freedom, through the thickness. The algebraic system in Eq. 4.11 can be solved in  $\mathbf{p}_R$  and  $\mathbf{p}_T$  obtaining the power transmission coefficient  $\tau$  associated with the couple of forcing wavenumbers  $k_X$  and  $k_Y$ .

$$\tau(k_X, k_Y) = \frac{(k_{Z,2}/\rho_2)\mathbf{S}|\mathbf{p}_T^2|}{(k_{Z,1}/\rho_1)\mathbf{S}|\mathbf{p}_I^2|}. \quad (4.12)$$

Finite size effects, can be included through correction factors, in order to increase the accuracy at low frequencies. While a formal and accurate spatial windowing approach is present in literature [38], the computational cost associated with this step might be high. For this reason, even losing some accuracy in the low frequency bandwidth range, the use of asymptotic formulas, as in [39], is here used to reduce the computational cost.

#### 4.2.4 A TMM-based extension for attached porous layers

While some works have been developed directly to model and analyse porous materials using WFE [99, 157], here a simple approach is proposed to couple the present approach with the modelling of infinite porous layers using TMM. Lets consider two laterally infinite sections, as in Fig. 4.7, where the first one represents a potential periodic structure analysed using WFE-based approach and the second one a porous material attached to the previous layer. By considering the continuity of the velocities at the interface between the structural cell and the porous layer (plane 2 in Fig. 4.5), the incoming pressure in the second layer can be derived using the surface impedance of the porous layer itself, assuming the surface to be fully covered by the subsequent one. First, by solving Eq. 4.11 and substituting  $p_T$  in Eq. 4.9, the averaged vibrational velocity, on the radiating side of the first layer, is calculated.

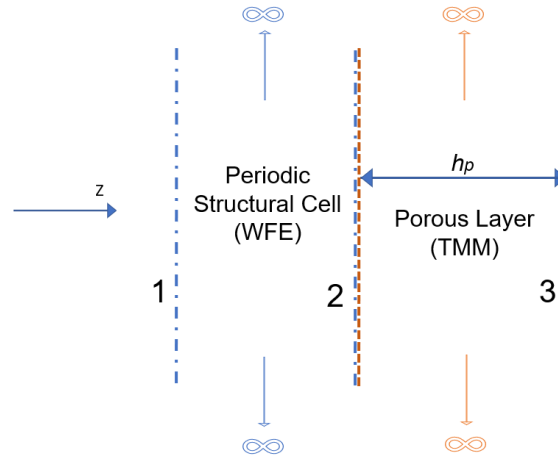


Figure 4.5: Illustration of the two laterally infinite sections representing the structural layer and the porous one.

Then, once the nature of the second layer is established, the surface impedance ( $Z_S$ ) can be derived and  $p_2$  calculated, using the equivalent fluid layer theory [35, 158]. In addition, no interaction between nodes on a face or cross face of the porous layer is assumed [35, 158]. Finally, the sound pressure in the radiating side (plane 3 in Fig. 4.7) is evaluated using the classic Transfer Matrix Method, as in Eq. 4.13.

$$\begin{bmatrix} p_2 \\ v_2 \end{bmatrix} = \begin{bmatrix} \cos k_Z h_p & iZ_c \sin k_Z h_p \\ iZ_c^{-1} \sin k_Z h_p & \cos k_Z h_p \end{bmatrix} \begin{bmatrix} p_3 \\ v_3 \end{bmatrix}, \quad (4.13)$$

where  $h_p$  represents the thickness of the porous layer,  $Z_c$  its characteristic impedance and the subscripts 2 and 3 are used to identify the sound pressure and the particle velocity at interface/plane 2 and 3 (Fig. 4.5), respectively. The transmission coefficient of the cell including the porous treatment equals the product of the transmission coefficients of the single stations 1 – 2 and 2 – 3 (see Fig. 4.5).

This extension, while exact and immediate for homogenised structures, it is an approximation for complex-shaped cells. A proper coupling for each structural part exposed or in contact with the subsequent fluid layer is not performed, but, as will be shown in the following sections, this approximation still provides accurate and predictive results in the case of complex shaped cells.

### 4.3 Stochastic Load Translation into Surface Waves

The sound transmission to plane wave excitation, as discussed in Sec. 4.2, is not sufficient for many applications. Herein, a method, to take into account a general type of excitation, is proposed. An illustration is reported in Fig. 4.6. The idea is to use a forcing surface wave excitation for each couple of forcing wavenumbers  $k_X$  and  $k_Y$ , able to represent the desired excitation, once its wall pressure spectra, in the wavenumber domain, is known. Using a vectorial form and omitting the harmonic dependence for the sake of readability, a sum of

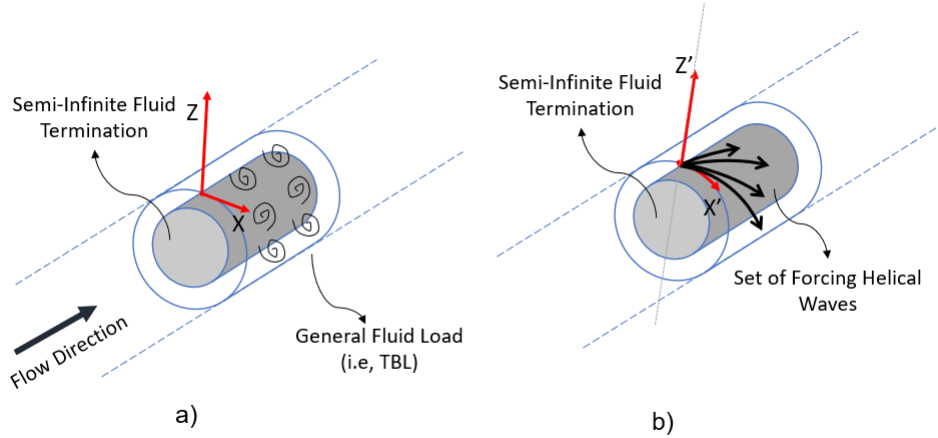


Figure 4.6: Illustration of the load simulation using surface waves in a general test-case. a) Real/Physical situation; b) Simulated case.

wall plane waves can be written as:

$$P(\bar{X}) = \sum_{j=1}^{N_w} A_j e^{-i\bar{K}_j \bar{X}}. \quad (4.14)$$

where  $\bar{X}$  stands for the couple of surface coordinates (i.e. X–Y in Fig. 4.1),  $\bar{K}_j$  is the wavenumber vector associated with each wall surface wave of amplitude  $A_j$ , and  $N_w$  is the total number of waves constituting the pressure field. It is worth recalling that the surface coordinates can be the global coordinates, if the structure is flat, or, equivalently, the local coordinates if a curvature is present. In the first case, Eq. 4.14 is physically representative of the classic sum of plane waves. In the other case, it reports a sum of wall helical waves on the curved cylindrical structures.

The description of the desired load is based on the knowledge of the proper values of  $\bar{K}_j$  and  $A_j$  (Eq. 4.14). They are obtained by equating the wavenumber spectra  $\phi_{PP}$ , of the pressure field (Eq. 4.14), with the one of the fluid excitation model to be simulated,  $\Phi_{PP}$ , for a specific fluid wavenumber  $\bar{K}$ . Many fluid excitation models are investigated in the wavenumber domain in literature [13]. The cross correlation of the pressure field  $P$  is:

$$R_{PP}(\Delta\bar{X}_1, \Delta\bar{X}_2) = \sum_{j=1}^{N_w} A_j^2 e^{-i\bar{K}_j(\Delta\bar{X}_1 - \Delta\bar{X}_2)} + \sum_{j=1}^{N_w} \sum_{n=1; n \neq j}^{N_w} A_j A_n e^{-i(\bar{K}_j \Delta\bar{X}_1 - \bar{K}_n \Delta\bar{X}_2)} \quad (4.15)$$

where the auto and cross correlations have been divided in two different summations. Performing the Fourier transform of Eq. 4.15, the wavenumber spectra is obtained:

$$\begin{aligned} \phi_{PP}(\bar{K}, \omega) = \Phi_{PP}(\bar{K}, \omega) = & \frac{1}{4\pi^2} \left( \sum_{j=1}^{N_w} A_j^2 \left[ \frac{e^{i(\bar{K}_j - \bar{K})(\Delta\bar{X}_1 - \Delta\bar{X}_2)}}{i(\bar{K}_j - \bar{K})} \right]_{-\infty}^{+\infty} \right. \\ & \left. + \sum_{j=1}^{N_w} \sum_{n=1; n \neq j}^{N_w} A_j A_n \left[ \frac{e^{i(\bar{K}_j - \bar{K})(\Delta\bar{X}_1)}}{-i(\bar{K}_j - \bar{K})} \right]_{-\infty}^{+\infty} \left[ \frac{e^{i(\bar{K}_n - \bar{K})(\Delta\bar{X}_2)}}{-i(\bar{K}_n - \bar{K})} \right]_{-\infty}^{+\infty} \right). \end{aligned} \quad (4.16)$$

The expressions in Eq. 4.16 are known and can be written as Dirac *delta*-functions ((Eq. 4.18)).

$$\left[ \frac{e^{i(\bar{K}_j - \bar{K})(\Delta \bar{X}_1)}}{-i(\bar{K}_j - \bar{K})} \right]_{-\infty}^{+\infty} \rightarrow \delta(\bar{K}_j - \bar{K}) \quad (4.17)$$

Moving from summations to integrals (Eq. 4.18) and after some algebra, the final expression of  $\phi_{PP}$  is given in Eq. 4.19.

$$\sum_j \delta(\bar{K}_j - \bar{K}) \rightarrow \int \frac{1}{\Delta \bar{K}_j} \delta(\bar{K}_j - \bar{K}) d\bar{K}_j \quad (4.18)$$

The second term in Eq. 4.19 can be erased since, by definition, the correlation indices  $j$  and  $n$  must be different while the integration of the product of the Dirac functions is not null only for  $\bar{K}_j = \bar{K}_n$ .

$$\begin{aligned} \phi_{PP}(\bar{K}) = \Phi_{PP}(\bar{K}) &= \int 4\pi^2 \frac{A_j^2}{\Delta \bar{K}_j} \delta(\bar{K}_j - \bar{K}) d\bar{K}_j \\ + \int \int 8\pi^4 \frac{A_j A_n}{\Delta \bar{K}_j \Delta \bar{K}_n} \delta(\bar{K}_j - \bar{K}) \delta(\bar{K}_n - \bar{K}) d\bar{K}_j d\bar{K}_n \end{aligned} \quad (4.19)$$

The amplitudes and the wavenumbers of the simulated waves, able to describe a fluid excitation with the wavenumber spectra  $\Phi_{PP}$ , are straightforwardly obtainable from Eq. 4.19. For each forcing  $k_X$  and  $k_Y$ , the desired loading model is simulated through the following surface wave:

$$P_W(X, Y, \omega) = \sqrt{\frac{\Phi_{PP}(k_X, k_Y, \omega) \Delta k_X \Delta k_Y}{4\pi^2}} e^{-i(k_X X + k_Y Y)}. \quad (4.20)$$

In conclusion, at each frequency and for each wavenumber of the fluid excitation model, a surface wave of specific wavenumbers and amplitudes can be used to simulate the load. No hypothesis on the correlation of the forcing waves is imposed as for the reference coordinates. The proposed approximation is thus valid for correlated and uncorrelated loads acting on plane and curved surfaces, independently on their complexity.

### 4.3.1 Sound Transmission Loss

In order to simulate the sound transmission for a specific excitation, an integration of the transmission coefficient is performed, in the wavenumber domain. Thus, the total transmission coefficient can be calculated as follows:

$$\tau_{TOT}(\omega) = \frac{\int \int \tau(k_X, k_Y) \times W_A(k_X, k_Y, \omega) dk_X dk_Y}{\int \int W_A(k_X, k_Y, \omega) dk_X dk_Y} \quad (4.21)$$

where  $W_A$  is the element corresponding to the wall surface wave of wavenumbers  $k_X$  and  $k_Y$ , in the matrix of the normalized amplitude functions of all the wavenumber couples involved in the integration process. Within the framework of sound transmission, as identifiable from Eq. 4.12, the variation of waves amplitudes does not have an influence. The difference among different fluid loads is given by the weighting functions  $W_A$  being involved in the integration. The convergence of the method is assured by the convergence of the integration process. The choice of the integration limits can be changed depending on the type of

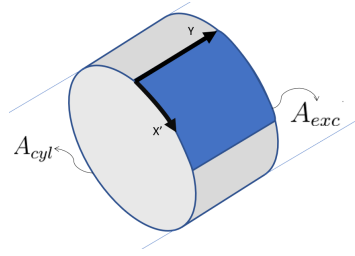


Figure 4.7: Excited surface comparison between a curved finite panel and its equivalent cylindrical portion.

load to be described. For example, for a diffuse acoustic field, at each frequency step, the wavenumber spectra  $\Phi_{PP}$  is null outside the acoustic border, so, there is no need for the use of higher integration limits. The final transmission loss is, by definition:

$$TL(\omega) = -10 \log_{10}(\tau_{TOT}(\omega)) \quad (4.22)$$

The TL expression in Eq. 4.22 includes the assumption, if a curvature is simulated, that the excited surface is a plan projection of the shell surface. The transmission coefficient in Eq. 4.21, must be multiplied by the ratio of cylindrical section and its plan projection. However, in the case of curved finite structures, instead of using a baffled window equivalence, for accounting the effects of the finiteness of the structure, an alternative approach based on the ratio of the excited surfaces is here proposed. With reference to Fig. 4.7, the ratio between the area of the equivalent cylindrical portion ( $A_{cyl}$ ), built starting from the finite curved panel analysed, and the effectively excited area ( $A_{exc}$ ), is multiplied, in a SEA (Statistical Energy Analysis) fashion, to the transmission coefficient in Eq. 4.21. The approach is consistent since, given a certain length of the panel, along the non-curved side, its area can increase just up to the one of the equivalent cylindrical portion. The resulting TL, thus, can asymptotically converge toward the one of the equivalent cylinder. In these cases, Eq. 4.22 becomes:

$$TL(\omega) = -10 \log_{10} \left( \tau_{TOT}(\omega) \frac{\pi A_{cyl}}{2 A_{exc}} \right). \quad (4.23)$$

The advantage of the present approach relies in its generality and applicability to a wide range of test-cases both in terms of structural shapes and excitation models. The wall surface wave approximation releases the constraints to the plane waves angles of incidence, generally implied in literature, widening the analysable combinations of structural and excitation models. On the structural point of view, the only requirement, for the applicability of the present approach, is given by the homogeneity or periodicity, independently on the reference direction (flat or curved). On the other hand, for the simulated excitation, the basic requirement is the knowledge of the wall pressure spectrum.

#### 4.4 Validations for Flat Structures

In this section, a series of comparisons are presented for validation purposes. In all the test-cases proposed here, the dispersion curves in the in the X and Y direction (Fig. 4.1,4.2) will be provided in order to observe acoustic coincidences in terms of waves.

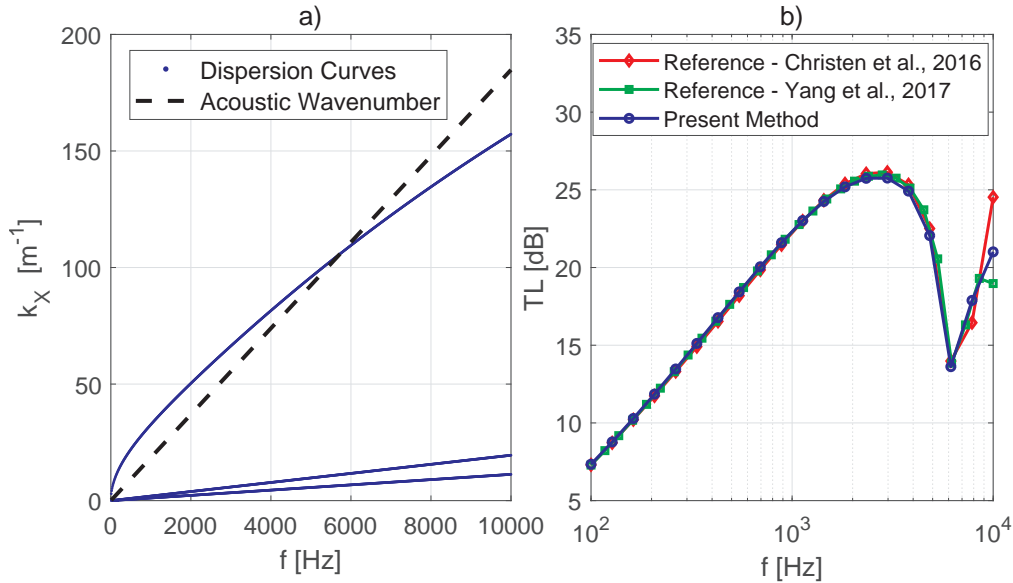


Figure 4.8: A sandwich flat panel under diffuse acoustic field excitation. a) Dispersion curves; b) Transmission Loss comparison with literature references ([153, 154]) in a logarithmic frequency step, between 100 Hz and 10KHz.

#### 4.4.1 Diffuse Acoustic Field load

In Fig. 4.8, a comparison among the proposed method and two other approaches available in literature is shown [153, 154]. The analysed sample is a 3mm thick flat sandwich panel made of 1mm-thick aluminium skins and a 1.5mm-thick isotropic core ( $E = 3$  GPa,  $\nu = 0.2$ ,  $\rho = 48$  Kg/m<sup>3</sup>). The cell is modelled using four ANSYS solid elements through thickness. The dispersion curves in Fig. 4.8a, show an acoustic coincidence at  $\approx 6$  kHz. In Fig. 4.8b an excellent agreement is observed for the sound transmission loss calculated using the present approach and the numerical ones in [153, 154]. Finite size effects are not included in the model and thus the comparisons in Fig. 4.8 are for infinite panels. The second test-cases consist in an aluminium double-wall flat panel with mechanical connections (Fig. 4.9a), and a sandwich panel with rectangular core (Fig. 4.9b) made in ABS ( $E = 1.8$  GPa,  $\nu = 0.35$ ,  $\rho = 998$  Kg/m<sup>3</sup>).

The dispersion curves of the two test-cases analysed are plotted in Fig. 4.10 with the acoustic wavenumbers versus frequency. The wavenumbers are derived from the propagations constants which are solutions of the eigenvalue problem in Eq. 4.2. Respectively, Fig. 4.11a shows the comparison for the TL, using an in-house reproduced code of the method presented by Christen et al. [153], whereas, Fig. 4.11b, shows the comparison for the TL of the sandwich rectangular-cored panel using, as a reference, the transfer matrix approach proposed by Parrinello et al. [37]. The double-wall cell is 5mm thick, 10mm long in the periodic direction (X), 1mm long in the homogeneous direction (Y) and the walls have a thickness of 1mm. The rectangular cored sandwich cell is 10mm thick, 10mm long both in X and Y, the skins and the core walls have a thickness of 0.6mm. Finite size effects are not included in the model and thus the comparisons in Fig. 4.11 are for infinite panels. Again excellent agreement is observed, even for this complex structural shape, validating

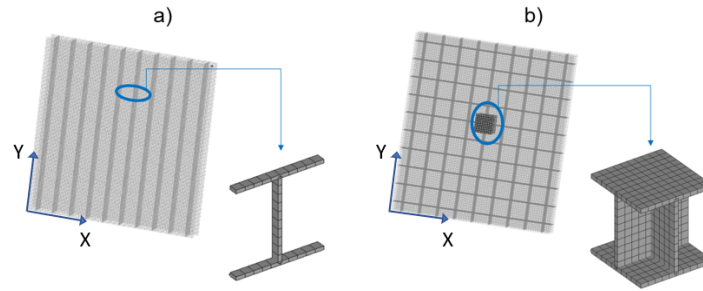


Figure 4.9: Portion of a double wall flat panel with structural links and the detail of the unit cell analysed

the proposed approach also for large heterogeneity scales and non-homogenised structure models. In this case, ANSYS *shell* elements are used instead, for the FE modelling. In all presented results, the mesh used for the calculations is verified to converge in the frequency band investigated.

#### 4.4.2 Turbulent Boundary Layer Excitation

The load approximation proposed in Section 6.1, leading to Eq. 4.21, allows the simulation for loads with different characteristics. In this section, for example, the flow-induced transmission caused by turbulent boundary layer (TBL) excitation is considered. This is known for being one of the main sources of radiated noise inside an aircraft cabin, in cruise flight conditions.

While many boundary layer models are proposed in literature, here, the characterisation of the wall pressure fluctuations proposed by Corcos is used [9, 13]. It is assumed that no-gradients effects are present and the TBL is fully developed. The wavenumber spectra,  $\Phi_{PP}$ , proposed by Corcos, is here reported for the sake of completeness assuming the directions X and Y as the stream-wise and cross-wise ones:

$$\Phi_{PP}(k_X, k_Y, \omega) = S_{pp}(\omega) \frac{4\alpha_X \alpha_Y}{\left[ \alpha_Y^2 + \frac{U_c^2 k_Y^2}{\omega^2} \right] \left[ \alpha_X^2 + \left( 1 + \frac{U_c k_X}{\omega} \right)^2 \right]} \quad (4.24)$$

where  $U_c$  is the convective flow speed,  $S_{pp}$  is the single-point auto spectral density of the wall pressure distribution. The stream-wise and cross-wise correlation coefficients,  $\alpha_X$  and  $\alpha_Y$ , are assumed to be 0.125 and 0.78, respectively, in all following test-cases.

First, a validation for the boundary layer transmission, in the case of a flat isotropic panel with simply-supported boundary conditions (edges), is proposed in Fig. 4.12. The reference solution is calculated using a full FE method, as proposed, and validated, in many works in literature [7, 21]. The eigen-frequencies and the modal shapes of the reference panel are calculated using analytic solutions, while the load matrix is described using a direct method [21]. The incident power, for the transmission loss calculation, in the FEM cases,

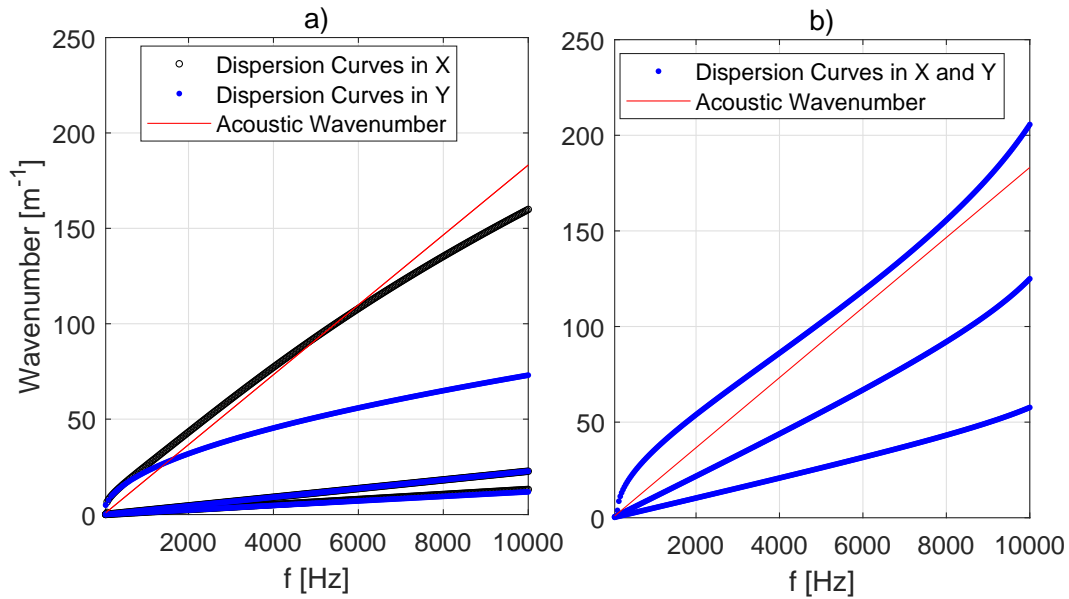


Figure 4.10: Dispersion Curves for the sandwich panel designs in Fig. 4.9. The wavenumbers represent derive from the eigenvalues of Eq. 4.2: a) Double-wall panel with structural link; b) Sandiwch panel with rectangular core.

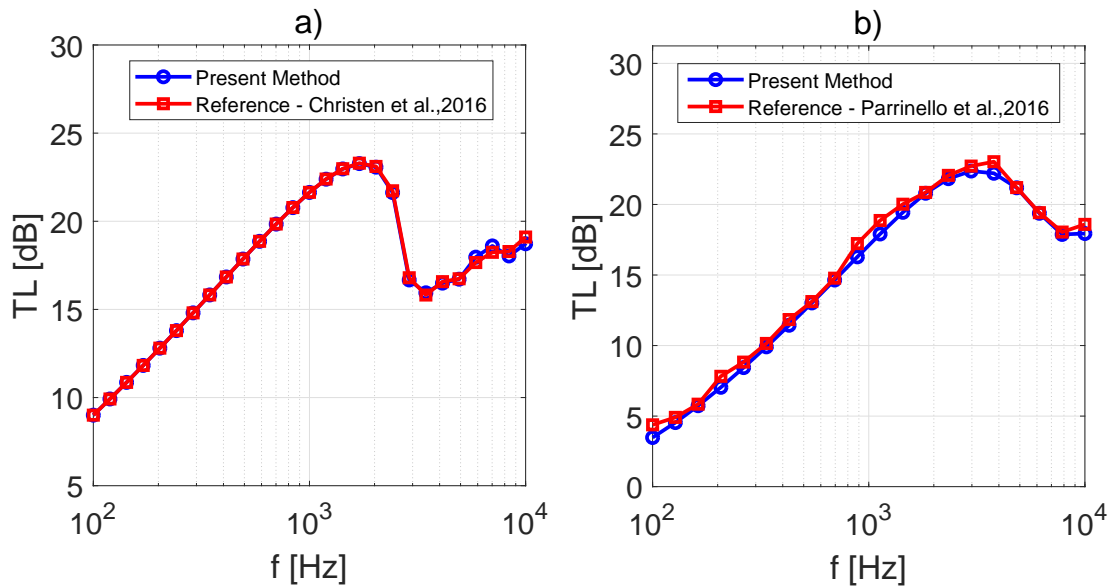


Figure 4.11: Transmission Loss comparison for the sandwich panel designs in Fig. 4.9, under diffuse acoustic field excitation. A logarithmic frequency step, between 100 Hz and 10KHz, is used to generate the curve labelled as *Present Method*. a) Reference method in [153]; b) Reference method in [37]

is calculated using Eq. 4.25 as proposed in literature [36, 159]:

$$\Pi_{\text{inc}} = \frac{AS_{pp}(\omega)}{4\rho_1 c_1} \quad (4.25)$$

where  $A$  is the excited area and  $c_1$  the speed of sound on the incident side. A modal behaviour can not be described using the present method, as in an SEA framework, since the wave propagation is considered to the infinite (reflections at the borders are neglected) and a semi-infinite fluid termination is assumed (no internal cavity modes). The averaged sound transmission losses are calculated in discrete frequencies (in logarithmic space), while the FEM calculation is in third octaves bands. In both the test-cases proposed here, the dispersion curves in the flow direction (X) is provided in order to show the convective/aerodynamic and acoustic coincidences.

For the aluminium case (Fig. 4.12), the aerodynamic and acoustic coincidences are at  $\approx 1.6$  kHz and  $\approx 6.0$  kHz, as shown in the dispersion curves in Fig. 4.12a. Here, the finite size effects are accounted using a radiation efficiency formulation for flat panels, as proposed by Leppington [39]. As shown in Fig. 4.12b, both the aerodynamic and acoustic coincidence dips are correctly identified in the sound transmission curves, as shown by the comparison with the octaves averaged FEM solution. The convective load induces a smoother and damped coincidence effect, with respect to the acoustic one.

Differently, an honeycomb-cored sandwich panel is analysed under a turbulent boundary layer in Fig. 4.13. A Corcos model is used for the loading description and the proposed approximation into surface waves is used. The panel is made of 1mm-thick aluminium skins and a 10mm-thick hexagonal Nomex honeycomb core (material properties in Table 4.1), homogenised in an equivalent orthotropic model. Both the aerodynamic and acoustic coincidences are well predicted in the sound transmission loss curves, in Fig. 4.13b. The first one is somewhat highly damped ( $\approx 600$  Hz; see Fig. 4.13a) while the second one is clearly visible ( $\approx 9$  KHz; Fig. 4.13a).

The strong agreement observed in Fig. 4.12 and 4.13, validates the proposed load approximation even for spatially-correlated random loads, as the TBL. It is worth underlying how the use of boundary layer excitation is here allowed even for infinite structures, differently from other methods in literature [36].

#### 4.4.3 TBL Models: A flow-induced noise comparison

Many works, dealing with flow-induced vibrations, compare the auto and cross correlation function of different TBL models [13]. Here, using the approach described in the present work, some of the most commonly used TBL models are compared in terms of induced noise on a flat isotropic plate. The choice of such a simple structural model is necessary to avoid filtering the effects and peculiarities of each single excitation model. The turbulent boundary models compared here are: Corcos [9], Chase [14], Cockburn-Robertson [11], Smolyakov-Tkachenko [12]. The same unitary auto spectral density is assumed for all the models, in order to evaluate the sensitivity to the cross-correlation model. The results here proposed, should be coherently scaled for the autospectra assumed in each TBL model, if the real transmission loss is the target.

In Fig. 4.18, the comparison shows how the Corcos model and the Cockburn-Robertson are in agreement almost in the whole frequency band. A higher transmission loss is observed, for the Cockburn-Robertson, around the aerodynamic coincidence, while a good agreement is evident among the other models. The Smolyakov-Tkachenko model, instead, seems the

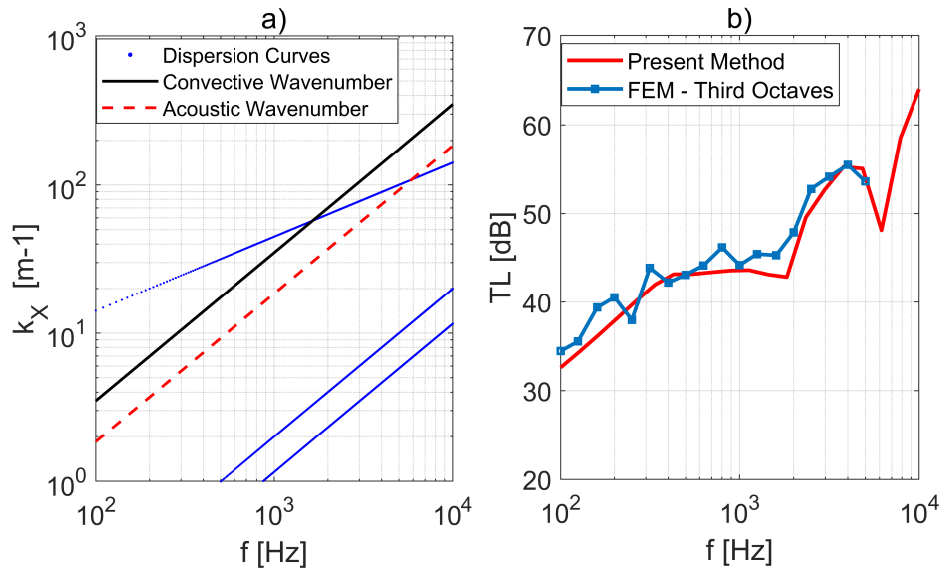


Figure 4.12: An aluminium plate under TBL excitation: a) Dispersion curves with convective and acoustic wavenumbers; b) TL numerical comparison with full FEM -  $U_c = 180$  m/s;  $A = 0.5 \times 0.3 \text{ m}^2$ . A logarithmic frequency step, between 100 Hz and 10KHz, is used to generate the curve labelled as *Present Method*.

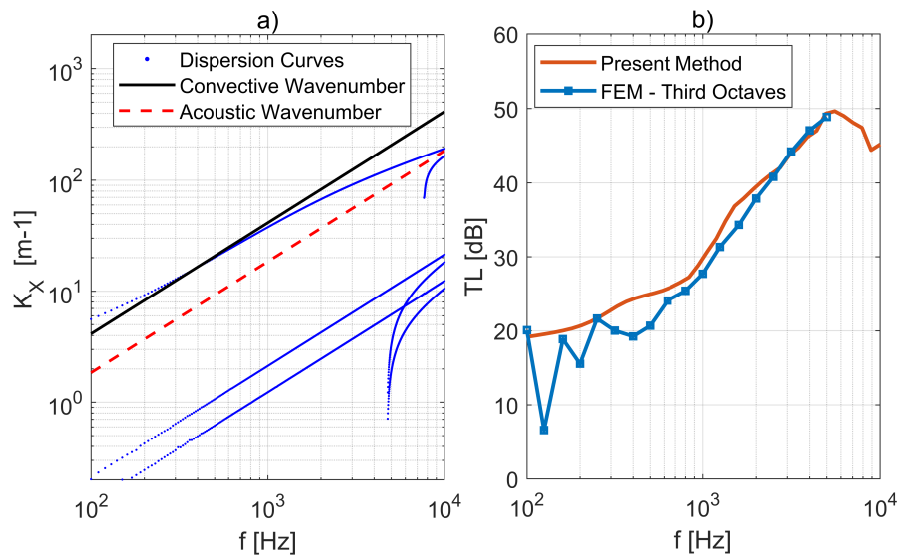


Figure 4.13: An honeycomb sandwich plate under TBL excitation: a) Dispersion curves with convective and acoustic wavenumbers; b) TL numerical comparison with FEM method -  $U_c = 152$  m/s;  $A = 0.8 \times 0.6 \text{ m}^2$ . A logarithmic frequency step, between 100 Hz and 10KHz, is used to generate the curve labelled as *Present Method*.

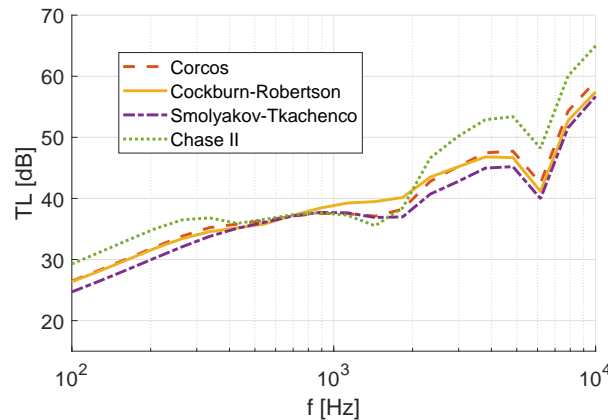


Figure 4.14: A comparison of the sound transmission resulting from different of TBL models ( $U_c = 190$  m/s). Flow data (see [13]):  $\delta = 0.027$  m;  $\delta^* = 0.0018$  m;  $u_T = 1.9$  m/s;  $\alpha = 0.125$ ;  $\beta = 0.83$

one that induces the highest sound transmission in the superconvective and subsonic frequency region, as in the subconvective one. On the other hand, with the modified Chase model (Chase II) a strong overestimation the transmission loss, above the convective ridge is simulated. In that case, the drop caused by the approach of the structural wavenumbers to the convective ones, starts critically before the other models and somewhat re-joins the others just before the real coincidence. The results are also in accordance with the ones in [160] where the difference in the radiated power of a plate, associated to each TBL model, is investigated. In accordance to Fig. 4.14, in [160], the Corcos model induces a higher radiated sound power with respect to the Chase one, in the low frequency range.

It must be pointed out that each model might fit specific operational conditions and thus a preliminary study of the excitation environment to be simulated, might lead to a better choice in selecting the most adequate model. In respect to this, the status of the research is such that the models are not generally predictive: each of them works well for specific cases and frequency ranges.

## 4.5 Validations for Cylindrical Shells

### 4.5.1 Diffuse Acoustic Field Transmission

The presence of curvature induces an alteration in the structural behaviour, at least, up to the ring frequency. This is the eigenfrequency corresponding to the first extensional mode at which the longitudinal wavelength is equal to the circumference of the structural element. At this frequency, the shell sound radiation is amplified similarly to a coincidence condition [41]. The transmission of curved panels and cylinders is here validated, under diffuse acoustic load, using, as a reference, numerical and experimental data available in literature.

The shell is a 3mm thick aluminium one and the curvature radius is 2m and the dispersion curves versus the acoustic wavenumbers are reported in Fig. 4.15a. First, in Fig. 4.15b, the transmission loss of an infinite cylinder is compared to the numerical work by Ghinet [45]. Both the ring frequency ( $\approx 400$  Hz; see Fig. 4.15a) and the acoustic coincidence ( $\approx$

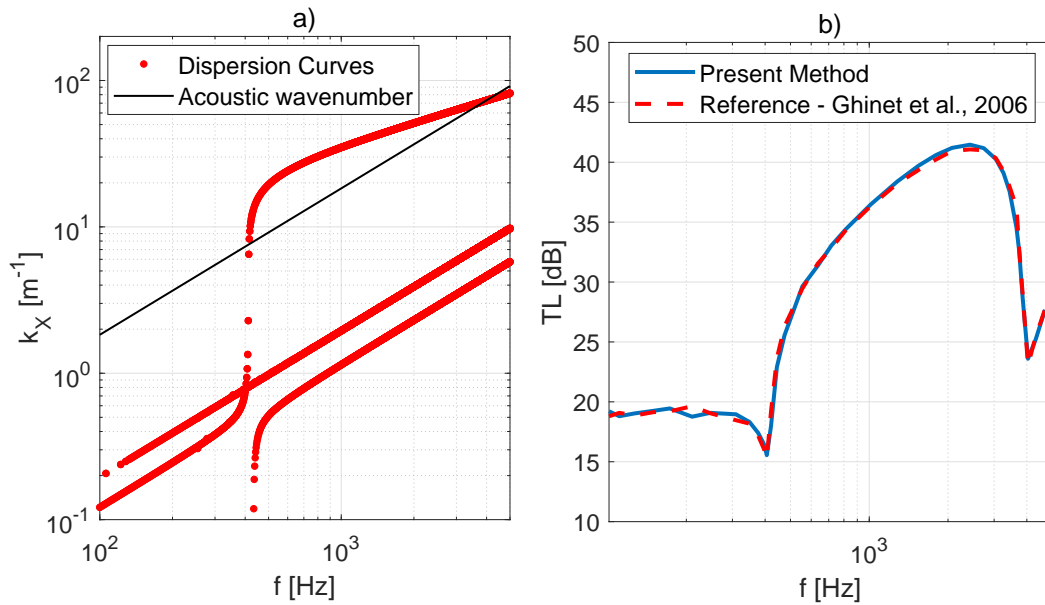


Figure 4.15: An isotropic cylinder under diffuse acoustic field excitation. a) Dispersion curves; b) Sound Transmission Loss comparison with numerical results from [45].

4.0 kHz; see Fig. 4.15a) are accurately described and the overall agreement is excellent.

### 4.5.2 The Effective Transmission Loss of Cylinders

In the case of shells, the load is translated in helical waves, instead of wall plane waves. For example, the effective transmission loss of a shell, in the case of simultaneous acoustic and aerodynamic excitation, can be estimated, assuming the axial direction of the shell as the stream-wise and the circumferential as an approximated cross-wise. In Fig. 4.16 the dispersion curves in the circumferential direction (wavenumbers of purely circumferential waves) are plotted for three different 3.2mm-thick aluminium shells; 3.0, 2.0 and 0.75 m curvature radii are considered and the ring frequencies are, respectively, 280, 400 and 1090 Hz. Differently, in Fig. 4.17, the effective transmission loss is calculated and compared. The aim, in this case, is to investigate how the aerodynamic coincidence influences the shell transmission.

In the case of the two bigger cylinders (see Fig. 4.16), the ratio between the ring frequency and the aerodynamic coincidence frequency is lower than one (on the flat case the radius equal to infinite). Right after the ring frequency, when the curvature effects start to vanish, these shells still behave in a sub-convective domain, thus, the effects of the coincidence are clearly visible in the sound transmission loss (see Fig. 4.17). On the other hand, in the case of the small cylinder, the ring frequency is superior to the critical aerodynamic frequency and the shell behaves in a sub-convective domain only when the curvature effects are important. The aerodynamic coincidence peak, in the transmission loss, is no more identifiable.

Similarly, if a single shell is analysed under different convective speeds, the aerodynamic coincidence region moves in accordance to what happens in the operative conditions of a

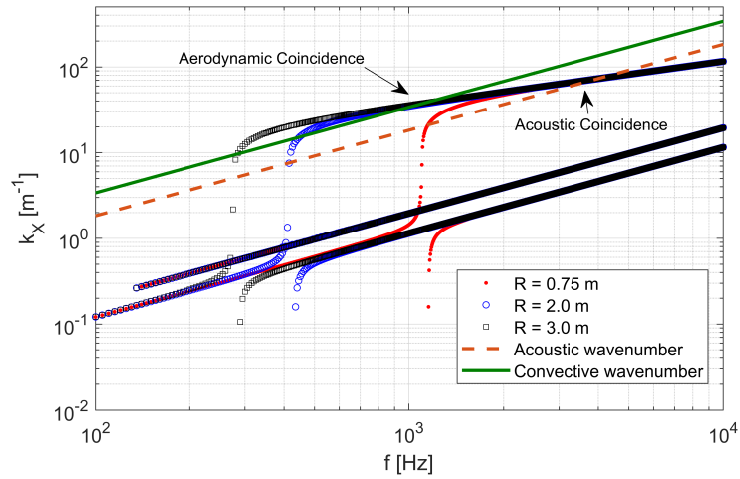


Figure 4.16: Dispersion curves in the circumferential direction of shells of different curvature. The acoustic and convective ( $U_c = 185$  m/s) wavenumbers are shown.

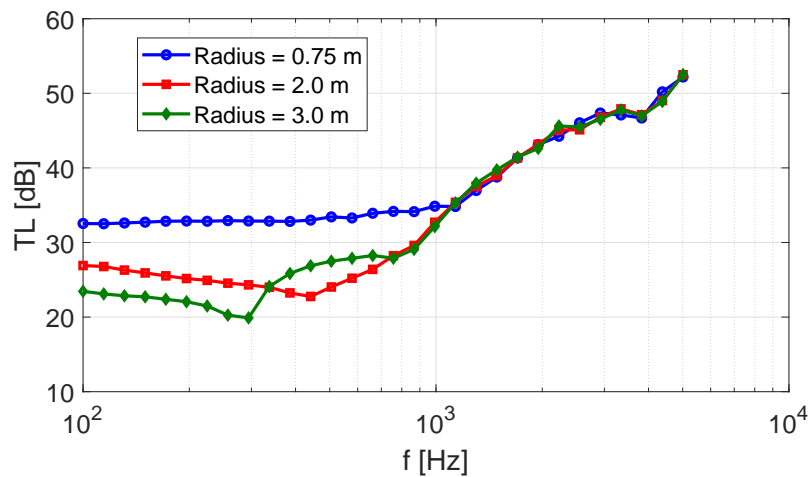


Figure 4.17: The effective transmission loss for shells of different curvature -  $U_c = 185$  m/s. A logarithmic frequency step, between 100 Hz and 5KHz, is used to generate the curves.

transport system as an aircraft, a train or a vehicle. The boundary layer effect vanishes when the speed lowers, since, the convective critical frequency lowers, up to getting inferior to the ring frequency.

## 4.6 Experimental Tests and Validations for Curved Panels

### 4.6.1 Comparison with Literature Results

On the other hand, in Figs. 4.18, a validation versus experimental measurements for curved finite panels is shown. In both cases the curvature radius is 2m; the skin and core material are reported in Table 4.1.

Fig. 4.18b shows the sound transmission loss for a 2x2.4m<sup>2</sup> sandwich composite panel whose skin and core are, respectively, 1.2mm and 12.7mm thick. The present method leads to a very good agreement even in the low frequency range. Again, both the ring frequency ( $\approx 400$  Hz) and the acoustic coincidence ( $\approx 1.0$  kHz), observable from the dispersion curves in Fig. 4.18a, are well predicted.

The proposed validations demonstrate the accuracy for both the methodology to account for curvature effects and the proposed approach to include finite size effects in the case of curved structures (Eq. 4.23 is used here) .

### 4.6.2 Experimental Set-Up - Transmission Loss Measurements

The measurements were performed in the coupled reverberant-anechoic rooms at Groupe d'acoustique de Université de Sherbrooke, following closely the standard (ISO 15186-1: 2000), as in [161, 162] (see Figs. 4.19 and 4.20). The reverberant room has dimensions 7.5 x 6.2 x 3 m<sup>3</sup> with an averaged reverberation time ( $T_{60}$ ) of 5.5 s in the frequency band [50-1000] Hz (Schroeder frequency =  $2000\sqrt{T_{60}/V} \approx 400$  Hz; [163]). The acoustic excitation is generated using loudspeaker installed close to a corner of the room, with a white noise input from 50 to 5000 Hz.

The transmitted sound power is estimated using a sound intensity probe in the receiving semi-anechoic room: a Bruel & Kjaer sound intensity probe composed of two half-inch microphones and a 12 mm spacer was used. The incident sound power is obtained by the averaged sound pressure level in the source room measured using a rotating boom microphone, as in Fig. 4.19. The sound transmission loss (TL) is finally calculated, assuming that the excited and radiating surfaces are the same, as:

$$TL = L_p - L_i - 6, \quad (4.26)$$

Table 4.1: Materials' properties for curved finite panels transmission loss validation

	Skin	Core
$E_1$ (GPa)	48.0	0.145
$G_{1,2}$ (GPa)	18.1	0.05
$G_{1,3}$ (GPa)	2.75	0.05
$\nu_{1,2}$	0.3	0.2
$\rho$ (Kg/m <sup>3</sup> )	1550.0	110.44

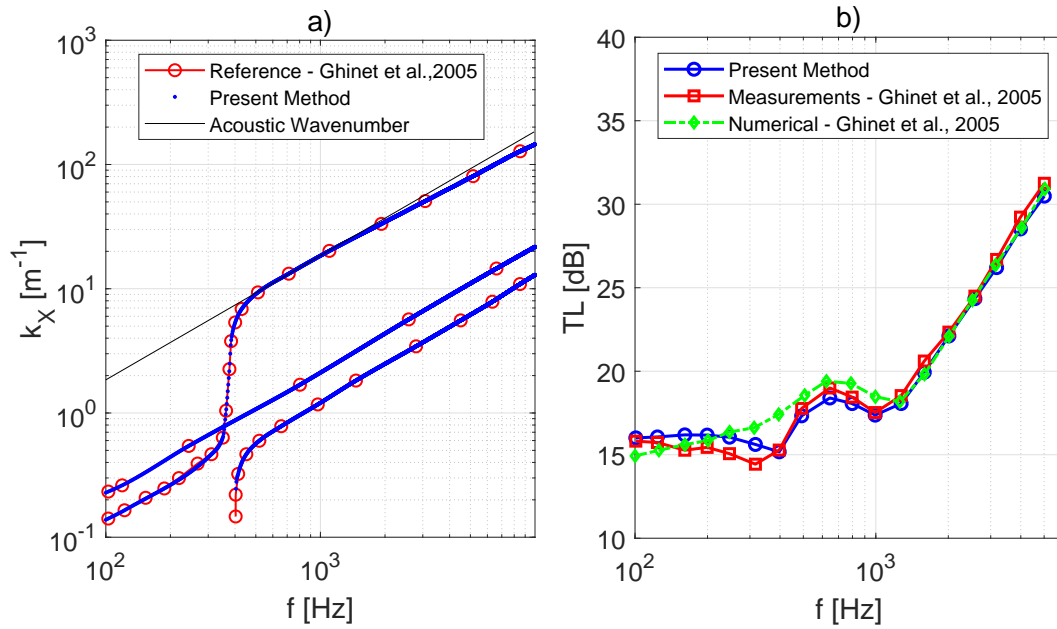


Figure 4.18: A finite curved sandwich composite panel under diffuse acoustic field excitation. a) Dispersion Curves comparison with results from [44]. b) TL comparison with measurements from [44] are compared with the actual method, in third octave bands.

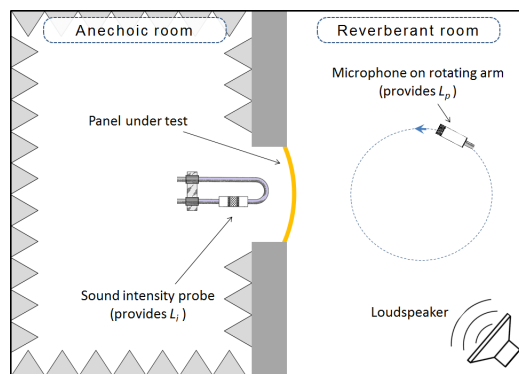


Figure 4.19: Illustration of the test facility with coupled reverberant-anechoic rooms. TL measurement following pressure-intensity standard.

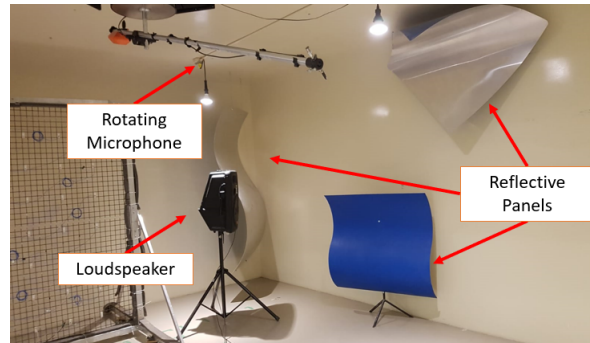


Figure 4.20: A detail of the reverberant room and the equipments used for the test.

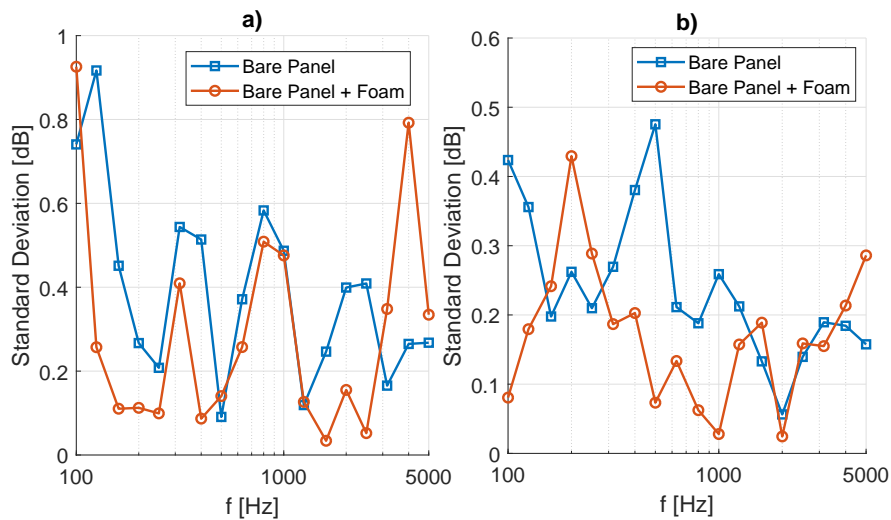


Figure 4.21: Standard deviation of the whole set of TL measurements following pressure-intensity standard. a) Composite Panel; b) Ribbed Panel

where  $L_p$  is the average pressure level measured in the reverberant room,  $L_i$  the average sound intensity level over the surface of the test-panels in the semi-anechoic room, while the -6 factor arises from reference values in dB conversion [164].

The tests have been performed multiple times and the curves presented in Fig. 4.24 and 4.26 represent a global average, in third octave bands. The standard deviation of the sound transmission loss, for the two tested panels, is reported in Fig. 4.21.

**Tested Panels** A thick sandwich composite panel and a thin aluminium stiffened with frames and stringers are considered (Figs. 4.22 and 4.23). The composite panel has dimensions 1.54 m x 1.62 m, with a 0.94 m radius of curvature. The ribbed panel has dimensions 1.45 m x 1.70 m, with a 1.30 m radius of curvature. For each of the two panels, two different configurations are tested and numerically simulated: a bare configuration and one with a 5cm-thick melamine layer attached (see Fig. 4.9). The material and property data for the sandwich composite panel are provided in Table 4.2; the physical properties of the melamine foam are given in Table 4.3; the geometrical parameters for the ribbed aluminium panel are in Table 4.4, while the material is aluminium for all its substructures.



Figure 4.22: A view of the two test panels hanged in the the semi-anechoic chamber.

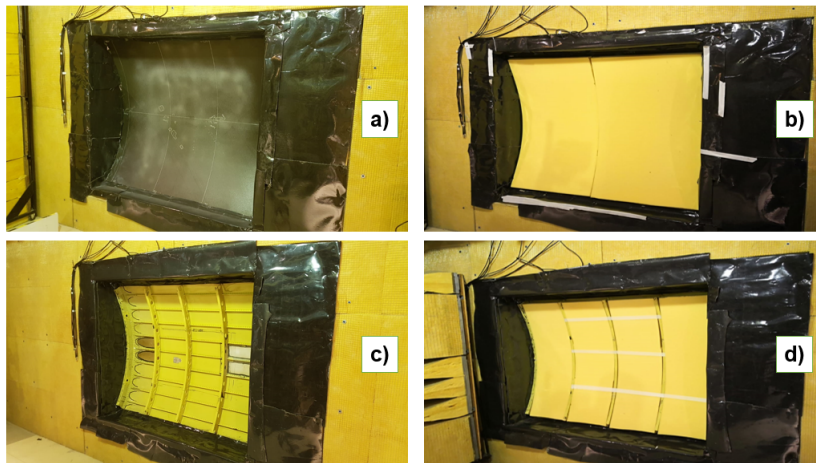


Figure 4.23: A view, from the semi-anechoic chamber, of the two test panels mounted in the linking window. Sandwich curved panel configurations: a) bare; b) with attached porous layers. Ribbed fuselage panel configurations: c) bare; d) with attached porous layers.

Table 4.2: Material properties for the thick curved composite sandwich panel.

	Skins	Core
$E_1$ (GPa)	46.0	$0.01 \times 10^{-3}$
$E_3$ (GPa)	46.0	0.179
$G_{1,2}$ (GPa)	17.7	$1.0 \times 10^{-3}$
$G_{1,3}$ (GPa)	17.7	$26.0 \times 10^{-3}$
$G_{2,3}$ (GPa)	17.7	$56.0 \times 10^{-3}$
$\nu_{1,2}$	0.3	0.45
$\nu_{1,3}$	0.3	0.01
$\rho$ (kg/m <sup>3</sup> )	1570	64
$h$ (mm)	0.98	25.5

Table 4.3: Physical properties for the porous layers attached to the panels [165].

Thickness	Open porosity	Flow resistivity	Tortuosity	Viscous length	Thermal length
5 cm	0.99	7920 [Nm <sup>-4</sup> s]	1.02	132 [ $\mu$ m]	149 [ $\mu$ m]

A double wall system links the rooms with a 2.44 m x 1.63 m test window, decoupled by a 12.7 mm air gap. Both panels were mounted in the test window using frames of adapted sizes, that were made of plywood with acoustic sealant made of neoprene adhesive and silicone. Only the panels' skin was actually clamped over approximately 20 mm in the mounting frame (stiffeners of the aluminium panel were thus not clamped). The frames and surrounding surfaces were finally covered with a flexible decoupled barrier material composed of an open-cell foam and a heavy PVC layer. Great care was used in mounting to avoid leakage and excellent repeatability of the experiments was observed.

### 4.6.3 Thick Sandwich Panel

First, the numerical results obtained with the presented method are compared with the measurements of the sound transmission for the curved composite sandwich panel. The unit cell is modelled using 20 solid elements (ANSYS SOLID45) through the thickness of the plate and using Eq. 3.9 to simulate the curvature. The porous layer is simulated using an equivalent fluid model [35].

The results in Fig. 4.24 show that, above the 400 Hz third octave, the numerical and experimental results are in agreement. The TMM-based extension for porous layers, described in Section 4.2, is here exact and gives excellent predictive results. Some discrepancies are present below 400 Hz and are attributable to a lack of accuracy of the measurements below the Schroeder frequency and to the way finite-size effects are accounted in the model. Being below the ring frequency region ( $\approx 500$  Hz), a strong stiffness of the shell, in the circumfer-

Table 4.4: Geometrical parameters of the ribbed fuselage panel.

	Frames	Stringers	Skin
Thickness (mm)	1.8	1.2	1.2
Height (mm)	72	28	
Spacing (mm)	40.6	15.2	

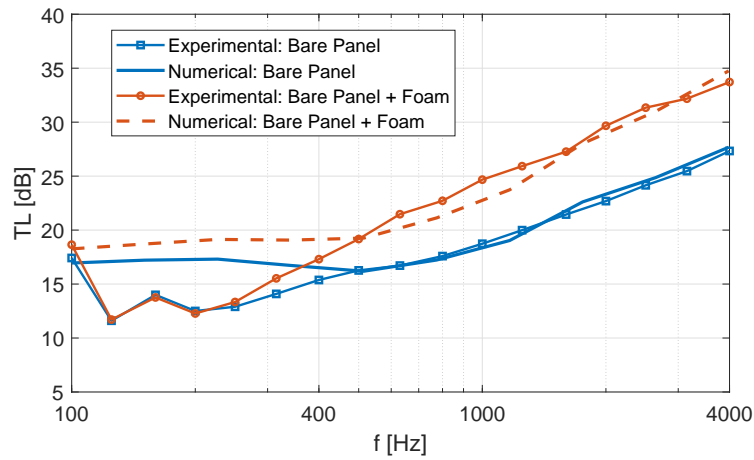


Figure 4.24: The Transmission Loss of a thick curved sandwich panel under diffuse acoustic field excitation. A comparison of the numerical results in log-space with measurements in third octaves.

ential direction increases the sound transmission loss in that frequency band. The averaged contribution for all the integration angles of a diffuse acoustic field, induces an horizontal trend of the TL curves versus frequency, as observed in the literature [41, 44].

A high level of damping is observed in the experimental TL curves (Fig. 4.24), since both the ring frequency ( $\approx 500$  Hz; numerically calculated from dispersion curves; Eq. 4.2) and the acoustic coincidence ( $\approx 1.5$  kHz; calculated from experimental dispersion curves) are characterised by very smooth dips. The structural damping is 3% in the whole frequency band, to simulate the increased damping added by the installation in the test window, leading to a good agreement of the numerical and experimental curves.

#### 4.6.4 Ribbed Aircraft Fuselage Panel

Next, the sound transmission for a curved and ribbed fuselage panel (Fig. 4.9 (c) and (d)), is measured and compared to the presented model. The averaged TL curves, in third octave bands, are presented in Fig. 4.18.

A numerical simulation is performed using the method presented in Section 4.2. The unit cell is illustrated in Fig. 4.25; shell elements (ANSYS SHELL181) are used for all structural parts, while joints and connections are not included in the model. In the real model, the stringer passes through a small hole in the frame; this is omitted in the cell model since not considered relevant for a sound radiation problem. In addition, the real panel is not perfectly periodic: some bays between the two last frames (on the left side, Fig. 4.23) are not coincident to the other ones in the whole panel, while the two frames at the lateral borders of the panel do not have the same geometry and size of the ones in the middle. Differences between the real structure and the ideally periodic model are thus present.

The modelled periodic cell has almost  $2.9 \cdot 10^4$  degrees of freedom; the modal order reduction reduces this number to less than 4000. More than 10 elements per wavelength are used to guarantee mesh convergence for the sound transmission up to 3 kHz. This was a trade-off choice to guarantee accurate results and keep a relatively low computational cost.

In Fig. 4.26, a good agreement with the numerical method is observed in the 300 Hz -

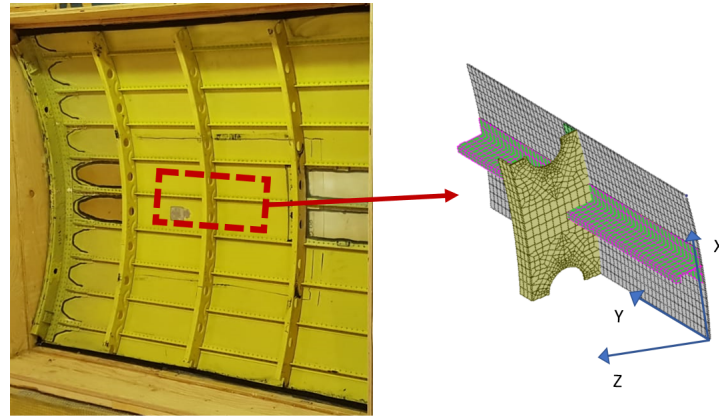


Figure 4.25: The unit cell used for the WFE simulation. The cell has global sizes given by the spacing of frames and stringers (Table 4.4).

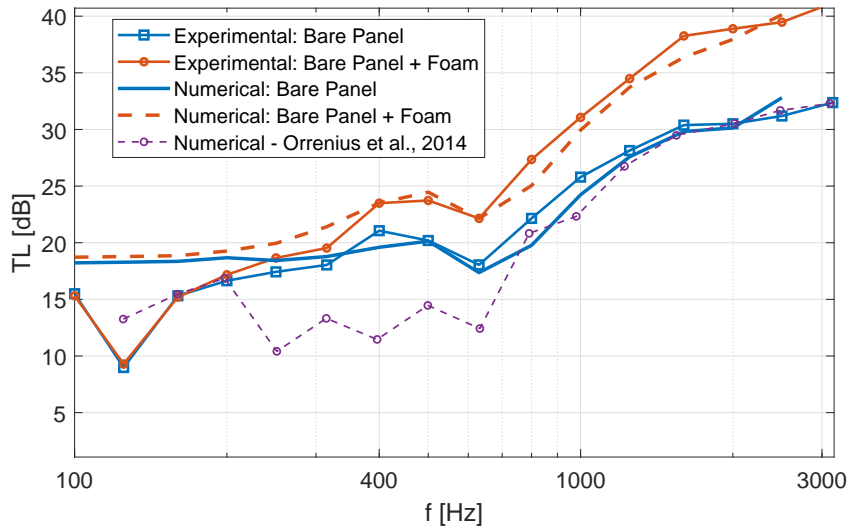


Figure 4.26: The Transmission Loss of the ribbed fuselage panel for a diffuse acoustic load. A comparison of the numerical results in log-space, with measurements in third octaves.

2500 Hz frequency range. Both for the bare configuration (Fig. 4.23 (c)) and the one with attached soundproofing material (Fig. 4.23 (d)), the numerical TL curves closely follows the experiments. The ring frequency ( $\approx 670$  Hz; [46]) gives a dip in the transmission loss, which is well described by the simulation, proving that the curvature simulation presented in Eq. 3.9 is still applicable even for large cell periods. Thus, unless small curvatures must be simulated, the periodic cell can be modelled as flat and Eq. 3.9 applied to simulate the desired curved shape.

Using the approach described in subsection 4.2.4 a proper fluid-structure coupling at cell scale is not performed. In addition, the air-gap between the radiating skins of the panel, between the fuselage bays, and the porous layer, have not been modelled. Considering the approximations regarding the handling of the sound package and the size effect, the discrepancies between the real structure and the model, the results observed in the test-case with the attached melamine layer, are accurate enough.

## 4.7 Discussion on approximations and limits of the approach

It is useful to discuss and emphasize some aspects regarding the approximations and the limits of the present numerical method, presented in Sections 4.2 and 6.1, using as reference and illustrative schemes Figs. 4.1, 4.2, 4.3, 4.6 and 4.7.

The curvature simulation in Eq. 3.9, is a good approximation for homogenised models. For periodic non-homogenised models, relatively small curvatures can be simulated. In fact, when the ratio between the length of the cell (in the curvature direction) and the radius of curvature is not small enough, the piecewise-flat approximation used here is critical even for fine structural meshes. In addition, great care must be placed on not curving even potential internal elements which can be flat (i.e resonator beams).

The interior acoustic field, as illustrated in Fig. 4.6, is assumed to be equivalent to a semi-infinite fluid termination: the modal behaviour of a finite cavity can not be described in this context, even for a closed cylindrical model. In analogy to what happens for an infinite flat structure, the internal acoustics is assumed to be composed by single out-going waves and internal acoustic waves' reflections/transmission are not modelled (see Eq. 4.9). These are the same assumptions/approximations used in [44, 45].

In this framework, the multiple harmonics that arise in the radiated acoustic field, for periodic non-homogenised structures, are numerically included in the structural response of the radiating side, when applying discrete periodic conditions for each couple of forcing wavenumbers  $k_X$  and  $k_Y$ . It, coherently to what has been discussed for the semi-infinite fluid termination condition, does not need to be analytically exploited since the only useful factor, in this method, for the acoustics in the radiating side is the  $k_Z$  term, dependent on the nature of the fluid itself (see Eq. 4.9). In fact, when comparing the present approach with the work by Ghinet et al. [45], for an infinite isotropic cylinder under a diffuse acoustic field the agreement is excellent in the whole frequency band; the reference method, in [45], which is semi-analytical, properly describes the acoustic field in global coordinates, with a full development using spherical harmonics.

Moreover, the structural wave propagating in the periodic media is here considered to the infinite. In other words, waves' reflections, transmission and absorption, typical at the borders of a finite media, are not accounted and, thus, a single-modal behaviour can not be described with this model. However, the finite size effects, which help in re-scaling the sound transmission loss versus frequency (with respect to the one of an infinite structure) can be included in the model using correction factors, as described in [40].

## 4.8 Convergence Aspects

The presented numerical method, requires some care on convergence aspects.

First the cell must have a size coherent with a proper description of the structural wavelengths, at the maximum frequency of analysis. Here, at least 6 elements per (minimum) wavelength are used. In addition, the integration scheme in Eq. 4.21 must be carried out using a proper mesh in the wavenumber space, to describe the wavenumber spectrum of the excitation model of interest, at each frequency step. No general approach is available since, depending on the characteristics of the load, a coarser or finer meshing of the wavenumber space can be a good compromise solution between accuracy and calculation time.

In the work by Maxit [29], a specific case for a flat plate under turbulent boundary layer is investigated and some rules are given with respect to the wavenumber sampling of the load. In that case, it is suggested to take, as limits of integration, the maximum between the flexural wavenumber and the convective one, for the stream-wise direction, and the maximum value of the structural bending wavenumber, for the cross-wise direction. These solutions, which are justified by the filtering effects of the structure, and thus represent an approximation of the total response, are not always applicable. In fact, when a complex media (i.e. multi-layered, ribbed, curved, etc.) is analysed, some coupled bending wavemodes might arise in the frequency band of interest and these can be equally excited by the turbulent layer load. Moreover, to set the choice of the integration limits on maximum frequency of analysis, as in [29], is computationally inefficient. The convective wavenumbers, as the structural ones connected to dispersive waves, are frequency dependent and, therefore, if the wavenumber resolution is fixed (as in [29]), keeping large integration limits even in the lower frequency bands would induce a useless higher computational cost. On the other hand, with respect to the wavenumber sampling, a general rule, to identify the correct resolution, is not given and a trial-error approach is suggested before launching the simulations [29].

Nevertheless, the present developments can be considered as an evolution of the work done in [29] since they are in the same research line aiming at the same goal. In this framework, a study on different criteria based solely on the fluid operator, is conducted for two different turbulent boundary layer models: the Corcos model [9] and the Chase one [14]. Two approaches are initially followed: first the wavenumber space is sampled using a fixed number of points in  $k_X$  and  $k_Y$ , for each frequency; then a fixed wavenumber resolution is used.

### 4.8.1 TBL Model: Corcos

Four integration domains are described in Table 4.5 and Fig. 4.27 and are valid for each frequency step. The use of reduced integrations limits stands in using the advantage coming from the symmetry of the wavenumber spectra of some excitation models, as the Corcos one (which is also used in this study). Differently from [29], the scaling factor for the limits of integration is assumed to be 1.9 (Table 4.5). The results in Fig. 4.28 show the transmission loss for the same isotropic plate tested in Fig. 4.7a, when the wavenumber spectrum is sampled first with a coarse scheme (50x50 mesh) and then with a finer one (120x120 mesh). In using integration limits that exclude the lowest amplitude sector of the wavenumber spectrum of the load, which coincides with the reverse-stream-wise wavenumber components ( $k_x \leq 0$ ; as Domain III; Table 4.5), the sound transmission levels are not affected. The integration of Eq. 4.21, being the ratio of equally weighted integrations, allows the use of symmetric domains (as Domain I or II; Table 4.1), with excellent accuracy even if coarse wavenumber meshes are used for the integration. On the contrary, when higher limits have to be imposed, a finer mesh is needed to avoid aliasing (see Domain IV in Fig. 4.28a).

Table 4.5: Integration limits in the wavenumber domain (see Fig. 4.8)

	I	II	III	IV
$k_{X,min}$ [ $m^{-1}$ ]	0	$-1.9 \omega/U_c$	0	$-1.9 \omega/U_c$
$k_{X,max}$ [ $m^{-1}$ ]	$1.9 \omega/U_c$	$1.9 \omega/U_c$	$1.9 \omega/U_c$	$1.9 \omega/U_c$
$k_{Y,min}$ [ $m^{-1}$ ]	0	0	$-1.9 \omega/U_c$	$-1.9 \omega/U_c$
$k_{Y,max}$ [ $m^{-1}$ ]	$1.9 \omega/U_c$	$1.9 \omega/U_c$	$1.9 \omega/U_c$	$1.9 \omega/U_c$

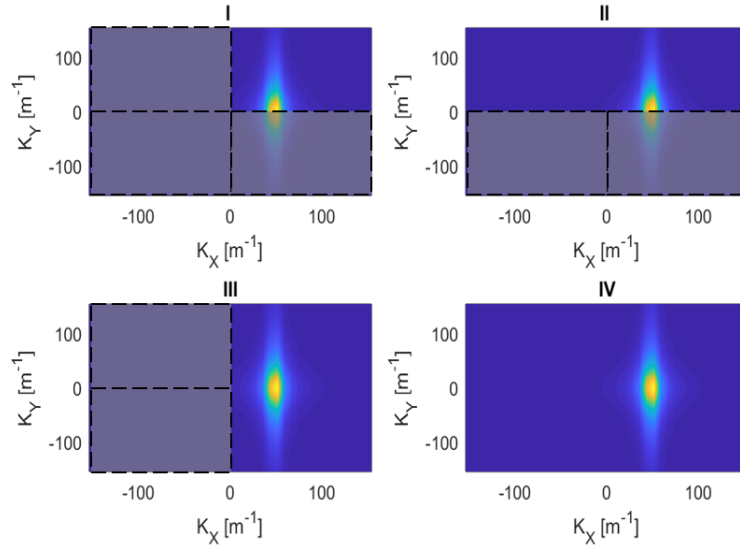


Figure 4.27: The wavenumber spectra of a TBL load (Corcos:  $U_c = 130$  m/s;  $f = 1$  kHz). The four solutions correspond to the four integration tests performed with variable domains in Eq. 4.21.

The computational cost in Fig. 4.28 is kept constant since the same mesh is used for each frequency.

It is worth to underline that, the use of Domain III is physically justified by the joint-acceptance of Corcos-like TBL models, which have a dominant amplitude of the spectra in the positive stream-wise direction, inducing dominant wavenumber components of the structural response in the positive  $k_x$  sector. Differently, the use of Domain I and II, derives from pure mathematical considerations on the form of the weighted integration in Eq. 4.21, which gives band-averaged sound transmission levels. In fact, for a purely structural response in weak coupling conditions, as in [7, 20, 21, 29], the use of these reduced domains as I and II (Fig. 4.27) would reduce the accuracy of the response, especially in the anti-resonance regions, due to an incomplete description of the single structural modes for the cutting of the negative-cross-wise structural wave components in the solution.

Differently, in Fig. 4.29, a fixed wavenumber resolution is kept. This approach increases, at each frequency step, the mesh size in the wavenumber domain and, thus, the computational cost of the integration, depending on the wavenumber limits of integration. In this case, thus, the integration over the domain I, II or III (Table 4.5) can speed up the total computation. In Fig. 4.29 it is observed how a finer resolution in the wavenumber domain gives a better accuracy, especially in the low frequency domain. This effect is physically justified by

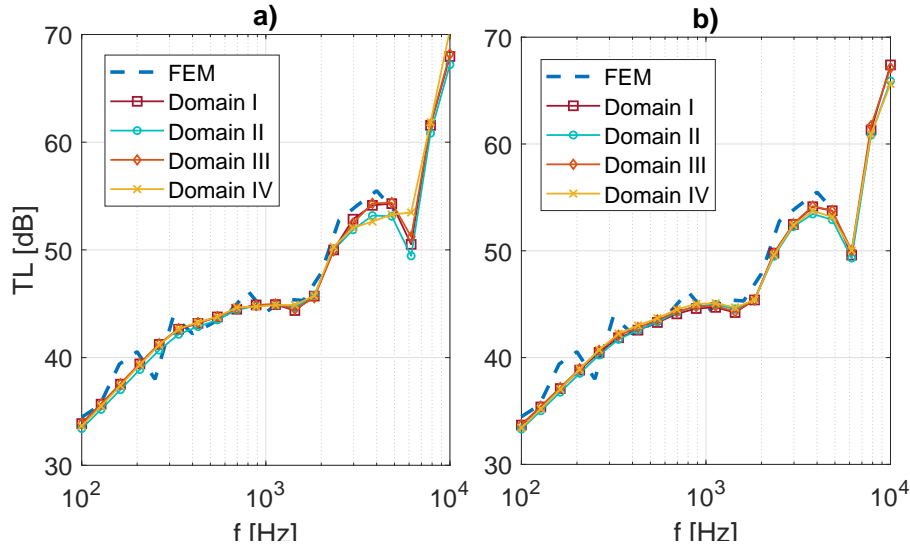


Figure 4.28: The sound transmission of a flat isotropic panel loaded with TBL (Corcos:  $U_c = 190$  m/s). The four integration domains in Fig. 4.8 are compared with a fixed mesh in the wavenumber domain. Mesh: a) 50x50; b) 120x120.

the enlargement of the boundaries of the convective region versus frequency. For a fixed wavenumber resolution, the smoother shape of the wavenumber spectrum, based on the model of Corcos, at higher frequencies, helps the predictive power of coarser resolutions.

#### 4.8.2 TBL Model: Chase

A similar investigation is conducted for the TBL model proposed by Chase [13, 14]. Differently from the model of Corcos, this model is dependent on the boundary layer thickness ( $\delta$ ), displacement thickness ( $\delta^*$ ) and the friction velocity ( $u_T$ ). The Chase II formulation [13] implemented here, is a modified version of the original Chase model. A comparison of the normalised wavenumber spectrum, in the positive stream-wise wavenumber space, is presented in Fig. 4.30: the Chase model presents a narrower convective peak and lower relative amplitudes at high and low wavenumbers.

First, in Fig. 4.31a a comparison among fixed wavenumber meshes of finer sampling, is proposed. The critical frequency, for a convective velocity of 80 m/s, is 380 Hz and is correctly captured in the TL curve. The sensitivity of the solutions is larger around the acoustic coincidence (6 kHz) since the Chase model (Chase II) is characterised by strong derivatives versus the cross-wise wavenumber components. Similarly, in Fig. 4.31b, the effect of the limits of integration are investigated using the domains described in Table 4.1. As for the Corcos model, the domain III (Table 4.1), physically justified by the form of the wavenumber spectrum of the Chase model, gives excellent results. Differently, enlarged domains as IV (Table 4.1), require finer meshes: in this case, in opposition to the case of Corcos, the effects are visible at higher frequencies.

#### 4.8.3 The Influence of the Cross-Flow Components

It is interesting to verify if the reduced cross-wise amplitude gradient of the wavenumber spectra, around the convective ridge region of the Corcos and Chase model, with respect

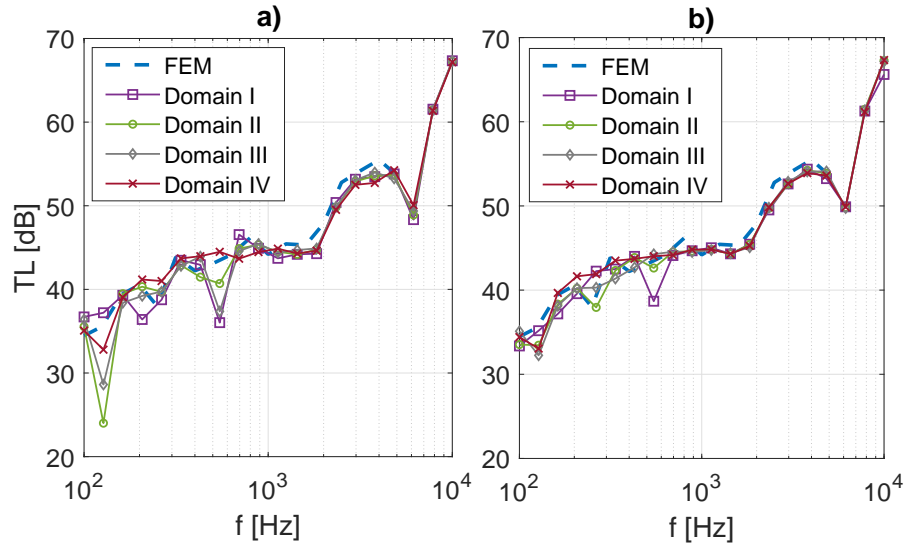


Figure 4.29: The sound transmission of a flat isotropic panel loaded with TBL (Corcos:  $U_c = 190$  m/s). The four integration domains in Fig. 4.27 are compared with a fixed resolution in the wavenumber domain. Sampling: a) Coarser; b) Finer.

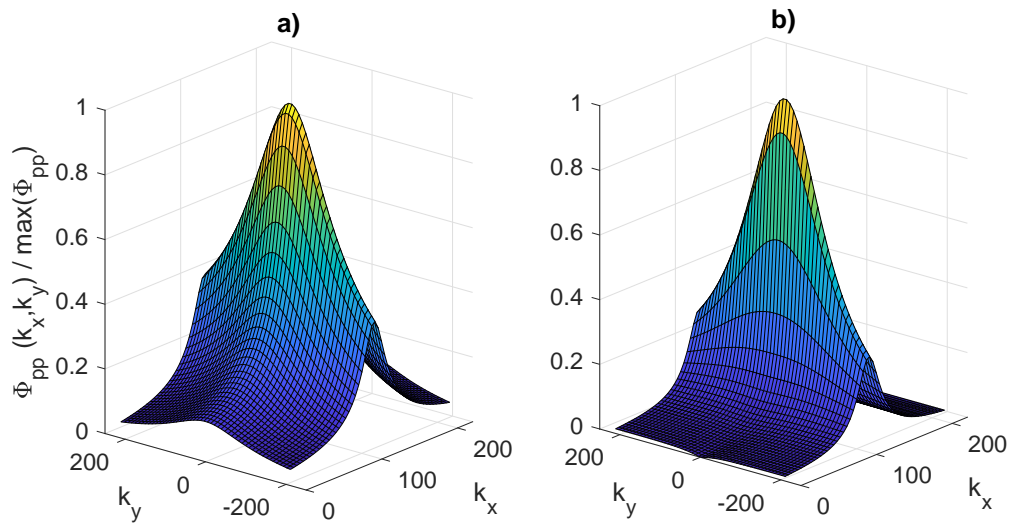


Figure 4.30: Normalised wavenumber spectrum of the TBL model ( $f = 1.5$  kHz;  $U_c = 80$  m/s) - a) Corcos [9]; b) Chase II [14].

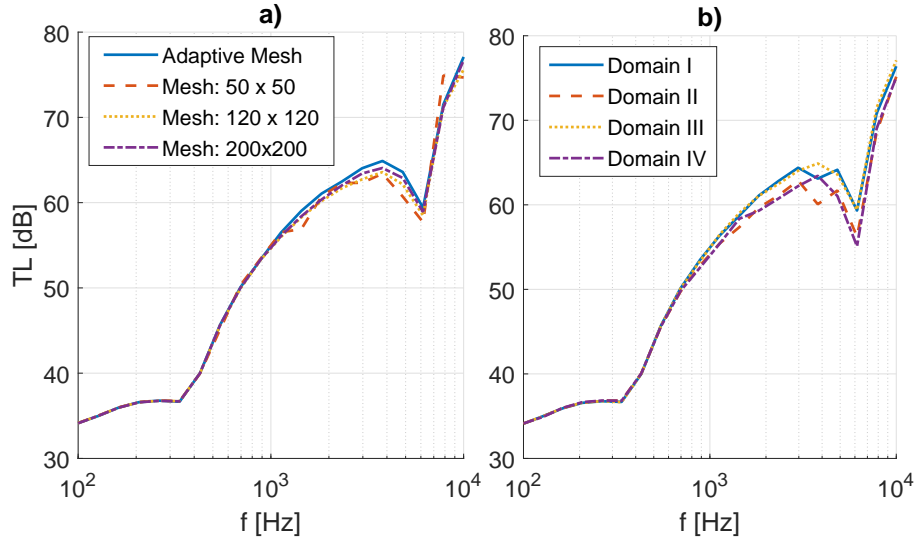


Figure 4.31: The sound transmission of a flat isotropic panel loaded with TBL (Chase II:  $U_c = 80$  m/s) - a) Comparison of mesh sizes; b) Comparison of integration domains for a 100x100 mesh (Fig. 4.8). Flow data (see [13]):  $\delta = 0.027$  m;  $\delta^* = 0.0018$  m;  $u_T = 1.9$  m/s.

to the stream-wise component, allows the use of larger sampling in the cross-flow direction. A simple example is reported in Fig. 4.32 where two computations are presented, with a fine stream-wise sampling and a larger cross-wise one and vice-versa. A full integration domain is used (Domain IV; Table 4.5). The results demonstrate that, in the case of Corcos (Fig. 4.32a), the stream-wise resolution has a higher impact than the cross-wise one. Thus, a strong speed-up of the computation, can be achieved by using larger cross-wise sampling and a restricted integration domain, making use of the symmetry of the loading wavenumber spectra and the smoother decay of the convective region in the cross-wise direction. However, as shown in Figs. 4.28 and 4.29, some sensitivity and variations are observed below the aerodynamic coincidence, which is the frequency band where the structural bending wavenumber is higher than the convective one. In these frequency bands, an integration criterion, based solely on the load, might be critical approximation, because the structural wavelength is lower than the convective one. On the other hand, a criterion based just on the excitation model has the advantage of not being case-dependent and not requiring an a-priori the knowledge of the structural filtering effects. When the model of Chase (Fig. 4.32b) is used instead, the sensitivity of the solutions seems to be higher for the cross-wise wavenumber components. As said, this can be addressed to strong amplitude gradients of the model in the acoustic region, which lead to a deficient description, not in accordance with many experimental data, as discussed extensively by Graham [13]. The convective region, on the other hand, does not seem to be sensitive to directional sampling parameters and is always well described.

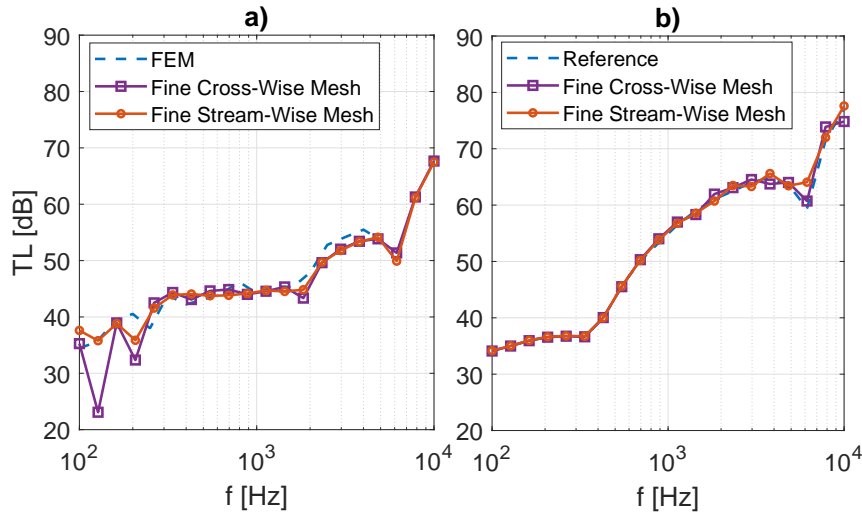


Figure 4.32: The sound transmission of a flat isotropic panel loaded with TBL. The wavenumber sampling is studied for single stream-wise and cross-wise resolutions. TBL Model: a) Corcos,  $U_c = 190$  m/s; b) Chase II,  $U_c = 80$  m/s

## 4.9 Conclusions

This work proposes a numerical approach for the estimation of the sound transmission loss of complex flat, curved and cylindrical periodic structures, under any type of acoustic and aerodynamic load. The approach involves a wave finite element method, for the structural part, and proposes a load simulation into surface waves. The fluid-structure interaction is performed in analogy to the acoustic wave excitation, discriminating among the different forcing models, using a weighted wavenumber integration. The only requirement is the knowledge of the wavenumber spectra of the wall pressure fluctuation. Finite size effects are accounted using the baffled window equivalence or asymptotic formulations, for flat structures. An alternative and efficient method is proposed in the case of curved finite structures, in similitude to the semi-infinite equivalent cases. Static and dynamic condensation can be applied if fine meshes are used in the modelling phase.

Both the accuracy and robustness of the present method are proved using analytic, numerical and experimental references. Both uncorrelated (diffuse acoustic field) and spatially-correlated loads (turbulent boundary layer) are used for the validations, in the case of flat and curved structures. Calculations performed using finite elements of different nature do not affect the accuracy of the estimations. The convergence of the approach is assured by the one of the wavenumber integration process. The choice of the integration limits must be calculated on the base of the wavenumber spectra of the load.

The combination of boundary layer and acoustic excitation is simulated in the case of shells, resulting in an effective sound transmission loss. The ring frequency, the aerodynamic and acoustic coincidences are efficiently estimated, independently on the curvature radius and convective velocity simulated. Moreover, the use of boundary layer excitation does not require the accounting of finite size effects and a comparison of the structural and acoustic design is possible, independently from the size of the analysed structure.



## Chapter 5

# Non-Lifting Aeroelastic Coupling using WFE

In classical aeroelasticity of plates and shells, instability analyses are carried out by using the natural modes of the structures with and without flow coupling. On the contrary, the study of travelling elastic waves in presence of flow, never had a deep and concrete application. Here, within a wave-based finite element framework, sub- and super-sonic aerodynamic theories are introduced to analyse the effect of self-excited aerodynamic loading terms on the dispersive characteristics of the structural waves. The method is validated by using two specific literature test-cases and is applicable both on isotropic and multi-layered flat and curved structures. The sound transmission is also computed under a sub- and super-sonic turbulent boundary layer excitations: the effect of including or not the aeroelastic coupling is analysed.

### 5.1 Introduction

Structural failures caused by aeroelastic phenomena have affected many fighter aircraft, spacecraft and jet engines, in the history of aviation and furthermore they are well present in the civil engineering too.

The aeroelasticity of plates and shells, extensively studied in the last decades, faces the difficulty of distinguishing between the self-induced vibration components and the external one. Phenomenological non-linearities induce fatigue failures instead of catastrophic instantaneous failures, typical of the aeroelasticity of lifting surfaces [48, 49]. In this context, the modal approach is often preferred to a wave-based one, because it allows a clear evaluation of the flutter conditions, analysing the effect of the aerodynamic-induced forces on each structural mode [48–50, 56, 57, 61]. Consequently, the effects of aerodynamics on the elastic structural waves' propagation, are rarely studied and few works are present in the literature [56, 61–63].

The infinite-plate problem, has been developed by Miles [56] and Crighton & Oswell [60]. The first [56] presents a work discussing the flutter of an isotropic infinite panel in a two-dimensional incompressible flow, identifying the flutter conditions versus the circular frequency in terms of wave speed. The latter [60] develops an analytical model that describes, in a neutral stability zone, some highly unusual wave propagation effects in presence of flow. On the other hand, the effect of mean flow on cylindrical structures has been then studied by the same Miles [57] and others authors [58, 64]. In particular, Peake [64] provides a

closed-form dispersion relation for circumferential waves in infinite cylinders in presence of incompressible external flow; this is here used for validation purposes.

Hereby, both subsonic and supersonic aerodynamic flows are introduced in models of homogenised periodic plates and shells; the elastic wave propagation is thus investigated, assuming that only one side of the structural domain is wetted by the flow. The sound transmission loss is also computed, using a set of aleatory surface waves [166] and discussed versus aeroelastic effects.

## 5.2 Aerodynamic Loading in Periodic Framework

The method here presented is based on the Wave Finite Element Method and the developments of Chapter 4.

To simulate a mean flow, working on one side (or two) of an infinite structural domain, a specific aerodynamic theory has to be used to model the self excited aerodynamic components of the load. Here, supersonic flows are described using the simplest aerodynamic theory, the *Piston Theory* [48, 167], while for subsonic aerodynamic flows, an approximated formula for incompressible flows is used, as proposed by Dowell [48].

Under the hypothesis of small disturbances, the aerodynamic pressure can be normally considered as made up of two components [48], as in Eq. (5.1): one is given by the pressure fluctuations for a rigid body ( $\Delta_P^E$ ); the second is dependent on the structural motion/elasticity ( $\Delta_P^M$ ). The following developments are connected to the second of these contributes; an illustration is given in Fig. 5.1.

$$\Delta_P = \Delta_P^M + \Delta_P^E \quad (5.1)$$

### 5.2.1 The Piston Theory

The Piston Theory, valid from Mach  $> 1.5$  [48, 167], assumes that the pressure fluctuations in any point of the system are independent. Using the notation of Chapter 4, the dispersion relation of an homogenised periodic cell can be written as:

$$\mathbf{\Lambda}^H [\mathbf{K} - \omega^2 \mathbf{M}] \mathbf{\Lambda} \mathbf{q}_1 = \mathbf{\Lambda}^H \mathbf{\Lambda} \mathbf{f} + \mathbf{\Lambda}^H \mathbf{\Lambda} (\mathbf{e}^M + \mathbf{e}^E) \quad (5.2)$$

where  $\mathbf{K}$  and  $\mathbf{M}$  are the stiffness and mass matrices of the periodic cell,  $\omega$  the circular frequency,  $\mathbf{\Lambda}$  the periodicity matrix and  $\mathbf{f}$  and  $\mathbf{e}$  are the nodal vectors of internal and external forces respectively. It is important to note that here the external forces are separated in two components as in Eq. 5.1. In particular, the self-excited force terms can be written as a function of the convective and continuity derivative, [48, 50, 56, 167]:

$$\mathbf{e}^M = -\rho_0 a_0 \mathbf{A}_n \left( \frac{\partial \mathbf{w}}{\partial t} + U \frac{\partial \mathbf{w}}{\partial x} \right) \quad (5.3)$$

where  $\mathbf{w}$  represents the vector of the out-of-plane displacements of the structural nodes belonging to the surfaces in contact with the flow (coordinate  $Z$  in Fig. 5.1),  $\rho_0$  is the fluid density,  $a_0$  the sound speed,  $\mathbf{A}_n$  the nodal area vector and  $U$  the flow-speed. The out-of-plane displacements can be expressed by multiplying  $\mathbf{q}$  for a matrix ( $\epsilon$ ) of 0 and 1 in the positions corresponding to the target degrees of freedom (i.e. the translations in  $Z$ ). For example, with reference to Fig. 5.2, the matrix  $\epsilon$ , can be built as such:

$$\epsilon_{i,j} = \begin{cases} 1 & \text{if } j = 3; i = 1, N; \\ 0 & \text{else} \end{cases} \quad (5.4)$$

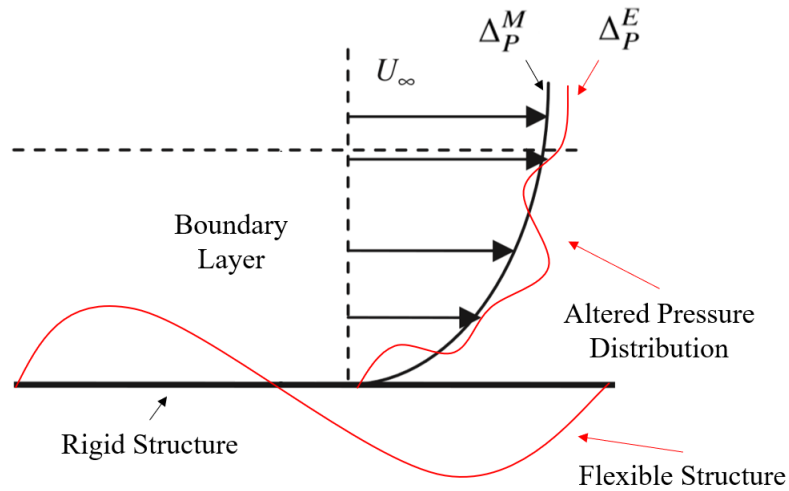


Figure 5.1: An illustration on the effects of a flexible structure in terms of variation of pressure distribution in a turbulent boundary layer.

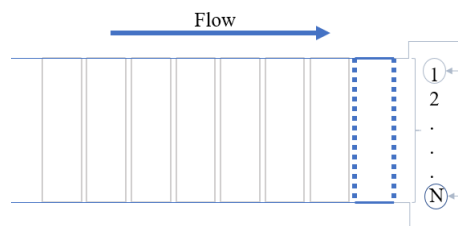


Figure 5.2: Distribution of degrees of freedom for a single cell with respect to the excited (flow) and radiating side.

where  $i$  represents the number of nodes, as in Fig. 5.2, and  $j$  the nodal degree of freedom (3 corresponds to translation along  $Z$ ). In a periodic structural framework, the spatial derivative in Eq. (5.3) is a function of the structural propagation constant ( $\lambda_x$ , assuming  $X$  as the flow direction), and can be expressed, using a simple numerical scheme for the first derivative, as follows:

$$\frac{\partial \mathbf{w}}{\partial x} = \mathbf{\Lambda} \left( \frac{\lambda_x - 1}{L_x} \right) \boldsymbol{\epsilon} \mathbf{q}_1 \quad (5.5)$$

The final dynamic stiffness equation can be derived, as in Eq. (5.6), substituting Eqs. (5.3) and (5.5) in Eq. (5.2).

$$\mathbf{\Lambda}^H \left[ \mathbf{K} - \omega^2 \mathbf{M} - i\omega \rho_0 a_0 \mathbf{A}_n \boldsymbol{\epsilon} + U \rho_0 a_0 \mathbf{A}_n \boldsymbol{\epsilon} \left( \frac{\lambda_x - 1}{L_x} \right) \right] \mathbf{\Lambda} \mathbf{q}_1 = \mathbf{\Lambda}^H \mathbf{\Lambda} \mathbf{f} = 0 \quad (5.6)$$

Additional damping and stiffness terms are observed in the new dynamic stiffness equation (Eq. (5.6)). The additional damping is proportional to the circular frequency, but, as discussed in [48], it is not a dominant term. A strong variation of the results of Eq. (5.2) versus the Eq. (5.6) ones, is given by the additional stiffness terms, which are proportional to the stream-wise elastic waves' propagation coefficient.

### 5.2.2 Subsonic Aerodynamic Flows

Similarly, when a different aerodynamic model is investigated, as a subsonic incompressible flow, the spatial derivatives can still be expressed as a function of the structural waves' propagation constants, using, generally, numerical schemes of higher order. The aerodynamic forces connected to the structure motion can be expressed, in this case, as follows [48]:

$$\mathbf{e}^M = \frac{\rho_0 U^2 \mathbf{A}_n}{\pi} \left[ \frac{\partial^2 \mathbf{w}}{\partial x^2} + \frac{2}{U} \frac{\partial^2 \mathbf{w}}{\partial x \partial t} + \frac{1}{U^2} \frac{\partial^2 \mathbf{w}}{\partial t^2} \right] \quad (5.7)$$

Substituting Eq. (5.7) in Eq. (5.2), using a second order numerical scheme for the second order spatial derivatives, the final dynamic stiffness matrix is obtained:

$$\begin{aligned} & \mathbf{\Lambda}^H \left[ \left( \mathbf{K} + \frac{2\rho_0 U^2 \mathbf{A}_{np}}{L_x^2} \boldsymbol{\epsilon} \right) - \omega^2 (\mathbf{M} - 2\rho_0 \mathbf{A}_{np} \boldsymbol{\epsilon}) + \right. \\ & \left. + \frac{\rho_0 U \mathbf{A}_{np}}{L_x} \left( 2i\omega + \left( 2i\omega - \frac{U}{L_x} \right) \lambda_x - \frac{U}{L_x} \lambda_x^{-1} \right) \boldsymbol{\epsilon} \right] \mathbf{\Lambda} \mathbf{q}_1 = 0 \end{aligned} \quad (5.8)$$

where  $\mathbf{A}_{np} = \frac{\mathbf{A}_n}{\pi}$ .

Here, the derivation schemes used are:

$$\frac{\partial^2 \mathbf{w}}{\partial x^2} = \mathbf{\Lambda} \left( \frac{\lambda_x - 2 + \lambda_x^{-1}}{L_x^2} \right) \boldsymbol{\epsilon} \mathbf{q}_1 \quad (5.9)$$

$$\frac{\partial^2 \mathbf{w}}{\partial x \partial t} = -i\omega \mathbf{\Lambda} \left( \frac{\lambda_x - 1}{L_x} \right) \boldsymbol{\epsilon} \mathbf{q}_1 \quad (5.10)$$

$$\frac{\partial^2 \mathbf{w}}{\partial t^2} = -\omega^2 \mathbf{\Lambda} \boldsymbol{\epsilon} \mathbf{q}_1 \quad (5.11)$$

Comparing Eq. (5.2) and Eq. (5.8), additional stiffness, damping and inertia terms, dependent on the flow speed and density, can be observed. In addition, some explicit influence

on the structural waves' propagation appears with stream-wise (terms proportional to  $\lambda_x$ ) and cross-wise (terms proportional to  $\lambda_x^{-1}$ ) aerodynamic components. Again, the eigenvalue problem is parametric and can be solved by fixing two parameters between  $k$ ,  $\omega$  and  $U$ . It is interesting to observe the absence of non-linearities in the eigenvalue problem.

### 5.3 Numerical Results

Here, the eigenvalue problems of Eqs. (5.6) and (5.8) are solved, for specific test-cases. A validation for flat plates in supersonic flows is performed using the travelling wave approach by Miles [56, 57, 61]. The dispersion curves for shells are also computed and a validation with the Donnel-Mushtari theory with and without flow is performed [64]. In both cases the external flow is assumed to be inviscid air.

Finally, the sound transmission under an external turbulent boundary layer excitation, is computed and compared when aeroelastic effects are accounted in the model, for both supersonic and subsonic flows. The approach used for fluid-structure coupling and random load simulation, within a wave finite element framework, follows the same proposed in [166]. Despite the numerical complexity in Eqs. (5.6) and (5.8), the proposed numerical framework allows simpler evaluations of the effective sound transmission loss, due to a turbulent boundary layer load, than classic modal approaches [27, 168, 169].

#### 5.3.1 Wave Propagation in Plates and Shells

First, a 2mm-thick flat aluminium plate is considered. The test-case analysed by Miles [56], is reproduced and the analytic solution is used to validate the proposed approach. In Fig. 5.3 the bending wave speed and wavenumbers of the plate in the stream-wise direction, are plotted and compared to the case a one-sided flow (Mach 1.6) is simulated; the present approach is compared to the approach of Miles [56]. A good agreement with the reference solution is observed, as a variation of the bending wavenumbers with respect to the purely structural case, in the lowest frequency bands. The increase of the wavenumbers is somewhat representing a reduction of bending stiffness of the plate, caused by the action of the flow, that vanishes when the frequency increases, approaching the purely structural solution.

Differently, in Fig. 5.4, the dispersion curves of an aluminium shell (2mm-thick; 1.5m radius), with and without flow, are plotted and compared, both in the axial direction (stream-wise), and the circumferential one. The use of the aerodynamic model presented in Section 5.2 (*Piston Theory*), which excludes three-dimensional effects is presented in some works in the literature [170, 171]. In fact, the mitigation of circumferential cross-flow pressure gradients by means of flow viscosity, justifies the use of the linear piston theory as a simplified aerodynamic model for shells [65].

In Fig. 5.4a, the wavenumbers in the direction of the flow (axial direction) are increased with respect to the purely structural case (absence of flow), as in the case of a flat plate [56]. On the other hand, for circumferential waves (Fig. 5.4b), the effects mainly visible around and above the ring frequency, because of the higher stiffness of shells before the first extensional mode. In both cases, for increasing frequency, the dispersion curves converge to the ones of the purely structural case (absence of flow) and only bending waves are affected by the presence of the flow; shear and longitudinal wavemodes are not excited by the pressure fluctuations. A good agreement with the reference solutions [64, 172] is observed, with and without flow.

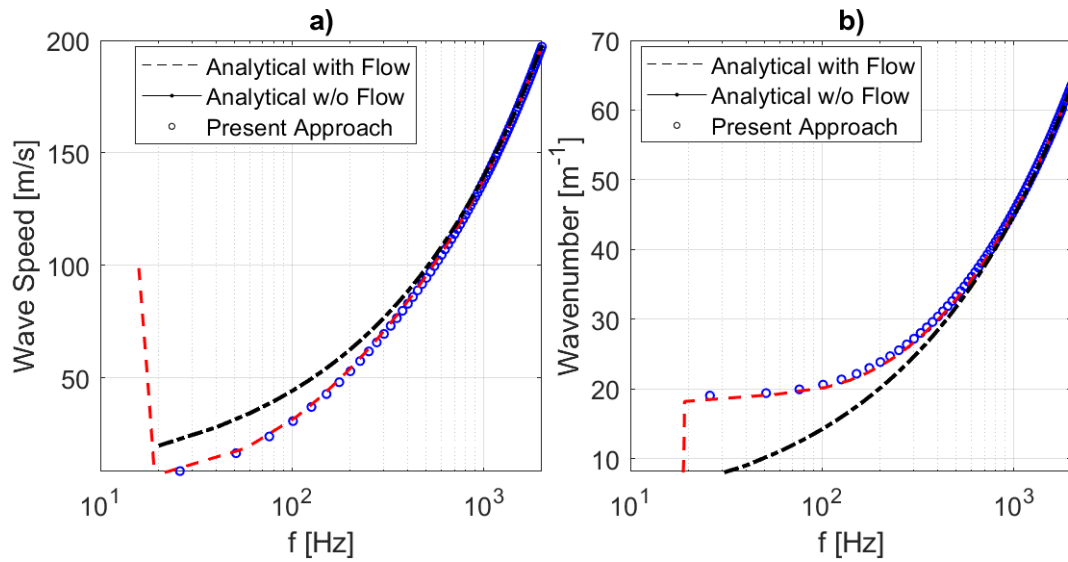


Figure 5.3: Stream-wise bending waves in a 2mm-thick flat aluminium panel with a one-sided flow at Mach 1.6. Reference solution from [56, 61]: a) Wave Speed; b) Wavenumber.

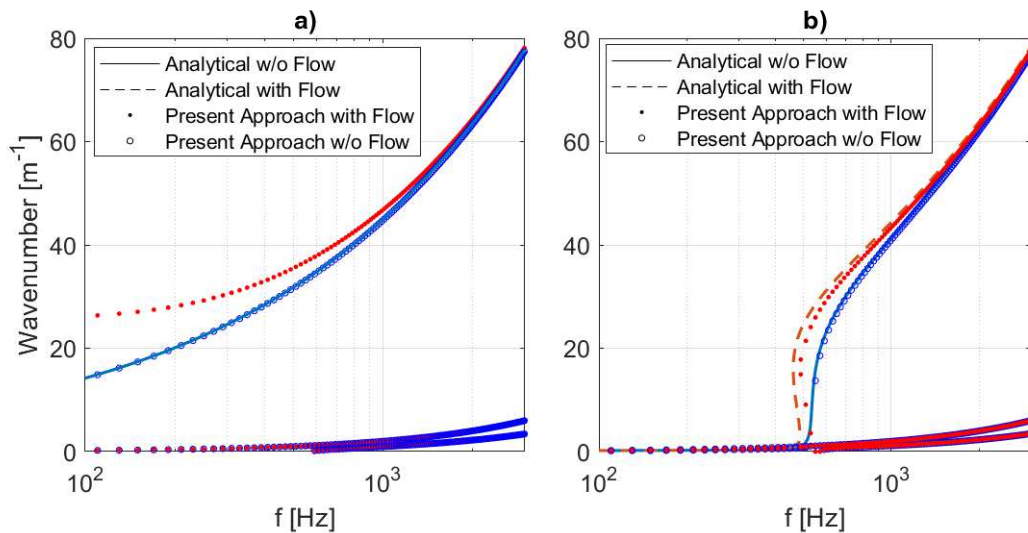


Figure 5.4: Dispersion curves for an aluminium shell (2mm-thick, 1.5m curvature) with a one-sided flow at Mach 2.5: a) Axial Waves; b) Circumferential Waves. Analytical model: Ref. [64].)

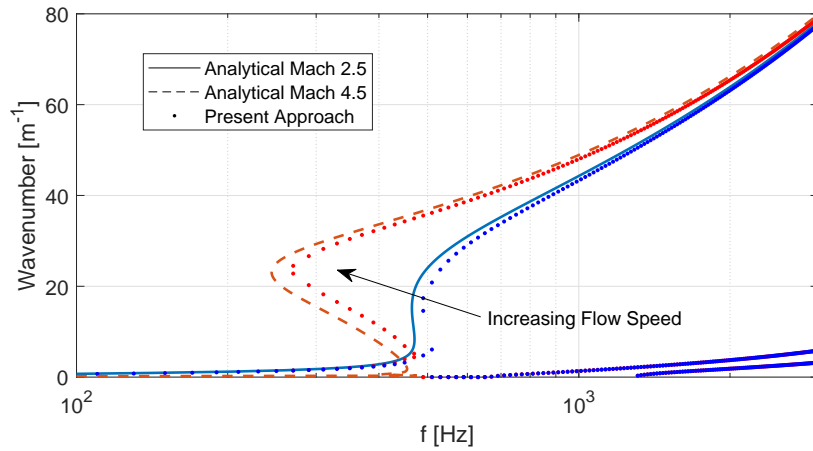


Figure 5.5: Dispersion curves for an aluminium shell (2mm-thick, 1.5m curvature) with a one-sided flow at Mach 2.5 and 4.5. Analytical model: Ref. [64].

The effects of increasing flow speed and circumferential order are shown in Fig. 5.5. In Fig. 5.5, a fixed circumferential order is considered and the flow speed is increased from Mach 2.5 to 4.5; a larger wavenumber region is affected, for increasing speed, inducing a distorted transition to the flat-plate bending behaviour after the cut-on frequency. Differently, in Fig. 5.6, the effect of increasing the circumferential order from 1 to 10 is shown; the effects seem independent on the presence of the flow, being coherent with the variation one has for the purely structural case [64]. A further validation is also provided in Figs. 5.5 and 5.6 by the presence of the analytical curves derived from [64].

### 5.3.2 Sound Transmission under Turbulent Boundary Layer

The effect of the mean flow on the sound transmission of flat and curved panels is here investigated. The external load, corresponding to a turbulent boundary layer, is simulated using a weighted integration of surface waves in the wavenumber space [166]. Finite size effects can be accounted using a baffled window approach [39]. First, a supersonic flow is simulated (Mach 1.35) and a Cockburn-Robertson TBL model is used [11] on flat and curved panels. In this case, the Piston Theory is used for the load contribution auto-generated by the structure elasticity ( $\Delta_P^M$  in Eq. (5.6)).

In Fig. 5.7, the sound transmission loss is affected by the aeroelastic effects in the low frequencies. This is caused by the strong alterations in bending waves' propagation, caused by the flow itself. However, differences are observed also before the acoustic coincidence ( $\approx 6$  kHz). In fact, the variation of wavemodes induced by the aeroelastic effects, eigenvectors from Eqs. (5.6), induces different structural reaction with respect to the case in absence of flow. The drop caused by the critical aerodynamic frequency is hardly visible being close to the acoustic coincidence ( $\approx 6.7$  kHz).

For the curved panel (Fig. 5.7b), before the ring frequency, the effects are strongly amplified.

On the other hand, a subsonic flow (Mach 0.5) is simulated in Fig. 5.8, using the TBL model of Corcos [9]. In this case, Eqs. (5.7) is used for the subsonic load contribution generated by the structural motion. Again, flat and curved panels are studied. Differently to the supersonic case, the effects of the flow are somewhat distributed in the whole frequency

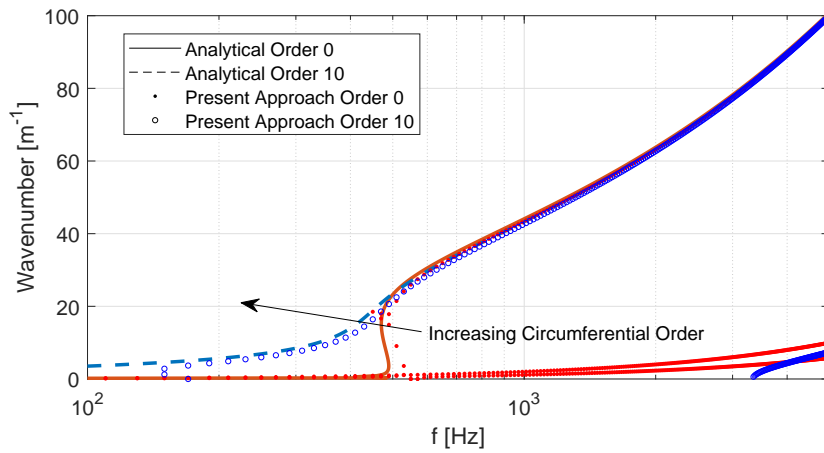


Figure 5.6: Dispersion curves for an aluminium shell (2mm-thick, 1.5m curvature) with a one-sided flow at Mach 2.5, for increasing circumferential order. Analytical model: Ref. [64].

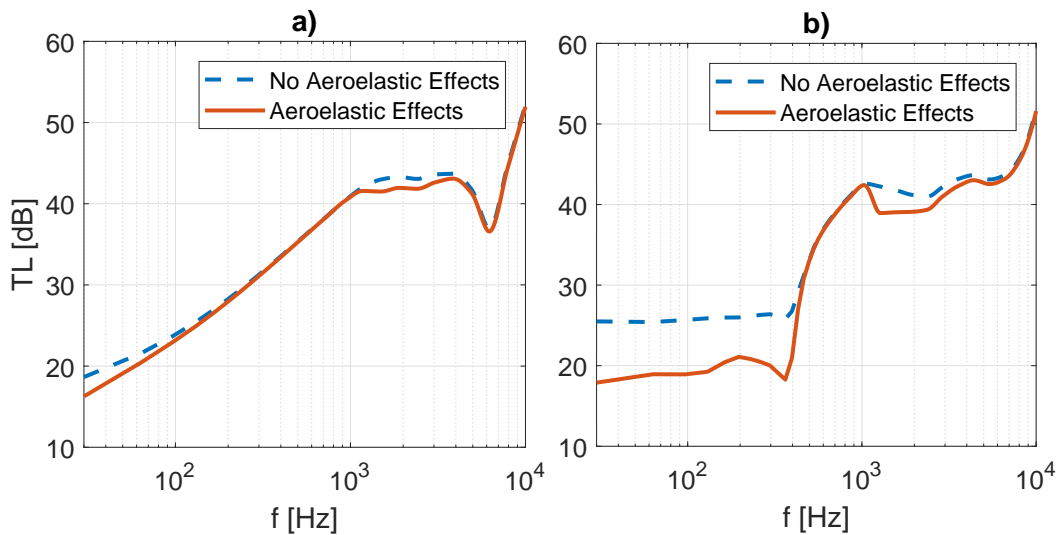


Figure 5.7: Sound transmission under a supersonic turbulent boundary layer load (Mach 1.35): a) Flat Panel ( $0.5 \times 0.3 \text{ m}^2$ ); b) Curved Panel ( $0.5 \times 0.3 \text{ m}^2$ ; 2m curvature)

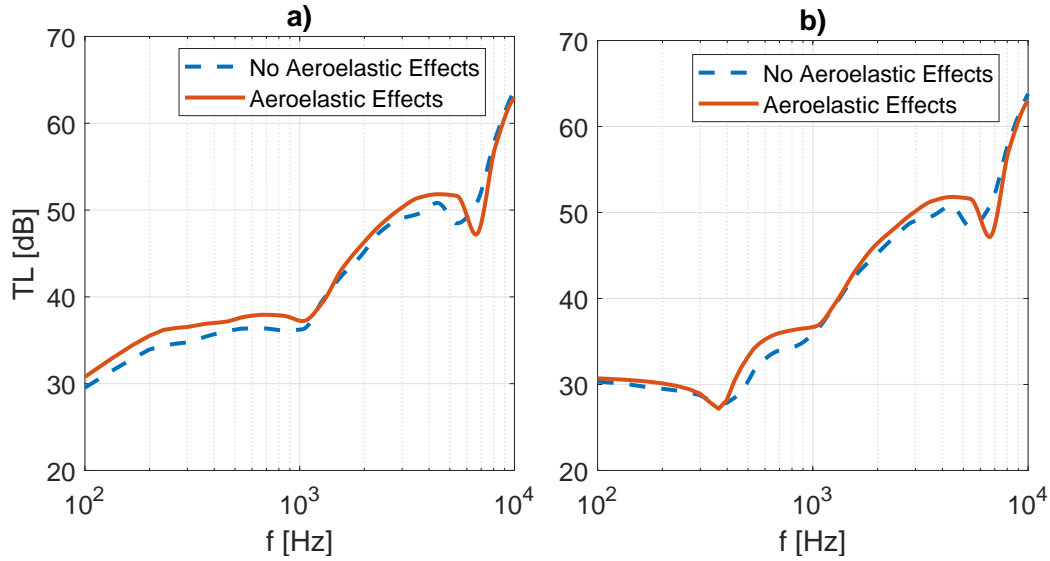


Figure 5.8: Sound transmission under a subsonic turbulent boundary layer load (Mach 0.5): a) Flat Panel ( $0.7 \times 0.5 \text{ m}^2$ ); b) Curved Panel ( $0.7 \times 0.5 \text{ m}^2$ ; 2m curvature).

Table 5.1: Materials' properties of the sandwich plate.

	Skins	Core
$E_1$ (GPa)	69.0	0.3
$\nu_{1,2}$	0.33	0.2
$\rho$ (Kg/m <sup>3</sup> )	2742	48
Thickness (mm)	1	10

band. The aeroelastic effects induce a slightly higher transmission loss and a shift of the aerodynamic and acoustic coincidence to higher frequencies. It is a classic *mass addition* effect, that, in term of elastic waves, can be read as a monotonic increase of bending waves' wavenumbers versus frequency.

It must be underlined that the physical mechanism that induces an increase of the wavenumbers (or reduction of bending wave speed) in the structure, is different between the supersonic and subsonic aerodynamics. While in the first case, a reduction of dynamic stability plays a role (travelling flutter [56]), in the subsonic case is physically similar, as said, to an added mass effect. In the latter case, given the aerodynamic model applied here, the effects of the presence of the mean flow might be neglected.

A more complex example is illustrated in Fig. 5.9 with a sandwich panel under a subsonic turbulent boundary layer; the material data are in Table 5.1. The mean-flow effects are observable in the whole frequency range and differently from the simple aluminium panel, the effects at higher frequencies seem to reduce the sound transmission loss. As expected (see Ref. [166]) the accuracy of the approach in the lowest frequency ranges is reduced. The present approach, in fact, considers a wave propagation to the infinite and does not take into account the boundaries of the finite structure (see Ref. [166]). One-dimensional wave-based finite element approaches (see Ref. [107]), on the contrary, can account for boundaries but require a higher computational cost. A comparison with a classic FEM approach (Ref. [107]) is also proposed in terms of computational cost in Table 5.2.

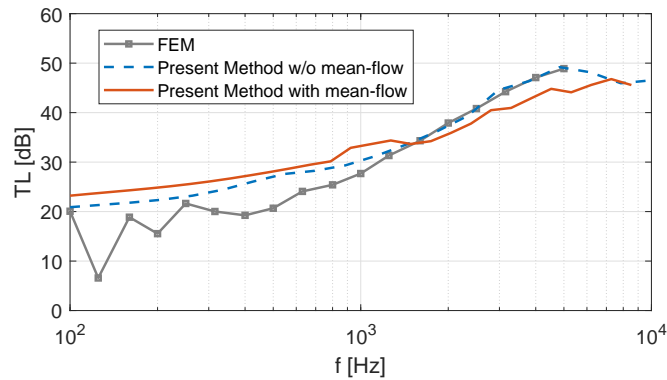


Figure 5.9: Sound transmission loss of a sandwich flat panel ( $0.8 \times 0.6 \text{ m}^2$ ) under a subsonic turbulent boundary layer load at Mach 0.62.

Table 5.2: Computational cost comparison for an Intel(R) Core(TM) i7-7700 CPU 3.60GHz processor (16Gb RAM).

Method	Model	DoFs	Time/freq [sec]	Reduction Ratio
FEM (Ref. [107])	Full	$120 \times 10^3$	440	–
Present Approach	Unit-cell	888	35	12.6

## 5.4 Conclusion

A procedure to account aeroelastic effects in the computation of dispersion curves and sound transmission of panels and shells is developed. The structural framework is based on the wave finite element method. The modelling of a single elementary cell is needed; homogeneous and multi-layered plates and shells can be studied with a reduced computational effort.

Once an aerodynamic theory is used, the components of the load connected to the pressure fluctuations that are produced by the motion of the flexible body, are described developing temporal and spatial derivatives in a periodic framework; the convective terms become function of the elastic waves' propagation constants and are injected in the new dynamic stiffness equation of the system.

A validation of the method is proposed using literature results for the travelling flutter of infinite thin plates. The supersonic flow effects on the bending waves of a plate and shell are studied. The resulting sound transmission, under turbulent boundary layer excitation, is computed and compared to the one in absence of flow. A similar study, with subsonic flows is also presented. Different effects are observed in the low frequency region and around the acoustic coincidence.

## Chapter 6

# Periodic Design for Reduced Sound Radiation

Three design investigations are carried out in this chapter. The first one, which is mainly experimental, is conducted on flat sandwich panels with acoustic excitation. The following two investigations are numerical and are focused on ribbed and sandwich curved panels under acoustic and aerodynamic load.

In the case of flat structures, a design investigation on two types of sandwich panels is performed using the periodic structure theory. A double-wall panel with mechanical links and a sandwich panel with rectangular core are studied. The elastic bending waves' propagation versus the acoustic wavenumbers is trimmed using folded and corrugated core walls, trying to keep the same mass and compression stiffness of the original configurations. Standard and proposed configurations are 3D-printed and sound transmission measurements are conducted using a facility with an uncoupled reverberant-anechoic configuration. The experimental evidences of enlarged bending band-gaps and deformation mechanisms are proved using a reverse approach based on the acoustic radiation of the panels.

For curved panels and shells, a first investigation is carried out on the effects of axial and ring stiffeners on the acoustic response of the panels. The effects of the stiffening direction are analysed and compared for diffuse acoustic and turbulent boundary layer excitation; physical explanations are given using the wavenumber domain. The effect of the pitch distance on sound radiation is also investigated.

Secondly, the use of periodic embedded resonators in curved panels under turbulent boundary layer is explored by tuning single or multiple resonant elements inside the core. Again a double wall panel is analysed in addition to a sandwich design with auxetic core. The resonant elements are analysed in different tuning combination to investigate the effect on the aerodynamic coincidences and the ring frequency of the shell. The advantages regarding the sound transmission and the cost associated to the added-masses of the periodic resonators, are also discussed

In the first two cases, the waves are tailored following the needs. In particular, the Bragg band-gap mechanism is targeted, especially in the case of the double-wall panel with mechanical links. Differently, in the last case, when using resonant elements, the resonance-induced local band gaps are investigated.

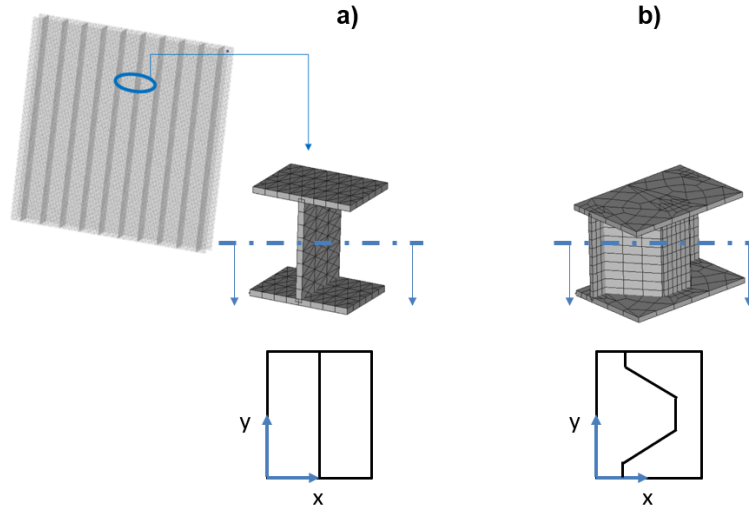


Figure 6.1: Cell models extracted from a Double-Wall Panel with Mechanical links. a) Standard design. b) Proposed Design.

## 6.1 Corrugated-Walls Design for Sandwich Panels

A core design with corrugated walls is here proposed for two classic types of sandwich panels. First a double-wall panel with rectilinear mechanical links (Fig. 6.1a) is analysed for a trapezoidal shape of the stiffener (Fig. 6.1b). A similar idea has been applied to a sandwich panel with rectangular core (Fig. 6.2a), where the core walls have been folded in one direction (Fig. 6.2b). Full geometrical details of the proposed cell designs are given in Appendix A.

The frequency band targeted for the optimization is 600 Hz to 10 kHz, corresponding to the frequency range of reliability of the measurements, for the facility used within this work.

### 6.1.1 Double-Wall Panel with Mechanical Links

The initial double-wall panel studied (Fig. 6.1a) is 1.06 cm thick (total thickness) has a 1.0 cm spacing between consecutive stiffeners, in the periodicity direction (axis  $x$  in Fig. 6.1). The thickness of the skins and core walls is 0.6 mm. A unit cell, as the one illustrated in Fig. 6.1a, is modelled with finite elements (ANSYS Shell181) and the eigenvalue problem developed in Chapter 2 solved to get the wave dispersion in the media.

The modified design, proposed here for increasing the flexural band-gap region versus frequency, in the periodicity direction, is characterised by a trapezoidal (top-view) shape of the stiffer (Fig. 6.1b). The same global thickness and stiffeners' spacing as the classic double-wall panel is used; the skins are 0.6 mm-thick and the core walls are 0.45 mm-thick, in order to keep the same mass of the system. The idea of using such a geometrical shape comes from the usually low bending and shear stiffness of this kind of panels in the direction normal to the stiffener envelope (axis  $x$ ). The addition of oblique elements, periodically repeated in the  $x$ - $y$  plane due to the periodicity of the system, has a main function: the core shear stiffness increases with respect to the classic design where the bending of the mechanical link was proving the whole core-shear stiffness in the  $x$  direction.

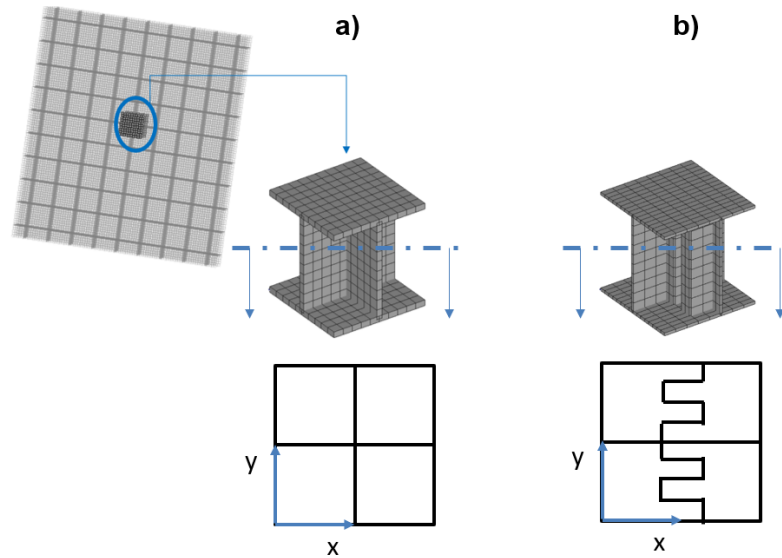


Figure 6.2: Cell models extracted from a Sandwich Panel with Rectangular Core. a) Standard design. b) Proposed Design.

### 6.1.2 Rectangular-Cored Sandwich Panel

For the rectangular-cored panel, the initial design (Fig. 6.2a) has a total thickness of 1.06 cm and a 1.0 cm spacing between consecutive stiffeners, in both directions (Fig. 6.2a). As for the double-wall panel, both skins and core-walls are 0.6 mm-thick. Similarly to the previous case, the modified design proposed here is characterised by a trapezoidal (top-view) shape of the stiffener in one direction (axis  $y$  in Fig. 6.2b), while the rectilinear geometry is kept in the other direction. To keep the same mass, global thickness and stiffeners spacing of the original system, the skins are 0.6 mm-thick and the core walls are 0.36 mm-thick. Hereby, the target is to tailor the elastic waves dispersion in the panel, against the acoustic wavenumbers. Differently from the previous case, the presence of additional components of the stiffener in the  $x$  direction (Fig. 6.2b) does not have the function of increasing the core-shear stiffness. The idea is to induce a larger deformation mechanism for the folded core walls both for bending in  $y$  and core-shear in  $x$ .

### 6.1.3 Experimental Set-Up

The work flow followed for the study and testing of the presented corrugated-walls based designs is illustrated in Fig. 6.3. Using the method described in Section 4.2, the numerical dispersion curves and transmission loss are computed and compared. Then, a CAD model is developed and transformed into a CAM input file for a Stratasys *Fortus 450mc* industrial 3D-printer with a maximum printable volume of  $40 \times 35 \times 40 \text{ cm}^3$  (Fig. 6.3). The material used for the modelling and 3D-printing of the panels is the ABS-M30 (Acrylonitrile butadiene styrene) [173]. The material was experimentally characterised and has the following properties:  $E = 1.8 \text{ GPa}$ ;  $\rho = 988 \text{ kg/m}^3$ ;  $\nu = 0.32$ . Both the 3D-printed panels with standard and proposed designs are shown in Figs. 6.6 and 6.7.

The sound transmission measurements were performed in an un-coupled reverberant-anechoic room as in Fig. 6.4. The reverberant room has volume of  $2.50 \times 1.40 \times 1.75 \text{ m}^3$ . The mea-

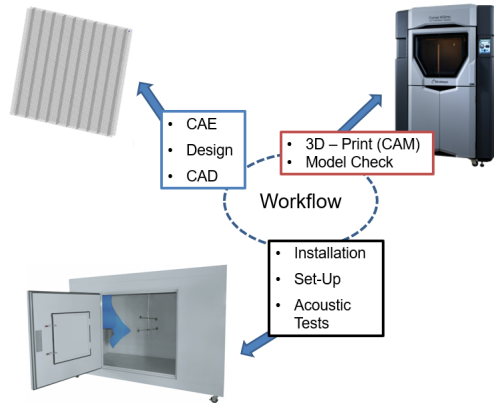


Figure 6.3: Work-flow scheme for panel design optimisation based on numerical and experimental data.

sured reverberation time ( $T_{60}$ ) of 2.75 s, at to 1000 Hz: the calculated Schroeder frequency is  $\approx 1.3$  kHz [163]. The acoustic excitation is generated using four speakers installed at the four top corners of the reverberant room, with an uncorrelated white noise input from 50 to 10 kHz.

The transmitted sound power is measured using a Bruel & Kjaer sound intensity probe with two half-inch microphones and a 6.0 mm spacer (see Figs. 6.4 and 6.5). The incident sound power is obtained by the sound pressure level measurements in the cabin room, averaged among four half-inch microphones disposed as in Fig. 6.4. The anechoic conditions of the receiving room are simulated by covering the room walls with absorbing layers, whose distance from the tested panel is larger than 2 m. The sound transmission loss (TL) is finally calculated, assuming that the excited and radiating surfaces are the same, as:

$$TL = L_p - L_i - 6.18, \quad (6.1)$$

where  $L_p$  is the average pressure level measured in the reverberant room,  $L_i$  the average sound intensity level over the surface of the test-panels in the semi-anechoic room, while the -6.18 factor arises from reference values in dB conversion [164].

#### 6.1.4 Waves Tailoring versus Acoustic Wavenumbers

The approach presented in Chapter 2 is used for studying the waves' propagation in the periodic structures proposed in Section 6.1. the main idea is to evidence two phenomena: an increase of the bending band-gap in the periodicity direction, for the double-wall panel with mechanical links; an increase of bending wavenumbers versus the acoustic ones, for the sandwich panel with rectangular core.

In Fig. 6.8, the dispersion curves for the two designs illustrated in Fig. 6.1 are compared in the direction orthogonal to the stiffening elements. The band-gap present in the standard design (standard Band-Gap in Fig. 6.8) extends from 3.3 kHz to 5.4 kHz and an acoustic coincidence is observed around 8.4 kHz. Differently, for the proposed design proposed in Fig. 6.1, the band-gap is strongly enlarged in frequency from 3.6 kHz to 9.1 kHz, while a coincidence is observed only at the end of the frequency band of interest ( $\approx 10$  kHz). A double advantage is thus observed both in structural waves' filtering (band-gap) and coincidence shift, keeping the same mass of the system.

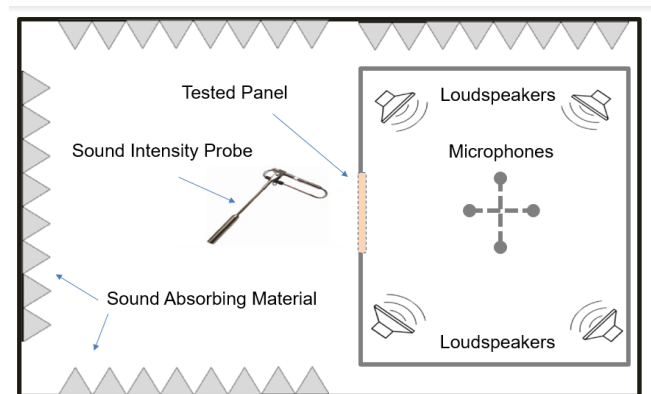


Figure 6.4: Illustration of the test facility with un-coupled reverberant-anechoic rooms for transmission loss measurements.



Figure 6.5: Facility and frame details: a) wooden external adaptive frame; b) clamping system on the internal chamber side; c) view of the open room with reflective panels and microphones.

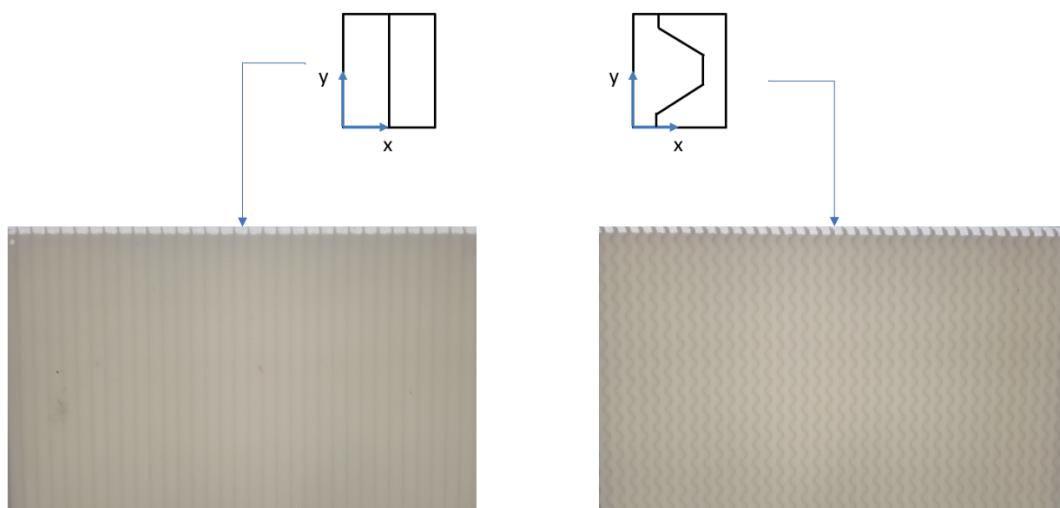


Figure 6.6: The 3D-printed panels front-view following the standard (left) and proposed (right) designs for the double-wall panel with mechanical links.

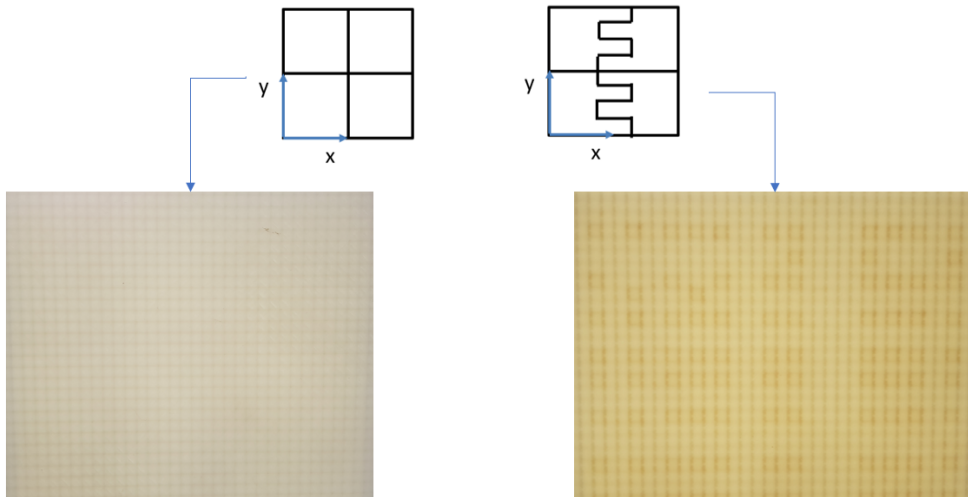


Figure 6.7: The 3D-printed panels front-view following the standard (left) and proposed (right) designs for the sandwich panel with rectangular core.

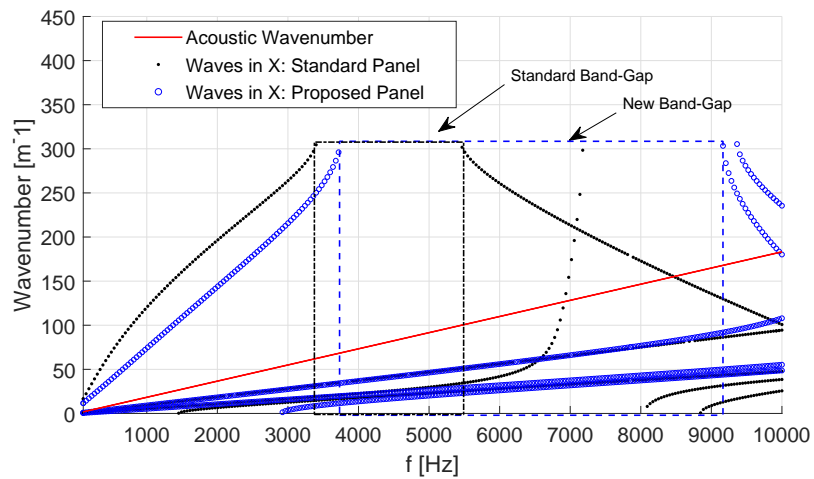


Figure 6.8: Dispersion Curves of the Double-Wall Panel designs; eigenvalue solutions of the eigenvalue problem in Eq. 4.2.

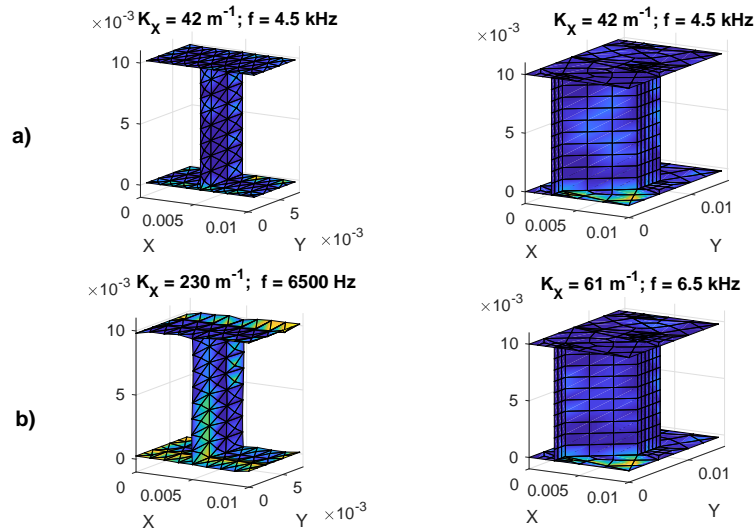


Figure 6.9: Wavemodes of the Double-Wall Panel designs for waves propagating in  $x$  direction; eigenvector solutions of the eigenvalue problem in Eq. 4.2. a)  $f = 4.5$  kHz; b)  $f = 6.5$  kHz.

In Fig. 6.9 the eigenvectors of Eq. 4.2, which represent wavemodes of the wave-type propagating in the media with the wavenumbers of Fig. 6.8, are showed for two frequencies. In particular, the wavemodes with the highest wavenumbers of the set of waves propagating at 4.5 kHz and 6.5 kHz are shown for the two designs in Fig. 6.1. It is interesting to observe how, in Fig. 6.9, the cell modal wave deformations are completely different. The increase of core-shear stiffness in the periodicity direction, for the proposed design, induces almost null modal out-of-plane displacements of the skin surfaces. In opposition, the wavemodes of the classic design still present mode-shapes efficient for sound transmission (non-null out-of-plane displacements).

Differently, for the classic sandwich panel with rectangular core, band-gaps are not present in the frequency range of interest (see Fig. 6.10). Here, a coincidence effect is not observed, but the bending waves follow closely and almost parallel the acoustic wavenumbers versus frequency. This means that the sound transmission loss is expected to be reduced in a large frequency bandwidth.

The target of the proposed design, in this case, was to distance the structural and acoustic wavenumbers for a large frequency band, by inducing a larger deformation mechanism of the folded core walls. Coherently, in Fig. 6.10, the waves' dispersion, both in  $x$  and  $y$  directions, is characterised by higher wavenumbers: the larger distance from the acoustic ones is expected to induce an enhanced sound transmission loss. In addition, a band-gap formation in  $x$ , at the end of the frequency band, is also observed for the proposed design. The wave shapes in  $x$  (wavemodes) at 4 and 6 kHz are presented in Fig. 6.11 for bending waves. As said before, the folded walls design offers a larger core deformation mechanism and this is clearly observable in Fig. 6.11 for both frequencies: a part of the vibrational energy is absorbed through the core deformation. In this way, the shear core waves reduce their speed and the corresponding wavenumbers increase, as targeted.

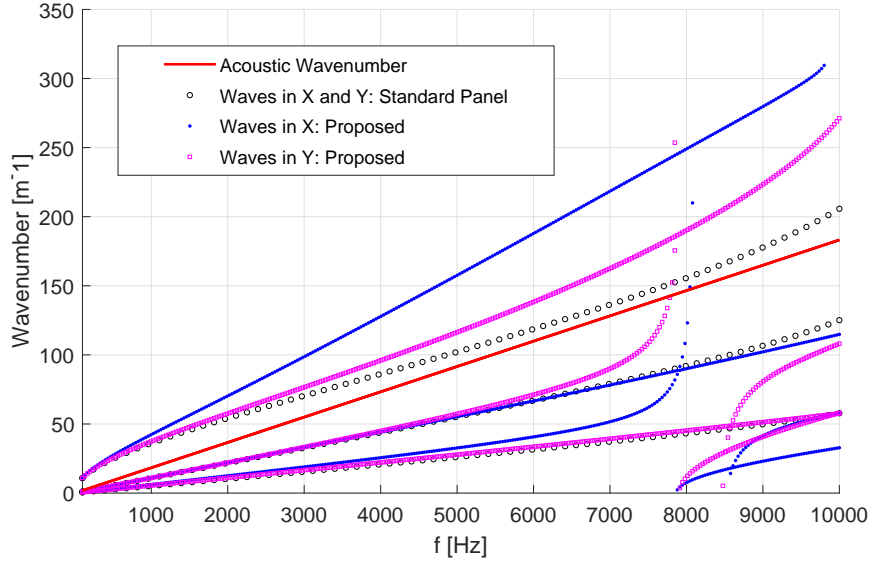


Figure 6.10: Dispersion Curves of the Sandwich Panel with Rectangular core designs; eigenvalue solutions of the eigenvalue problem in Eq. 4.2.

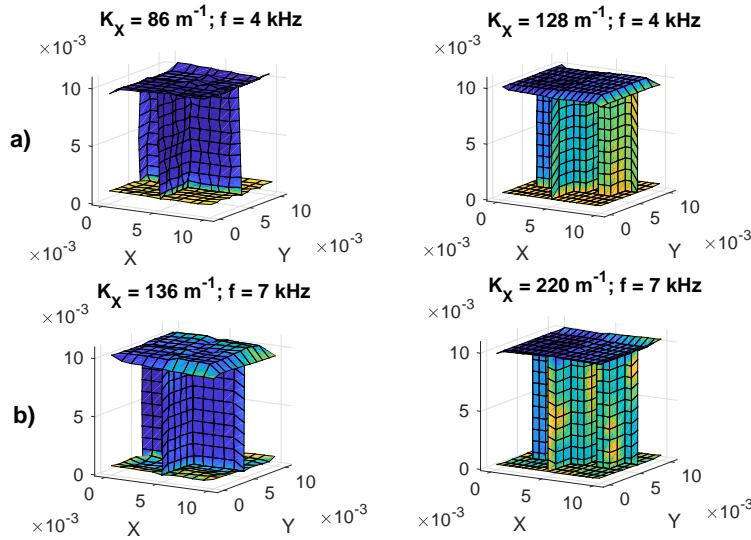


Figure 6.11: Wavemodes of the Sandwich Panel with Rectangular core designs for waves propagating in  $x$  direction; eigenvector solutions of the eigenvalue problem in Eq. 4.2. a)  $f = 4.0$  kHz; b)  $f = 6.0$  kHz

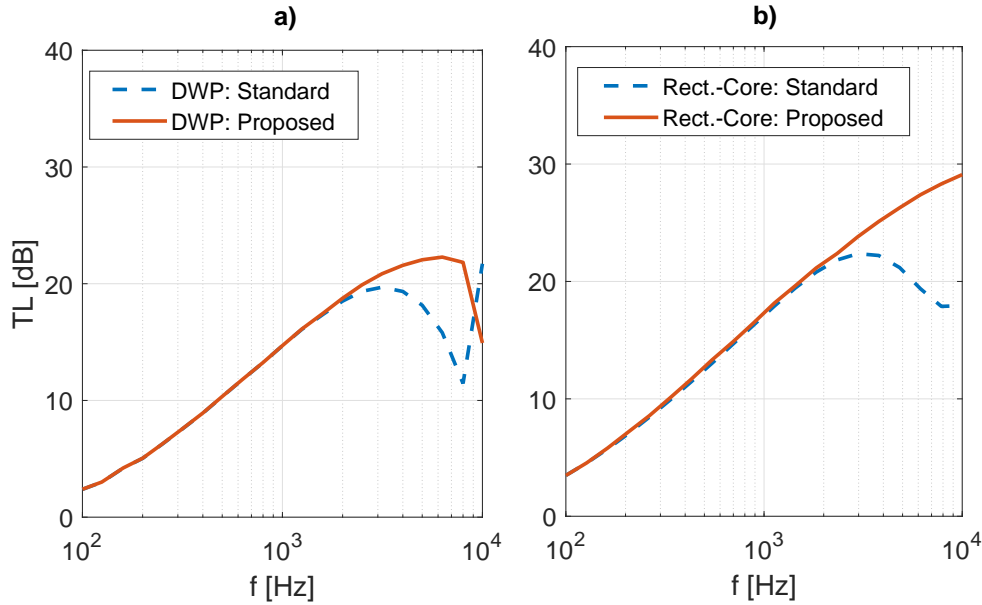


Figure 6.12: Calculated Transmission Loss for infinite panels the proposed designs. a) Double-Wall panels designs; b) Rectangular-Cored Sandwich panel designs.

### 6.1.5 Sound Transmission Loss under DAF excitation

The sound transmission loss of the two couples of designs is numerically simulated for equivalent infinite panels. The effects of the design optimisation, observed in terms of waves in Figs. 6.8 and 6.10, are specular in the transmission loss curves presented in Fig. 6.12. In Fig. 6.12a, the double-wall panel with mechanical links is studied and the effect of the enlarged band-gap effect is visible in shifting the coincidence frequency: starting from 1.5kHz, the sound transmission loss of the proposed panel is constantly larger than the one of the standard plate design with the same mass.

On the other hand, in Fig. 6.12b, as observed from the dispersion curves, while a real coincidence region is not observed for the standard sandwich plate design, a drop of the transmission loss is still evident due to the proximity of the structural and acoustic wavenumbers/wavelengths. Differently, for the proposed design, the induced distance of structural and acoustic wavenumber results in a constant increase of the sound transmission loss versus frequency, in absence of evident drops: from 1.5 kHz to 10 kHz, the new design assures a larger sound transmission loss with the same global mass of the panel.

To experimentally prove the increase of sound transmission loss for the proposed designs, the 3D-printed panels are installed and clamped in the TL facility, as in Fig. 6.4. The expected and real weights of the printed panels are reported in Table 6.1. It is observed in Table 4.1 that, when the geometrical complexity of the single cell design increases (proposed designs), the discrepancies between the expected and real weight of the 3D-printed panels increases too. To compare mass-normalised results, the approach proposed by De Rosa in [174] is used to scale the measured transmission loss curves of the proposed panels versus the ones of the lighter (standard; see Table 6.1) panels.

In Fig. 6.13, the measured sound transmission losses of the two design couples proposed in Section 6.1 are compared. While the total surface of the plates is  $0.40 \times 0.35 \text{ m}^2$ , the

Table 6.1: Expected and Measured weights of the 3D-printed panels

	Expected [gr]	Measured [gr]	Difference [%]
Standard (Fig. 6.1a)	246	245	- 0.4
Proposed (Fig. 6.1b)	246	287	+ 16.6
Standard (Fig. 6.2a)	341	346	+ 1.4
Proposed (Fig. 6.2b)	342	360	+ 5.3

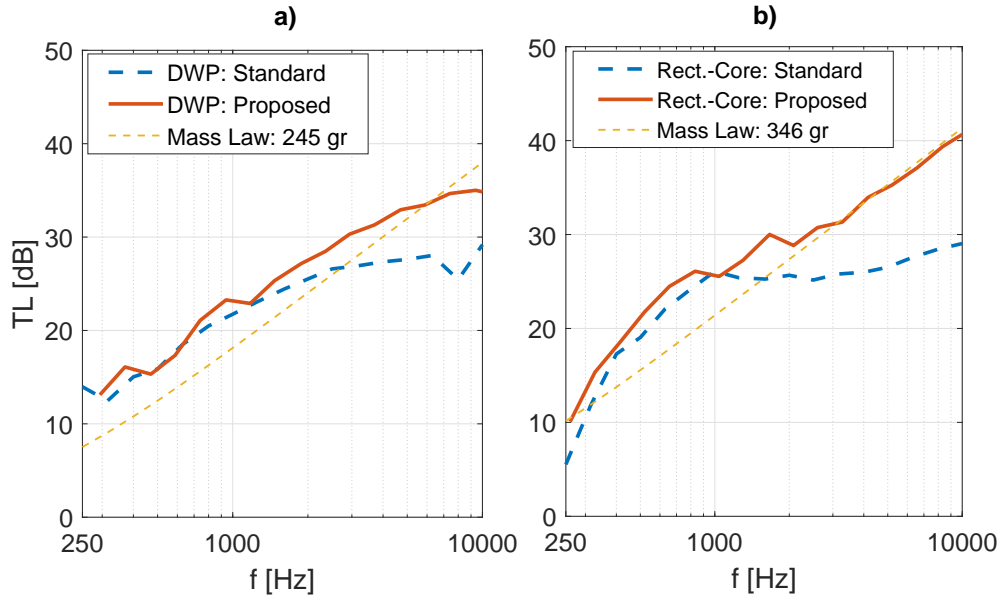


Figure 6.13: Measured Transmission Loss for the 3D-printed panels. Total panel surface:  $0.40 \times 0.35 \text{ m}^2$ . Exposed panel surface:  $0.34 \times 0.29 \text{ m}^2$ . a) Double-Wall panels designs; b) Rectangular-Cored Sandwich panel designs.

exposed panel surface is  $0.34 \times 0.29 \text{ m}^2$ . In Fig. 6.13a, the measured sound transmission loss trends are strongly in accordance to the simulated ones for an equivalent infinite plate in Fig. 6.12a: as expected, the increase of sound transmission loss starts from 1.5 kHz and continues up to the end of the frequency band of interest. It must be highlighted that the damping induced by the 3D-printing, the installation and the clamping in the TL cabin might be high. It is also observed by the measured transmission loss curve around the coincidence region ( $\approx 8.4 \text{ kHz}$ ) for the standard DWP in Fig. 6.13a, with respect to the simulated drop in Fig. 6.12a.

Similarly, in Fig. 6.13b, the same trends of the simulation Fig. 6.12b, for the sandwich plate with rectangular core, are experimentally observed. Again, the reduction of transmission loss expected for the standard design is highly damped with respect to the simulation. The agreements is, however, satisfying and validates the expected trends versus frequencies. The increase of sound transmission loss, as in the previous case, appears in a very large frequency band that goes from 1 kHz to 10 kHz, at least, for a fixed mass of the panel.

Although there is a general agreement between expected results and experimental evidence, some discrepancies are present. For example, in both cases the sound transmission loss increase starts in frequencies a bit lower than the expected ones. This should be addressed

to two factor that act simultaneously. First, as discussed before, the Schroeder frequency of the TL cabin ( $\approx 1.3$  kHz) is very close to the expected frequency of transmission loss increase (in both cases  $\approx 1.5$  kHz) and a this can have an influence on the reliability of the measurements in that low frequency bands. In addition to that, the uncertainties connected to the 3D-printing and the effective differences among the ideal models and the real structures are not perfectly controlled and might, obviously, induce discrepancies by the predictions and the measurements.

## 6.2 Axial and Ring Stiffening of Curved Panels

A bare test case panel is considered, then a periodic distribution of stiffeners is applied in the axial and in the circumferential directions, separately. The curvature radius  $R = 1.0$  m and thickness equal to 1.2 mm. The material properties are chosen similar to a standard aeronautical aluminum alloy, with Young's modulus  $E = 70.0$  GPa, mass density  $\rho = 2700.0$  kg m<sup>-3</sup> and Poisson coefficient  $\nu = 0.33$ . From this properties, the ring frequency (the frequency at which the longitudinal wavelength is equal to the vehicle circumference and it coincides with the first extension mode) results equal to:

$$f_R = \frac{1}{2\pi R} \sqrt{\frac{E}{\rho}} = 800 \text{ Hz.} \quad (6.2)$$

The FE model is built using solid structural elements (ANSYS SOLID73). For the stiffeners three different cross-sections are analysed: *T*-, *H*- and  $\Omega$ -*shape*, as shown in Fig. 6.14; the cross-section properties are listed in Table 6.2. The stiffeners are modelled trying to keep constant the cross-section properties, in particular the Moments of Inertia, choosing the *T*-*shape* as reference. All the stiffeners are built using the same element property and the same material employed for the skin.

The periodic stiffeners are placed in the axial and in the circumferential direction, as shown in Fig. 6.15 respectively. The effect of the shape on the vibroacoustic response is analyzed keeping equal to 6 cm the stiffeners inter-spacing.

### 6.2.1 Effects on the Sound Transmission Loss

In this section the effects of the different stiffeners are evaluated in terms of sound transmission. The numerical approach adopted for the acoustic simulations is given in [175, 176]. The structure is modelled using a periodic cell approach and using ANSYS SOLID45 elements. The calculations are carried out considering two excitation models: a purely diffuse acoustic field (DAF) and a simultaneous presence of a diffuse acoustic field and a turbulent boundary layer (DAF + TBL) to simulate more realistic loading conditions in some transportation sectors. The hypothesis of semi-infinite fluid termination is applied in the

Table 6.2: Cross-section properties of the stiffeners.

	<i>T</i> - <i>shape</i>	<i>H</i> - <i>shape</i>	$\Omega$ - <i>shape</i>
Cross-section Area [m <sup>2</sup> ]	$3.46 \cdot 10^{-5}$	$3.70 \cdot 10^{-5}$	$2.78 \cdot 10^{-5}$
Moment of Inertia, $I_{xx}$ [m <sup>4</sup> ]	$2.54 \cdot 10^{-10}$	$2.85 \cdot 10^{-10}$	$2.61 \cdot 10^{-10}$
Moment of Inertia, $I_{yy}$ [m <sup>4</sup> ]	$8.01 \cdot 10^{-10}$	$8.11 \cdot 10^{-10}$	$7.87 \cdot 10^{-10}$

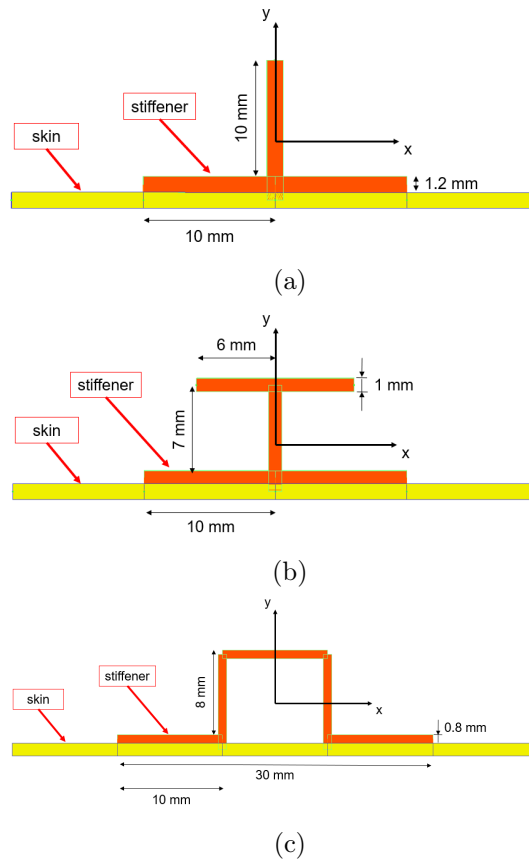


Figure 6.14: Front view of the stiffeners cross-section: a) *T-shape*; b) *H-shape*; c)  $\Omega$ -*shape*.

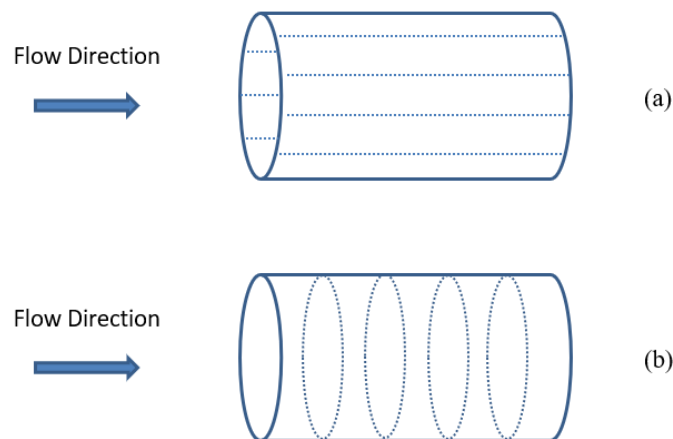


Figure 6.15: Direction of the flow on the shell for: a) Axial stiffeners; b) Ring Stiffeners.

internal radiating domain and thus single acoustic cavity modes are not considered while a band-averaged result (in classic SEA fashion) are given [175]. The numerical approach proposed is validated with measurements of real ribbed aircraft panels by Errico et al [176]. The three configurations described in Fig. 6.14, are analysed under a diffuse acoustic field in Fig. 6.16. Both configurations with axial and circumferential stiffeners are considered. In all cases, two phenomena are observed. First, as before, the ring frequency of the shell is reduced and thus the first drop of sound transmission loss is anticipated in the frequency band. At the same time, an increase of transmission loss is evident in the region before the ring frequency because of the strong stiffening of the structure compared to the bare test case.

Among all the configurations, the main differences between the axial and circumferential stiffening are observed for the  $H$  shape, in the whole frequency band after the ring frequency. Even though the differences are not important, the circumferential stiffening provides a slightly reduced sound radiation. Comparing the three shapes the  $T$  shape seems to provide a higher sound transmission loss than the other configurations in the band between 1000 and 2000 Hz.

Differently, when changing the excitation model as in Fig. 6.17, the differences between structures with axial and circumferential stiffeners became more important. The TBL model used is the one of Corcos [177], with flow direction always along the axis of the shell:  $U_c = 190$  m/s; stream-wise and cross-wise correlation coefficients equal to 0.125 and 0.81.

In contrast with the diffuse acoustic excitation, the convective nature of the TBL load requires stiffening elements in the direction of the flow; the axial stiffening provides a sound transmission loss at least 5 dB higher in the whole frequency band, as observable from Fig. 6.17. This can be explained by looking at the wavenumber transforms (see Fig. 6.18) of the structures in bare, axially-stiffened and ring-stiffened configurations. The response to turbulent boundary layer load, in fact, can be calculated starting from the product of the wavenumber transforms of the structure and the load model; the joint-acceptance is a fundamental parameter [178]. In Fig. 6.18 the wavenumber transforms show how the bare configuration is characterised by axially propagating waves (see Fig. 6.18a) with almost the same wavenumber as the convective ridge of the load model in Fig. 6.18d. At the same frequency, the ring stiffeners reduce the peaks of the circumferential wavenumbers in the circumferential direction by stiffening the structure (see Fig.6.18b); only small changes are present on the ones in the axial direction, that couple very well with the convective load. Differently, when axial stiffeners are adopted (see Fig.6.18b), the axial wavenumber peaks shift to lower frequencies (stiffer structure in this direction) and thus distance from the convective ridge of the TBL model at that frequency; the result is a reduced vibration and sound radiation of the shell.

It is also worth to observe how, with convective load, the  $\Omega$  shaped stiffeners give the better results, in Fig. 6.17, due to their higher torsional stiffness, that induced a reduced local bending of the skins that contributes to the sound radiation.

### 6.2.2 The effect of pitch distance on sound radiation

The effect of the pitch distance on the sound radiation is analysed here for the  $T$  shaped stiffeners. Two different inter-spacings are chosen: 6 cm and 10 cm. Again, both a pure diffuse acoustic excitation and turbulent boundary layer load are considered. The main differences observed are in the low-frequency region. A slight variation of the ring frequency is followed by a global reduction of sound transmission loss that eventually approaches the one of the un-stiffened shell for increasing pitch. This is of course given by the reduced

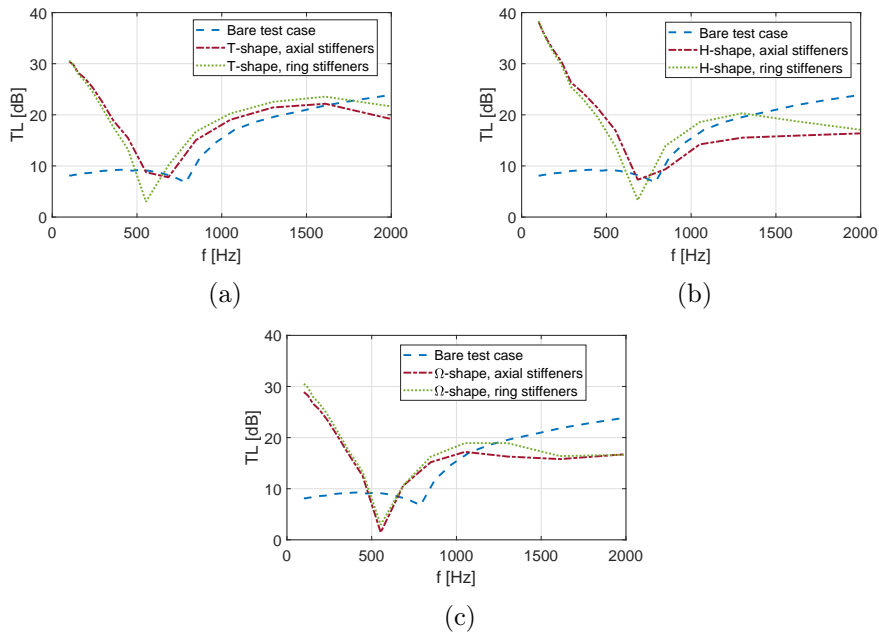


Figure 6.16: Sound Transmission Loss for the stiffened panels under DAF excitation: a) *T-shape*; b) *H-shape*; c) *Ω-shape*.

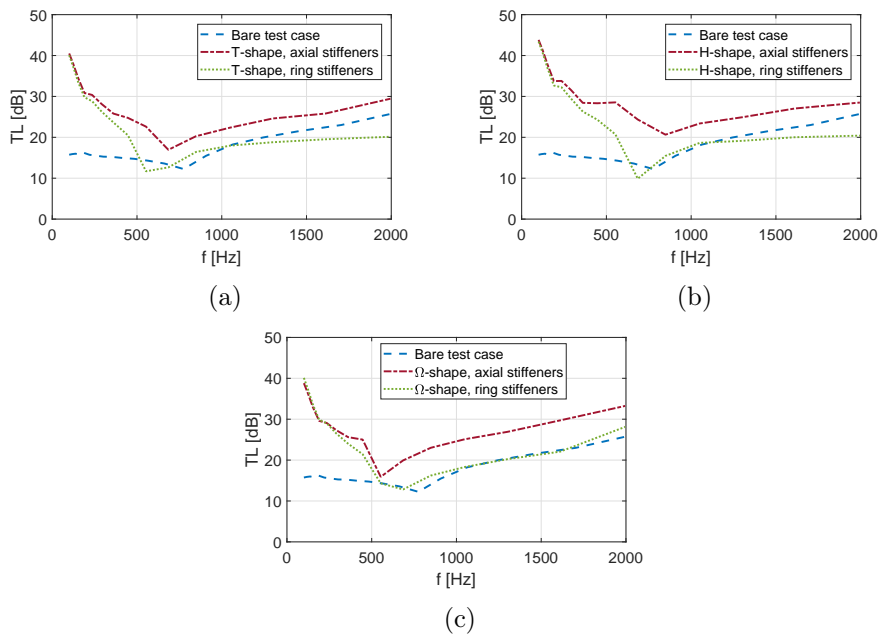


Figure 6.17: Sound Transmission Loss for the stiffened panels under DAF and TBL excitations: a) *T-shape*; b) *H-shape*; c) *Ω-shape*.

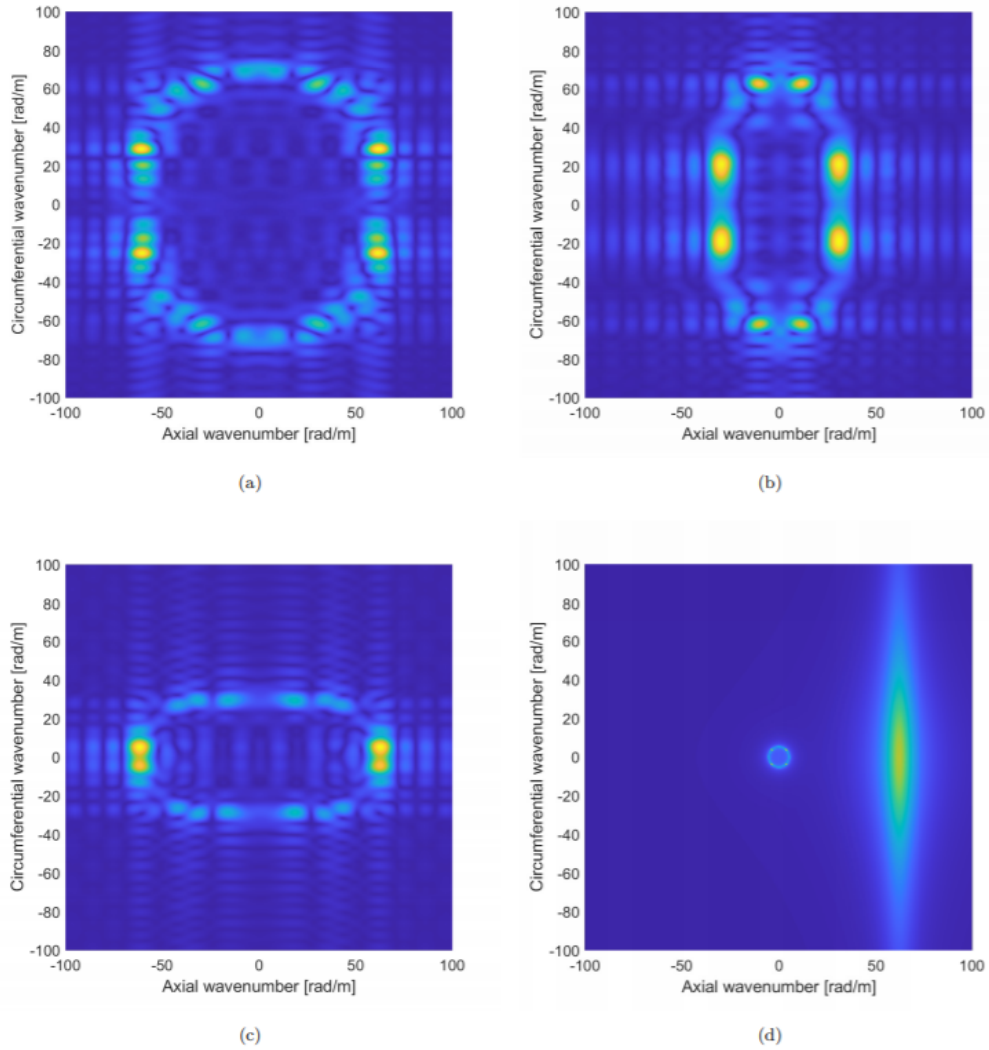


Figure 6.18: Wavenumber transforms for the structures and the load model at 1.5kHz: a) Unstiffened Shell; b) Shell with Axial  $T$  shaped Stiffeners; c) Shell with Ring  $T$  shaped Stiffeners; d) DAF and TBL load spectra.

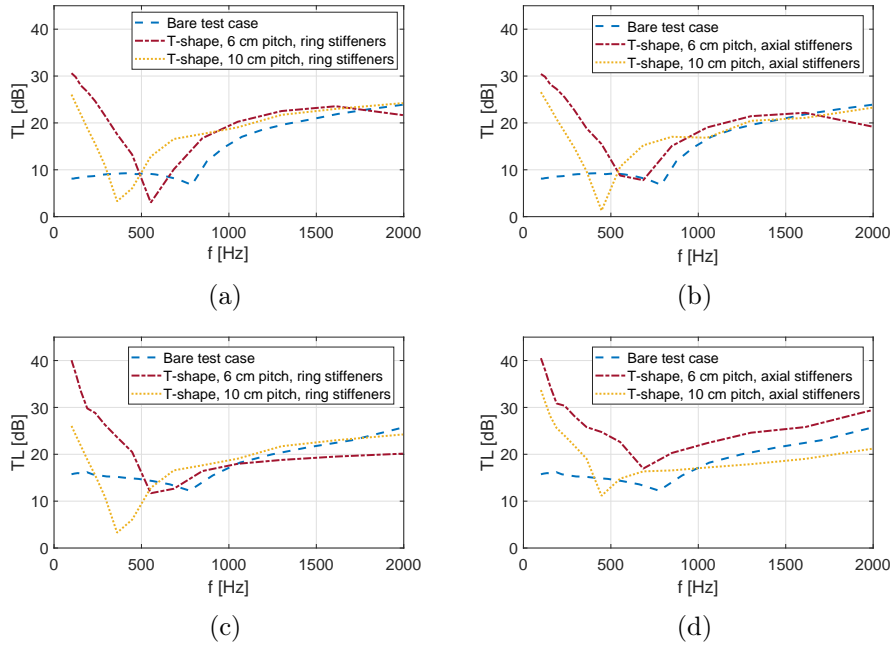


Figure 6.19: Sound Transmission Loss for the  $T$  shape stiffened panels with different pitch distances: a) Ring Stiffeners and DAF load; b) Axial Stiffeners and DAF load; c) Ring Stiffeners and DAF + TBL load; d) Axial Stiffeners and DAF + TBL load.

stiffening of the global structure compared to the cases with small pitch, as observed also in [144].

In particular, being the axial stiffening important when a turbulent boundary layer excitation is applied, the different pitches induce a frequency broadband variation of the sound transmission loss (see Fig. 6.19), in contrast to the mainly low-frequency effects in the cases of pure acoustic excitation (see Fig. 6.16).

### 6.3 Embedded Resonators in Curved Panels

As discussed in Chapter 2, the periodic mismatch of impedance typical in periodic media causes the phenomena of the Bragg scattering. In this Section, the resonance-induced band-gap mechanism is targeted to enhance the sound transmission loss of two types of structures.

#### 6.3.1 Resonators' Efficiency for Different Excitation Models

Depending on the excitation model assumed, the sound transmission loss of a panel changes. Similarly, the exotic nature of some excitation models might reduce the efficiency of the use of resonators. With reference to Eq. 4.21, each couple of forcing wavenumbers  $k_X$  and  $k_Y$ , contributes to the final transmission coefficient as a function of the weighting factors  $W_A(k_X, k_Y, \omega)$ . For a diffuse acoustic field, the integration scheme is equivalent to integrating all plane-wave inclinations [37]. In Fig. 6.23a, some acoustic plane-wave trace wavenumbers versus frequency are plotted with the flexural ones of a 2mm-thick aluminium plate; the coincidences shift depending on the inclination angle and the final coincidence we

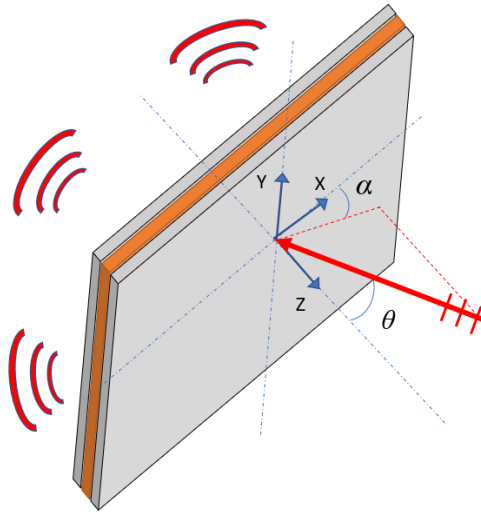


Figure 6.20: Illustration of the inclination of the single plane wave exciting the panel.

would obtain from integrating on every angle (Eq. 4.21), is the one given by assuming the acoustic wavenumber  $\omega/c_0$ , where  $c_0$  is the speed of sound in the media analysed.

This means that tuning a single resonator on a specific coincidence/inclination (see Fig. 6.20), even if the global one, means, averaging its increased sound transmission losses over a large number of cases where the resonator is "mis-tuned" and thus induces a lower transmission loss, as shown in [46]. The global advantages in using the resonant elements are attenuated (cancelled, in the worst cases), by the diffusiveness of the loading model. For example, in Fig. 6.21, the sound transmission of the auxetic-cored sandwich panel in Fig. 6.28, with a mis-tuned resonant element, is investigated for different angles of incidence. In any of the cases presented, the bad tuning of the first natural frequency of the resonator (bending mode) creates zones of increased TL, followed immediately by a reduction of TL; the effects is more or less evident depending on the inclination of the forcing plane waves (see Fig. 6.21). On the other hand, in Fig. 6.22, the sound transmission loss of an aluminium-made honeycomb panel is analysed by using a resonant element tuned on the acoustic coincidence of the panel; this configuration is here considered as properly-tuned since it is the only one that avoids any anti-resonance drop of the TL (see Fig.6.22a). However, as explained before, even in this "optimal" case, when changing the inclination of the plane waves, the effects typical of mis-tuned resonators appears; in a diffuse field, the excellent effects observable in Fig. 6.22a, are constantly integrated with many drops of TL that appear for most of other angles of incidence.

Differently, for a turbulent boundary layer model, the aerodynamic coincidence (or critical frequency; see Fig. 6.23b) is stream-wise filtered by the physical nature of the load itself. Similarly, the structural-induced acoustic drops, as for the ring frequency of shells/curved panels, are not dependent on any inclination. For these reasons, the use of simple resonant elements (as beams) to contrast these frequency-fixed issues, can be a valid approach; the resonators "mis-tuning" effects are somewhat damped with respect to the ones integrated for a diffuse acoustic field.

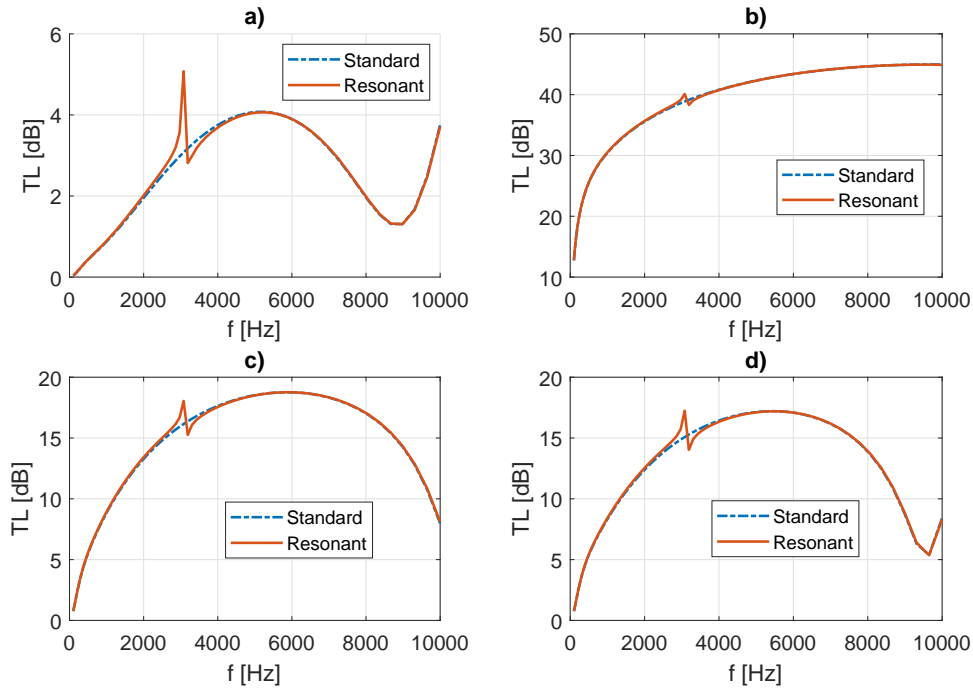


Figure 6.21: Sound Transmission Loss of for the auxetic-cored sandwich panel in Fig. 6.28 with a mis-tuned resonant element: a)  $\theta = \pi/2, \alpha = 0$ ; b)  $\theta = \pi/4, \alpha = 0$ ; c)  $\theta \approx \pi/2, \alpha = \pi/2$ ; d)  $\theta \approx \pi/2, \alpha = \pi/4$ ;

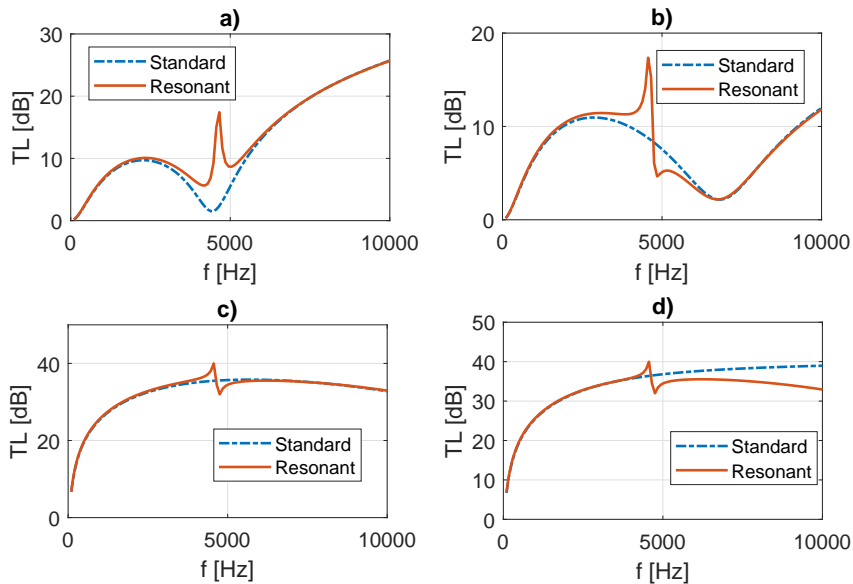


Figure 6.22: Sound Transmission Loss of for a 12mm-thick aluminium honeycomb panel with a properly-tuned resonant element: a)  $\theta \approx \pi/2, \alpha = 0$ ; b)  $\theta \approx \pi/2, \alpha = \pi/2$ ; c)  $\theta = \pi/4, \alpha = 0$ ; d)  $\theta = \pi/4, \alpha = \pi/2$ ;

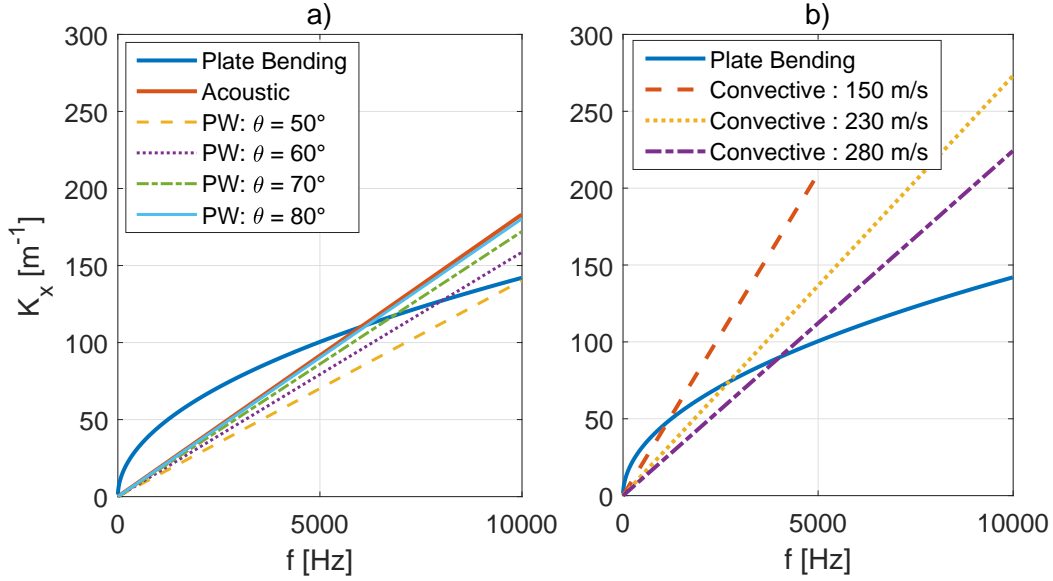


Figure 6.23: Dispersion Curves - The bending wavenumbers of a flat isotropic plate with: a) acoustic wavenumbers for different plane wave angles. b) convective wavenumbers for different flow speeds

### 6.3.2 Resonators' Efficiency around the Ring Frequency of Shells

Differently from the acoustic coincidences, that shift depending on the anisotropy and inclination of the plane waves, the ring frequency of a shell is an angle-invariant property and thus represents a tonal (fixed-frequency) problem in this context (see Fig. 6.24). For this reason, a resonant metamaterial can be easily tuned to absorb energy at that frequency. However, it is still important to evaluate the right direction of operation for this device.

In fact, the ring frequency can be identified as the first extensional mode of the shell along its circumference. Because of the coupling between bending and normal forces, this causes a breathing mode of the shell, as illustrated in Fig. 6.25. Two ideal resonant configurations are considered to test the efficiency of these devices in the ring frequency zone. Considering Fig. 6.25, the first resonant configuration explicitly targets the out-of-plane vibrations, while the second one targets the extensional vibrations caused by the ring mode.

In Fig. 6.26, the sound transmission loss of the three configurations of Fig. 6.25 is calculated and compared for different angles of plane-wave incidence. In both cases the resonant beams are tuned around the ring frequency ( $\approx 50$  Hz), but they operate along different directions, both involved in the ring mode of the shell. However, in terms of acoustic radiation, the only efficient one is the one acting on the out-of-plane displacements, as observable in Fig. 6.26. This can be explained by observing that, even though the resonant configuration acting for displacements along the circumference might damp the vibrations, still a resonance condition (steady mode) is present for the acoustic cavity, while, in the other configuration acting specifically on the out-of-plane displacements, the ring mode can be almost suppressed at that frequency. Thus the TL strongly increases at the resonance condition of the beams.

In the next proposed analyses, when targeting the ring frequency of the shell using resonators, the configuration denoted by *Resonator 1* in Fig. 6.25 is used.

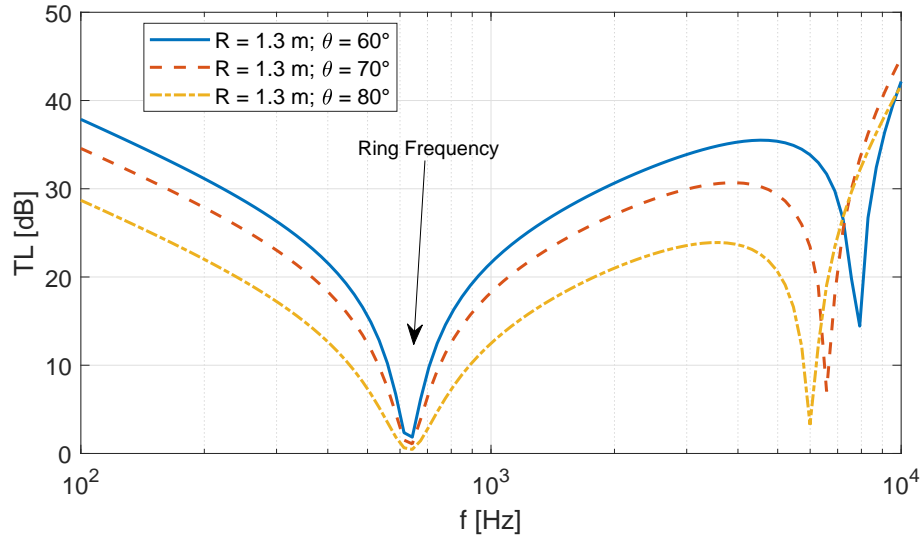


Figure 6.24: The sound transmission loss of a shell for different angles of incidence.

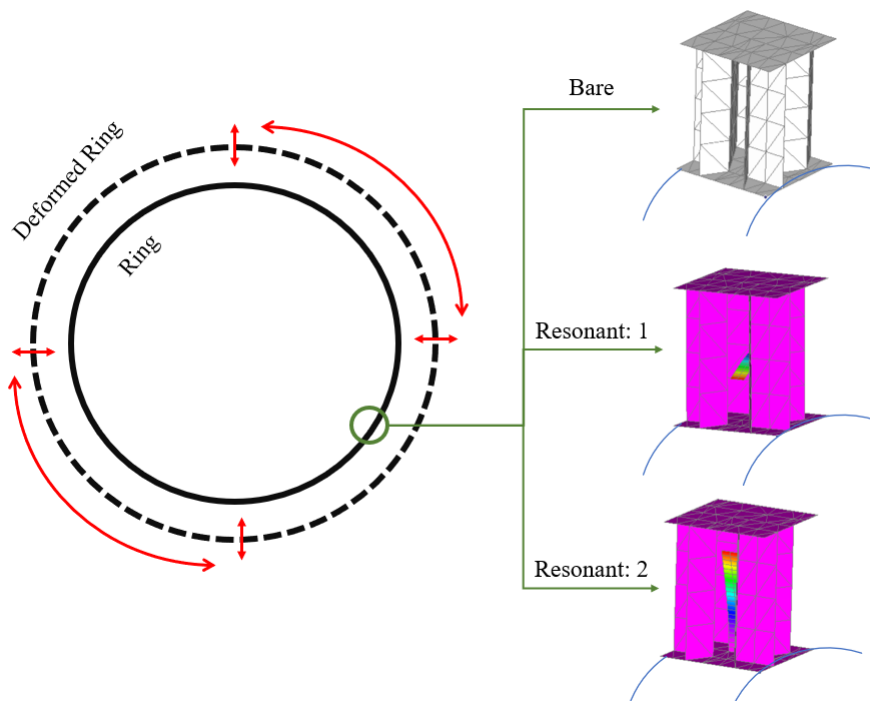


Figure 6.25: Illustration of ring mode of a shell (a) and the potential applications for resonant metamaterials (b).

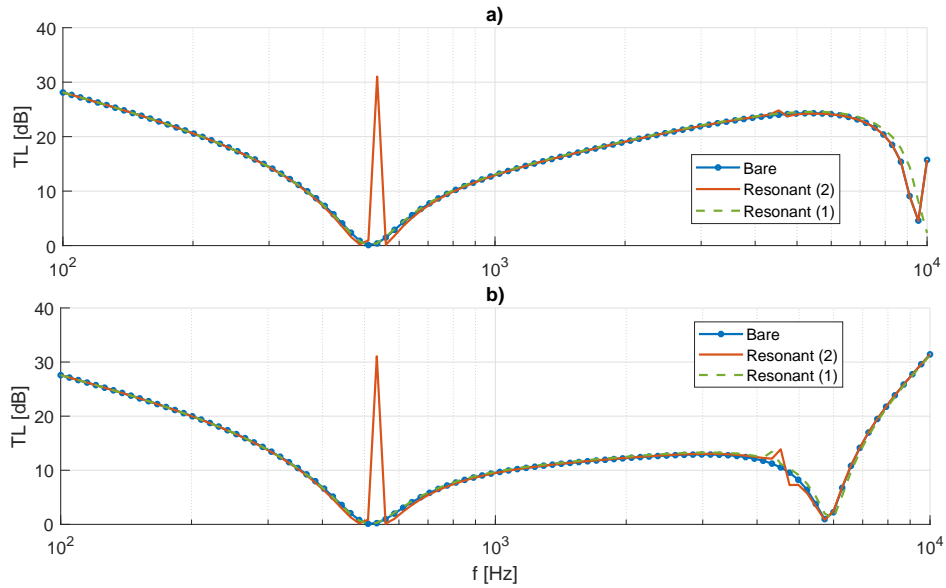


Figure 6.26: The sound transmission loss of a curved shell with embedded resonators as in Fig. 6.25: a)  $\theta \approx \pi/2$ ,  $\alpha = \pi/2$ ; b)  $\theta \approx \pi/2$ ,  $\alpha = 0$ ;

### 6.3.3 Metamaterial Designs Analysed

The original panel designs analysed in this work are a double-wall with mechanical link (see Fig. 6.27a) and an auxetic-cored sandwich (see Fig. 6.28a). In both cases resonant laminas/beams are attached to the core walls (see Figs. 6.27b and 6.28b,c) and case-by-case tuned considering the first cantilever-beam-like mode. Both the models are made with skins in aluminium. The double-wall panels have a core in aluminium too and both skins and core walls are 0.6mm-thick, while the global thickness is 15mm. The auxetic core of the sandwich plates, which have a total thickness of 14mm, is instead made of an isotropic material with the following properties:  $E = 1.45 \text{ GPa}$ ,  $\nu = 0.27$ ,  $\rho = 1100 \text{ Kg/m}^3$ . In this case, the skins are 1mm-thick and the core walls are 0.5mm-thick.

Depending on the tuning and the number of the resonant elements, different configurations

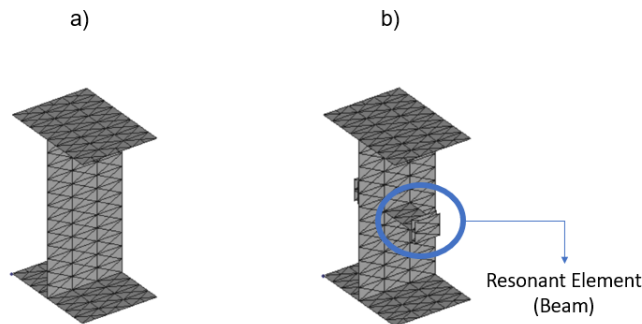


Figure 6.27: The periodic cell extracted from the double-wall panel with mechanical links. a) Standard design; b) Designs with Resonant Elements.

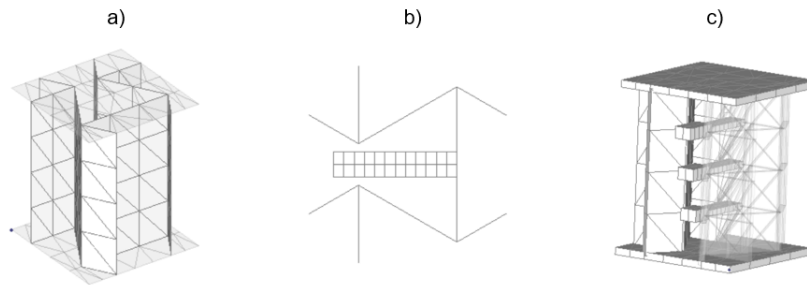


Figure 6.28: The periodic cell extracted from the Auxetic-Cored Sandwich Plate. a) Standard design; b) Designs with single Resonant Elements; c) Designs with triple Resonant Elements.

Table 6.3: Double-Wall plate with mechanical links: Configurations Info

ID	Number of Resonantors	Added Mass [%]	Target Coincidence	Curvature [m]
Standard	0	0	N/A	1.6
Resonant (Ring) - D1	1	6	Ring Mode	1.6
Resonant (Aero)- D2	1	15	Aerodynamic	1.6
Doubly-Resonant (Aero)- D3	2	18	Aerodynamic	1.6

are studied: for the double-wall plate three configurations are analysed and reported in Table 6.3; for the auxetic-cored sandwich panel four configurations are analysed instead and are reported in Table 6.4.

Considering the mass ratio influence, as discussed in [46], the effects of the resonant elements should be strongly visible for the double-wall panels, where the added masses are largely superior to the ones added in the auxetic-core configurations (see Tables 6.3 and 6.4)

The approach described in Chapter 4 is applied to simulate the sound transmission loss of the panel designs described in Sec. 6.1 under a turbulent boundary layer excitation (TBL). The Corcos model [9, 13] is used in these cases; the flow data are:  $\delta = 0.027$  m,  $\alpha = 0.125$  and  $\beta = 0.83$ .

Table 6.4: Auxetic-Cored Sandwich Plate: Configurations Info

ID	Number of Resonantors	Added Mass [%]	Target Coincidence	Curvature [m]
Standard	0	0	N/A	1.0
Resonant (C1)	1	0.78	Ring Mode	1.0
Resonant (C2)	3	2.36	Ring Mode	1.0
Resonant (C3)	2	1.49	Ring Mode	1.0
Resonant (C4)	1	0.52	Aerodynamic	1.0

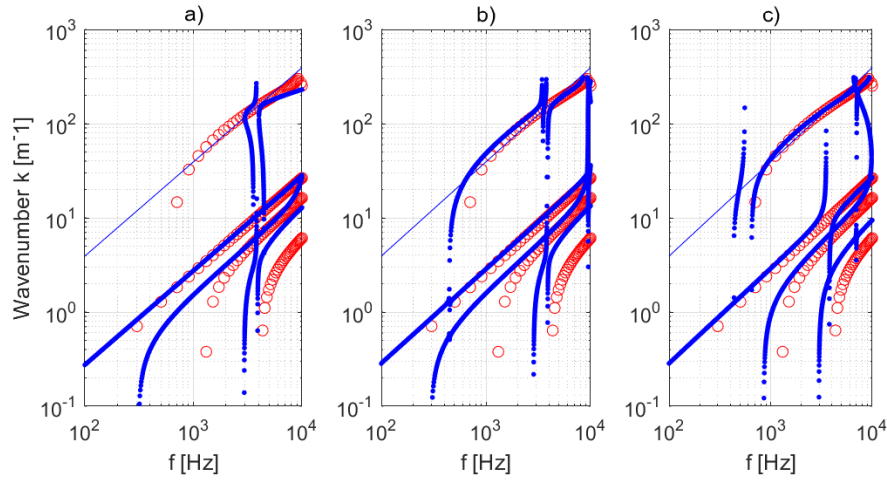


Figure 6.29: Dispersion curves for the double-wall panel with a 1.6m curvature. With reference to Table 6.3: a) D2; b) D3; c) D1. Legend: Or) Standard Configuration; .b) Resonant Configurations; -) Convective Wavenumbers for  $U_c = 160$  m/s.

### 6.3.4 Dispersion Curves

First, the dispersion curves of the panel designs described in Sec. 6.1 are plotted in Figs. 6.29 and 6.30. In Fig. 6.29, the double-wall panel with mechanical links is analysed imposing a 1.6m curvature; due to the typical low core-shear stiffness of these types of structures, the presence of the resonant beam (see Fig. 6.27) seems to strongly influence even the ring frequency zone and, as shown later for the transmission loss, this will cause a shift of the ring frequency to lower values. For the resonant configurations targeting the aerodynamic coincidence (see Table 6.3 and Figs. 6.29a,b), resonance-induced band-gaps appear around the critical frequency.

Differently, in Fig. 6.30, the dispersion curves of three configurations presented in Table 6.4 for the auxetic-cored sandwich plate with a 1.0m curvature, are compared to the standard circumferential waves. In these cases, the presence of the resonant beams embedded in the auxetic core, does not influence the wave propagation in the original structure in frequency regions outside the resonance modes of the beams, as happens for the double-wall panel. This effect is connected to the reduced mass addition of this test-cases (see Table 6.4).

### 6.3.5 Sound Transmission Loss under TBL excitation

Here, the sound transmission loss is finally calculated and compared, for all the configurations analysed, using the approach of Chapter 4. Infinite shells made with the elementary cells of Figs. 6.27 and 6.28 are simulated under an axial turbulent boundary layer flow. As a rule of thumb, the lower the mass addition the lower should be the advantages of the resonant elements around their frequency of resonance, in terms of sound transmission loss; with reference to Table 6.3 and 6.4 the addition of mass is between 6-18% for the double wall panel and between 0.5-2.4% for the auxetic-cored sandwich panel.

In Fig. 6.31 the sound transmission loss for the double-wall panel under a 160 m/s flow is presented. As evidenced also in the dispersion curves, the presence of the resonators shifts the ring frequency of the modified configurations and, thus, a mis-tuning of the resonance frequency of the embedded beams appears when targeting the original ring frequency of

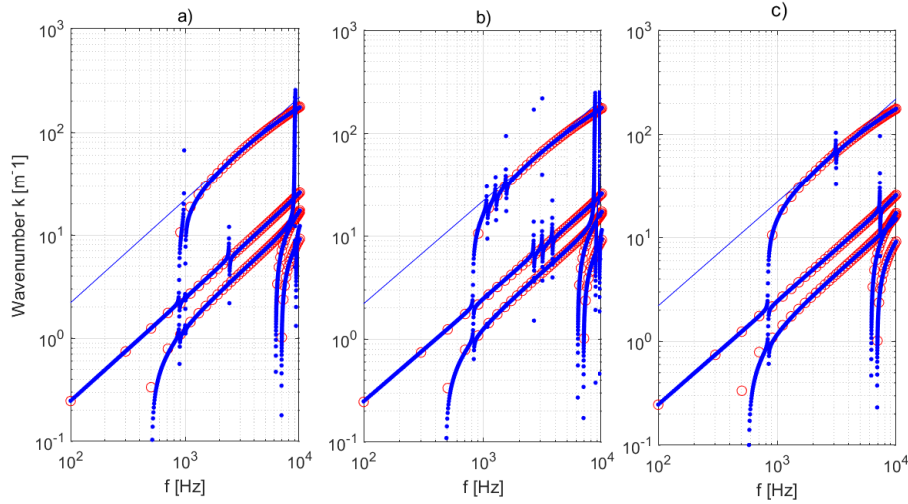


Figure 6.30: Dispersion curves for the Auxetic-cored sandwich panel with a 1.0 m curvature. With reference to Table 6.4: a) C1; b) C2; c) C4. Legend: Or) Standard Configuration; .b) Resonant Configurations; -) Convective Wavenumbers for  $U_c = 285$  m/s.

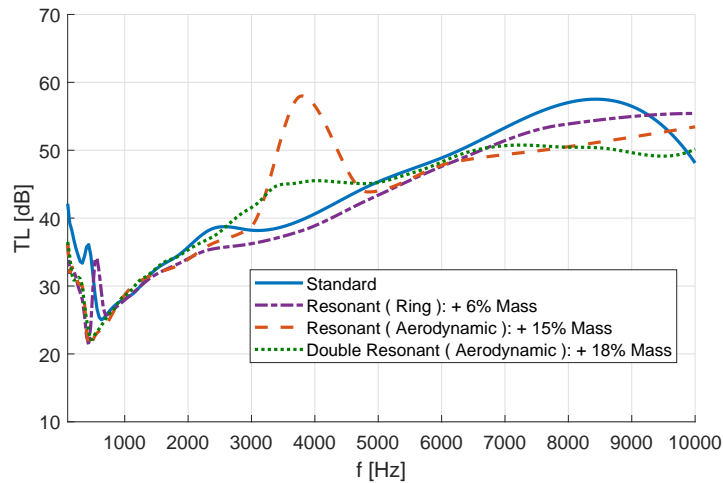


Figure 6.31: The sound transmission loss of the panel design in Fig. 6.27, with a 1.6 m curvature, under a TBL excitation at  $U_c = 160$  m/s. Comparison between design configurations in Table 6.3.

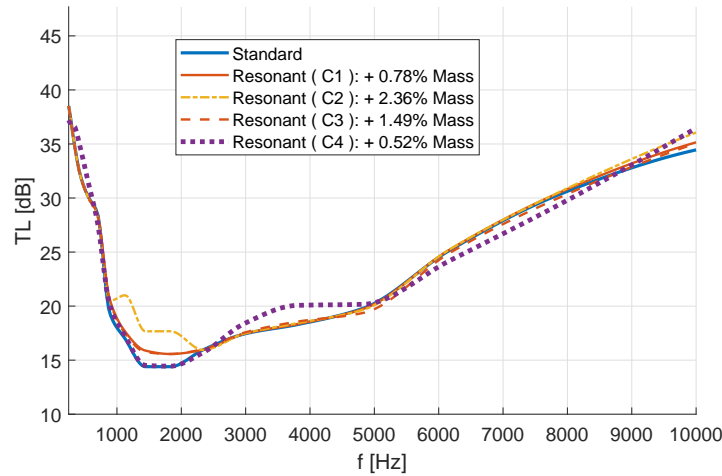


Figure 6.32: The sound transmission loss of the panel design in Fig. 6.28, with a 1.0 m curvature, under a TBL excitation at  $U_c = 285$  m/s. Comparison between design configurations in Table 6.4.

the shell. Differently, for the other configurations targeting the aerodynamic coincidence, a strong increase of the sound transmission loss is observed; a narrower band is targeted when using a single resonant beam, while a larger one, with a reduced peak of STL, is targeted when using two beams with a slightly different natural frequency. It is worth notice that the bands of increase of the sound transmission loss, when targeting the aerodynamic coincidence, are larger than expected by looking at the free wave propagation of the dispersion curves. This effect is attributable to the flow-induced increase of damping around the critical frequency (typical of TBL; [166, 179]), usually larger than the one observed for the acoustic coincidences.

On the other hand, in Fig. 6.32 the sound transmission loss for the sandwich panel with auxetic core, under a 285 m/s flow, is presented. Differently from the previous case, the increases of the STL are reduced because of the minimum addition of mass. Still, the configurations C1, C2 and C3 (see Table 6.4) induce a non-negligible increase of performance around the ring frequency region, as observed in Fig. 6.32. The use of three resonant elements with slightly shifted first natural frequencies (see C2 in Table 6.4 and Fig. 6.28c) helps in enlarging the coverage in frequency of the resonance-induced band-gaps and, thus, also the region of STL increase. Differently, the resonant configuration targeting the aerodynamic frequency (see C4 in Table 6.4) gives a relatively good increase of sound transmission loss even being single-element based and adding less than 1% of mass to the system.

This last configuration is analysed also using a combination of simultaneous TBL and DAF excitation in Fig. 6.33. The convective flow speed is again 285 m/s and the curvature equal to 1.0 m. The results show how the drop of transmission loss linked to the convective coincidence is efficiently contrasted using the embedded resonant beams between 2.0 kHz and 4.0 kHz with peaks of increased TL around 5 db.

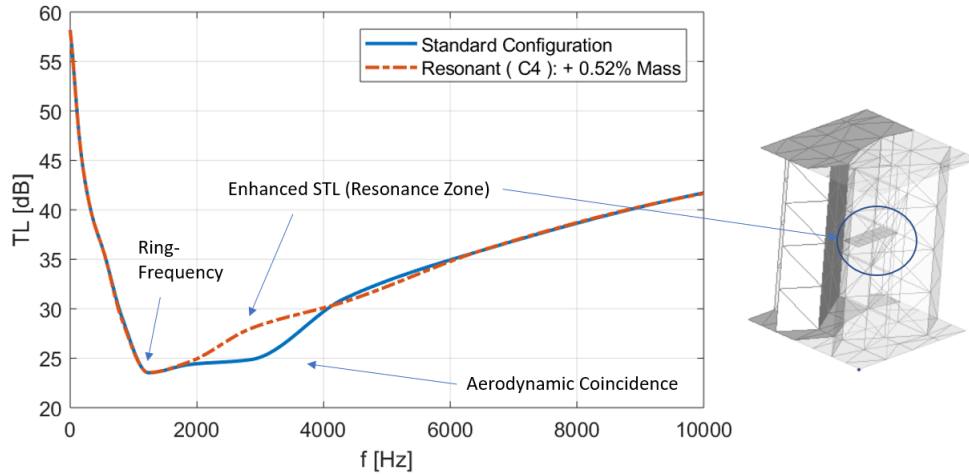


Figure 6.33: The effective sound transmission loss of the panel design in Fig. 6.28, with a 1.0 m curvature, under simultaneous TBL and DAF excitation at  $U_c = 285$  m/s. Comparison with design configuration C4.

## 6.4 Concluding Remarks

Three different types of design rules are investigated: one based on the corrugation of core walls for sandwich panels, a second one based on the placement of periodic axial or ring stringers in fluid-loaded shells and the last one based on the addition/embedding of resonant mechanical elements.

**Corrugated Walls Design** In the first case, two sandwich panels are analysed in terms of waves' propagation and sound transmission loss by using periodic structure theory. A double-wall panel with mechanical links and a sandwich panel with rectangular core are considered. A core optimization using corrugated core walls is proposed targeting the structural waves' propagation versus the acoustic wavenumbers, forcing the mass to be fixed to the value of the original designs. For the double-wall panel with mechanical links an enlarged bending band-gap is achieved in a large frequency band, shifting the acoustic coincidence almost out of the frequency band of interest.

For the sandwich panel with rectangular core, an increased core deformation mechanisms is achieved distancing the structural(bending) and acoustic wavenumbers versus frequency. Standard and proposed configurations are 3D-printed and sound transmission loss measurements are carried out using a small facility with uncoupled reverberant and semi-anechoic configuration. Numerical simulations and experimental tests evidence an increased vibro-acoustic performance of the new designs. The transmission loss measurements showed that, even keeping the same total mass of the panels, the sound transmission loss is increased in a very large frequency band that goes from  $\approx 1.5$  kHz to 10 kHz.

**Axial and Ring Stiffening** In the second case, the role of axial and ring stiffeners is exploited for curved shells under acoustic and fluid excitation. The effect of stiffeners in the direction of the flow is fundamental when convective loads are present while the direction of stiffening does not influence the sound transmission loss for purely acoustic loads. The form of the stiffeners has important impacts below the ring frequency while is reduced after. The

pitch distance, similarly, has effects only in the low frequency range but is coupled with the effects of axial stiffeners, when a turbulent boundary layer excitation is applied, providing a broadband increase of sound transmission loss when the pitch is reduced.

**Embedded Resonators** In the third case, again two sandwich cylindrical panels are analysed embedding resonant beams inside the core and under a turbulent boundary layer excitation. A double-wall panel with mechanical links and a sandwich panel with auxetic core are considered. The resonant elements are analysed in different resonance tuning combination to investigate the effect on the aerodynamic coincidences and the ring frequency of the shell. A discussion on the use of such devices to target specific coincidences or resonances is also given. The effects of the resonant structural configurations with respect to the wave propagation, sound transmission and added-masses are observed and discussed.



## Chapter 7

# Conclusions and Prospectives

### 7.1 Achievements

Within the present thesis different approaches are developed, validated and later applied for design and simulation purposes. In terms of methodologies, two macro-approaches are developed. These can be categorised by considering the wave propagation tracked in the structure: for structural vibrations a one-dimensional wave propagation is considered, while for the flow-induced noise a two-dimensional wave propagation is analysed.

For structural vibrations, the main achievements with respect to the previous literature, are linked to a reduced modelling complexity and the release of mesh constraints in the periodicity/homogeneity direction. This allows to keep the same accuracy of a standard finite element approach while reducing the computational cost of the calculation. Moreover, the formulations developed in Chapter 3 are quite general and applicable for flat, curved and axisymmetric structures even in presence of impedance variations along the direction of wave propagation. Differently, the literature is limited to simple geometries and reduced frequency bands to constrain the computational cost.

In terms of flow-induced noise, the approach proposed in Chapter 4, is generally applicable independently on the curvature, load model and model homogeneity/heterogeneity. Validations are provided with analytical, numerical and experimental data for acoustic and aerodynamic load, for flat and curved structures, with and without attached noise control materials. The method requires a simple FE modelling (unit cell) and provides accurate band-averaged results (as SEA) and a strongly reduced computational cost. The sensibility of the approach to meshing and wavenumber resolutions is also investigated.

The method is also further developed by introducing mean-flow effects (aeroelastic coupling) at cell scale. The convective derivatives of the (aerodynamic) load components are expressed in terms of waves' propagation constants in the structure. Validations are provided with available semi-analytic models for plates and shells.

However, some drawbacks are present in the developed methodologies:

- Increasing number of operations for increasing number of target degrees of freedom.
- Eigenvalue problem to be solved at each frequency step, to move in the wave base.
- Increasing computational cost if a proper baffled window integration has to be calculated for finite size effects in 2D approaches.

- Requires a modal order reduction at cell scale if the model has too many internal degrees of freedom.
- For 2D approaches, the boundary effects (reflections) are not accounted and thus a purely modal behaviour can not be captured.

The methods developed in Chapters 3, 4 and 5 are then applied for the investigation of periodic design tools to enhance the vibro-acoustic capabilities of standard structures. Three approaches are developed and applied to different structural models. In the first cases, corrugated core walls are used targeting the structural waves' propagation versus the acoustic wavenumbers, forcing the mass to be fixed to the value of the original designs. Standard and enhanced configurations are 3D-printed and sound transmission loss measurements are carried out using a facility with uncoupled reverberant and semi-anechoic configuration. The results proved that, even keeping the same total mass of the panels, the sound transmission loss is increased in a very large frequency band that goes from  $\approx 1.5$  kHz to 10 kHz.

In the second case, the influence of axial and ring stiffeners on curved shells is studied in terms of the sound radiation under acoustic and aerodynamic load. The effects of the axial stiffening for convective load is studied and compared to ring stiffening identifying the physical reasons of the increase of sound transmission loss.

In the third case, the approach consisted in embedding resonant beams inside the core of curved panels, targeting the ring frequency mode and the aerodynamic coincidence. The effects of the resonant configurations is discussed relating the advantages in terms of sound transmission with the drawbacks of increasing the total mass of the system.

## 7.2 Future Developments

As the manuscript is basically divided into a mainly methodological part and an applicative part, some future developments might be strictly connected to the drawbacks of the numerical approaches and further optimizations of the raw schemes proposed here for increasing the vibroacoustic performance of plates.

For the numerical part, a more efficient modal order reduction scheme is needed for both the 1D and 2D WFE approached developed here. In fact, as the size of the unit cell increases (number of nodes) the computational cost raises, especially considering the integration in Chapter 4. The potential solutions can be:

- Exploring a more efficient reduction scheme that involves the modes of the loaded surface, thus allowing to reduce significantly the size of the reduced matrices in Chapter 4.
- Use a more accurate selection of the integration domains in the wavenumber space to reduce to the minimum the combinations of wavenumbers to be involved in the scheme, thus reducing the total number of operations.
- Developing a more detailed approach to include finite size effects even at low-frequencies, without sacrificing the computational cost.

In terms of design solutions, the ones proposed in this manuscript did not mean to be proper optimizations but rather types of solutions. Further developments can be achieved by employing machine learning of other automatic numerical schemes to explore different similar solutions and performing a proper optimization of the unit cell design.

# Appendices



## Appendix A

# Geometrical Details of Proposed Designs

Full geometrical details for the designs analysed in Chapter 6 are given: the double wall panel with mechanical link is illustrated in Fig. C.19, while the sandwich panel with rectangular core is illustrated in Fig. A.2.

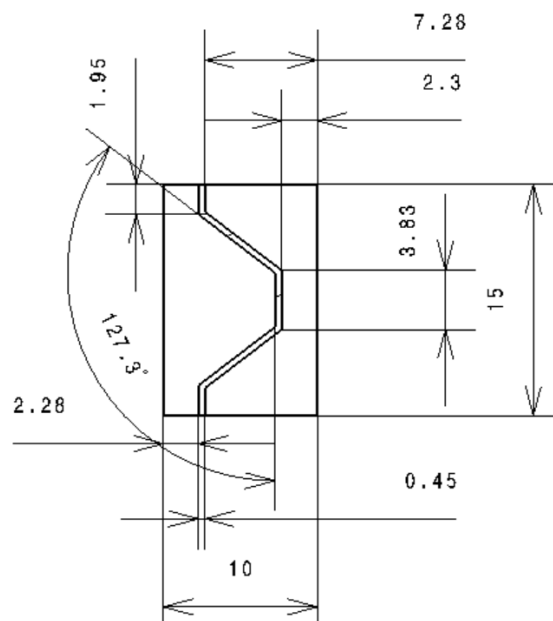


Figure A.1: Cell model extracted from the optimized double-wall panel with mechanical links. Distances in millimetres.

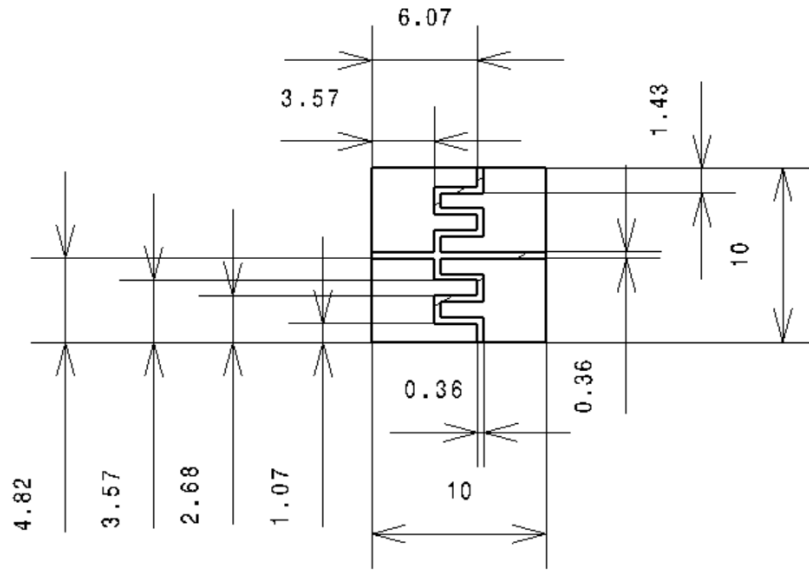


Figure A.2: Cell model extracted from the optimized sandwich panel with rectangular core. Distances in millimetres.

## Appendix B

# Reducing Tyre Vibrations using Embedded Mechanical Resonators

An investigation is carried out on structure-borne vibration and noise propagation of tyres' models at low frequencies. The idea is to use embedded resonant meta-materials to damp the tyres' vibrations and thus reduce the transferred energy to the main attached structures. A simplified tyre model is used, being the investigation of the effects of the embedded substructures the main target of the work; internal pressure and tyre rotation effects are neglected at this stage. Different configurations are tested targeting different natural modes of the tyre, while mechanical excitation is assumed on one section of the tyres. The results show how the proposed designs are a feasible solution for vibration control.

### B.1 Introduction

Tyre noise and vibrations are becoming some key comfort parameters in the automotive industry, even before 40 km/h [180, 181], because of the advent of hybrid and electric power-units [182]. In fact, the broadband noise distribution coming from an ICE (Internal Combustion Engine) is replaced by a generally high-frequency tonal whistling, which allows other noise sources, as tyre/road noise, to become dominant in other frequency ranges. Among these, the tyre noise, is dominant both in terms of structure-borne and air-borne propagations, respectively before and after 500Hz [183–185]. The structure-borne contributions derive mainly from the first natural modes of the tyre while the air-borne ones are mainly due to higher frequency circumferential modes of the tyre [185–188]. Modelling techniques based on finite elements (FEM) are often limited to low frequencies due to a high computational cost [185, 186]; wave-based approaches are also efficient to investigate the wave propagation in the tyre [189].

### B.2 Proposed design

To investigate the effect of embedded resonant substructures on tyre vibrations, the configuration in Fig. B.1b is proposed.

First, it is fundamental to know the frequencies or frequency bands to target with the embedded substructures. The transversal modes appear in lower band with respect to the mainly radial ones and thus the resonant configurations will be tuned depending on the

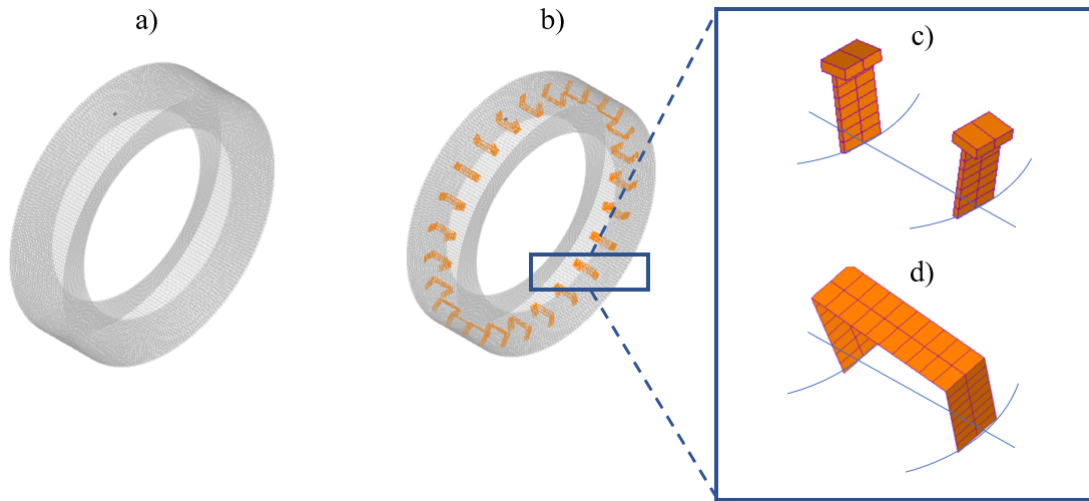


Figure B.1: Simplified tyre model with shell elements. Tyre Configuration: a) Bare; b) Resonant. Target: c) Transversal Vibrations; d) Radial Vibrations.

needs. A modal analysis is conducted on the bare tyre configuration using NX NASTRAN shell elements (CQUAD4) and using more than 20 elements per wavelength at 2KHz. The first four modes of the structure are illustrated in Fig. B.2. The material properties used are:  $E = 19.8 \text{ GPa}$ ,  $\nu = 0.32$  and  $\rho = 1850 \text{ Kg/m}^3$ .

The targets of this work will be the first two modes in Fig. B.2, for the transversal vibrations, and the fourth mode (and higher orders) in Fig. B.2, for the radial vibrations. For this reason, when targeting the transversal motion of the tyre, the concept in Fig. B.1c is used, while the one in Fig. B.1d is employed when the radial motion of the tyre is targeted too. In the case of Fig. B.1c, the first vibration modes of the embedded beams, which are classic cantilever-beam modes, are in the same direction of the transversal tyre motion. In the case of Fig. B.1d, the resonator behaves as a bridge structure with two main vibration modes in the transversal direction (cantilever-beam modes of the pylon) and radial direction (simply-supported beam mode of the deck). The idea is to create resonance-induced band-gaps around the targeted tyre modes, in order to control vibrations in that region.

### B.2.1 Force vibrations of resonant configurations

A set of forces normal to the tyres' plane, in order to simulate a mechanical road input, are used as white noise load. The response of the tyre is numerically calculated in a set of ten random points around the tyre and plotted in Figs. B.3 and B.4. Only structural damping is considered and the effect of pressure and tyre rotation is neglected.

In Fig. B.3, the resonant configuration illustrated in Fig. B.2c is tuned once on the first and once on the second transversal mode of the tyre. Two circumferential rows of 10 resonant elements are considered in both cases. The results show how the modal peaks in the response are strongly reduced, even if anti-resonances of the beams appear close to the modal frequencies, increasing the vibrations compared to the bare configuration. The effects, for both tuning conditions, are identical. No coupling between the tyre and the beam motion is observed and the resonators behave as classic TVAs (Tuned Vibration Absorbers)

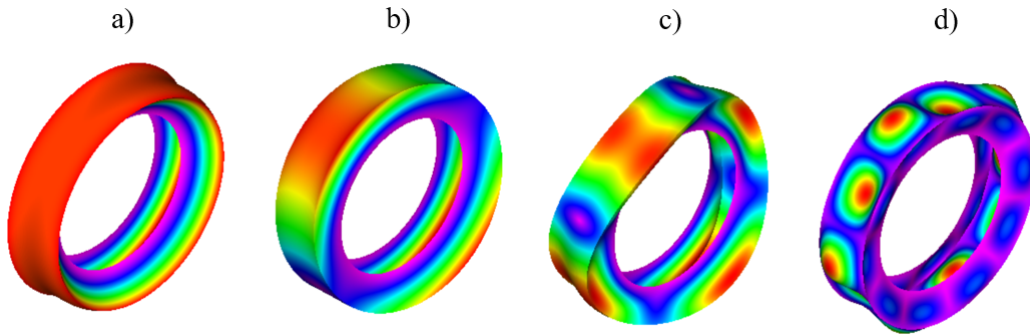


Figure B.2: First four modes of the bare tyre. Transversal Modes: a) 243.6 Hz; b) 338.5 Hz; c) 610.6 Hz. Radial Mode: d) 702.4 Hz.

with every narrow band effect.

In Fig. B.4, the resonant configuration illustrated in Fig. B.2d is tuned on the first purely radial mode of the tyre at  $\approx 703$  Hz and targets also the transversal vibration of the tyre at  $\approx 330$  Hz. A single circumferential row of 25 and then 5 resonant elements are considered, with added masses of  $\approx 20\%$  and  $\approx 3\%$  respectively. The average vibrations of the tyre in Fig. B.4 show some main effects. First, the appearance of band-gaps around the targeted frequency bands with the second transversal mode of the tyre ( $\approx 330$  Hz) always well damped. In the configuration with five circumferential resonators, the band-gap opens also around the 600-750 Hz band, allowing a decrease of vibration levels of 15dBs. On the other hand, the same effect is not achieved when more resonators are added, since a strong coupling with the tyre dynamics is present, probably given by the excessive added mass. For this reason, there is a frequency shift to lower frequencies and vibrations are increased in the 400-500 Hz frequency band.

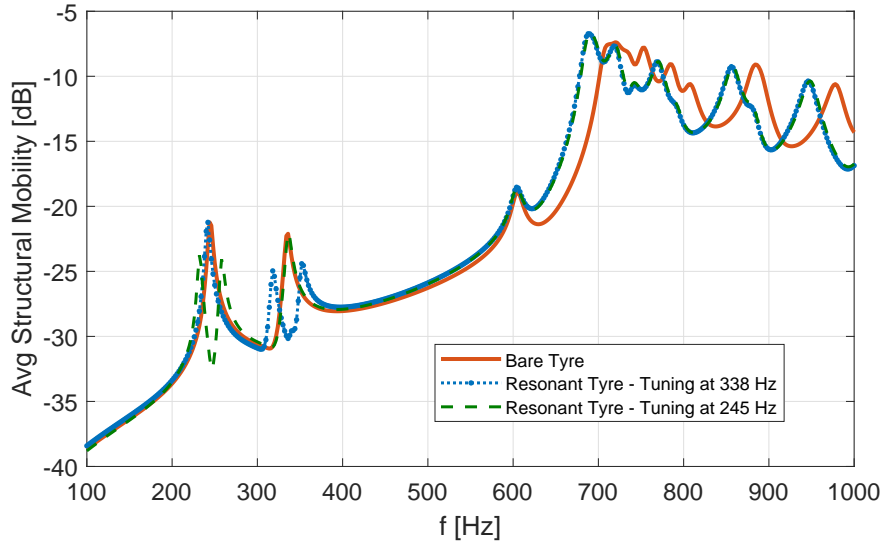


Figure B.3: Average structural mobility of the tyre with and w/o mechanical resonators for transversal vibration control.

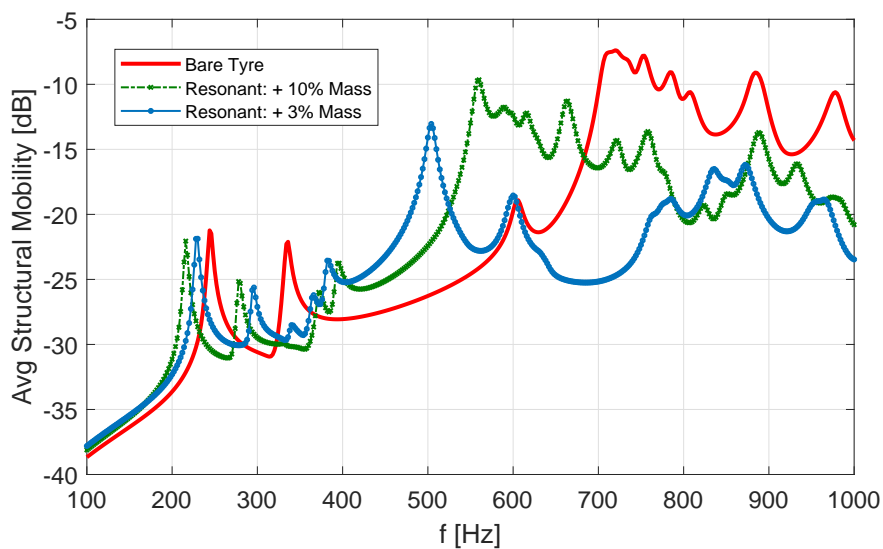


Figure B.4: Average structural mobility of the tyre with and w/o mechanical resonators for radial vibration control.

### B.3 Concluding remarks

The effects of embedded mechanical resonators in a tyre compound is analysed in terms of forced vibrations on a simplified tyre model. Two main configurations are analysed in order to target two main regions of tyre dynamics, strongly related to the structure-borne and air-borne issues respectively. Numerical simulations are carried out using a FEM approach and average vibrations on random tyre points are computed. The resonant substructures are observed to be very efficient when targeting the transversal motion of the tyre, while higher order coupling between the resonators and the tyre dynamics appears when targeting radial vibrations. The latter effect can be investigated with a detailed modelling of the tyre. Further investigations could target the efficiency of the resonant configurations as a function of the resonators' shape and added mass.



## Appendix C

# Dispersion of Periodic Media through Modal Analysis of Rings

This work presents an approach for using a modal analysis on an equivalent finite cylindrical model, to predict the elastic waves in infinite, isotropic or composite, panels. In the description of the infinite paths, an analogy, between the classical topologies of a straight line and a circumference, is exploited and tested. Different aspects, concerning the wave-mode duality and the discretization and the needed radii of curvature, are investigated to frame the problem and test the robustness of the methodology. The analysis presents a well conditioned problem and solution for any propagation wave angle by transforming the original problem into a simple modal analysis.

### C.1 Introduction

The correct knowledge of how elastic waves freely behave inside a specific structure is mandatory for a correct modelling and analysis of the structure itself. Moreover, the generally frequency-dependent wavelengths, to be described in the modelling phase, must be known in advance for a correct discretization of the model. In FEA (Finite Element Analysis) [190], the knowledge of the wavelength is absolutely mandatory for the mesh sizing and for selecting the proper elements in the frequency range of analysis; in SEA, [191], detailed information about the group velocity and the modal density are necessary for the characterization of the specific subsystem and to analyse the energy exchange among them.

For an isotropic and homogeneous panel, three wave types are, present: bending, shear and longitudinal waves. An analytic procedure is available in literature for the corresponding wavenumbers, assuming the Kirchhoff-Love plate theory [172, 192]. In order to deal with composite laminates, the CLPT (Classical Laminate Plate Theory) [193] can be used once the characteristic matrices of the laminate are calculated and is the simplest available theory. More recently, some authors have proposed alternative methodologies for the calculation of the dispersion curves of more complex composite structures [194–198].

Among the finite-element based methods, the SFEM (Spectral Finite Element Method) is a wavenumber-based procedure which reformulates the wave propagation problem through a linear algebraic eigenproblem in the wavenumber space, assuming a three-dimensional displacement field within the plate [80, 196–198].

The WFEM (Wave Finite Element Method) is also used similarly to the SFEM for obtaining the dispersion curves of homogeneous and periodic structures. The method makes use of

the Bloch-Floquet theory, [72], and analyses the wave propagation in the media imposing the periodicity conditions to a single repetitive cell [72, 73, 87, 89, 95, 96, 101].

Both these procedures are affected by numerical conditioning when an heading angle, different from a few specific values, is imposed. For example, in the case of the WFEM, the polynomial eigenproblem, to be solved, when an general angle is imposed, might turn to a transcendental eigenvalue problem which is characterized by numerical instabilities and eigenvalue tracking issues, [89]. Moreover, it is fundamental determining which solutions of the eigenvalue problem are artefacts of the spatial discretisation and which are valid estimates of wavenumbers in the continuous structure, [95, 146, 150].

The tracking of eigenwaves, performed through a Wave Assurance Criterion, [95, 199], is a time-consuming task and it does not assure correct and robust results for two dimensional waveguides. Other issues of the method are associated with the periodicity effects: the solution scheme gives the same result for the wave modes and the frequencies of the propagation constants with period  $2\pi$ , because of the spatial periodicity, giving rise to aliasing effects, [89].

On the other hand, the wave propagation in curved waveguides, i.e. cylinders and cones, is deeply analysed in the literature [152, 200]. The propagation of longitudinal and flexural waves in axial-symmetric circular cylindrical shells with periodic circular axial curvature is studied using a finite element method in [201]. The waves in thin uniform cylindrical shells, periodically stiffened by uniform circular frames of general cross-section, is analysed in [200]. Modern methods appeared continuously in the literature, for curved structures, both for the free wave propagation and the forced response [107, 202].

A wave-based methodology for the free and forced analysis of the circumferential wave propagation of axial-symmetric structures, whatever they complexity and tapering, is proposed in [107].

Differently, some attempts to use a finite model to gather informations of an infinite waveguide are present in literature, with success in the identification of the periodic structural band-gaps [203, 204].

The issues of having a correct mathematical formulation for the out-of-resonance wave-mode duality is analysed and discussed by Langley in [205]. It is stated and proved that, at least in the case of a 1D wave propagation, in a resonance condition a mode can be represented using a wave description [205].

To authors knowledge, very few works, dealing with a full representation of the dispersion curves of the periodic (or homogeneous) waveguide, are present in literature and, in this work, an alternative approach is proposed which allows to overcome all the numerical instabilities. The approach produces results for every heading angle, through a simple real modal analysis of a cylindrical equivalent finite element model, performable with any available in-house or commercial code.

The paper is structured as follows: Section 2 gives an overview of all the reference solutions adopted; Section 3 describes the analogy proposed and Section 4 contains the analytic and numerical validations for all the analysed test-cases.

## C.2 Reference Solutions

In the following section an overview of the adopted reference solutions is given for isotropic beams and plates and for composite laminates.

### C.2.1 Isotropic beam and plate

Considering a beam with  $E$  as the Young modulus,  $I$  the area moment of inertia,  $\rho$  the mass density and  $A$  the cross-sectional area; The phase wave speed in a flexural beam can be expressed as follows, [73, 147, 172]:

$$c_b = \left(\frac{EI}{\rho A}\right)^{1/4} \sqrt{2\pi f} \quad (\text{C.1})$$

Similarly a uniform thin and flat plate is here considered, made of an homogeneous material. From classical thin plate theory, [172], three wave types propagate in the material of thickness  $h$ : longitudinal, shear and bending waves. Each of these is associated with the respective wavenumber:  $k_l$ ,  $k_s$ ,  $k_b$ .

$$k_l = 2\pi f \sqrt{\frac{\rho(1-\nu^2)}{E}} \quad k_s = 2\pi f \sqrt{\frac{2\rho(1+\nu)}{E}} \quad k_b = \sqrt{2\pi f} \left(\frac{\rho h}{D}\right)^{1/4} \quad (\text{C.2})$$

where  $D$  is the well known flexural stiffness of the plate and  $\nu$  the Poisson ratio. By using these relationships, any information for a predictive methodology can be gathered. For example, the discretization of the predictive finite element model could be designed to work up to a given excitation frequency, once the wavelengths are known.

### C.2.2 The Classical Lamination Theory (CLPT)

The basic analytic equations for a thin composite plate are here summarized. For a laminate, the relations between forces/moments and strain/curvatures can be written as, [80, 193]:

$$\mathbf{N} = \mathbf{A}\boldsymbol{\epsilon}_0 + \mathbf{B}\boldsymbol{\gamma}_0 \quad \mathbf{M}_I = \mathbf{B}\boldsymbol{\epsilon}_0 + \mathbf{D}\boldsymbol{\gamma}_0 \quad (\text{C.3})$$

where  $\boldsymbol{\epsilon}_0$  are the strains of the middle plane and  $\boldsymbol{\gamma}_0$  the curvatures of it.

$\mathbf{A}$ ,  $\mathbf{B}$  and  $\mathbf{D}$  are the matrices which compose the well known matrices which depends on stress-strain relation of each lamina and the chosen layup sequence [80, 193].

$$\boldsymbol{\epsilon}_0 = \begin{bmatrix} \frac{\partial u}{\partial x} \\ \frac{\partial v}{\partial y} \\ \frac{\partial u}{\partial y} + \frac{\partial v}{\partial x} \end{bmatrix} \quad (\text{C.4})$$

$$\boldsymbol{\gamma}_0 = \begin{bmatrix} -\frac{\partial^2 w}{\partial x^2} \\ \frac{\partial^2 w}{\partial y^2} \\ -2\frac{\partial^2 w}{\partial y \partial x} \end{bmatrix} \quad (\text{C.5})$$

where  $u$  and  $v$  are the in-plane displacements, while  $w$  is the out-of-plane displacement. Following the procedure explained in [193], a 3D displacements wave is assumed to propagate along the plate:

$$\begin{bmatrix} u \\ v \\ w \end{bmatrix} = \begin{bmatrix} U \\ V \\ W \end{bmatrix} e^{j[k(\cos(\theta)x + \sin(\theta)y) - \omega t]} \quad (\text{C.6})$$

where  $\theta$  is the heading angle of the wave and  $U, V, W$  the displacement field variables. It is possible to converge to a polynomial problem in  $k$  (the wavenumber).

The following expressions can be used to compute the wavenumbers of the laminated waveguide, once the material is chosen, [80, 193].

$$k_b(\theta, f) = \sqrt{2\pi f} \left( \frac{\rho_s}{\mathbf{P}^T \mathbf{D} \mathbf{P}} \right)^{1/4} \quad (\text{C.7})$$

$$k_s(\theta, f) = 2\pi f \sqrt{\frac{\rho_s}{\eta_s(\theta)}} \quad (\text{C.8})$$

$$k_l(\theta, f) = 2\pi f \sqrt{\frac{\rho_s}{\eta_l(\theta)}} \quad (\text{C.9})$$

where:

$$\mathbf{P}^T = [\cos(\theta)^2 \quad \sin(\theta)^2 \quad 2\sin(\theta)^2 \cos(\theta)^2] \quad (\text{C.10})$$

$$\mathbf{L} = \begin{bmatrix} \cos(\theta) & 0 \\ 0 & \sin(\theta) \\ \sin(\theta) & \cos(\theta) \end{bmatrix} \quad (\text{C.11})$$

$\eta_l$  and  $\eta_s$  eigenvalues of the matrix  $\mathbf{L}^T \mathbf{A} \mathbf{L}$ .

### C.3 The Proposed Analogy

The method, presented here, is based on the assumption that the free wave propagation in an infinite flat media, i.e. a panel, can be also described considering a free wave propagation along a circumferential path. In fact, in a local reference system which follows the geometrical (circumferential; Fig. C.1) path, the waves are free to propagate in analogy to what they do in the case of the equivalent infinite flat structure. The finiteness of the circular structure does not affect the wave propagation since no impedance variations are encountered running in loop along the curved path. Equivalently, this is a way to describe an infinite periodic condition, in a local coordinate system, as resulting from the Bloch-Floquet theorem [72, 73]. The difference stands in its implicit geometrical definition through a finite circular structure, instead of explicitly defining a propagation relation on a reference line. In a periodic waveguide, the link between a wavefield  $\Gamma$  (displacement, velocity, force, etc.), at two points  $x$  and  $x + \Delta_x$ , is given by complex propagating constants, [72, 73]:

$$\Gamma(x + \Delta_x, f) = \Gamma(x, f) e^{j\Delta_x k_n(f)} \quad (\text{C.12})$$

where  $k_n$  is the wavenumber associated with the wavetype  $n$  and  $f$  the frequency. On the other hand, for a circumferential mode of order  $i$ , the field in two points is related, similarly, as follows:

$$\Gamma(\theta + \Delta_\theta, f) = \Gamma(x, f) e^{j\Delta_\theta i/2\pi R} \quad (\text{C.13})$$

where  $i/2\pi R$  is the circumferential wavenumber associated with the mode of order  $i$ .

In a set of discrete (natural) frequencies, each specific circumferential mode is representative of the corresponding wavemode and Eq. (C.12) and (C.13) are equivalent. Figure C.1 and C.2 illustrate the previous concepts.

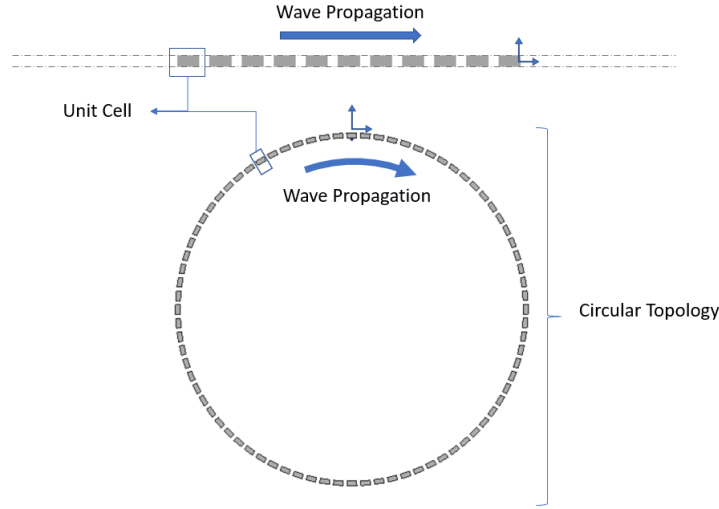


Figure C.1: The analogy proposed: (a) Free wave propagation along an infinite flat waveguide; (b) equivalence in a circular topology generated from the original model.

It is worth to emphasize that the aim of the approach is not related to the analysis of the waves in a cylindrical waveguide. The equivalent circular geometry is here used only to simulate a wave propagation in an infinite domain: in this way, the wave properties in an infinite panel (or beam) can be calculated working on the circumferential wave propagation in a finite circle.

A modal analysis (Eq. C.14) of cylinders or rings, built from the reference structure, gives a discrete set of frequencies (natural modal frequencies) where the modal circumferential wavelength represents the wave propagation in the infinite media. The dispersion curves of the laminate can be thus calculated in discrete points.

By using the equation of motion in discrete coordinates and assuming no external forces are applied to the system, the eigenvalue problem can be written as:

$$[\mathbf{K} - \omega^2 \mathbf{M}] \mathbf{q} = \mathbf{0} \quad (\text{C.14})$$

where  $\mathbf{q}$  is the nodal vector of degrees of freedom (DoFs);  $\mathbf{K}$  and  $\mathbf{M}$  are the stiffness and mass matrices. Damping can be modelled by including, in Eq. C.14, appropriate complex matrices and/or coefficients. The operation is easily performable using any commercial FE software.

It is useful to remind the role of the modal wavelengths in rings; a purely circumferential mode for a circular structural model is in Fig. C.2. Given a certain radii ( $R$ ), in general, the wavelength associated to a given mode is given by:

$$\lambda_i = \frac{2\pi R}{i} \quad (\text{C.15})$$

where  $i$  is the order of the circumferential mode and can be rawly identified in the number of lobes present in the modal deformed shape.

A key parameter is, here, the modal angular sampling factor, given by the ratio of the modal wavelength and the radii of the circumference:  $2\pi/i$ . Its importance, within the present method, is discussed in next section.

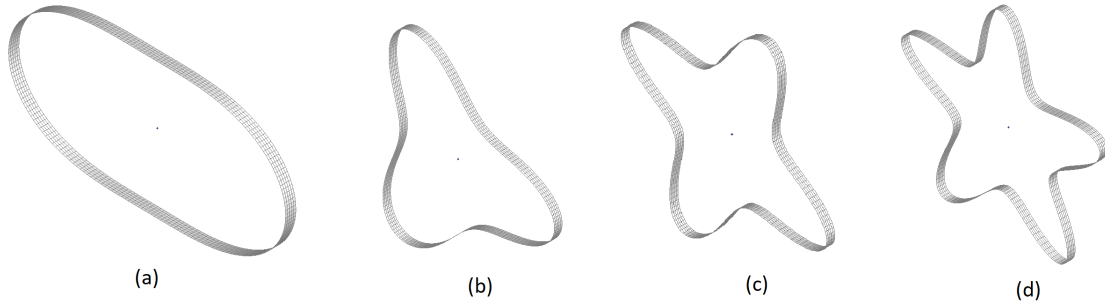


Figure C.2: Purely circumferential bending modes in a circular structure: (a) Circumferential Order = 2; (b) Circumferential Order = 3; (c) Circumferential Order = 4; (d) Circumferential Order = 5.

The modes of a finite structure describe a steady wave condition while the dispersion curves, for any structure, describe a wave propagation [205]. Any wave type propagating in an infinite media, can be described using this analogy. However, to correctly and easily identify the bending, shear and longitudinal wavemodes singularly, the circular waveguide can be constrained, in a Finite Element Solution, in order to show only the desired circumferential wave types. For example, in the case of bending waves, the constraints of the cylindrical domain must allow only out-of-plane displacements and rotations. Similar considerations are applied for shear and longitudinal waves.

In summary, the proposed method is composed by the following sequential passages:

1. Generate a finite element model of the unit cell of the structure to be analysed, as usually done in a SFEM or WFEM framework (Fig. C.1(a))
2. Generation of a circular topology using the elementary cell as a base. The radius and the number of elements has to be chosen in accordance to the target frequency band (Fig. C.1(b))
3. Perform a modal analysis of the circular structure (Eq. C.14)
4. Identify the wave branches and evaluate the circumferential wavenumbers (Eq. C.15) of the structural eigenmodes calculated at the previous step
5. Plotting the  $\lambda_i$  for each natural frequency and for each branch.

## C.4 Validations

In the following section the validation of the proposed approach is performed for different test-cases.

### C.4.1 Analytic Validation: Infinite Beam and Ring

A first test-case is the one of a beam. This is particularly convenient since both the bending wave speed of an infinite beam and the natural frequencies of a beam-ring can be calculated using analytic formulas. For every ring wavelength  $\lambda_i$ , where  $i$  is the circumferential order,

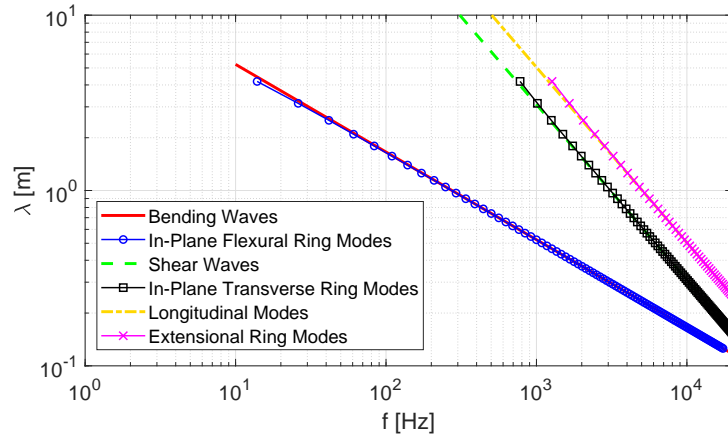


Figure C.3: Bending, shear and longitudinal wavemodes wavelength in an infinite beam and the corresponding beam-ring circumferential modes

the natural frequencies for bending, shear and longitudinal modes, respectively  $f_{b,i}$ ,  $f_{s,i}$  and  $f_{l,i}$ , are given by Blevins in [206]:

$$f_{b,i} = \frac{i(i^2 - 1)}{2\pi R^2 i} \left( \frac{EI}{\rho A} \right)^{1/4}; \quad f_{s,i} = \frac{\sqrt{i^2 + 1}}{2\pi R} \sqrt{G/\rho}; \quad f_{l,i} = \frac{\sqrt{i^2 + 1}}{2\pi R} \sqrt{E/\rho}; \quad (C.16)$$

with  $E$  as the Young modulus,  $G$  the shear modulus,  $I$  the moment of inertia,  $\rho$  the mass density and  $A$  the cross-sectional area.

In Fig. C.3, a beam with rectangular section is used as a test-case and the results obtained with Eq. (C.1) and (C.16) are compared. The results show a very good agreement which validates the analogy proposed. The results introduce a range of validity of the approach starting from a specific value of the modal sampling factor (modal order). The accuracy of the proposed method is high enough starting from the sixth modal order and it is independent on the radii and length of the ring considered, as expected (Fig. C.4).

#### C.4.2 Analytic Validation: Infinite Cylinder Ovaling Modes

Another analytic validation is here proposed, using the natural ovaling modes of an infinite cylinder. The natural frequencies, for this specific modes of the infinite cylinder, can be calculated using the formulas proposed by Blevins in [206], here reported for completeness in Eq. (C.17). For every ring wavelength  $\lambda_i$ , where  $i$  is the circumferential order, the natural frequency  $f_{n,i}$  is:

$$f_{n,i} = \frac{h}{2\pi R^2 \sqrt{12}} \sqrt{\frac{E}{\rho(1 - \nu^2)}} \frac{i(i^2 - 1)}{\sqrt{i^2 + 1}} \quad (C.17)$$

In Fig. C.5, an infinite plate of thickness  $h$  is used as a test-case and the results obtained with Eq. (C.1) and (C.17) are compared for bending waves. The results show a very good agreement, validating the analogy proposed also for a higher order model. Moreover, again, the range of validity depends on the modal sampling factor. In Fig.C.4, the relative error for this specific case is shown for different radii. The error, in percentage, is independent on the radii of the cylinder and is inferior to 2% starting from the sixth modal order, as found in the previous section.

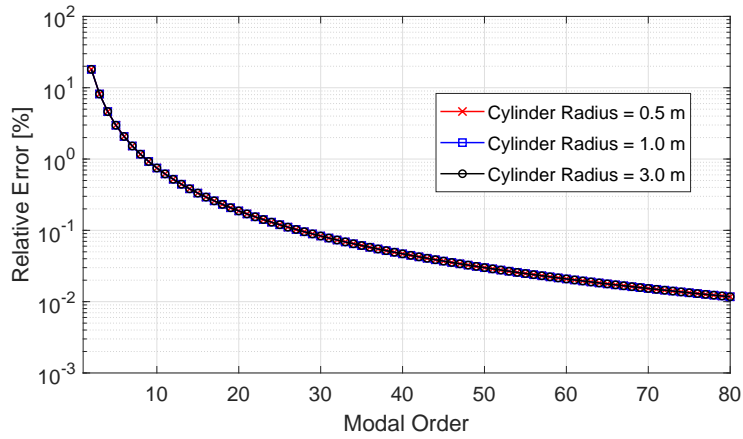


Figure C.4: Relative error (log-scale) between the bending wavelength in an infinite panel and the modal wavelengths of an infinite cylinder

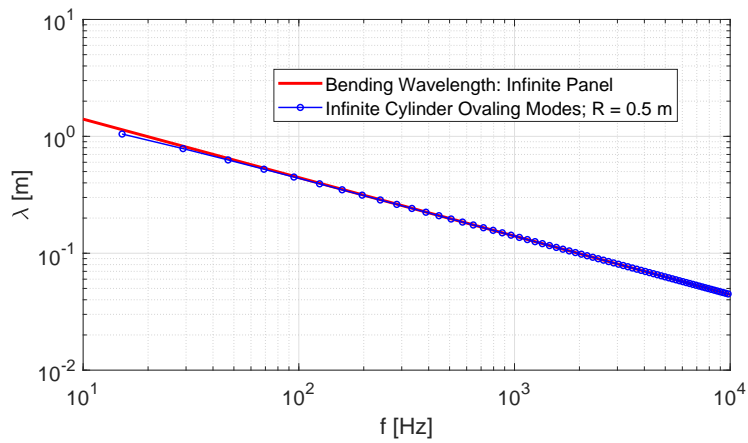


Figure C.5: Bending wavelength in an infinite panel and the ovaling modes of an infinite cylinder

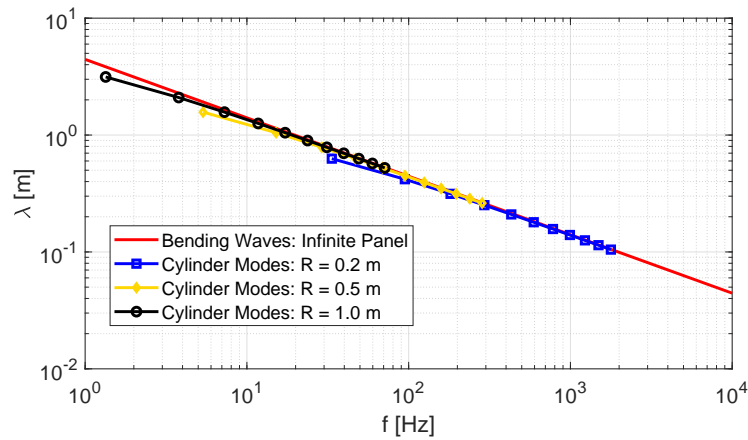


Figure C.6: Isotropic uniform plate: infinite panel solution and the circumferential modes of a cylindrical finite structure made of plate elements

### C.4.3 Numerical Validation: Isotropic Panel

A first validation with an isotropic aluminium material is performed:  $E = 7.0 \times 10^{10}$  Pa,  $\rho = 2750$  kg/m<sup>3</sup>,  $\nu = 0.33$ . The analytic solution is used as a reference. In Fig. C.6 a comparison of the infinite plate bending wavelength (versus frequency) with the results of a modal analysis on cylinders of different radii is shown. As in the case of the beam, the accuracy of the method is only dependent on the modal angular sampling factor; as soon as it reaches the unitary value, thus the sixth modal order is reached, the relative error of the present method is inferior to 2%. This is illustrated more specifically in the case of laminates, comparing the error for every heading angle.

Depending on the value of  $R$ , the region of accuracy moves with the frequency, approaching higher bands when  $R$  lowers, and vice-versa, since any modal order shifts with the frequency. Depending on the discretization adopted, the accuracy method can strongly vary. Two cases are here analysed: fixed radii  $R$  (Fig. C.7) and fixed element size  $\Delta_X$  (Fig. C.8).

In the first case the question moves to a classic sampling problem. Given a number of elements ( $N_{el}$ ), through which the circumference is discretized, assuming, as a rule of thumb, at least four elements per wavelength as an acceptable approximation (six or ten are, in general, preferred), the maximum modal order predicted is given by the integer of the ratio  $N_{el}/4$ . The error starts increasing up to modal order  $N_{el}/2$  before diverging (Fig. C.9).

On the other hand, keeping the element size fixed and increasing the number of elements means increasing the circumference radii  $R$  (Fig. C.10). The expected effect is a frequency shift of the validity region, in the wavenumber domain, when moving from one case to the other, as in Fig. C.10.

### C.4.4 Laminated Panel

An heading angle can be specified in order to analyse the wave propagation in a specific direction (Fig. C.11). In this solutions scheme, the problem is never ill-conditioned and can be normally solved with a simple real modal analysis, independently on the value of the angle itself. The graphite-epoxy lamina elastic properties, used in the present work, are in Table C.1. The thickness of each lamina is 1mm.

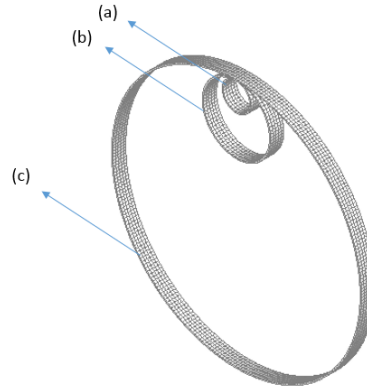


Figure C.7: Comparison for increasing number of elements for a given element size . (a) 32, (b) 80, (c) 300 elements

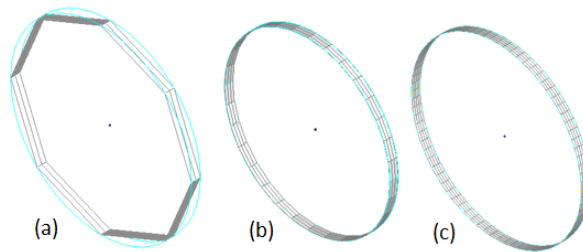


Figure C.8: Comparison for increasing number of elements for a given circumference radii  $R$ . From the left side: 8, 32, 80 elements

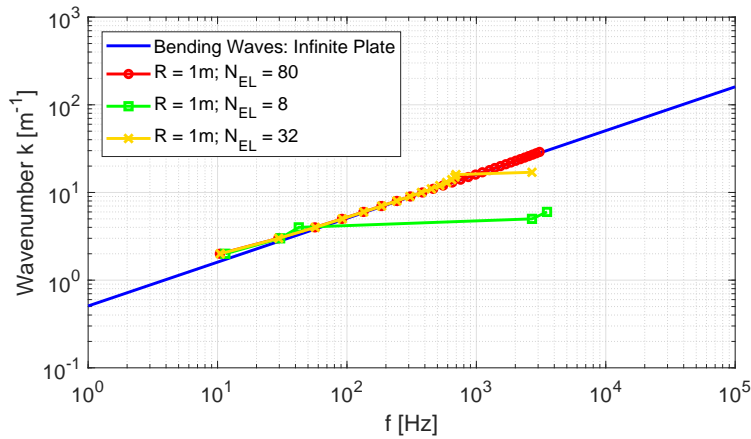


Figure C.9: Effect of the mesh: comparison for increasing number of elements for a given circumference radii  $R$  (isotropic panel). Elements size variable.

Table C.1: Lamina elastic properties and stacking sequence

$E_{11}$	$E_{22}$	$G_{12}$	$\nu_{12}$	Layup
125 GPa	12.5 GPa	6.89 GPa	0.38	$[90^\circ, 0^\circ, 0^\circ, 90^\circ]$

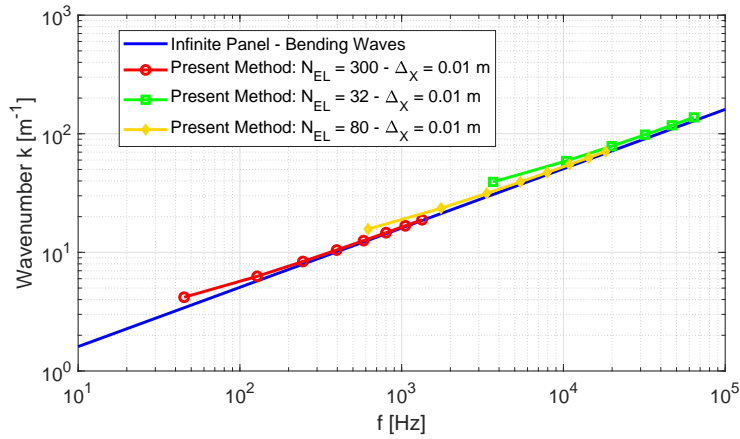


Figure C.10: Effect of the mesh: comparison for increasing number of elements for a given element size (isotropic panel). Circumference radii  $R$  variable: Fig. C.7(a) 0.05 m, Fig. C.7(b) 0.13 m, Fig. C.7(c) 0.48 m

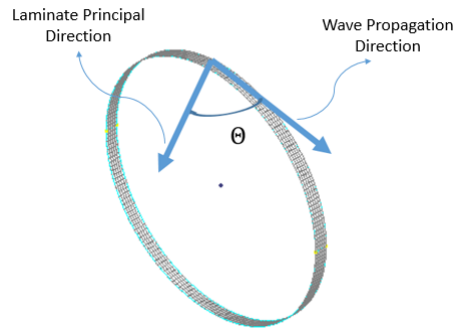


Figure C.11: Scheme of the laminate heading angle with respect to the wave propagation direction.

In the framework of the present approach, a cut-on wavenumber can be defined; below this value, a cylinder with radii  $R$ , has no predictive capability. In general, given a certain radii  $R$  the cut-on wavenumber can be defined from the smallest modal order ( $i = 2$ ):  $2/R$ . This aspect has an impact only for bending waves, as evident in Fig. C.12, C.13 and C.14, where, in addition, the accuracy of the method is shown also for shear and longitudinal wave types. Increasing the size of the radii, this limit moves to lower wavenumbers and frequencies.

As previously stated, the accuracy of the method is only dependent on the modal angular sampling factor, and, when it reaches the unitary value, the accuracy is acceptable as in Fig. C.15, where the relative errors are compared. For a modal order superior to the fifth, the relative error is inferior to 2% and keeps lowering for increasing the frequency, as found in all previous test-cases.

The great advantage is in the ease of use and the possibility to arbitrarily choose an heading angle, without taking care about the eventual ill-conditioning of the mathematical problem, [80, 89, 95]. Moreover, the eigenvalue tracking is no more needed since any wave type evolves singularly if specific boundary conditions are imposed to the the finite cylinder before the modal analyses, as previously discussed. In Fig. C.16 a pattern of bending wavenumbers

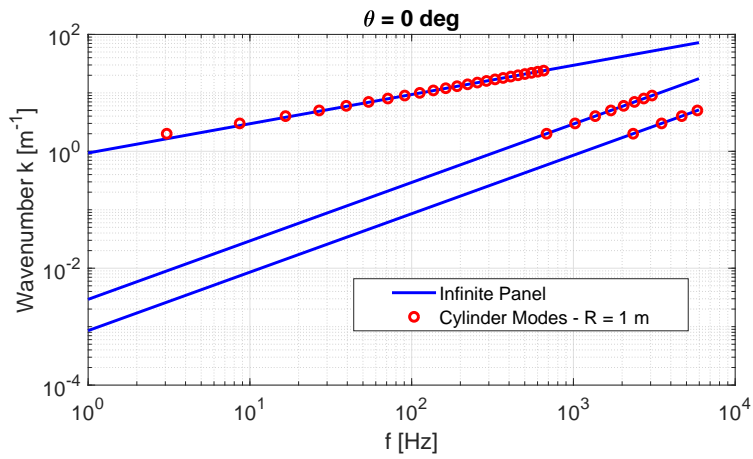


Figure C.12: Dispersion curves of the laminate panel; heading angle  $0^\circ$ . CLPT results used as a reference.

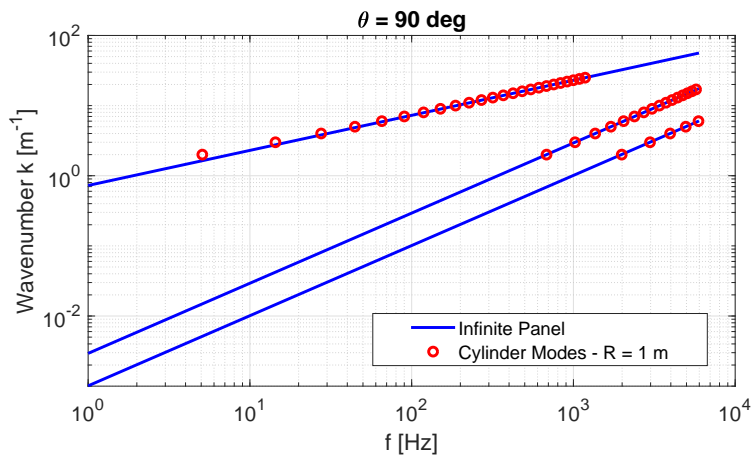


Figure C.13: Dispersion curves of the laminate panel; heading angle  $90^\circ$ . CLPT results used as a reference.

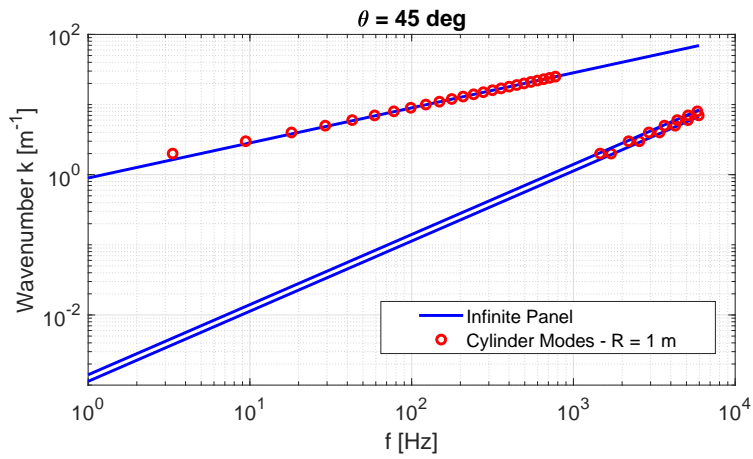


Figure C.14: Dispersion curves of the laminate panel; heading angle  $45^\circ$ . CLPT results used as a reference.

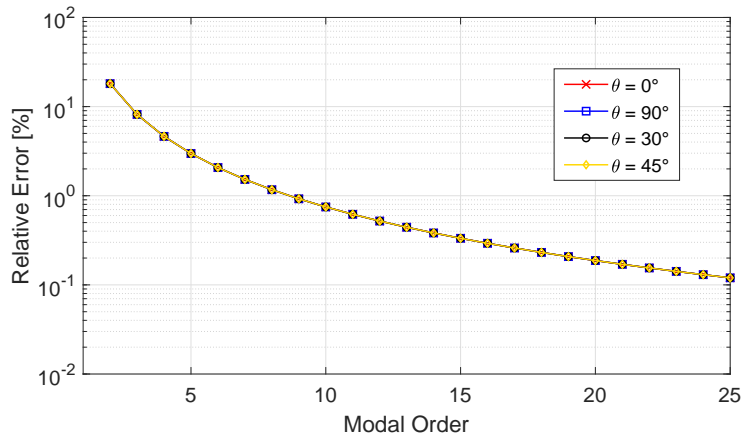


Figure C.15: Relative errors (log-scale) for different heading angles (bending waves). The CLPT results used as reference.

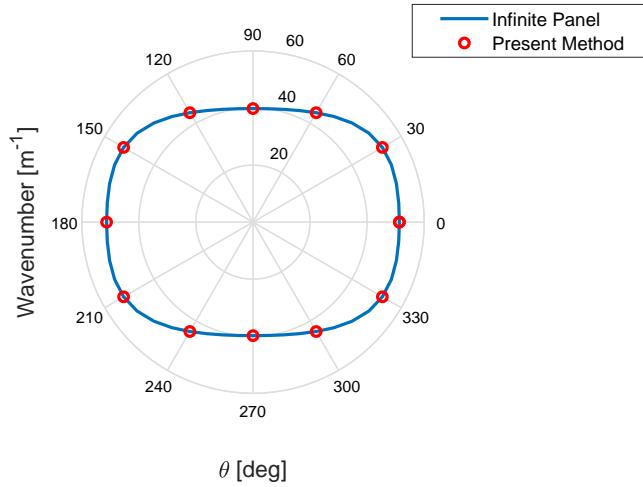


Figure C.16: Pattern of the bending wavenumbers for the laminate plate analysed; 3000 Hz

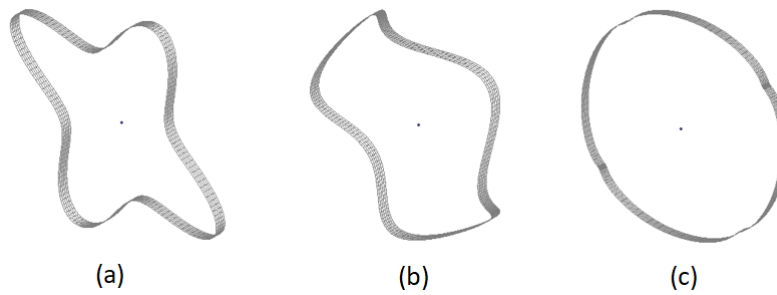


Figure C.17: Purely circumferential modes in a laminate infinite panel; X-Y as cross sectional plane. Fourth circumferential mode - (a) Bending: 16.6 Hz; (b) Shear: 1364 Hz; (c) Longitudinal: 4674 Hz

is calculated, for a specific frequency, with the present method, and compared to the one obtained using the CLPT.

Once a modal analysis is performed, the modal shapes can be extracted straightforwardly. A better way to visualize the mode shapes, will be the stretching of the circumferential modes along a rectilinear path. In Fig. C.17 a fourth order mode has been chosen and the mode shapes are visualized for bending, shear and longitudinal wave types, along the circular model. On the other hand, in Fig. C.18, the same modes are visualised in a rectified model.

### C.4.5 Complex Structural Shapes

In order to prove the accuracy of the analogy, even for non-homogeneous structures and large heterogeneity scales, an aluminium-made double-wall panel with mechanical connections is used as a test-case (Fig. C.19). A wave finite element method (WFEM) is used for obtaining the reference results [89, 101, 107]. Figure C.20 shows the comparison among the modes generated by the cylindrical model ( $R = 0.4$  m), built from the elementary cell representing the reference waveguide, and the flat infinite reference waveguide. In this case only bending

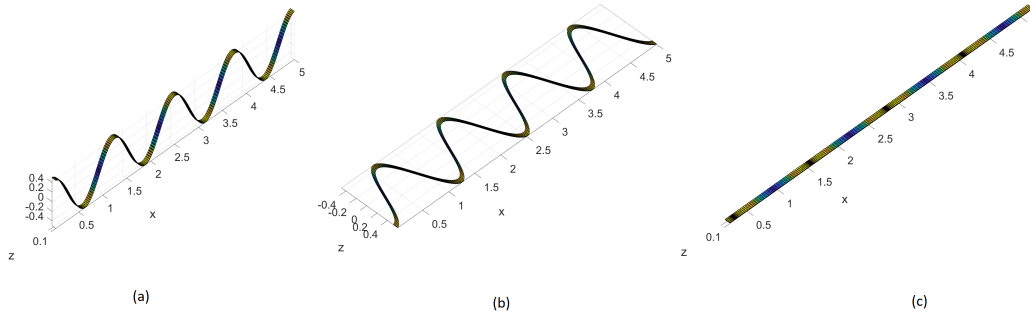


Figure C.18: Rectified circumferential modes in a laminate infinite panel; X-Y as cross sectional plane. Fourth circumferential mode - (a) Bending: 16.6 Hz; (b) Shear: 1364 Hz; (c) Longitudinal: 4674 Hz

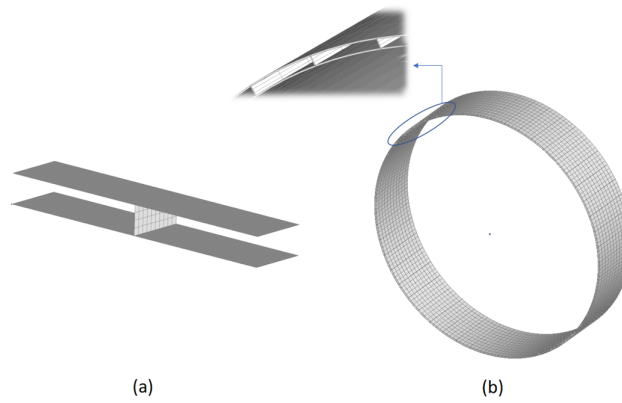


Figure C.19: A double-wall panel with mechanical connection: (a) Elementary FE Cell; (b) Cylindrical Model.

waves have been analysed. Even in this complex case the agreements is excellent above the sixth modal order.

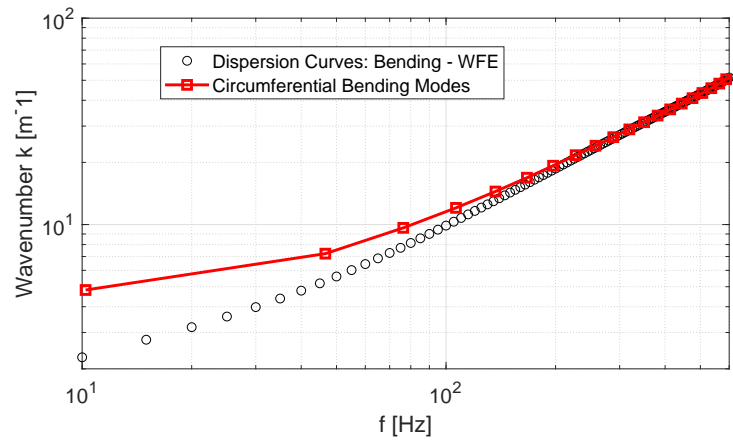


Figure C.20: Bending Waves for the double-wall panel with mechanical connection. Numerical comparison between the WFEM and the present analogy.

### C.5 Conclusions

The proposed analogy proved to be accurate and robust in predicting the dispersion curves of beams and plates through a simple modal analysis of a cylindrical finite element model. The calculations are always well-conditioned for every heading angle chosen, differently from most of the methods present in literature. The results are accurate and the relative error is independent on the cylinder axial length and radii ( $R$ ). A test on a double-wall panels with mechanical connections shows how the features of the method are applicable also to complex structural shapes.

The predictive region can be easily trimmed using different values of the curvature or, instead, using a high value of  $R$  and a fine mesh in order to be able to move from low (low cut-on wavenumber) to high frequencies. The computational cost associated with such meshes, especially for a simple real modal analysis, is not a relevant parameter and, moreover, the numerical conditioning is null.

A generic FE-based code can be used for the purpose and both plate and solid elements have been tested and validated for the accuracy of the results. Again, it must be highlighted that for bending motion, the results start to have an acceptable accuracy (lower than 2%) starting from the fifth modal order. A correct mesh size is required to avoid aliasing problems at higher frequencies.

Further developments might be related to the possibility of predicting also coupled wave-types which arise to higher frequencies and the possibility to include global and through-thickness damping.

# List of Figures

1.1	Typical noise levels in a jet aircraft cabin during take-off and climb to cruising altitude, as described in [1]; A) start of take-off roll; B) lift-off from the runway; C) stabilized level flight at cruising altitude and air speed. . . . .	18
1.2	Typical aeroacoustic loadings on a space launcher structure during the lift-off (a) and the ascent phase (b). . . . .	19
1.3	Conceptual map of the present work. . . . .	21
2.1	Representation of a TBL wall pressure spectrum for different frequency ranges [8]. . . . .	25
2.2	Correlation spectra $\Gamma_{pp}$ in the wavenumber domain [16]. . . . .	28
2.3	Wavenumber–frequency spectra for $S_h = 248$ : —) Corcos [9]; — —) Emtsov [15]; - - -) Smol’yakov and Tkachenko [12]; · · ·) Ffowcs Williams [18]; — — —) Chase I [14]; - - - ·, Chase II [13, 14]. The spectra are plotted against longitudinal wavenumber non-dimensionalized on the convective wavenumber [13].	30
2.4	The structural, convective and acoustic wavelengths versus frequency for a 3mm-thick panel - Flow speed $U_0 = 100m/s$ . . . . .	31
2.5	Sketch of the elastic plate in the rigid aerodynamic baffle. . . . .	32
2.6	The structural and aerodynamic wavelengths versus frequency - Convective speed $U_c = 100m/s$ . . . . .	34
2.7	Graphical sketch of the energy exchange between SEA subsystems. . . . .	35
2.8	Sketch of a multi-layered laterally infinite system with pressure and velocities particles inward and outward of each layer. . . . .	36
2.9	A simple scheme summarizing the main methods for the flow-induced vibrations and noise in finite structures and the frequency ranges where they are applicable, given hypotheses and computational cost. . . . .	36
2.10	Example of buckled cylinder due to inclined supersonic/hypersonic flow [55].	37
2.11	A bi-dimensional periodic structure with rectangular unit cell and its Brillouin zone [74]. . . . .	39
2.12	Example of a FE cell model with periodicity along the X-Y directions. . . . .	41
2.13	Example of an in-plane (X-Y) homogenised FE cell model. . . . .	42
2.14	Two adjacent elementary cells of a waveguide. . . . .	43
3.1	Illustration of degrees of freedom distribution in a transfer matrix framework: target ( $t$ ) degrees of freedom and wetted/loaded ones ( $m$ ). . . . .	48
3.2	The rotation of the global reference into the local one in each location and layer of the cell. . . . .	50
3.3	Waves in a finite waveguide excited by point load. . . . .	52
3.4	Waves in an axial-symmetric jointed structure excited by a point load . . . . .	55

3.5	Mesh adaptation scheme . . . . .	56
3.6	Simple representation of two in-plane jointed waveguides . . . . .	57
3.7	Nodal mobility on the first waveguide for a point load in the second one (see Fig. 3.6). The reference solution is calculated using FEM. Boundary conditions: Free-Free. . . . .	58
3.8	Two waveguides (stiffened cylinders) connected with a complex junction in between. . . . .	59
3.9	Nodal mobility on the first waveguide for a point load (see Fig. 3.8). The reference solution is calculated using FEM. Boundary conditions: Simply-Supported at the edges. . . . .	59
3.10	Axial-symmetric Models analysed - (a) Conical; (b) Cylindrical; (c) Complex - SYLDA . . . . .	60
3.11	The relative substructures of the axial-symmetric models - (a) Cylindrical; (b) Complex - SYLDA . . . . .	61
3.12	Mobility on the cylindrical model [dB ref. 1 m/s] - Numerical comparison between the present technique (formulation for curved wave paths - $\theta WFE$ ) and the full FEM for a point load excitation. . . . .	61
3.13	Mobility on the conical model [dB ref. 1 m/s] - Numerical comparison between the present technique (formulation for curved wave paths - $\theta WFE$ ) and the full FEM for a point load excitation. . . . .	62
3.14	Mobility on the SYLDA model [dB ref. 1 m/s] - Numerical comparison between the present technique (formulation for curved wave paths - $\theta WFE$ ) and the full FEM for a point load excitation. . . . .	62
3.15	The circumferential and coupled modes for the SYLDA test-case; (a) 229.6 Hz, (b) 357.2 Hz, (c) 640.2 Hz, (d) 984.5 Hz . . . . .	63
3.16	A cylindrical structure with impedance variations along the circumference. . . . .	63
3.17	Nodal displacement on the model shown in Fig. 3.16 [dB ref. 1 m] - Numerical comparison between the present technique ( $\theta WFE$ ) and the full FEM for a point load excitation. . . . .	64
3.18	Analytic-Numerical results comparison for a flat panel subjected to TBL - Auto Spectral Density in one point, [dB ref. 1 m/s]. . . . .	66
3.19	Numerical results comparison for a cylinder subjected to TBL - Auto Spectral Density in one point, [dB ref. 1 m/s]. . . . .	66
3.20	Numerical results comparison. Cylinder under TBL (Radius 0.36m) - Auto Spectral Density averaged on four response points, [dB ref. 1 m/s]. . . . .	68
3.21	Numerical results comparison. Cylinder under TBL (Radius 0.20m) - Auto Spectral Density averaged on four response points, [dB ref. 1 m/s]. . . . .	69
3.22	Numerical results comparison. Cylinder under TBL (Radius 0.12m) - Auto Spectral Density averaged on four response points, [dB ref. 1 m/s]. . . . .	69
3.23	The elementary substructure used to analyse the structural response using the $\theta WFE$ method . . . . .	69
3.24	Numerical results comparison for a stiffened cylinder subjected to TBL - Auto Spectral Density in one response point, [dB ref. 1 m/s]. . . . .	70
3.25	Numerical results for the SYLDA models subjected to DAF load - Auto Spectral Density in one point, [dB ref. 1 m/s]. . . . .	71
3.26	A tapered axisymmetric structure, used as a test-case: full finite element model (a); substructure in the framework of the proposed method (b). . . . .	71

3.27	Numerical results comparison for a fairing-like structure under diffuse acoustic excitation - Auto Spectral Density in one point, [dB ref. 1 m/s]. . . . .	72
4.1	Example of a FE cell model with periodicity along the X-Y directions. a) Isometric view; b) Top view with nodes' subsets. . . . .	77
4.2	Rotation of the local system of reference for each node of the periodic cell FE model . . . . .	78
4.3	Global and Local reference systems used for waves along curved structures and shells. a) Global Cartesian reference; b) Local Curved Reference. . . . .	79
4.4	Illustration of an infinite the structure excited by a plane wave and radiating sound. . . . .	79
4.5	Illustration of the two laterally infinite sections representing the structural layer and the porous one. . . . .	82
4.6	Illustration of the load simulation using surface waves in a general test-case. a) Real/Physical situation; b) Simulated case. . . . .	83
4.7	Excited surface comparison between a curved finite panel and its equivalent cylindrical portion. . . . .	85
4.8	A sandwich flat panel under diffuse acoustic field excitation. a) Dispersion curves; b) Transmission Loss comparison with literature references ([153, 154]) in a logarithmic frequency step, between 100 Hz and 10KHz. . . . .	86
4.9	Portion of a double wall flat panel with structural links and the detail of the unit cell analysed . . . . .	87
4.10	Dispersion Curves for the sandwich panel designs in Fig. 4.9. The wavenumbers represent derive from the eigenvalues of Eq. 4.2: a) Double-wall panel with structural link; b) Sandiwch panel with rectangular core. . . . .	88
4.11	Transmission Loss comparison for the sandwich panel designs in Fig. 4.9, under diffuse acoustic field excitation. A logarithmic frequency step, between 100 Hz and 10KHz, is used to generate the curve labelled as <i>Present Method</i> . a) Reference method in [153]; b) Reference method in [37] . . . . .	88
4.12	An aluminium plate under TBL excitation: a) Dispersion curves with convective and acoustic wavenumbers; b) TL numerical comparison with full FEM - $U_c = 180$ m/s; $A = 0.5 \times 0.3 \text{m}^2$ . A logarithmic frequency step, between 100 Hz and 10KHz, is used to generate the curve labelled as <i>Present Method</i> . . . . .	90
4.13	An honeycomb sandwich plate under TBL excitation: a) Dispersion curves with convective and acoustic wavenumbers; b) TL numerical comparison with FEM method - $U_c = 152$ m/s; $A = 0.8 \times 0.6 \text{m}^2$ . A logarithmic frequency step, between 100 Hz and 10KHz, is used to generate the curve labelled as <i>Present Method</i> . . . . .	90
4.14	A comparison of the sound transmission resulting from different of TBL models ( $U_c = 190$ m/s). Flow data (see [13]): $\delta = 0.027$ m; $\delta^* = 0.0018$ m; $u_T = 1.9$ m/s; $\alpha = 0.125$ ; $\beta = 0.83$ . . . . .	91
4.15	An isotropic cylinder under diffuse acoustic field excitation. a) Dispersion curves; b) Sound Transmission Loss comparison with numerical results form [45]. . . . .	92
4.16	Dispersion curves in the circumferential direction of shells of different curvature. The acoustic and convective ( $U_c = 185$ m/s) wavenumbers are shown. . . . .	93

4.17 The effective transmission loss for shells of different curvature -  $U_c = 185$  m/s. A logarithmic frequency step, between 100 Hz and 5KHz, is used to generate the curves. . . . . 93

4.18 A finite curved sandwich composite panel under diffuse acoustic field excitation. a) Dispersion Curves comparison with results from [44]. b) TL comparison with measurements from [44] are compared with the actual method, in third octave bands. . . . . 95

4.19 Illustration of the test facility with coupled reverberant-anechoic rooms. TL measurement following pressure-intensity standard. . . . . 95

4.20 A detail of the reverberant room and the equipments used for the test. . . . 96

4.21 Standard deviation of the whole set of TL measurements following pressure-intensity standard. a) Composite Panel; b) Ribbed Panel . . . . . 96

4.22 A view of the two test panels hanged in the the semi-anechoic chamber. . . . 97

4.23 A view, from the semi-anechoic chamber, of the two test panels mounted in the linking window. Sandwich curved panel configurations: a) bare; b) with attached porous layers. Ribbed fuselage panel configurations: c) bare; d) with attached porous layers. . . . . 97

4.24 The Transmission Loss of a thick curved sandwich panel under diffuse acoustic field excitation. A comparison of the numerical results in log-space with measurements in third octaves. . . . . 99

4.25 The unit cell used for the WFE simulation. The cell has global sizes given by the spacing of frames and stringers (Table 4.4). . . . . 100

4.26 The Transmission Loss of the ribbed fuselage panel for a diffuse acoustic load. A comparison of the numerical results in log-space, with measurements in third octaves. . . . . 100

4.27 The wavenumber spectra of a TBL load (Corcos:  $U_c = 130$  m/s;  $f = 1$  kHz). The fours solutions correspond to the four integration tests performed with variable domains in Eq. 4.21. . . . . 103

4.28 The sound transmission of a flat isotropic panel loaded with TBL (Corcos:  $U_c = 190$  m/s). The fours integration domains is Fig. 4.8 are compared with a fixed mesh in the wavenumber domain. Mesh: a) 50x50; b) 120x120. . . . 104

4.29 The sound transmission of a flat isotropic panel loaded with TBL (Corcos:  $U_c = 190$  m/s). The fours integration domains is Fig. 4.27 are compared with a fixed resolution in the wavenumber domain. Sampling: a) Coarser; b) Finer. . . . . 105

4.30 Normalised wavenumber spectrum of the TBL model ( $f = 1.5$  kHz;  $U_c = 80$  m/s) - a) Corcos [9]; b) Chase II [14]. . . . . 105

4.31 The sound transmission of a flat isotropic panel loaded with TBL (Chase II:  $U_c = 80$  m/s) - a) Comparison of mesh sizes; b) Comparison of integration domains for a 100x100 mesh (Fig. 4.8). Flow data (see [13]):  $\delta = 0.027$  m;  $\delta^* = 0.0018$  m;  $u_T = 1.9$  m/s. . . . . 106

4.32 The sound transmission of a flat isotropic panel loaded with TBL. The wavenumber sampling is studied for single stream-wise and cross-wise resolutions. TBL Model: a) Corcos,  $U_c = 190$  m/s; b) Chase II,  $U_c = 80$  m/s . . . . . 107

5.1 An illustration on the effects of a flexible structure in terms of variation of pressure distribution in a turbulent boundary layer. . . . . 111

5.2	Distribution of degrees of freedom for a single cell with respect to the excited (flow) and radiating side. . . . .	111
5.3	Stream-wise bending waves in a 2mm-thick flat aluminium panel with a one-sided flow at Mach 1.6. Reference solution from [56, 61]: a) Wave Speed; b) Wavenumber. . . . .	114
5.4	Dispersion curves for an aluminium shell (2mm-thick, 1.5m curvature) with a one-sided flow at Mach 2.5: a) Axial Waves; b) Circumferential Waves. Analytical model: Ref. [64].) . . . . .	114
5.5	Dispersion curves for an aluminium shell (2mm-thick, 1.5m curvature) with a one-sided flow at Mach 2.5 and 4.5. Analytical model: Ref. [64]. . . . .	115
5.6	Dispersion curves for an aluminium shell (2mm-thick, 1.5m curvature) with a one-sided flow at Mach 2.5, for increasing circumferential order. Analytical model: Ref. [64]. . . . .	116
5.7	Sound transmission under a supersonic turbulent boundary layer load (Mach 1.35): a) Flat Panel ( $0.5 \times 0.3 \text{ m}^2$ ); b) Curved Panel ( $0.5 \times 0.3 \text{ m}^2$ ; 2m curvature)	116
5.8	Sound transmission under a subsonic turbulent boundary layer load (Mach 0.5): a) Flat Panel ( $0.7 \times 0.5 \text{ m}^2$ ); b) Curved Panel ( $0.7 \times 0.5 \text{ m}^2$ ; 2m curvature).	117
5.9	Sound transmission loss of a sandwich flat panel ( $0.8 \times 0.6 \text{ m}^2$ ) under a subsonic turbulent boundary layer load at Mach 0.62. . . . .	118
6.1	Cell models extracted from a Double-Wall Panel with Mechanical links. a) Standard design. b) Proposed Design. . . . .	120
6.2	Cell models extracted from a Sandwich Panel with Rectangular Core. a) Standard design. b) Proposed Design. . . . .	121
6.3	Work-flow scheme for panel design optimisation based on numerical and experimental data. . . . .	122
6.4	Illustration of the test facility with un-coupled reverberant-anechoic rooms for transmission loss measurements. . . . .	123
6.5	Facility and frame details: a) wooden external adaptive frame; b) clamping system on the internal chamber side; c) view of the open room with reflective panels and microphones. . . . .	123
6.6	The 3D-printed panels front-view following the standard (left) and proposed (right) designs for the double-wall panel with mechanical links. . . . .	123
6.7	The 3D-printed panels front-view following the standard (left) and proposed (right) designs for the sandwich panel with rectangular core. . . . .	124
6.8	Dispersion Curves of the Double-Wall Panel designs; eigenvalue solutions of the eigenvalue problem in Eq. 4.2. . . . .	124
6.9	Wavemodes of the Double-Wall Panel designs for waves propagating in $x$ direction; eigenvector solutions of the eigenvalue problem in Eq. 4.2. a) $f = 4.5 \text{ kHz}$ ; b) $f = 6.5 \text{ kHz}$ . . . . .	125
6.10	Dispersion Curves of the Sandwich Panel with Rectangular core designs; eigenvalue solutions of the eigenvalue problem in Eq. 4.2. . . . .	126
6.11	Wavemodes of the Sandwich Panel with Rectangular core designs for waves propagating in $x$ direction; eigenvector solutions of the eigenvalue problem in Eq. 4.2. a) $f = 4.0 \text{ kHz}$ ; b) $f = 6.0 \text{ kHz}$ . . . . .	126
6.12	Calculated Transmission Loss for infinite panels the proposed designs. a) Double-Wall panels designs; b) Rectangular-Cored Sandwich panel designs. . . . .	127

6.13 Measured Transmission Loss for the 3D-printed panels. Total panel surface: 0.40x0.35 m<sup>2</sup>. Exposed panel surface: 0.34x0.29 m<sup>2</sup>. a) Double-Wall panels designs; b) Rectangular-Cored Sandwich panel designs. . . . . 128

6.14 Front view of the stiffeners cross-section: a) *T-shape*; b) *H-shape*; c) *Ω-shape*. 130

6.15 Direction of the flow on the shell for: a) Axial stiffeners; b) Ring Stiffeners. 130

6.16 Sound Transmission Loss for the stiffened panels under DAF excitation: a) *T-shape*; b) *H-shape*; c) *Ω-shape*. . . . . 132

6.17 Sound Transmission Loss for the stiffened panels under DAF and TBL excitations: a) *T-shape*; b) *H-shape*; c) *Ω-shape*... . . . . 132

6.18 Wavenumber transforms for the structures and the load model at 1.5kHz: a) Unstiffened Shell; b) Shell with Axial *T* shaped Stiffeners; c) Shell with Ring *T* shaped Stiffeners; d) DAF and TBL load spectra. . . . . 133

6.19 Sound Transmission Loss for the *T* shape stiffened panels with different pitch distances: a) Ring Stiffeners and DAF load; b) Axial Stiffeners and DAF load; c) Ring Stiffeners and DAF + TBL load; d) Axial Stiffeners and DAF + TBL load. . . . . 134

6.20 Illustration of the inclination of the single plane wave exciting the panel. . . 135

6.21 Sound Transmission Loss of for the auxetic-cored sandwich panel in Fig. 6.28 with a mis-tuned resonant element: a)  $\theta = \pi/2, \alpha = 0$ ; b)  $\theta = \pi/4, \alpha = 0$ ; c)  $\theta \approx \pi/2, \alpha = \pi/2$ ; d)  $\theta \approx \pi/2, \alpha = \pi/4$ ; . . . . . 136

6.22 Sound Transmission Loss of for a 12mm-thick aluminium honeycomb panel with a properly-tuned resonant element: a)  $\theta \approx \pi/2, \alpha = 0$ ; b)  $\theta \approx \pi/2, \alpha = \pi/2$ ; c)  $\theta = \pi/4, \alpha = 0$ ; d)  $\theta = \pi/4, \alpha = \pi/2$ ; . . . . . 136

6.23 Dispersion Curves - The bending wavenumbers of a flat isotropic plate with: a) acoustic wavenumbers for different plane wave angles. b) convective wavenumbers for different flow speeds . . . . . 137

6.24 The sound transmission loss of a shell for different angles of incidence. . . . 138

6.25 Illustration of ring mode of a shell (a) and the potential applications for resonant metamaterials (b). . . . . 138

6.26 The sound transmission loss of a curved shell with embedded resonators as in Fig. 6.25: a)  $\theta \approx \pi/2, \alpha = \pi/2$ ; b)  $\theta \approx \pi/2, \alpha = 0$ ; . . . . . 139

6.27 The periodic cell extracted from the double-wall panel with mechanical links. a) Standard design; b) Designs with Resonant Elements. . . . . 139

6.28 The periodic cell extracted from the Auxetic-Cored Sandwich Plate. a) Standard design; b) Designs with single Resonant Elements; c) Designs with triple Resonant Elements. . . . . 140

6.29 Dispersion curves for the double-wall panel with a 1.6m curvature. With reference to Table 6.3: a) D2; b) D3; c) D1. Legend: Or) Standard Configuration; .b) Resonant Configurations; -) Convective Wavenumbers for  $U_c = 160$  m/s. . . . . 141

6.30 Dispersion curves for the Auxetic-cored sandwich panel with a 1.0 m curvature. With reference to Table 6.4: a) C1; b) C2; c) C4. Legend: Or) Standard Configuration; .b) Resonant Configurations; -) Convective Wavenumbers for  $U_c = 285$  m/s. . . . . 142

6.31 The sound transmission loss of the panel design in Fig. 6.27, with a 1.6 m curvature, under a TBL excitation at  $U_c = 160$  m/s. Comparison between design configurations in Table 6.3. . . . . 142

6.32 The sound transmission loss of the panel design in Fig. 6.28, with a 1.0 m curvature, under a TBL excitation at  $U_c = 285$  m/s. Comparison between design configurations in Table 6.4. . . . . 143

6.33 The effective sound transmission loss of the panel design in Fig. 6.28, with a 1.0 m curvature, under simultaneous TBL and DAF excitation at  $U_c = 285$  m/s. Comparison with design configuration C4. . . . . 144

A.1 Cell model extracted from the optimized double-wall panel with mechanical links. Distances in millimetres. . . . . 151

A.2 Cell model extracted from the optimized sandwich panel with rectangular core. Distances in millimetres. . . . . 152

B.1 Simplified tyre model with shell elements. Tyre Configuration: a) Bare; b) Resonant. Target: c) Transversal Vibrations; d) Radial Vibrations. . . . . 154

B.2 First four modes of the bare tyre. Transversal Modes: a) 243.6 Hz; b) 338.5 Hz; c) 610.6 Hz. Radial Mode: d) 702.4 Hz. . . . . 155

B.3 Average structural mobility of the tyre with and w/o mechanical resonators for transversal vibration control. . . . . 156

B.4 Average structural mobility of the tyre with and w/o mechanical resonators for radial vibration control. . . . . 156

C.1 The analogy proposed: (a) Free wave propagation along an infinite flat waveguide; (b) equivalence in a circular topology generated from the original model. 163

C.2 Purely circumferential bending modes in a circular structure: (a) Circumferential Order = 2; (b) Circumferential Order = 3; (c) Circumferential Order = 4; (d) Circumferential Order = 5. . . . . 164

C.3 Bending, shear and longitudinal wavemodes wavelength in an infinite beam and the corresponding beam-ring circumferential modes . . . . . 165

C.4 Relative error (log-scale) between the bending wavelength in an infinite panel and the modal wavelengths of an infinite cylinder . . . . . 166

C.5 Bending wavelength in an infinite panel and the ovaling modes of an infinite cylinder . . . . . 166

C.6 Isotropic uniform plate: infinite panel solution and the circumferential modes of a cylindrical finite structure made of plate elements . . . . . 167

C.7 Comparison for increasing number of elements for a given element size . (a) 32, (b) 80, (c) 300 elements . . . . . 168

C.8 Comparison for increasing number of elements for a given circumference radii  $R$ . From the left side: 8, 32, 80 elements . . . . . 168

C.9 Effect of the mesh: comparison for increasing number of elements for a given circumference radii  $R$  (isotropic panel). Elements size variable. . . . . 168

C.10 Effect of the mesh: comparison for increasing number of elements for a given element size (isotropic panel). Circumference radii  $R$  variable: Fig. C.7(a) 0.05 m, Fig. C.7(b) 0.13 m, Fig. C.7(c) 0.48 m . . . . . 169

C.11 Scheme of the laminate heading angle with respect to the wave propagation direction. . . . . 169

C.12 Dispersion curves of the laminate panel; heading angle  $0^\circ$ . CLPT results used as a reference. . . . . 170

C.13 Dispersion curves of the laminate panel; heading angle  $90^\circ$ . CLPT results used as a reference. . . . . 170

C.14 Dispersion curves of the laminate panel; heading angle $45^\circ$ . CLPT results used as a reference. . . . .	171
C.15 Relative errors (log-scale) for different heading angles (bending waves). The CLPT results used as reference. . . . .	171
C.16 Pattern of the bending wavenumbers for the laminate plate analysed; 3000 Hz	172
C.17 Purely circumferential modes in a laminate infinite panel; X-Y as cross sectional plane. Fourth circumferential mode - (a) Bending: 16.6 Hz; (b) Shear: 1364 Hz; (c) Longitudinal: 4674 Hz . . . . .	172
C.18 Rectified circumferential modes in a laminate infinite panel; X-Y as cross sectional plane. Fourth circumferential mode - (a) Bending: 16.6 Hz; (b) Shear: 1364 Hz; (c) Longitudinal: 4674 Hz . . . . .	173
C.19 A double-wall panel with mechanical connection: (a) Elementary FE Cell; (b) Cylindrical Model. . . . .	173
C.20 Bending Waves for the double-wall panel with mechanical connection. Numerical comparison between the WFEM and the present analogy. . . . .	174

# List of Tables

2.1	TBL autospectrum models and input parameters . . . . .	27
3.2	Cylinder Geometry . . . . .	58
3.1	Material constants for cylinder skins . . . . .	58
3.3	Hat-Stiffener Geometry . . . . .	58
3.4	Axial-symmetric models geometrical parameters . . . . .	60
3.5	Panel geometrical parameters . . . . .	65
3.6	Computational cost comparison for a flat panel to TBL load . . . . .	65
3.7	Computational cost for a cylindrical structure to TBL load . . . . .	67
3.8	Material Data of the Lamina . . . . .	67
3.9	Stacking Sequences . . . . .	67
3.10	Stiffeners geometrical parameters . . . . .	68
3.11	Computational cost for a stiffened cylindrical structure to TBL load . . . . .	70
3.12	Computational cost for a complex axial-symmetric structure to DAF load . . . . .	71
4.1	Materials' properties for curved finite panels transmission loss validation . . . . .	94
4.2	Material properties for the thick curved composite sandwich panel. . . . .	98
4.3	Physical properties for the porous layers attached to the panels [165]. . . . .	98
4.4	Geometrical parameters of the ribbed fuselage panel. . . . .	98
4.5	Integration limits in the wavenumber domain (see Fig. 4.8) . . . . .	103
5.1	Materials' properties of the sandwich plate. . . . .	117
5.2	Computational cost comparison for an Intel(R) Core(TM) i7-7700 CPU 3.60GHz processor (16Gb RAM). . . . .	118
6.1	Expected and Measured weights of the 3D-printed panels . . . . .	128
6.2	Cross-section properties of the stiffeners. . . . .	129
6.3	Double-Wall plate with mechanical links: Configurations Info . . . . .	140
6.4	Auxetic-Cored Sandwich Plate: Configurations Info . . . . .	140
C.1	Lamina elastic properties and stacking sequence . . . . .	168



# Bibliography

- [1] Bishop, D. E., “Cruise Flight Noise Levels in a Turbojet Transport Airplane,” *Noise Control*, Vol. 7, No. 2, 1961, pp. 37–42. doi:10.1121/1.2369437, URL <https://doi.org/10.1121/1.2369437>.
- [2] Bhat., W., “Flight test measurement of measurement of exterior turbulent boundary layer pressure uctuations on boeing model 737 airplane,” *Journal of Sound and Vibration*, Vol. 14(4), 1971, pp. 439–457.
- [3] da Rocha, J. L. T., “Coupled Structural-Acoustic Analytical Models for the Prediction of Turbulent Boundary-Layer-Induced Noise in Aircraft Cabins,” *PhD thesis*, Vol. University of Victoria, 2010.
- [4] Waye, K., “On the effects on environmental low frequency noise,” *Technical report*, Vol. Department of Environmental Medicine, Goteborg University Publication, 1995.
- [5] Elishakoff, I., “Probabilistic Method in Theory of Structures,” *John Wiley and Sons*, 1983, p. New York. doi:/10.2514/3.48790.
- [6] Ichchou, M., Hiverniau, B., and Troclet, B., “Equivalent ‘rain on the roof’ loads for random spatially correlated excitations in the mid frequency range,” *Journal of Sound and Vibration*, Vol. 322, 2009, pp. 926–940. doi:/10.1016/j.jsv.2008.11.050.
- [7] De Rosa, S., and Franco, F., “Exact and numerical responses of a plate under a turbulent boundary layer excitation,” *Journal of Fluids and Structures*, Vol. 24, 2008, pp. 212–230. doi:/10.1016/j.jfluidstructs.2007.07.007.
- [8] Hwang, Y., Bonness, W. K., and Hambric, S. A., “Comparison of semi-empirical models for turbulent boundary layer wall pressure spectra,” *Journal of Sound and Vibration*, Vol. 319, No. 1, 2009, pp. 199 – 217. doi:/10.1016/j.jsv.2008.06.002, URL <http://www.sciencedirect.com/science/article/pii/S0022460X08005506>.
- [9] Corcos, G., “Resolution of pressure in turbulence,” *Journal of the Acoustical Society of America*, Vol. 35, 1963, pp. 192–199. doi:/10.1121/1.1918431.
- [10] Finnveden, S., Birgersson, F., Ross, U., and Kremer, T., “A model of wall pressure correlation for prediction of turbulence-induced vibration,” *Journal of Fluids and Structures*, Vol. 20, No. 8, 2005, pp. 1127 – 1143. doi:/10.1016/j.jfluidstructs.2005.05.012, URL <http://www.sciencedirect.com/science/article/pii/S0889974605000885>.
- [11] Cockburn, J., and Robertson, J., “Vibration response of spacecraft shrouds to in-flight fluctuating pressures,” *Journal of Sound and Vibration*, Vol. 33, No. 4, 1974, pp. 399–425. doi:/10.1016/S0022-460X(74)80226-9.

- [12] Smol'yakov, A., and Tkachenko, V., "Model of pseudosonic turbulent wall pressures and experimental data," *Soviet Physics—Acoustic*, Vol. 37 (6), 1991, pp. 627–631. doi:/10.1121/1.4960516.
- [13] Graham, W., "A Comparison of models for the wavenumber-frequency spectrum of turbulent boundary layer pressures," *Journal of Sound and Vibration*, Vol. 206(4), 1997, pp. 541–565. doi:/10.1006/jsvi.1997.1114.
- [14] Chase, D., "Modelling the wavevector-frequency spectrum of turbulent boundary layer wall pressure," *Journal of Sound and Vibration*, Vol. 70 (1), 1953, pp. 29–67. doi:/10.1016/0022-460X(80)90553-2.
- [15] Efimtsov, B., "Characteristics of the field of turbulent wall pressure fluctuations at large Reynolds numbers," *Soviet Physics—Acoustics*, Vol. 28 (4), 1982, pp. 289–292.
- [16] Howe, M. S., "Surface pressures and sound produced by turbulent flow over smooth and rough walls," *The Journal of the Acoustical Society of America*, Vol. 90, No. 2, 1991, pp. 1041–1047. doi:10.1121/1.402292, URL <https://doi.org/10.1121/1.402292>.
- [17] Blake, W. K., *Mechanics of Flow-Induced Sound and Vibration, Volume 2 (Second Edition)*, second edition ed., Academic Press, 2017. doi:/10.1016/B978-0-12-809274-3.00002-7, URL <http://www.sciencedirect.com/science/article/pii/B9780128092743000027>.
- [18] Williams, J. F., "Boundary layer pressures and the Corcos model: a development to incorporate low wavenumber constraints," *Journal of Fluid Mechanics*, Vol. 125, 1982, pp. 9–25. doi:/10.1017/S0022112082003218.
- [19] Ciappi, E., Magionesi, F., Rosa, S. D., and Franco, F., "Analysis of the scaling laws for the turbulence driven panel responses," *Journal of Fluids and Structures*, Vol. 32, 2012, pp. 90–103. doi:/10.1016/j.jfluidstructs.2011.11.003.
- [20] Hambric, S., Hwang, Y., and Bonness, W., "Vibrations of plates with clamped and free edges excited by low-speed turbulent boundary layer flow," *Journal of Fluids and Structures*, Vol. 19, No. 1, 2004, pp. 93–110. doi:/10.1016/j.jfluidstructs.2003.09.002.
- [21] Franco, F., De Rosa, S., and Ciappi, E., "Numerical approximations on the predictive responses of plates under stochastic and convective loads," *Journal of Fluids and Structures*, Vol. 42, 2013, pp. 296–312. doi:/10.1016/j.jfluidstructs.2013.06.006.
- [22] Rocha, J., "Impact of the chosen turbulent flow empirical model on the prediction of sound radiation and vibration by aircraft panels," *Journal of Sound and Vibration*, Vol. 373, 2016, pp. 285 – 301. doi:/10.1016/j.jsv.2016.03.026, URL <http://www.sciencedirect.com/science/article/pii/S0022460X16300013>.
- [23] De Rosa, S., F.Franco, and E.Ciappi, "A simplified method for the analysis of the stochastic response in discrete coordinates," *Journal of Sound and Vibration*, Vol. 339, 2015, pp. 359–375. doi:/10.1016/j.jsv.2014.11.010.
- [24] De Rosa, S., and Franco, F., "A scaling procedure for the response of an isolated system with high modal overlap factor," *Mechanical Systems and Signal Processing*, Vol. 22, 2008, pp. 1549–1565. doi:/10.1016/j.ymsp.2008.01.007.
- [25] Rosa, S. D., Franco, F., Capasso, D., and Costagliola, S., "The effect of concentrated masses on the response of a plate under a turbulent boundary layer excitation," *Mechanical Systems and Signal Processing*, Vol. 25, No. 4, 2011, pp. 1192 – 1203. doi:https://doi.org/10.1016/j.ymsp.2010.11.011, URL <http://www.sciencedirect.com/science/article/pii/S0888327010004140>.

- [26] Ciappi, E., Rosa, S. D., Franco, F., Vitiello, P., and Miozzi, M., “On the dynamic behavior of composite panels under turbulent boundary layer excitations,” *Journal of Sound and Vibration*, Vol. 364, 2016, pp. 77 – 109. doi:/10.1016/j.jsv.2015.11.024, URL <http://www.sciencedirect.com/science/article/pii/S0022460X15009219>.
- [27] Vitiello, P., Rosa, S. D., and Franco, F., “Convected field analysis of flat panels response to turbulent boundary layer induced excitation,” *Aerospace Science and Technology*, Vol. 12, No. 1, 2008, pp. 91 – 104. doi:<https://doi.org/10.1016/j.ast.2007.10.003>, URL <http://www.sciencedirect.com/science/article/pii/S1270963807001241>.
- [28] Bonness, W. K., Fahnline, J. B., Lysak, P. D., and Shepherd, M. R., “Modal forcing functions for structural vibration from turbulent boundary layer flow,” *Journal of Sound and Vibration*, Vol. 395, 2017, pp. 224 – 239. doi:/10.1016/j.jsv.2017.02.023, URL <http://www.sciencedirect.com/science/article/pii/S0022460X17301177>.
- [29] Maxit, L., “Simulation of the pressure field beneath a turbulent boundary layer using realisations of uncorrelated wall plane waves,” *Journal of the Acoustical Society of America*, Vol. 140, 2016, pp. 1268–1285.
- [30] Birgersson, F., Ferguson, N., and Finnveden, S., “Application Of The Spectral Finite Element Method To Turbulent Boundary Layer Induced Vibration Of Plates,” *Journal of Sound and Vibration*, Vol. 259, No. 4, 2003, pp. 873 – 891. doi:/10.1006/jsvi.2002.5127, URL <http://www.sciencedirect.com/science/article/pii/S0022460X02951278>.
- [31] Ichchou, M., Bareille, O., and Jacques, Y., “Energy predictions of turbulent boundary layer induced mid-high frequency structural vibrations,” *Journal of Wind Engineering and Industrial Aerodynamics*, Vol. 97, No. 2, 2009, pp. 63 – 76. doi:<https://doi.org/10.1016/j.jweia.2008.11.001>, URL <http://www.sciencedirect.com/science/article/pii/S0167610508001761>.
- [32] Finnveden, S., “Evaluation of modal density and group velocity by a finite element method,” *Journal of Sound and Vibration*, Vol. 273, No. 1, 2004, pp. 51 – 75. doi:/10.1016/j.jsv.2003.04.004, URL <http://www.sciencedirect.com/science/article/pii/S0022460X03008897>.
- [33] Orrenius, U., Liu, H., Wareing, A., Finnveden, S., and Cotoni, V., “Wave modelling in predictive vibro-acoustics: Applications to rail vehicles and aircraft,” *Wave Motion*, Vol. 51, No. 4, 2014, pp. 635–649. doi:/10.1016/j.wavemoti.2013.11.007.
- [34] Orrenius, U., Cotoni, V., and Wareing, A., “Analysis of sound transmission through aircraft fuselages excited by turbulent boundary layer or diffuse acoustic pressure fields,” *38th International Congress and Exposition on Noise Control Engineering 2009, INTER-NOISE 2009*, Vol. 4, 2009, pp. 2637–2645.
- [35] Allard, J., and Atalla, N., “Propagation of Sound in Porous Media: Modelling Sound Absorbing Materials,” *John Wiley & Sons*, 2009. doi:/10.1002/9780470747339.
- [36] Atalla, N., “Modelling the sound transmission through complex structures with attached noise control materials,” *Wave Motion*, Vol. 51, 2014, pp. 650–663. doi:/10.1016/j.wavemoti.2013.11.001.
- [37] Parrinello, A., and Ghiringhelli, G., “Transfer matrix representation for periodic planar media,” *Journal of Sound and Vibration*, Vol. 371, 2016, pp. 196–209. doi:/10.1016/j.jsv.2016.02.005.
- [38] Rhazi, D., and Atalla, N., “A simple method to account for finite size effects in the transfer matrix method,” *J. Acoust. Soc. Am.*, Vol. 127 (2), 2010, pp. EL30–EL36. doi:/10.1121/1.3280237.

- [39] Leppington, F., Broadbent, E., and Heron, K., "The acoustic radiation efficiency from rectangular plates," *Proc. R. Soc.*, Vol. 382, 1982, pp. 245–271. doi:/10.1098/rspa.1982.0100.
- [40] Villot, M., Guigou, C., and Gagliardini, L., "Predicting the Acoustical Radiation of Finite Size Multi-Layered Structures by Applying Spatial Windowing on Infinite Structures," *Journal of Sound and Vibration*, Vol. 245, No. 3, 2001, pp. 433–455. doi:/10.1006/jsvi.2001.3592.
- [41] Koval, L., "On sound transmission into an orthotropic shell," *Journal of Sound and Vibration*, Vol. 63 (1), 1979, pp. 51–59. doi:/10.1016/0022-460X(79)90376-6.
- [42] Koval, L., "Sound transmission into a laminated composite cylindrical shell," *Journal of Sound and Vibration*, Vol. 71, No. 4, 1980, pp. 523–530. doi:/10.1016/0022-460X(80)90724-5.
- [43] Koval, L., "On sound transmission into a thin cylindrical shell under "flight conditions"," *Journal of Sound and Vibration*, Vol. 48, No. 2, 1976, pp. 265–275. doi:/10.1016/0022-460X(76)90465-X.
- [44] Ghinet, S., Atalla, N., and Osman, H., "The transmission loss of curved laminates and sandwich composite panels," *J. Acoust. Soc. Am.*, Vol. 118 (2), 2005, pp. 774–790. doi:/10.1121/1.1932212.
- [45] Ghinet, S., Atalla, N., and Osman, H., "Diffuse field transmission into infinite sandwich composite and laminate composite cylinders," *Journal of Sound and Vibration*, Vol. 289, 2006, pp. 745–778. doi:/10.1016/j.jsv.2005.02.028.
- [46] Liu, B., Feng, L., and Nilsson, A., "Sound transmission through curved aircraft panels with stringer and ring frame attachments," *Journal of Sound and Vibration*, Vol. 300, 2007, pp. 949–973. doi:/10.1016/j.jsv.2006.09.008.
- [47] Liu, B., "Noise radiation of aircraft panels subjected to boundary layer pressure fluctuations," *Journal of Sound and Vibration*, Vol. 314, 2008, pp. 693–711. doi:/10.1016/j.jsv.2008.01.045.
- [48] Dowell, E., *Aeroelasticity of Plates and Shells*, Mechanics: Dynamical Systems, Springer Netherlands, 1974. URL <https://books.google.fr/books?id=qRpof4bV-VoC>.
- [49] Bisplinghoff, R., *Aeroelasticity*, Addison-Wesley series in mechanics, Addison-Wesley Pub. Co., 1955. URL <https://books.google.fr/books?id=uP9TAAAMAAJ>.
- [50] E.H. Dowell, C. V., "Flutter of Low Aspect Ratio Plates," *AIAA Journal*, Vol. 8 (6), 1970, pp. 1162–1164. doi:/10.2514/3.5858.
- [51] Amabili, M., and Pellicano, F., "Nonlinear supersonic flutter of circular cylindrical shells," *AIAA journal*, Vol. 39, No. 4, 2001, pp. 564–573. doi:/10.2514/2.1365.
- [52] Amabili, M., Pellicano, F., and Paidoussis, M., "Non-Linear Dynamics and Stability of Circular Cylindrical Shells Containing Flowing Fluid. Part I: Stability," *Journal of Sound and Vibration*, Vol. 225, No. 4, 1999, pp. 655 – 699. doi:/10.1006/jsvi.1999.2255, URL <http://www.sciencedirect.com/science/article/pii/S0022460X99922551>.
- [53] Amabili, M., Pellicano, F., and Paidoussis, M. P., "Non-linear dynamics and stability of circular cylindrical shells conveying flowing fluid," *Computers Structures*, Vol. 80, No. 9, 2002, pp. 899 – 906. doi:/10.1016/S0045-7949(02)00055-X, URL <http://www.sciencedirect.com/science/article/pii/S004579490200055X>.
- [54] Amabili, M., and Pellicano, F., "Multimode Approach to Nonlinear Supersonic Flutter of Imperfect Circular Cylindrical Shells," *J. Appl. Mech*, Vol. 69, No. 2, 2001, pp. 117 – 129. doi:/10.1115/1.1435366.

- [55] Klock, R. J., and Cesnik, C. E., “Local Aeroelastic Instability of High-Speed Cylindrical Vehicles,” *AIAA Journal*, 2019, pp. 1–9. doi:/10.2514/1.J057705.
- [56] Miles, J., “On the Aerodynamic Instability of Thin Panels,” *Journal of the Aeronautical Sciences*, Vol. 23 (8), 1956, pp. 771–791.
- [57] Miles, J., “Supersonic Flutter of A Cylindrical Shell,” *Journal of the Aeronautical Sciences*, Vol. 24, 1957, pp. 107–118. doi:/10.2514/3.5858.
- [58] Sinha, B. K., Plona, T. J., Kostek, S., and Chang, S., “Axisymmetric wave propagation in fluid-loaded cylindrical shells. I: Theory,” *The Journal of the Acoustical Society of America*, Vol. 92, No. 2, 1992, pp. 1132–1143. doi:10.1121/1.404040, URL <https://doi.org/10.1121/1.404040>.
- [59] Benjamin, T. B., “The threefold classification of unstable disturbances in flexible surfaces bounding inviscid flows,” *Journal of Fluid Mechanics*, Vol. 16, No. 3, 1963, p. 436–450. doi:/10.1017/S0022112063000884.
- [60] Crighton, D. G., and Oswell, J. E., “Fluid loading with mean flow. I. Response of an elastic plate localized excitation,” *Philosophical Transactions of the Royal Society of London. Series A: Physical and Engineering Sciences*, Vol. 335, No. 1639, 1991, pp. 557–592. doi:10.1098/rsta.1991.0060, URL <https://royalsocietypublishing.org/doi/abs/10.1098/rsta.1991.0060>.
- [61] Dugundji, J., Dowell, E., and Perkin, B., “Subsonic Flutter of Panels on Continuous Elastic Foundations,” *AIAA Journal*, Vol. 1 (5), 1963, pp. 1146–1154. doi:/10.2514/3.1738.
- [62] Atkins, D. J., “The Effect of Uniform Flow on the Dynamics and Acoustics of Force-Excited Infinite Plates,” *No. AMTE (N)/TM82087 - ADMIRALTY MARINE TECHNOLOGY ESTABLISHMENT TEDDINGTON*, 1982. URL <https://apps.dtic.mil/docs/citations/ADA124576>.
- [63] Lucey, A. D., “The excitation of waves on a flexible panel in a uniform flow,” *Philosophical Transactions of the Royal Society of London. Series A: Mathematical, Physical and Engineering Sciences*, Vol. 356, No. 1749, 1998, pp. 2999–3039. doi:10.1098/rsta.1998.0306, URL <https://royalsocietypublishing.org/doi/abs/10.1098/rsta.1998.0306>.
- [64] PEAKE, N., “On the behaviour of a fluid-loaded cylindrical shell with mean flow,” *Journal of Fluid Mechanics*, Vol. 338, 1997, p. 387–410. doi:/10.1017/S0022112097005144.
- [65] Olson, M. D., *Supersonic Flutter of Circular Cylindrical Shells*, PhD Thesis, California Institute of Technology, 1966. URL <http://resolver.caltech.edu/CaltechETD:etd-12022005-075701>.
- [66] Fung, Y., and Olson, M., “Supersonic flutter of circular cylindrical shells subjected to internal pressure and axial compression,” *AIAA Journal*, Vol. 4, No. 5, 1966, pp. 858–864. doi:/10.2514/3.3558.
- [67] Horn, W., Barr, G., Carter, L., and Stearman, A. D., “Recent Contributions to Experiments on Cylindrical Shell Panel Flutter,” *AIAA journal*, Vol. 12, No. 11, 1974, pp. 1481–1490. doi:/10.2514/3.49533.
- [68] Sorokin, S., and Peake, N., “On symmetry-breaking effects in propagation of waves in sandwich plates with and without heavy fluid loading,” *Journal of Sound and Vibration*, Vol. 295, No. 1, 2006, pp. 114 – 128. doi:/10.1016/j.jsv.2005.12.055, URL <http://www.sciencedirect.com/science/article/pii/S0022460X06001015>.

- [69] Bloch, F., “Über die Quantenmechanik der Elektronen in Kristallgittern,” *Zeitschrift für Physik*, Vol. 52, No. 7, 1929, pp. 555–600. doi:10.1007/BF01339455, URL <https://doi.org/10.1007/BF01339455>.
- [70] Floquet, G., “Sur les équations différentielles linéaires à coefficients périodiques,” *Annales scientifiques de l’École Normale Supérieure*, Vol. 2e série, 12, 1883, pp. 47–88. doi:10.24033/asens.220, URL [http://www.numdam.org/item/ASENS\\_1883\\_2\\_12\\_\\_47\\_0](http://www.numdam.org/item/ASENS_1883_2_12__47_0).
- [71] Bragg, W. H., and Bragg, W. L., “The reflection of X-rays by crystals,” *Proceedings of the Royal Society of London. Series A, Containing Papers of a Mathematical and Physical Character*, Vol. 88, No. 605, 1913, pp. 428–438. doi:10.1098/rspa.1913.0040.
- [72] Brillouin, L., “Wave Propagation in Periodic Structures: Electric Filters and Crystal Lattices,” *2nd edition*, Vol. Dover Publications, No. Mineola, New York, 1953. doi:10.1016/S0031-8914(53)80099-6.
- [73] Mead, D., “Wave propagation in continuous periodic structures: research contributions from Southampton,” *Journal of Sound and Vibration*, Vol. 190 (3), 1996, pp. 495–524. doi:10.1006/jsvi.1996.0076.
- [74] Zhou, C., “Wave and modal approach for multi-scale analysis of periodic structures,” *PhD thesis*, Vol. Ecole Centrale de Lyon, 2014.
- [75] Ruzzene, M., Scarpa, F., and Soranna, F., “Wave beaming effects in two-dimensional cellular structures,” *Smart Materials and Structures*, Vol. 12, No. 3, 2003, pp. 363–372. doi:10.1088/0964-1726/12/3/307, URL <https://doi.org/10.1088/0964-1726/12/3/307>.
- [76] Goffaux, C., Sánchez-Dehesa, J., Yeyati, A. L., Lambin, P., Khelif, A., Vasseur, J. O., and Djafari-Rouhani, B., “Evidence of Fano-Like Interference Phenomena in Locally Resonant Materials,” *Phys. Rev. Lett.*, Vol. 88, 2002, p. 225502. doi:10.1103/PhysRevLett.88.225502, URL <https://link.aps.org/doi/10.1103/PhysRevLett.88.225502>.
- [77] Liu, Z., Chan, C. T., and Sheng, P., “Three-component elastic wave band-gap material,” *Phys. Rev. B*, Vol. 65, 2002, p. 165116. doi:10.1103/PhysRevB.65.165116, URL <https://link.aps.org/doi/10.1103/PhysRevB.65.165116>.
- [78] Achaoui, Y., Khelif, A., Benchabane, S., Robert, L., and Laude, V., “Experimental observation of locally-resonant and Bragg band gaps for surface guided waves in a phononic crystal of pillars,” *Phys. Rev. B*, Vol. 83, 2011, p. 104201. doi:10.1103/PhysRevB.83.104201, URL <https://link.aps.org/doi/10.1103/PhysRevB.83.104201>.
- [79] Manconi, E., “Modelling Wave Propagation in Two-Dimensional Structures Using a Wave/Finite Element Technique,” *PhD thesis*, Vol. Department of Industrial Engineering, University of Parma, 2008. URL <http://dspace-unipr.cineca.it/handle/1889/935>.
- [80] Barbieri, E., Cammarano, A., De Rosa, S., and Franco, F., “Waveguides of a Composite Plate by using the Spectral Finite Element Approach,” *Journal of Vibration and Control*, Vol. 15 (3), 2009, pp. 347–367. doi:10.1177/1077546307087455.
- [81] Orris, R. M., and Petyt, M., “A finite element study of harmonic wave propagation in periodic structures,” *Journal of Sound and Vibration*, Vol. 33, No. 2, 1974, pp. 223 – 236. doi:10.1016/S0022-460X(74)80108-2, URL <http://www.sciencedirect.com/science/article/pii/S0022460X74801082>.
- [82] Thompson, D., “Wheel-rail Noise Generation, Part III: Rail Vibration,” *Journal of Sound and Vibration*, Vol. 161, No. 3, 1993, pp. 421 – 446. doi:10.1006/jsvi.1993.1084, URL <http://www.sciencedirect.com/science/article/pii/S0022460X83710849>.

- [83] Gry, L., “Dynamic Modelling of Railway Track Based on Wave Propagation,” *Journal of Sound and Vibration*, Vol. 195, No. 3, 1996, pp. 477 – 505. doi:/10.1006/jsvi.1996.0438, URL <http://www.sciencedirect.com/science/article/pii/S0022460X96904381>.
- [84] Mencik, J.-M., and Ichchou, M., “Wave finite elements in guided elastodynamics with internal fluid,” *International Journal of Solids and Structures*, Vol. 44(7.8), 2007, pp. 2148–2167. doi:/10.1016/j.ijsolstr.2006.06.048.
- [85] Mencik, J.-M., “On the low- and mid-frequency forced response of elastic structures using wave finite elements with one-dimensional propagation,” *Computers and Structures*, Vol. 88, 2010, pp. 674–689. doi:/10.1016/j.compstruc.2010.02.006.
- [86] Mace, B. R., Duhamel, D., Brennan, M. J., and Hinke, L., “Finite element prediction of wave motion in structural waveguides,” *The Journal of the Acoustical Society of America*, Vol. 117, No. 5, 2005, pp. 2835–2843. doi:10.1121/1.1887126, URL <https://doi.org/10.1121/1.1887126>.
- [87] Waki, Y., Mace, B., and Brennan, M., “Numerical issues concerning the wave and finite element method for free and forced vibrations of waveguides,” *Journal of Sound and Vibration*, Vol. 327, 2009, pp. 92–108. doi:/10.1016/j.jsv.2009.06.005.
- [88] Duhamel, D., “Finite element computation of Green’s functions,” *Engineering Analysis with Boundary Elements*, Vol. 31, No. 11, 2007, pp. 919 – 930. doi:/10.1016/j.enganabound.2007.04.002, URL <http://www.sciencedirect.com/science/article/pii/S0955799707000781>.
- [89] Manconi, E., and Mace, B. R., “Modelling wave propagation in two dimensional structures using finite element analysis,” *Journal of Sound and Vibration*, Vol. 318(4–5), 2008, pp. 884–902. doi:/10.1016/j.jsv.2008.04.039.
- [90] Manconi, E., and Mace, B. R., “Wave characterization of cylindrical and curved panels using a finite element method,” *The Journal of the Acoustical Society of America*, Vol. 125, No. 1, 2009, pp. 154–163. doi:/10.1121/1.3021418.
- [91] Manconi, E., and Mace, B. R., “Estimation of the loss factor of viscoelastic laminated panels from finite element analysis,” *Journal of Sound and Vibration*, Vol. 329, No. 19, 2010, pp. 3928 – 3939. doi:/10.1016/j.jsv.2010.04.014.
- [92] Collet, M., Ouisse, M., Ruzzene, M., and Ichchou, M., “Floquet–Bloch decomposition for the computation of dispersion of two-dimensional periodic, damped mechanical systems,” *International Journal of Solids and Structures*, Vol. 48, No. 20, 2011, pp. 2837 – 2848. doi:/10.1016/j.ijsolstr.2011.06.002, URL <http://www.sciencedirect.com/science/article/pii/S0020768311002125>.
- [93] Bouchoucha, F., Ichchou, M. N., and Haddar, M., “Stochastic wave finite element method in uncertain elastic media through the second order perturbation,” *Journal of Applied Mechanics and Technical Physics*, Vol. 58, No. 2, 2017, pp. 362–370. doi:10.1134/S0021894417020225, URL <https://doi.org/10.1134/S0021894417020225>.
- [94] Fan, Y., Collet, M., Ichchou, M., Li, L., Bareille, O., and Dimitrijevic, Z., “Enhanced wave and finite element method for wave propagation and forced response prediction in periodic piezoelectric structures,” *Chinese Journal of Aeronautics*, Vol. 30, No. 1, 2017, pp. 75 – 87. doi:/10.1016/j.cja.2016.12.011, URL <http://www.sciencedirect.com/science/article/pii/S1000936116302308>.
- [95] Droz, C., Zhou, C., Ichchou, M., and Laine, J.-P., “A hybrid wave-mode formulation for the vibro-acoustic analysis of 2D periodic structures,” *Journal of Sound and Vibration*, Vol. 363, 2016, pp. 285–302. doi:/10.1016/j.jsv.2015.11.003.

- [96] Droz, C., Laine, J.-P., Ichchou, M., and Inquiere, G., “A reduced formulation for the free-wave propagation analysis in composite structures,” *Composite Structures*, Vol. 113, 2014, pp. 134–144. doi:/10.1016/j.compstruct.2014.03.017.
- [97] Zhou, C., Laine, J.-P., Ichchou, M., and Zine, A., “Wave Finite Element Method Based on Reduced Model for One-Dimensional Periodic Structures,” *International Journal of Applied Mechanics*, Vol. 7 (2), 2015, pp. 32–47. doi:/10.1142/S1758825115500180.
- [98] Zhou, C., Lainé, J., Ichchou, M., and Zine, A., “Multi-scale modelling for two-dimensional periodic structures using a combined mode/wave based approach,” *Computers & Structures*, Vol. 154, 2015, pp. 145 – 162. doi:https://doi.org/10.1016/j.compstruc.2015.03.006, URL <http://www.sciencedirect.com/science/article/pii/S0045794915000887>.
- [99] Serra, Q., Ichchou, M., and Deü, J.-F., “Wave properties in poroelastic media using a Wave Finite Element Method,” *Journal of Sound and Vibration*, Vol. 335, 2015, pp. 125–146. doi:/10.1016/j.jsv.2014.09.022.
- [100] Manconi, E., Mace, B. R., and Garziera, R., “The loss-factor of pre-stressed laminated curved panels and cylinders using a wave and finite element method,” *Journal of Sound and Vibration*, Vol. 332, No. 7, 2013, pp. 1704 – 1711. doi:/10.1016/j.jsv.2012.09.039.
- [101] Morsbol, J., and Sorokin, S., “Elastic wave propagation in curved flexible pipes,” *International Journal of Solids and Structures*, Vol. 75–76, 2015, pp. 143–155. doi:/10.1016/j.ijsolstr.2015.08.009.
- [102] Mencik, J.-M., “A wave finite element approach for the analysis of periodic structures with cyclic symmetry in dynamic substructuring,” *Journal of Sound and Vibration*, Vol. 431, 2018, pp. 441 – 457. doi:/10.1016/j.jsv.2018.05.027, URL <http://www.sciencedirect.com/science/article/pii/S0022460X18303171>.
- [103] Chronopoulos, D., “Prediction of the vibroacoustic response of aerospace composite structures in a broadband frequency range,” *PhD thesis*, Vol. Ecole Centrale de Lyon, 2012.
- [104] Renno, J. M., and Mace, B. R., “Vibration modelling of structural networks using a hybrid finite element/wave and finite element approach,” *Wave Motion*, Vol. 51, No. 4, 2014, pp. 566–580. doi:/10.1016/j.wavemoti.2013.09.001.
- [105] Renno, J., and Mace, B., “Calculating the forced response of cylinders using the wave and finite element method,” *Journal of Sound and Vibration*, Vol. 333, 2014, pp. 5340–5355. doi:/10.1016/j.jsv.2014.04.042.
- [106] Errico, F., Ichchou, M., De Rosa, S., Bareille, O., and Franco, F., “A WFE and hybrid FE/WFE technique for the forced response of stiffened cylinders,” *Advances in Aircraft and Spacecraft Science, An Int’l Journal*, Vol. 5 (1), 2018, pp. 1–16. doi:/10.12989/aas.2018.5.1.0012.
- [107] Errico, F., Ichchou, M., De Rosa, S., Bareille, O., and Franco, F., “The modelling of the flow-induced vibrations of periodic flat and axial-symmetric structures with a wave-based method,” *Journal of Sound and Vibration*, Vol. 424, 2018, pp. 32–47. doi:/10.1016/j.jsv.2018.03.012.
- [108] Lang, M. A., and Dym, C. L., “Optimal acoustic design of sandwich panels,” *The Journal of the Acoustical Society of America*, Vol. 57, No. 6, 1975, pp. 1481–1487. doi:10.1121/1.380588, URL <https://doi.org/10.1121/1.380588>.
- [109] Moore, J. A., and Lyon, R. H., “Sound transmission loss characteristics of sandwich panel constructions,” *The Journal of the Acoustical Society of America*, Vol. 89, No. 2, 1991, pp. 777–791. doi:10.1121/1.1894638, URL <https://doi.org/10.1121/1.1894638>.

- [110] Dym, C. L., Ventres, C. S., and Lang, M. A., “Transmission of sound through sandwich panels: A reconsideration,” *The Journal of the Acoustical Society of America*, Vol. 59, No. 2, 1976, pp. 364–367. doi:10.1121/1.380871, URL <https://doi.org/10.1121/1.380871>.
- [111] Dym, C. L., and Lang, M. A., “Transmission of sound through sandwich panels,” *The Journal of the Acoustical Society of America*, Vol. 56, No. 5, 1974, pp. 1523–1532. doi:10.1121/1.1903474, URL <https://doi.org/10.1121/1.1903474>.
- [112] Kurtze, G., and Watters, B. G., “New Wall Design for High Transmission Loss or High Damping,” *The Journal of the Acoustical Society of America*, Vol. 31, No. 6, 1959, pp. 739–748. doi:10.1121/1.1907780, URL <https://doi.org/10.1121/1.1907780>.
- [113] Franco, F., Cunefare, K. A., and Ruzzene, M., “Structural-Acoustic Optimization of Sandwich Panels,” *ASME J. Vib. Acoust*, Vol. 129 (3), 2006, pp. 330–340. doi:10.1115/1.2731410.
- [114] Fahy, F., “Statistical energy analysis: a critical overview,” *A.J. Keane, W.G. Price (Eds.), Statistical Energy Analysis: An Overview, with Applications in Structural Dynamics*, Cambridge University Press, Cambridge, 1997.
- [115] Clarkson, B., and Ranky, M., “Modal density of honeycomb plates,” *Journal of Sound and Vibration*, Vol. 91, No. 1, 1983, pp. 103 – 118. doi:[https://doi.org/10.1016/0022-460X\(83\)90454-6](https://doi.org/10.1016/0022-460X(83)90454-6), URL <http://www.sciencedirect.com/science/article/pii/0022460X83904546>.
- [116] Han, J., Yu, K., Li, X., and Zhao, R., “Modal density of sandwich panels based on an improved ordinary sandwich panel theory,” *Composite Structures*, Vol. 131, 2015, pp. 927 – 938. doi: <https://doi.org/10.1016/j.compstruct.2015.06.039>, URL <http://www.sciencedirect.com/science/article/pii/S0263822315005036>.
- [117] Renji, K., Nair, P., and Narayanan, S., “MODAL DENSITY OF COMPOSITE HONEY-COMB SANDWICH PANELS,” *Journal of Sound and Vibration*, Vol. 195, No. 5, 1996, pp. 687 – 699. doi:<https://doi.org/10.1006/jsvi.1996.0456>, URL <http://www.sciencedirect.com/science/article/pii/S0022460X96904563>.
- [118] Palumbo, D. L., and Klos, J., “Development of quiet honeycomb panels, Virginia, Langley Research Center; NASA/TM-2009-215954,” , 2009.
- [119] Grosveld, F. W., Palumbo, D. L., Klos, J., and Castle, W. D., “Finite element development of honeycomb panel configurations with improved transmission loss,” *INTER-NOISE 2006 - 35th International Congress and Exposition on Noise Control Engineering; 3-6 Dec. 2006; Honolulu, HI; United States (2006)*, 2006.
- [120] Hambric, S., Shepherd, M., Koudela, K., Wess, D., Snider, R., May, C., Kendrick, P., Lee, E., and Cai, L.-W., “Acoustically Tailored Composite Rotorcraft Fuselage Panels, Virginia, Langley Research Center; NASA/CR-2015-218769,” , 2015.
- [121] Baho, O., Zergoune, Z., Ichchou, M., Harras, B., Benamar, R., Troclet, B., and Bareille, O., “On global bending–shear core transition effects for the vibroacoustic of sandwich structures: Analytical and numerical investigations,” *Composite Structures*, Vol. 154, 2016, pp. 453 – 463. doi:<https://doi.org/10.1016/j.compstruct.2016.07.062>, URL <http://www.sciencedirect.com/science/article/pii/S0263822316312909>.
- [122] Zergoune, Z., Ichchou, M., Bareille, O., Harras, B., Benamar, R., and Troclet, B., “Assessments of shear core effects on sound transmission loss through sandwich panels using a two-scale approach,” *Computers & Structures*, Vol. 182, 2017, pp. 227 – 237. doi:<https://doi.org/10.1016/j.compstruc.2016.11.017>, URL <http://www.sciencedirect.com/science/article/pii/S0045794916304217>.

- [123] Droz, C., Zergoune, Z., Boukadia, R., Bareille, O., and Ichchou, M., “Vibro-acoustic optimisation of sandwich panels using the wave/finite element method,” *Composite Structures*, Vol. 156, 2016, pp. 108 – 114. doi:<https://doi.org/10.1016/j.compstruct.2016.01.025>, URL <http://www.sciencedirect.com/science/article/pii/S0263822316000386>, 70th Anniversary of Professor J. N. Reddy.
- [124] Claeys, C., Sas, P., and Desmet, W., “On the acoustic radiation efficiency of local resonance based stop band materials,” *Journal of Sound and Vibration*, Vol. 333, No. 14, 2014, pp. 3203 – 3213. doi:<https://doi.org/10.1016/j.jsv.2014.03.019>, URL <http://www.sciencedirect.com/science/article/pii/S0022460X14001990>.
- [125] Claeys, C., Vergote, K., Sas, P., and Desmet, W., “On the potential of tuned resonators to obtain low-frequency vibrational stop bands in periodic panels,” *Journal of Sound and Vibration*, Vol. 332, No. 6, 2013, pp. 1418 – 1436. doi:<https://doi.org/10.1016/j.jsv.2012.09.047>, URL <http://www.sciencedirect.com/science/article/pii/S0022460X1200853X>.
- [126] Liu, Z., Rumpler, R., and Feng, L., “Broadband locally resonant metamaterial sandwich plate for improved noise insulation in the coincidence region,” *Composite Structures*, Vol. 200, 2018, pp. 165 – 172. doi:<https://doi.org/10.1016/j.compstruct.2018.05.033>, URL <http://www.sciencedirect.com/science/article/pii/S0263822318303520>.
- [127] Liu, Z., Rumpler, R., and Feng, L., “Investigation of the sound transmission through a locally resonant metamaterial cylindrical shell in the ring frequency region,” *Journal of Applied Physics*, Vol. 125, No. 11, 2019, p. 115105. doi:10.1063/1.5081134.
- [128] Arnold, R. N., Warburton, G. B., and Born, M., “Flexural vibrations of the walls of thin cylindrical shells having freely supported ends,” *Proceedings of the Royal Society of London. Series A. Mathematical and Physical Sciences*, Vol. 197, 1949, pp. 238–256. doi:10.1098/rspa.1949.0061.
- [129] Hoppmann, W. H., “Some Characteristics of the Flexural Vibrations of Orthogonally Stiffened Cylindrical Shells,” *The Journal of the Acoustical Society of America*, Vol. 30, 1958, pp. 77–82. doi:10.1121/1.1909392.
- [130] Mustafa, B. A. J., and Ali, R., “Prediction of natural frequency of vibration of stiffened cylindrical shells and orthogonally stiffened curved panels,” *Journal of Sound and Vibration*, Vol. 113, 1987, pp. 317–327. doi:10.1016/S0022-460X(87)80218-3.
- [131] Mustafa, B. A. J., and Ali, R., “Sound transmission through curved aircraft panels with stringer and ring frame attachments,” *Journal of Sound and Vibration*, Vol. 300, 2007, pp. 949–973. doi:10.1016/j.jsv.2006.09.008.
- [132] Lee, J.-H., and Kim, J., “Analysis of sound transmission through periodically stiffened panels by space harmonic expansion,” *Journal of Sound and Vibration*, Vol. 251, 2002, pp. 349–366. doi:10.1006/jsvi.2001.4008.
- [133] Mejdi, A., and Atalla, N., “Dynamic and acoustic response of bidirectionally stiffened plates with eccentric stiffeners subject to airborne and structure-borne excitations,” *Journal of Sound and Vibration*, Vol. 329, 2010, pp. 4422–4439. doi:10.1016/j.jsv.2010.04.007.
- [134] Lin, T. R., and Pan, J., “A closed form solution for the dynamic response of finite ribbed plates,” *The Journal of the Acoustical Society of America*, Vol. 119, 2010, pp. 917–925. doi:10.1121/1.2146111.
- [135] Mace, B. R., “Periodically stiffened fluid-loaded plates, I: Response to convected harmonic pressure and free wave propagation,” *Journal of Sound and Vibration*, Vol. 73, 1980, pp. 473–486. doi:10.1016/0022-460X(80)90662-8.

- [136] Mace, B. R., “Periodically stiffened fluid-loaded plates, II: Response to line and point forces,” *Journal of Sound and Vibration*, Vol. 73, 1980, pp. 487–504. doi:10.1016/0022-460X(80)90663-X.
- [137] Maxit, L., “Wavenumber space and physical space responses of a periodically ribbed plate to a point drive: A discrete approach,” *Applied Acoustics*, Vol. 70, 2009, pp. 563–578. doi:10.1016/j.apacoust.2008.06.012.
- [138] Mejdi, A., and Atalla, N., “Vibroacoustic analysis of laminated composite panels stiffened by complex laminated composite stiffeners,” *International Journal of Mechanical Sciences*, Vol. 58, 2012, pp. 13–26. doi:10.1016/j.ijmecsci.2012.02.003.
- [139] Williams, E. G., Houston, B. H., and Bucaro, J. A., “Broadband nearfield acoustical holography for vibrating cylinders,” *The Journal of the Acoustical Society of America*, Vol. 86, 1990, pp. 674–679. doi:10.1121/1.398245.
- [140] Williams, E. G., Houston, B. H., and Bucaro, J. A., “Experimental investigation of the wave propagation on a point-driven, submerged capped cylinder using K-space analysis,” *The Journal of the Acoustical Society of America*, Vol. 87, 1990, pp. 513–522. doi:10.1121/1.398922.
- [141] Photiadis, D. M., Houston, B. H., and Williams, E. G., “Wave-number space response of a near periodically ribbed shell,” *The Journal of the Acoustical Society of America*, Vol. 101, 1997, pp. 877–886. doi:10.1121/1.418108.
- [142] Meyer, V., Maxit, L., Renou, Y., and Audoly, C., “Experimental investigation of the influence of internal frames on the vibroacoustic behavior of a stiffened cylindrical shell using wavenumber analysis,” *Mechanical Systems and Signal Processing*, Vol. 93, 2017, pp. 104–117. doi:10.1016/j.ymsp.2017.01.039.
- [143] Laulagnet, B., and Guyader, J., “Sound radiation by finite cylindrical ring stiffened shells,” *Journal of Sound and Vibration*, Vol. 138, No. 2, 1990, pp. 173 – 191. doi:https://doi.org/10.1016/0022-460X(90)90536-9, URL <http://www.sciencedirect.com/science/article/pii/0022460X90905369>.
- [144] LEE, J.-H., and KIM, J., “SOUND TRANSMISSION THROUGH PERIODICALLY STIFFENED CYLINDRICAL SHELLS,” *Journal of Sound and Vibration*, Vol. 251, No. 3, 2002, pp. 431 – 456. doi:https://doi.org/10.1006/jsvi.2001.4009, URL <http://www.sciencedirect.com/science/article/pii/S0022460X0194009X>.
- [145] Liao, C.-J., Jiang, W.-K., Duan, H., and Wang, Y., “Vibration and sound radiation from submerged finite cylindrical shells reinforced with axially periodic stiffeners,” *Journal of Vibration and Control*, Vol. 17, No. 10, 2011, pp. 1472–1480. doi:10.1177/1077546310380515, URL <https://doi.org/10.1177/1077546310380515>.
- [146] Chronopoulos, D., Ichchou, M., Troclet, B., and Bareille, O., “Computing the broadband vibroacoustic response of arbitrarily thick layered panels by a wave finite element approach,” *Applied Acoustics*, Vol. 77, 2014, pp. 89–98. doi:10.1016/j.apacoust.2013.10.002.
- [147] D’Alessandro, V., “Investigation and Assessment of the wave and finite element method for structural waveguides,” *PhD thesis*, Vol. University of Naples Federico II, 2014. URL <http://www.fedoa.unina.it/9931/>.
- [148] Mitrou, G., Ferguson, N., and Renno, J., “Wave transmission through two-dimensional structures by the hybrid FE/WFE approach,” *Journal of Sound and Vibration*, Vol. 389, 2017, pp. 484 – 501. doi:https://doi.org/10.1016/j.jsv.2016.09.032, URL <http://www.sciencedirect.com/science/article/pii/S0022460X16305004>.

- [149] Groby, J.-P., Wirgin, A., De Ryck, L., Lauriks, W., Gilbert, R. P., and Xu, Y. S., “Acoustic response of a rigid-frame porous medium plate with a periodic set of inclusions,” *The Journal of the Acoustical Society of America*, Vol. 126, No. 2, 2009, pp. 685–693. doi:/10.1121/1.3158936.
- [150] Chronopoulos, D., Troclet, B., Bareille, O., and Ichchou, M., “Modeling the response of composite panels by a dynamic stiffness approach,” *Composite Structures*, Vol. 96, 2013, pp. 111–120. doi:/10.1016/j.compstruct.2012.08.047.
- [151] Li, Y., Zhang, Y., and Kennedy, D., “Random Vibration analysis of axially compressed cylindrical shells under turbulent boundary layer in a symplectic system,” *Journal of Sound and Vibrations*, Vol. 406, 2017, pp. 161–180. doi:/10.1016/j.jsv.2017.06.018.
- [152] Renno, J. M., and Mace, B. R., “Calculating the forced response of cylinders and cylindrical shells using the wave and finite element method,” *Journal of Sound and Vibration*, Vol. 333, No. 21, 2014, pp. 5340–5355. doi:/10.1016/j.jsv.2014.04.042.
- [153] Christen, J.-L., Ichchou, M., Zine, A., and Troclet, B., “Wave Finite Element Formulation of the Acoustic Transmission Through Complex Infinite Plates,” *Acta Acustica united with Acustica*, Vol. 102(6), 2016, pp. 984–991. doi:/10.3813/AAA.919013.
- [154] Yang, Y., Mace, B., and Kingan, M., “Prediction of sound transmission through, and radiation from, panels using a wave and finite element method,” *J. Acoust. Soc. Am.*, Vol. 141 (4), 2017, pp. 2452–2460. doi:/10.1121/1.4977925.
- [155] Kingan, M., Yang, Y., and Mace, B., “Application of the Wave and Finite Element Method to Calculate Sound Transmission Through Cylindrical Structures,” *Journal of Physics: Conference Series*, Vol. 744, No. 1, 2016, p. 012240. URL <http://stacks.iop.org/1742-6596/744/i=1/a=012240>.
- [156] Mace, B., “Sound radiation from fluid loaded orthogonally stiffened plates,” *Journal of Sound and Vibration*, Vol. 79, No. 3, 1981, pp. 439–452. doi:[https://doi.org/10.1016/0022-460X\(81\)90321-7](https://doi.org/10.1016/0022-460X(81)90321-7).
- [157] Serra, Q., Ichchou, M., and Deü, J.-F., “A wave based condensation method for computing the acoustic efficiency of sound packages submitted to sliding or clamped lateral boundary conditions,” *International Conference on Noise and Vibration Engineering (ISMA 2014)*, 2014. URL <https://hal.archives-ouvertes.fr/hal-01699540>.
- [158] Kesour, K., and Atalla, N., “A hybrid patch transfer-Green functions method to solve transmission loss problems of flat single and double walls with attached sound packages,” *Journal of Sound and Vibration*, Vol. 429, 2018, pp. 1–17. doi:<https://doi.org/10.1016/j.jsv.2018.05.008>, URL <http://www.sciencedirect.com/science/article/pii/S0022460X18302827>.
- [159] Barisciano Jr, L., “Broadband transmission loss due to reverberant excitation,” *NASA/CR-1999-209687, Langley Research Center, Hampton, Virginia*, 1999.
- [160] De Rosa, S., Franco, F., and Gaudino, D., “Numerical investigations on the turbulence driven responses of a plate in the subcritical frequency range,” *Wind and Structures: an International Journal*, Vol. 15 (3), 2012, pp. 247–261.
- [161] Acoustics, “Measurement of sound insulation in buildings and of building elements using sound intensity – Part 1: Laboratory measurements ISO 15186-1:2000, International Standard Organization, Geneva,” , 2000.
- [162] ASTM-International-E2249-02, “Standard Test Method for Laboratory Measurement of Airborne Sound Transmission Loss of Building Partitions and Elements using Sound Intensity, West Conshohocken,” , 2016.

- [163] Schroeder, M. R., “The Schroeder frequency revisited,” *The Journal of the Acoustical Society of America*, Vol. 99, No. 5, 1996, pp. 3240–3241. doi:/10.1121/1.4148682.
- [164] London, A., *Transmission of Reverberant Sound Through Single Walls, Department of Commerce National Bureau of Standard, Part of the Journal of Research of the National Bureau of Standards 42*, Vol. 42, 1949.
- [165] Robin, O., Amedin, C., Berry, A., Atalla, N., Doutres, O., , and Sgard, F., “Sound Absorption Measurements: Comparison of Standard Tests in Reverberant Room with Measurements using a Synthetized Diffuse Acoustic Field,” *Internoise 2016, Hamburg*, 2016.
- [166] Errico, F., Ichchou, M., Franco, F., De Rosa, S., Bareille, O., and Droz, C., “Schemes for the sound transmission of flat, curved and axisymmetric structures excited by aerodynamic and acoustic sources,” *Journal of Sound and Vibration*, Vol. 476, 2019, pp. 221–238. doi:/10.1016/j.jsv.2019.05.041.
- [167] Rodden, W., Farkas, E., Malcom, H., and Kliszewski, A., *Aerodynamic Influence Coefficients from Supersonic Strip Theory: Analytical Development and Computational Procedure*, Defense Technical Information Center, 1962. URL <https://books.google.fr/books?id=pBi5twAACAAJ>.
- [168] Sgard, F., Atalla, N., and Nicolas, J., “Coupled FEM-BEM approach for mean flow effects on vibro-acoustic behavior of planar structures,” *AIAA Journal*, Vol. 32, No. 12, 1994, pp. 2351–2358. doi:10.2514/3.12299, URL <https://doi.org/10.2514/3.12299>.
- [169] Maestrello, L., “Radiation from and panel response to a supersonic turbulent boundary layer,” *Journal of Sound and Vibration*, Vol. 10, No. 2, 1969, pp. 261 – 295. doi:[https://doi.org/10.1016/0022-460X\(69\)90200-4](https://doi.org/10.1016/0022-460X(69)90200-4), URL <http://www.sciencedirect.com/science/article/pii/0022460X69902004>.
- [170] Kariappa, O., Shah, C., and Somashekar, B., “Discrete element approach to flutter of skew panels with in-plane forces under yawed supersonic flow,” *AIAA Journal*, Vol. 8 (11), 1970, pp. 2017–2022. doi:/10.2514/3.6040.
- [171] Krumhaar, H., “The accuracy of linear piston theory when applied to cylindrical shells,” *AIAA Journal*, Vol. 1 (6), 1963, pp. 1448–1449. doi:/10.2514/3.1832.
- [172] Leissa, A., “Vibration of Plates,” *Scientific and Technical Information Division, National Aeronautics and Space Administration*, Vol. 160, 1969.
- [173] Croccolo, D., Agostinis, M. D., and Olmi, G., “Experimental characterization and analytical modelling of the mechanical behaviour of fused deposition processed parts made of ABS-M30,” *Computational Materials Science*, Vol. 79, 2013, pp. 506 – 518. doi:/10.1016/j.commatsci.2013.06.041, URL <http://www.sciencedirect.com/science/article/pii/S0927025613003741>.
- [174] Rosa, S. D., Capobianco, M., Nappo, G., and Pagnozzi, G., “Models and comparisons for the evaluation of the sound transmission loss of panels,” *Proceedings of the Institution of Mechanical Engineers, Part C: Journal of Mechanical Engineering Science*, Vol. 228, No. 18, 2014, pp. 3343–3355. doi:10.1177/0954406214530597, URL <https://doi.org/10.1177/0954406214530597>.
- [175] Errico, F., Ichchou, M., Franco, F., De Rosa, S., Bareille, O., and Droz, C., “Schemes for the sound transmission of flat, curved and axisymmetric structures excited by aerodynamic and acoustic sources,” *Journal of Sound and Vibration*, Vol. 476, 2019, pp. 221–238. doi:/10.1016/j.jsv.2019.05.041.

- [176] Errico, F., Tufano, G., Robin, O., Guenfoud, N., Ichchou, M., and Atalla, N., “Simulating the sound transmission loss of complex curved panels with attached noise control materials using periodic cell wavemodes,” *Applied Acoustics*, Vol. 156, 2019, pp. 21 – 28. doi:<https://doi.org/10.1016/j.apacoust.2019.06.027>, URL <http://www.sciencedirect.com/science/article/pii/S0003682X1930177X>.
- [177] Corcos, G., “Resolution of pressure in turbulence,” *Journal of the Acoustical Society of America*, Vol. 35, 1963, pp. 192–199. doi:[10.1121/1.1918431](https://doi.org/10.1121/1.1918431).
- [178] Ichchou, M., Hiverniau, B., and Troclet, B., “Equivalent ‘rain on the roof’ loads for random spatially correlated excitations in the mid frequency range,” *Journal of Sound and Vibration*, Vol. 322, 2009, pp. 926–940. doi:[10.1016/j.jsv.2008.11.050](https://doi.org/10.1016/j.jsv.2008.11.050).
- [179] Gardonio, P., “Boundary Layer Noise – Part 2: Interior Noise Radiation and Control,” *Springer Vienna*, 2013, pp. 379–448. doi:[10.1007/978-3-7091-1458-2\\_7](https://doi.org/10.1007/978-3-7091-1458-2_7).
- [180] Sandberg, U., and Ejsmont, J., “Tyre/road noise. Reference book.” 2002.
- [181] Kropp, W., “Structure-borne sound on a smooth tyre,” *Applied Acoustics*, Vol. 26, No. 3, 1989, pp. 181 – 192. doi:[https://doi.org/10.1016/0003-682X\(89\)90051-0](https://doi.org/10.1016/0003-682X(89)90051-0), URL <http://www.sciencedirect.com/science/article/pii/0003682X89900510>.
- [182] Czuka, M., Pallas, M. A., Morgan, P., and Conter, M., “Impact of Potential and Dedicated Tyres of Electric Vehicles on the Tyre-road Noise and Connection to the EU Noise Label,” *Transportation Research Procedia*, Vol. 14, 2016, pp. 2678 – 2687. doi:<https://doi.org/10.1016/j.trpro.2016.05.443>, URL <http://www.sciencedirect.com/science/article/pii/S2352146516304501>, transport Research Arena TRA2016.
- [183] Kim, Y.-J., and Bolton, J., “Effects of rotation on the dynamics of a circular cylindrical shell with application to tire vibration,” *Journal of Sound and Vibration*, Vol. 275, No. 3, 2004, pp. 605 – 621. doi:<https://doi.org/10.1016/j.jsv.2003.06.003>, URL <http://www.sciencedirect.com/science/article/pii/S0022460X03008575>.
- [184] Kindt, P., Sas, P., and Desmet, W., “Measurement and analysis of rolling tire vibrations,” *Optics and Lasers in Engineering*, Vol. 47, No. 3, 2009, pp. 443 – 453. doi:<https://doi.org/10.1016/j.optlaseng.2008.06.017>, URL <http://www.sciencedirect.com/science/article/pii/S0143816608001516>, optical Measurements.
- [185] Brinkmeier, M., Nackenhorst, U., Petersen, S., and von Estorff, O., “A finite element approach for the simulation of tire rolling noise,” *Journal of Sound and Vibration*, Vol. 309, No. 1, 2008, pp. 20 – 39. doi:<https://doi.org/10.1016/j.jsv.2006.11.040>, URL <http://www.sciencedirect.com/science/article/pii/S0022460X07001198>.
- [186] Cho, J., Kim, K., and Jeong, H., “Numerical investigation of tire standing wave using 3-D patterned tire model,” *Journal of Sound and Vibration*, Vol. 305, No. 4, 2007, pp. 795 – 807. doi:<https://doi.org/10.1016/j.jsv.2007.04.049>, URL <http://www.sciencedirect.com/science/article/pii/S0022460X0700346X>.
- [187] Pinnington, R., “A wave model of a circular tyre. Part 1: belt modelling,” *Journal of Sound and Vibration*, Vol. 290, No. 1, 2006, pp. 101 – 132. doi:<https://doi.org/10.1016/j.jsv.2005.03.023>, URL <http://www.sciencedirect.com/science/article/pii/S0022460X05002634>.
- [188] Grip, M., “The tyre,” 2001.

- [189] Waki, Y., Mace, B., and Brennan, M., “Free and forced vibrations of a tyre using a wave/finite element approach,” *Journal of Sound and Vibration*, Vol. 323, No. 3, 2009, pp. 737 – 756. doi: <https://doi.org/10.1016/j.jsv.2009.01.006>, URL <http://www.sciencedirect.com/science/article/pii/S0022460X09000145>.
- [190] Cook, R., Malkus, D., Plesha, M., and Witt, R., “Concepts and Applications of Finite Element Analysis,” *John Wiley & Sons Inc*, 2001.
- [191] Cremer, L., Heckl, M., and Petersson, B., “Structure-Borne Sound - Structural Vibrations and Sound Radiation at Audio Frequencies,” *Springer*, 2005. doi:/10.1007/b137728.
- [192] Love, A., “The small free vibrations and deformation of a thin elastic shell,” *Philosophical Transactions of the Royal Society of London A: Mathematical, Physical and Engineering Sciences*, Vol. 179, 1888, pp. 491–546. doi:/10.1098/rsta.1888.0016.
- [193] “Mechanics of composite materials,” *Taylor & Francis*, 1999.
- [194] Mace, B., Duhamel, D., Brennan, M., and Hinke, L., “Finite element prediction of wave motion in structural waveguides,” *The Journal of Acoustical Society of America*, Vol. 117, 2005, pp. 2835–2843. doi:/10.1121/1.1887126.
- [195] Shorter, P., “Wave propagation and damping in linear viscoelastic laminates,” *The Journal of the Acoustical Society of America*, Vol. 115, 2004, pp. 1917–1925. doi:/10.1121/1.1689342.
- [196] Chitnis, M., Desai, Y., and Kant, T., “Wave propagation in laminated composite plates using higher order theory,” *Journal of Applied Mechanics*, Vol. 68 (3), 2001, pp. 503–505. doi:/10.1115/1.1352062.
- [197] Baz, A., “Spectral nite-element modelling of the longitudinal wave propagation in rods treated with active constrained layer damping,” *Smart Materials and Structures*, Vol. 9, 2000, pp. 372–377. doi:/10.1088/0964-1726/9/3/319.
- [198] Chakraborty, A., and Gopalakrishnan, S., “A Spectral Finite Element Model for Wave Propagation Analysis in Laminated Composite Plate,” *Journal of Vibration and Acoustics*, Vol. 128 (4), 2006, pp. 477–488. doi:/10.1115/1.2203338.
- [199] Magliacano, D., Ouisse, M., Khelif, A., De Rosa, S., Franco, F., and Atalla, N., “Validation of the shift cell approach for the modelling of acoustic properties of porous materials embedding periodic inclusions,” *Novem2018 Conference, Balearic Islands, Spain*, 2018.
- [200] Mead, D. J., and Bardell, N. S., “Free vibration of a thin cylindrical shell with periodic circumferential stiffeners,” *Journal of Sound and Vibration*, Vol. 115 (3), 1987, pp. 499–520. doi:/10.1016/0022-460X(87)90293-8.
- [201] Ghoshal, A., Accorsi, M., and Bennett, M., “Wave propagation in circular cylindrical shells with periodic axial curvature,” *Wave Motion*, Vol. 23, 1996, pp. 339–352. doi:/10.1016/0165-2125(95)00056-9.
- [202] B.Liu, Y.F.Xing, M.S.Qatu, and A.J.M.Ferreira, “Exact characteristic equations for free vibrations of thin orthotropic circular cylindrical shells,” *Composite Structures*, Vol. 94 (2), 2012, pp. 484–493. doi:/10.1016/j.compstruct.2011.08.012.
- [203] Brun, M., Giaccu, G., Movchan, A., and Movchan, N., “Asymptotics of eigenfrequencies in the dynamic response of elongated multi-structures,” *Proceedings of The Royal Society A Mathematical Physical and Engineering Sciences*, Vol. 468, 2012, pp. 378–394. doi:/10.1098/rspa.2011.0415.

- [204] Brun, M., Movchan, A., and Jones, I., “Phononic Band Gap Systems in Structural Mechanics: Finite Slender Elastic Structures and Infinite Periodic Waveguide,” *Journal of Vibration and Acoustics*, Vol. 135, 2013. doi:/10.1115/1.402381.
- [205] Langley, R. S., “Some Perspectives on Wave-Mode Duality in SEA,” *IUTAM Symposium on Statistical Energy Analysis*, 1999, pp. 1–12. doi:/10.1007/978-94-015-9173-7\_1.
- [206] Blevins, R., “Formulas for Natural Frequency and Mode Shape,” *Krieger, Malabar, Florida*, 1979. doi:/10.1121/1.384246.

## AUTORISATION DE SOUTENANCE

Vu les dispositions de l'arrêté du 25 mai 2016,

Vu la demande des directeurs de thèse

Messieurs M. ICHCHOU et S. DE ROSA

et les rapports de

M. R. LEUNG

Maître de Conférences HDR - The Hong-Kong Polytechnic University - 11 Yuk Choi Rd  
Hung Hom - Hong Kong

et de

M. A. BERRY

Professeur - Université de Sherbrooke - GAUS - 2500 Boulevard de l'Université  
Sherbrooke QC J1K 0A5 - Canada

**Monsieur ERRICO Fabrizio**

est autorisé à soutenir une thèse pour l'obtention du grade de **DOCTEUR**

**Ecole doctorale MECANIQUE, ENERGETIQUE, GENIE CIVIL ET ACOUSTIQUE**

Fait à Ecully, le 16 janvier 2020

P/Le directeur de l'E.C.L.  
Le directeur des Etudes



Grégory VIAL